The Dissertation Committee for Todd Christopher Bailey Certifies that this is the approved version of the following dissertation:

Imprint Template Advances and Surface Modification, and Defect Analysis for Step and Flash Imprint Lithography

Committee:

John G. Ekerdt, Supervisor

C. Grant Willson, Supervisor

Roger T. Bonnecaze

Peter F. Green

Sanjay K. Banerjee

Imprint Template Advances and Surface Modification, and Defect Analysis for Step and Flash Imprint Lithography

by

Todd Christopher Bailey, S.B., A.S.

Dissertation

Presented to the Faculty of the Graduate School of

The University of Texas at Austin

in Partial Fulfillment

of the Requirements

for the Degree of

Doctor of Philosophy

The University of Texas at Austin

August, 2003

ProQuest Information and Learning Company
300 North Zeeb Road
PO Box 1346
Ann Arbor, MI 48106-1346

Dedication

This is dedicated to my loving wife, Carla, and to my parents and stepparents.

Acknowledgements

This has been a very long and difficult journey, and I have many people to thank for helping me accomplish this work. This work would not have been possible without Carla's support, and I am forever indebted to her for her patience and understanding. My parents were a source of motivation, and their support guided me through difficult times. I want to thank Drs. John G. Ekerdt and C. Grant Willson for their supervision and guidance, and for challenging my abilities. It was difficult at times answering to two people, but I am glad I had the opportunity to work with them both. I would like to thank Drs. S.V. Sreenivasan and Nicholas A. Stacey, current and former UT SFIL group members Drs. Matthew E. Colburn and Byung Jin Choi, Steve C. Johnson, Britain J. Smith, Kai Wu, Michael D. Dickey, E.K. Kim, and Saleh Shaya for useful discussions, and help designing and building equipment, and planning and carrying out experiments. Special thanks to Kathleen Sparks, Kay Costales-Swift, Tiajuana Stockman, and Eduardo Ibarra, for being integral and supportive Departmental staff. I would also like to thank Dr. Douglas J. Resnick for allowing me to work at Motorola Labs, and Dr. Michael Gostein for allowing me to work at Philips Analytical. Both experiences were very enjoyable, and they were tremendous learning experiences.

I want to thank those who aided in this work: I gratefully acknowledge Dave Mancini for his mentoring, Bill Dauksher, Kevin Nordquist, Eric Ainley, Steve Smith, Dolph Rios, Eric Newlin, David Standfast, Lyndi Noetzel, Lester Casoose, Kathy Palmer and Diane Convey at Motorola Labs for useful discussions, film deposition and characterization, and template processing, Jose Lozano and Yangming Sun for XPS analysis, Andrew Lemonds for TPD analysis, and Paul Kirsch and Ward Engbrecht for help in design and assembly of the vapor pressure system. Special thanks to Dr. David Dickey for statistical analysis discussions; Franklin Kalk, Cece Philbin, and Ric Diola for help in designing and fabricating imprint templates; David Adler, David Soltz, Kirk Bertsche, David Randall, Ernesto Pon, Melissa Gonzales, Lam Nguyen and Dale Sheu for their help in defect analysis; and Daniel Miller, Michael Rich, Georgia Rich and David Stark for supplying the BARC-coated wafers. I thank Motorola Labs, International SEMATECH, KLA-Tencor, and Brewer Science for generous gifts and technical consultation. Special thanks to Michael Becker for help with the modeling code.

To all my friends who helped keep me relatively sane, whether playing golf, throwing social parties, mixing margaritas or mountain biking: I thank you for your time and friendship; this would have been much more difficult without all y’all. Finally, I gratefully acknowledge the financial support of Dr. and Mrs. Z. D. Bonner and DARPA (MDA972-97-1-0010).

Imprint Template Advances and Surface Modification, and Defect Analysis for Step and Flash Imprint Lithography

Publication No._____________

Todd Christopher Bailey, Ph.D.
The University of Texas at Austin, 2003

Supervisors: John G. Ekerdt and C. Grant Willson

Step and flash imprint lithography (SFIL) is a relatively new technique for patterning high-resolution polymer features on planar substrates. This technique has been used to produce features smaller than 30 nm in size through many imprints, pattern a substrate with existing topography, and also to produce functional optical and electric devices. The ultimate manufacturability of SFIL for high-resolution applications depends on the ability to manufacture high-resolution imprint templates, and also to produce imprint fields that are relatively free of defects caused during the imprint process. The primary goal of this work was to investigate the generation and propagation of defects produced during the imprint process, and this involved various material and process development efforts.

A process analogous to that used in the photomask manufacturing process has been created for manufacturing imprint templates with features smaller than 30 nm. Using a thin layer of electron beam resist and a thin Cr film resulted in the

mitigation of the shift in feature sizes during the etching steps. Additionally, by substituting ITO and deposited SiO_2 for the Cr allows similar feature resolution, and the final template possesses charge dissipation capabilities needed for end-of-line inspection. The quality of the surface treatments deposited on the template using a fluoroalkyltrichlorosilane is dependent on the substrate used, and also on the degree of hydration of the substrate. Several materials were tested for compatibility with the current surface treatment, and it was found that deposition of the surface treatment on Si_3N_4 and SiO_xN_y resulted in films that possessed coverage and durability similar to that of SiO_2, but that films deposited on ITO lacked mechanical wear durability. It was found that exposing a dehydrated SiO_2 substrate to water vapor for various times followed by the surface treatment precursor resulted in greater deposition of film species on the surface with increasing water exposure.

A defect analysis was performed for SFIL, and it was discovered that the defect trends over time are strongly dependent on photopolymer material properties. Early results indicated that the dominant failure mode during template/substrate separation was that of cohesive polymer failure. By redesigning the etch barrier material blend, the elongation-to-break of the photopolymer was increased by more than one order of magnitude. This material change resulted in the elimination of the cohesive failure mode, and allowed faithful replication of features through more than 400 imprints. It was discovered that imprint film thickness variations can have a dramatic effect on the pattern contrast. This pattern contrast was modeled for various film thickness combinations, and this effect is believed to impact defect detection in optical inspection equipment.

Table of Contents

List of Tables

List of Figures

INTRODUCTION

Chapter 1: Introduction and Dissertation Focus

1.1 INVENTION OF THE TRANSISTOR AND INTEGRATED CIRCUIT

The history of semiconductor devices began in 1940 when Russell Ohl was trying to create a receiver that would be more effective than vacuum tubes.[1] He examined a silicon sample that had a crack down the middle, and observed that current flowing across the crack jumped significantly when the sample was exposed to light. He had stumbled on a Si sample wherein the material on each side of the crack possessed different impurities, and one side had an excess of electrons, while the other had a deficiency of electrons. Thus, the *p*-*n* junction was discovered.

John Bardeen, Walter Brattain, and William Shockley developed the first solid state transistor in 1947 while at Bell Labs using a configuration known as a "point-contact" transistor. This was further modified by using *p*-*n* junctions in a bipolar transistor configuration. Jack Kilby of Texas Instruments in 1958, and Robert Noyce of Fairchild Semiconductor in 1959, both independently developed working integrated circuits, which combined all the parts of a semiconductor transistor on a single semiconductor crystal. Their discoveries began the modern microelectronics industry.

A modern version of the metal-oxide-semiconductor field effect transistor (MOSFET) is shown in Figure 1.1, which depicts a *p*-channel transistor. The “source” and “drain” regions are Si doped with atoms that have five valence electrons, such as P, creating *n*-type semiconductor material. The “channel,” or the thin region beneath the gate oxide, is doped with atoms that have three valence electrons, such as B, creating *p*-type semiconductor material. The gate oxide provides electrical separation between the gate and the channel, preventing a short circuit; the gate is usually metal or highly doped Si, which behaves as a metal. The bulk Si beneath the transistor is lightly *p*-doped. The dopants participate in bonding in the Si matrix. Those which possess five valence electrons yield a free electron, and those which possess three valence electrons yield an incomplete bond; these charge carriers are known as electrons and holes, or *n*- and *p*-type carriers, respectively.

When there is no voltage applied across the gate, the electrical circuit between the source and drain is incomplete, and ideally no current flows, as in Figure 1.1a. A bias applied to the gate induces a mirror charge under the gate oxide in a thin layer known as the channel. If voltage is then applied across the source and drain regions, the charge in the channel completes the circuit, and allows current to flow, as in Figure 1.1b. A transistor in which current flows from source to drain is in the “on” state, and one in which no current flows is in the “off” state. These states are then used as the true and false or 1 and 0 in Boolean operations.

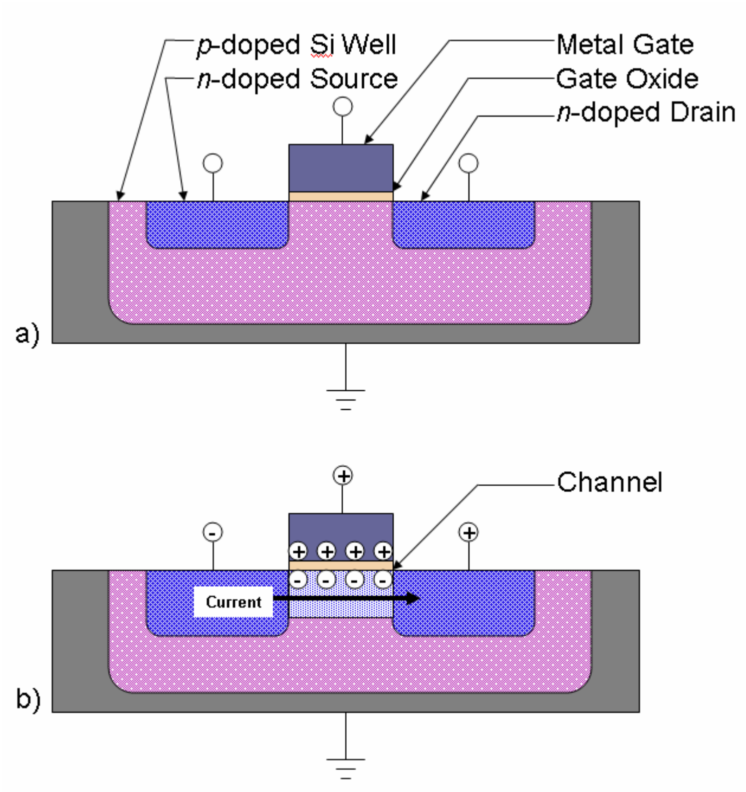

Figure 1.1. Schematic of modern MOSFET in Si in the “off” state (a) and the “on” state (b).

1.2 TECHNOLOGY TRENDS

The drive to produce faster devices, which translates into smaller and more densely packaged devices, is to a degree governed by the need for more computing power. As computer hardware technology advances, so does the complexity and computing power requirements of software. Today’s fastest supercomputer, the NEC Earth Simulator costing $350M, can perform nearly 36,000,000,000 floating point operations per second,[2] and was designed to perform detailed simulations of the Earth’s atmosphere, protein folding, and other applications where supreme computing power is required. Microprocessors produced to handle every-day applications are less powerful, and also much less costly, but the advances in technology are still driven by the need for consumer computing power. The progression of microprocessor technology shows an exponential trend in integrated circuit (IC) density, and minimum critical dimension (CD), over time, and has become known as Moore's Law. In 1965 Gordon Moore noted that the density of transistors on microprocessor chips had doubled every year since the invention of the transistor,[3] and he predicted that the trend would continue. This can be seen pictorially in Figure 1.2, which was adapted from the Semiconductor Industry Association International Technology Roadmap for Semiconductors.[4]

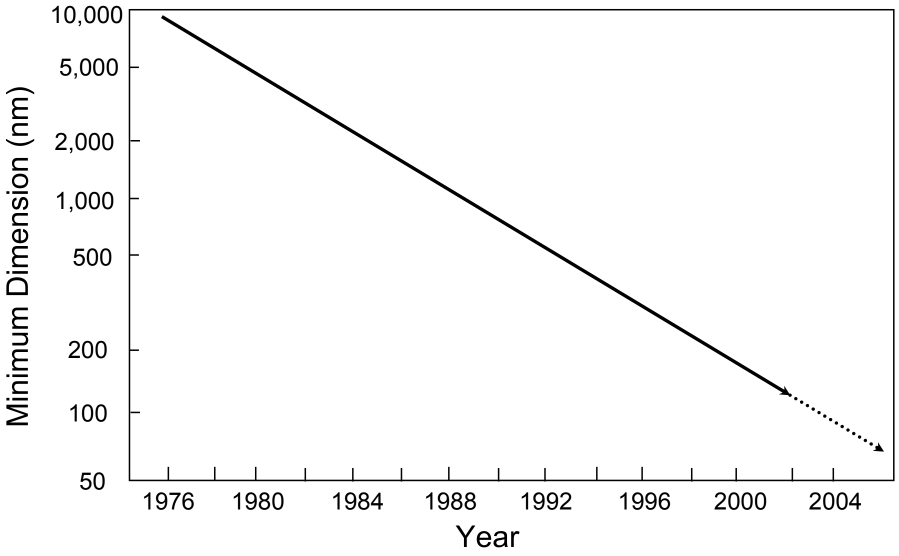

Figure 1.2. Trend of minimum dimension as a function of time.[4]

The speed of a microprocessor is to a large extent a function of the number of transistors on the chip, and reducing the size of the transistor allows this increase in chip density. A benchmark for the ability to increase chip density has been the minimum line width, or critical dimension (CD), of the gate in a MOSFET. The current technology used to pattern these small features is known as photolithography. If this trend in increasing microprocessor density is to continue, photolithography must continue to be a cost-effective solution.

1.3 PHOTOLITHOGRAPHY

A typical photolithography process is shown in Figure 1.3. A Si wafer is coated with a photosensitive compound known as "photoresist", or "resist" for short, which changes in chemical nature upon irradiation to become more or less soluble in a given solvent. Negative tone resists undergo changes upon exposure that reduce the solubility in the exposed regions. Positive tone resists change in chemical nature making them more soluble in developer. The polymer image remaining after removing the more soluble material is then used as an etch mask in a reactive ion etch (RIE) process, which transfers the physical image into the underlying material.

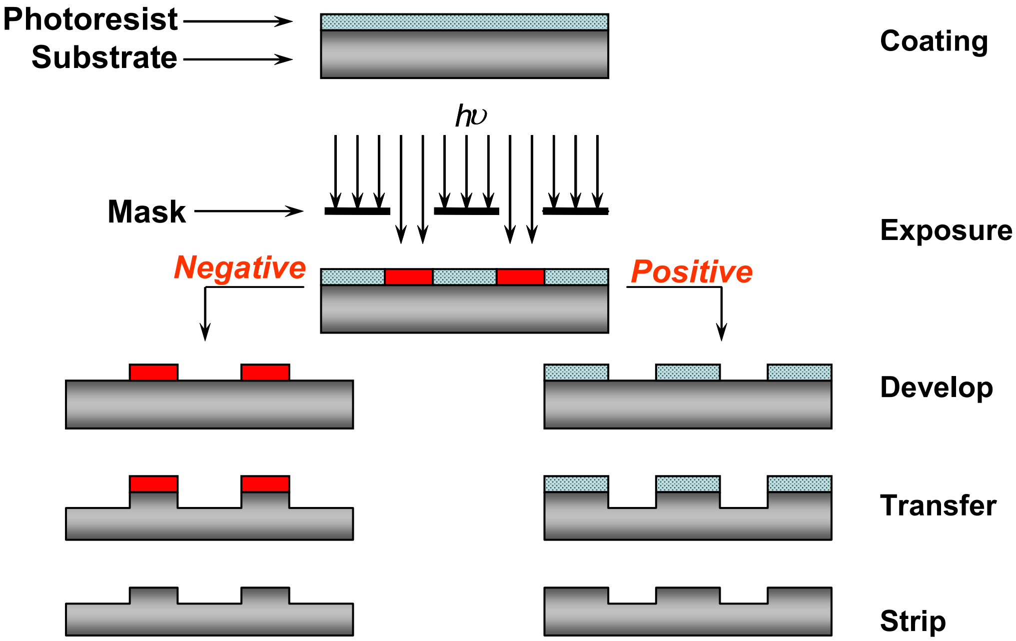

Figure 1.3. Process flow in a typical photolithography process.

The resolution, R, of a conventional projection lithography system is governed by the laws of diffraction and can be simplified to Rayleigh's equation:[5]

Equation 1.1
$$R = k_1 \frac{\lambda}{NA}$$

where k_1 is a system-dependent parameter that includes, for example, resist material properties and lens aberrations, λ is the wavelength of the light, and NA is the numerical aperture of the lens, which describes the lens size and its ability to capture diffracted orders. Reduction in R, or improvement in resolution, can be achieved by modifying the materials and equipment to affect k_1, using a shorter exposure wavelengths, or increasing the NA of the lens system. The k_1 parameter approaches 0.5 in the theoretical limit of diffraction. Increasing the *NA* has an adverse effect on the depth of focus (*DOF*), which describes the aerial image blur through the thickness of the resist:[5]

Equation 1.2
$$DOF = k_2 \frac{\lambda}{(NA)^2}$$

where k_2 is again a system-dependent parameter. There is a balance between increasing *NA* in order to achieve better resolution, and decreasing *NA* in order to achieve larger *DOF*. Many of the significant advances in resolution have come as a result of using shorter exposure wavelengths.

These resolution improvements, along with the use of different wavelengths, require new light sources, new resist materials, new lens materials and systems, and improvements in machine tolerances, among others. These improvements come at a cost, as can be seen in Figure 1.4, which shows the exponentially increasing cost of photolithography tools over time. The next generation lithography (NGL) technologies that are currently expected to allow further resolution improvements may in fact depart upwards from this trend, resulting in an even greater tool cost.

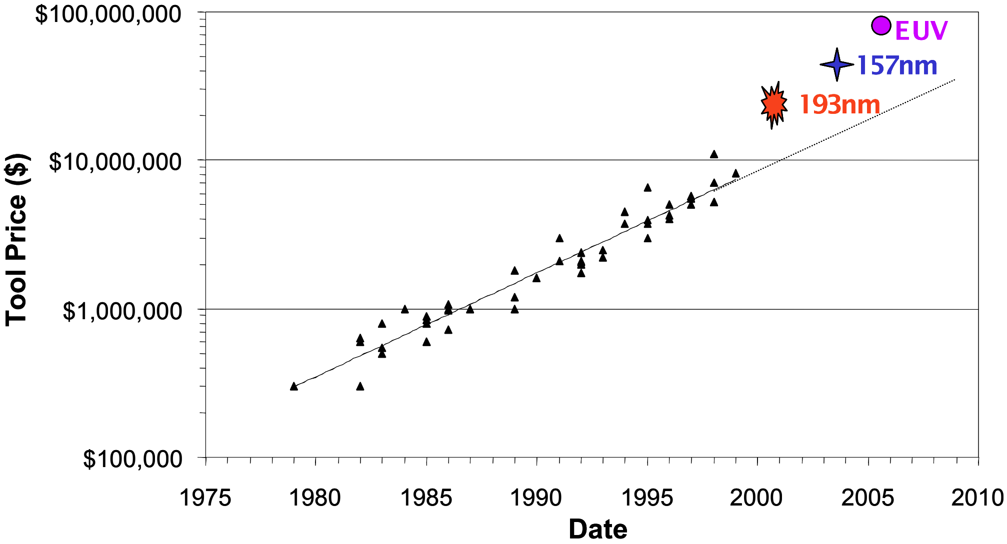

Figure 1.4. Exponential cost of photolithography tools over time. The black triangles are real tool cost data, and the labeled points are projected costs for NGL tools. Figure adapted from the NGL Workshop.[6]

The natural question is whether this trend can continue and still maintain the affordability of consumer microprocessors. One can draw an analogy to commercial air travel – the technology exists to travel beyond the speed of sound (military jets, the Concorde), but that technology is not affordable to the general public. Perhaps this trend of the increasing cost of lithography will result in a similar situation for microprocessors – the technology will exist to produce much faster processors, but the cost of such technology will prohibit including those processors in standard consumer computers. The Semiconductor Industry Association International Technology Roadmap for Semiconductors[7] has identified alternative next generation lithography (NGL) imaging techniques based on X-ray and extreme ultraviolet (EUV) ionizing radiation, as well as techniques based on projection and direct-write electron beam lithography. Each technique has its advantages and disadvantages, and all are expensive. If the mainstream microprocessor technology is to progress, then there must be a significant departure from the lithography cost trend in the near future.

1.4 IMPRINT LITHOGRAPHY

Many research groups are exploring alternative forms of imprint lithography as an inexpensive patterning method capable of sub-100 nm resolution on various substrates.[8-13] Imprint equipment requires precision X-Y stages, layer-to-layer alignment systems, and wafer handling equipment common to other lithography techniques, but imprint lithography realizes significant cost savings because it does not require lasers or projection optics. Imprint lithography has several important advantages over conventional optical lithography and NGL techniques: It is non-optical by design, and the resolution appears to be limited only by the structures that can be generated in a master template. Imprint templates are typically fabricated using imaging tools such as electron beam writers that provide high resolution but lack the throughput required for mass production. By using imprint templates defined by e-beam lithography, imprint lithography makes use of this resolution capability without being limited by e-beam throughput issues. Since the main advances required to improve resolution are expected to be in the area of the imprint template development and process chemistry, an imprint tool built for one technology generation could conceivably extend to future technology nodes.

There are many imprint lithography techniques, all based on the concept that a template or mold with a prefabricated topography is pressed into a displaceable material. This material takes the shape of the pattern defined in the template, and through some curing process, the shaped material is hardened into a solid. Researchers systematically studied imprint lithography techniques in the 1990s.[8-11,14,15] The research approach is divided between imprinting into a thermoplastic or thermoset polymer, and imprinting into an ultraviolet (UV) light-curable material. Chou and coworkers[8,16,17] use an imprint technique based on embossing a thin film of poly(methyl methacrylate) (PMMA), or similar polymer, during a heating cycle that allows the film to conform to a template containing a topography. The group has become quite adept at producing structures that do not require overlay registration. Chou and coworkers have demonstrated high density magnetic storage disks[18] and high density compact disks,[19] waveguide polarizers,[20] photodetectors[21] and light-emitting structures,[22] field effect transistors[23] and single-electron transistor memory,[24] none of which required significant overlay control.

Scheer and coworkers[15,25] have also focused on high temperature imprint lithography, although their work is more related to the fundamentals of imprint patterning. The authors found that the process is limited by material transport, and that pressures of around 100 bar and temperatures 90 ºC above the polymer glass transition temperature (T_g) are optimal for material displacement.[15,25] These studies were performed using imprint molds with a global average pattern density near 50%. The authors conclude that regular repeating patterns and areas in positive tone are ideal for this type of patterning,[15] where "positive" pattern areas are defined to require less material displacement, and conversely for "negative" pattern areas.

Jaszewski, *et al.*[14] have developed a "hot embossing" technique of patterning, which is fundamentally similar to the Chou[8] and Scheer[15] methods. The authors have demonstrated compatibility with metal lift-off techniques using titanium.[14]

These groups and others[26,27] follow the same basic concept: A polymer heated above its T_g is imprinted with a mold. The system is cooled to below the T_g of the polymer while the mold is in contact, thus curing the shape of the imprint. This process is similar in nature to injection molding. There are three serious challenges to face if this technique is to be used for semiconductor or optical devices that require layer-to-layer alignment: (i) heating cycles cause thermal expansion mismatch of template to substrate and are inherently slow relative to desired manufacturing throughput, (ii) non-transparent templates commonly used in this approach make layer-to-layer alignment difficult, and (iii) the high applied pressures that are required to displace high-viscosity polymers such as PMMA cause mechanical distortion and introduce potential for catastrophic failure of brittle underlying semiconductor materials. To address the thermal cycle issue, Chou and coworkers have developed a new set of polymers with lower T_g that enable process temperatures to be reduced to 100 °C.[28] The authors do not disclose the details of the polymer composition, so their work cannot be duplicated. They have also developed customized alignment schemes to demonstrate course overlay with about one micron accuracy via a set of Vernier patterns.[29]

Early in the imprint lithography program at The Univerity of Texas at Austin, researchers investigated the prospect of imprinting into an organosilicon thermoplastic at elevated temperatures and pressures, known as “Step and Squish Imprint Lithography.” [9] The goal was to generate a bilayer structure analogous to that produced by bilayer or tri-layer lithographic processes.[30] An organic thermoset planarizing/transfer layer was coated on a silicon wafer and then cured. A thin layer of organosilicon thermoplastic was spin-coated on the transfer layer. An etched polysilicon/silicon template was brought into contact with the coated substrate. This "sandwich" structure was then placed in a press and heated to 150 °C under pressure for 15 min. An advantage of such a bilayer process is that one needs only to generate low aspect ratio features. These features can then be transferred through the transfer layer via an anisotropic O_2 reactive ion etching (RIE) process analogous to that used in bilayer lithography, to generate high aspect ratio, high-resolution images.

Early results using this process demonstrated that imprinting with varying pattern density results in incomplete displacement of the thermoplastic even at elevated temperature and high pressure for long periods of time.[9] Partial pattern transfer, failure to displace material completely, release difficulties, and harsh process conditions seemed to limit the potential of this approach. Scheer, *et al.* [15] also have documented these problems in compression molding of PMMA derivatives. More importantly, it was decided that the use of high temperatures and high pressures would severely limit our ability to achieve the layer-to-layer alignment required for microelectronic device fabrication.

The second fundamental route to imprint lithography relies on curing a photosensitive material with ultraviolet light, rather than using the heated polymer method described above. Philips Research has demonstrated a photo-polymer process which produces high-resolution polymer features,[10] and this method has been used in the production of optical disks.[31] In this process, a liquid acrylate formulation sandwiched between a glass template and a substrate was photopolymerized to generate the required topographical features. While the Philips process showed promise for creating high-resolution images, it did not produce high aspect ratio features, and the patterned acrylate polymers lack the etch resistance required for semiconductor manufacturing. Because of our experience and that of others, we choose to refocus our efforts on a different technique that we call "Step and Flash Imprint Lithography," which combines the UV-curing approach of Philips and the bilayer imprint approach of "Step and Squish."

1.5 STEP AND FLASH IMPRINT LITHOGRAPHY

Step and Flash Imprint Lithography (SFIL) uses photopolymerization of an organosilicon solution through a rigid transparent imprint template to define the pattern topography on a substrate. The use of a low-viscosity UV curing solution allows imprinting at room temperature with minimal applied pressure. Typically the imprinting process is performed over a blanket layer of organic polymer, creating a bilayer structure. This removes the need to imprint high aspect ratio features, since the pattern aspect ratio can be subsequently amplified by reactive ion etching (RIE). The use of a rigid transparent imprint template allows flood exposure of the photopolymer to achieve cure, and enables classical optical techniques commonly used in mask aligners, photolithography steppers, and scanners for layer-to-layer alignment.

Details of the SFIL process are shown in Figure 1.5. An organic polymer layer (transfer layer) is spin-coated on a substrate, typically silicon. A low viscosity, photopolymerizable, organosilicon solution (etch barrier) is then dispensed on the wafer in the area to be imprinted. A transparent template bearing patterned relief structures is aligned over the coated silicon substrate. The template is lowered onto the substrate, displacing the etch barrier that fills the imprint field and trapping the etch barrier solution in the template relief. Irradiation with UV light through the backside of the template cures the etch barrier into a crosslinked polymer film. A fluorocarbon release layer on the template allows separation from the substrate, leaving an organosilicon relief image that is a replica of the template pattern. A halogen RIE is used to break through the undisplaced etch barrier material (residual layer) exposing the underlying transfer layer. An oxygen RIE is used to transfer the image through the transfer layer thereby amplifying the aspect ratio of the imprinted image.

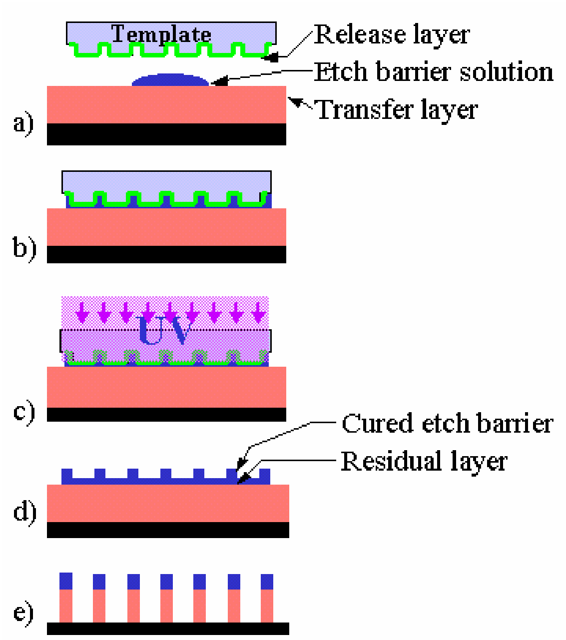

Figure 1.5. SFIL process flow. The process employs a template/substrate alignment scheme to bring a rigid template and substrate into parallelism (a), trapping the etch barrier (b). The template is pressed onto the substrate, and the imprint is illuminated through the backside of the template (c) to cure the etch barrier. The template is withdrawn (d), leaving a relief in the etch barrier. A halogen RIE removes the residual etch barrier, and an O_2 RIE transfers ithe image into the transfer layer (e), creating high-aspect ratio, high resolution polymer features.

1.6 SFIL CHALLENGES

Imprint lithography is by nature a contact patterning process that transfers topography without scaling. There are common challenges to all of these imprint techniques, the foremost being the dependence of this technology on 1-X imprint master resolution and the potential for defect production and propagation because of the contact nature of the replication process.

Contact lithography predates the projection lithography described above, and was cursed with catastrophic defect trends. In contact lithography, a photographic film mask, and later a Cr-on-glass mask, was placed in direct contact with the resist surface. The mask allowed selective exposure to the resist, creating the latent, chemical image necessary for subsequent processing. The direct contact between the mask and resist resulted in transfer of resist material to the mask, which affected both the processing of the current field and also processing of subsequent fields, and resulted in catastrophic trends of defects over time.[32] This phenomenon ultimately caused the abandonment of contact lithography for proximity lithography, which allows a small gap between the mask and resist, and ultimately for projection lithography. Skeptics of SFIL and other imprint techniques claim that the problems plaguing defect generation and propagation in contact lithography may be common to all forms of lithography where there is intimate contact between the master pattern (mask, reticle, or imprint template) and the imaging layer (resist, etch barrier).

1.7 FOCUS OF DISSERTATION

The goal of the current work was two-fold, and was centered around determining whether the contact nature of SFIL resulted in a catastrophic trend of defects over time. This study required overcoming significant challenges in regards to equipment and materials performance, and therefore resulted in various efforts to develop and improve those aspects of the SFIL process and equipment. There were three key requirements to completing this work: (1) a viable imprint process, including high resolution imprint templates (Chapter 2), a mechanically stable etch barrier (Chapter 3), a durable template surface treatment (Chapters 4 and 5), and a transfer layer that adhered to the wafer and etch barrier while not swelling while in contact with the liquid etch barrier; (2) an imprint apparatus that allowed consistent, hands-free operation in order to remove much of the human component from the imprinting experiment (Chapter 7); and (3) a defect inspection tool that would give an accurate count of defects per imprint in a manner acceptable by the scientific community (Chapter 7).

The end result of this work is a clear understanding of the fundamental process and equipment requirements for a defect study in imprint lithography, as well as a benchmark of defects over time using the SFIL process, which can be used as a launch pad for further process and equipment development.

1.8 REFERENCES

1. Scanlon, L., *No P-N Intended*, in *Technology Review*, 2003. **106**(1): 88.

2. Tristram, C., *Supercomputing Resurrected*, in *Technology Review*, 2003. **106**(1): 52-60.

3. Moore, G., Proc. SPIE, 1995. **2438**: p. 2-17.

4. *International Technology Roadmap for Semiconductors*. 1999, Semiconductor Industry Association: www.semichips.org.

5. Thompson, L.F., C.G. Willson, and M.J. Bowden, *Introduction to Microlithography*. 2nd ed. 1994, Washington, D.C.: ACS.

6. *3rd International SEMATECH Next Generation Lithography Workshop*. 1999: Colorado.

7. Association, S.I., *International Technology Roadmap for Semiconductors*. 2001: available at http://public.itrs.net/Files/2001ITRS/Home.html.

8. Chou, S.Y., P.R. Krauss, and P.J. Renstrom, J. Vac. Sci. Tech. B, 1996. **14**(6): p. 4129.

9. Colburn, M., *et al.*, Proc. SPIE, 1999. **3676(I)**: p. 379.

10. Haisma, J., *et al.*, J. Vac. Sci. Tech. B, 1996. **14**(6): p. 4124.

11. Xia, Y. and G.M. Whitesides, Angew. Chem. Int. Ed. Engl., 1998. **37**: p. 550.

12. Hirai, Y., *et al.*, J. Photopolym. Sci. Tech., 2001. **14**(3): p. 457.

13. Bender, M., *et al.*, Microelectronic Engineering, 2002. **61-62**: p. 407.

14. Jaszewski, R.W., *et al.*, Microelectronic Engineering, 1998. **41/42**: p. 575.

15. Scheer, H.-C., *et al.* in *Electron, Ion and Photon Beam Technol. and Nanofabrication*. 1998. Chicago.

16. Chou, S.Y., *http://www.ee.princeton.edu/~chouweb/newproject/page3.html*.

17. Chou, S.Y., P.R. Krauss, and P.J. Renstrom, Appl. Phys. Lett., 1995. **67**(21): p. 3114.

18. Chou, S.Y., P.R. Krauss, and L.Kong, J. Appl. Phys., 1996. **79**(8): p. 6101.

19. Krauss, P.R. and S.Y. Chou, Appl. Phys. Lett., 1997. **71**(21): p. 3174.

20. Wang, J., *et al.*, J. Vac. Sci. Tech. B, 1999. **17**(6): p. 2957.

21. Yu, Z., S.J. Schablitsky, and S.Y. Chou, Appl. Phys. Lett., 1999. **74**(16): p. 2381.

22. Wang, J., *et al.*, Applied Physics Letters, 1999. **75**(18): p. 2767.

23. Guo, L., P.R. Krauss, and S.Y. Chou, Appl. Phys. Lett., 1997. **71**(13): p. 1881.

24. Guo, L., E. Leobandung, and S.Y. Chou, Science, 1997. **275**(5300): p. 649.

25. Schultz, H., *et al.*, J. Vac. Sci. Tech. B, 2000. **18**(4): p. 1861.

26. Hirai, Y., *et al.*, Jpn. J. Appl. Phys., 2002. **41**: p. 4186-4189.

27. Chen, Y., *et al.*, J. Vac. Sci. Tech. B, 2002. **20**(6): p. 2887-2890.

28. Li, M.*, et al.* in *Electron, Ion and Photon Beam Technol. and Nanofabrication*. 2000. Palms Springs ,CA.

29. Zhang, W. and S.Y. Chou, J. Vac. Sci. Tech. B, 2001. **79**(6): p. 845-847.

30. Shaw, J.*, et al.*, Solid State Technology, 1987. **30**(6): p. 83.

31. Bouwhuis, G.*, et al.*, *Principles of Optical Disc Systems*. 1985, Bristol: Adam Hilger.

32. Bruning, J.H., Proc. SPIE: Optical Microlithography, 1997. **3049**: p. 14-27.

SFIL IMPRINT PROCESS DEVELOPMENT

Chapter 2: SFIL Imprint Template Technology

2.1 INTRODUCTION TO IMPRINT TEMPLATE TECHNOLOGY

2.1.1 Imprint Template/Mold Background

The imprint replication process is by nature a contact process through which topography on a template or mold is transferred to a compliant material. This requires that the topography on the template be of the same dimensions as the desired imprinted pattern. Various forms of imprint lithography use different methods to transfer these patterns.

"Molecular stamping," a method pioneered by Whitesides,[1-5] uses a compliant stamp, usually poly(dimethylsiloxane) (PDMS) on a rigid support (Si or SiO_2), from which a "molecular coupling agent" is transferred to the substrate on contact. The patterned PDMS stamp allows contact between the coupling agent and the substrate only in the non-recessed areas of the stamp, and the stamped pattern is therefore a negative image of the stamp pattern. The compliant and flexible nature of these stamps allows patterning on various surface geometries, including on curved surfaces, but limits the capability of high-resolution overlay alignment.

"Nanoimprint lithography," pioneered by Chou[6-8] and later adopted by other groups under "hot embossing" or other names,[9-14] involves imprinting on a polymer that has been heated to some extent above its T_g, thus reducing the polymer viscosity and allowing it to flow. There is no need for the mold to possess transparency during the imprinting process, and so many groups opt to use patterned Si wafers as imprint molds. Chou has demonstrated crude overlay alignment capabilities of this method by aligning notches on the wafer and the mold.[15] This method has potential throughput limitations as defined by the time necessary to displace the viscous polymer melt during imprinting.[16]

SFIL[16-30] and other UV-curing imprint lithographies[31-34] rely on UV-transparency of either the substrate or the imprint template. SFIL uses rigid templates made using an analog of the photomask production process, which yields templates that are 0.25 inches in thickness. This is the standard thickness for modern photomasks, and helps to minimize template compliance and resulting pattern distortion during imprinting.

In all cases, the imprint stamps, molds, and templates must possess a pattern that is the same size as the desired imprint pattern, and therefore high-resolution lithography is required during template production. High-resolution lithographic techniques such as ion beam[29] and electron beam lithography[35] provide some of the best resolution available, and the latter is the most common for imprint molds and templates.[26,28,36,37]

2.1.2 Electron Beam Lithography

An introduction to electron beam lithography is given in Thompson, Willson, and Bowden,[35] and so the purpose of discussing the topic here is merely to acquaint the reader with the concept. Briefly, electron beam (or “e-beam” for short) lithography is similar to projection lithography in that there is a resist on the substrate that changes in chemical nature upon exposure to an energy source. In this case, the energy source is a beam of electrons and not photons as is the case in optical lithography. Electron beam lithography can provide higher resolution images than photolithography.

The simplest e-beam resist is poly(methyl methacrylate) (PMMA), which undergoes chain scission upon exposure rendering the exposed areas more soluble than the unexposed areas; PMMA therefore behaves as a positive-tone resist material. Other resists are available, such as the ZEP family (Nippon Zeon), which are also positive-tone, and the NEB family (Sumitomo), which are negative-tone resists. In a manufacturing process, resist performance can be measured in terms of the e-beam dose required to obtain a desired feature size, and also by the highest resolution features possible with the resist. The highest-resolution resists are often the slowest (higher dose requirements), requiring the user to balance resolution and throughput requirements.

2.1.3 Introduction to Photomask Technology

The simplest form of a photomask is that which allows light transmission (at a particular wavelength or wavelength range) in certain areas, and does not allow transmission in other areas. Most conventional masks are made using chromium as the light absorber/reflector on a 0.25-in fused silica ("quartz" for short) substrate. An abbreviated photomask process flow is shown in Figure 2.1. (a) A fused silica plate coated with ~1000 Å Cr and a layer of e-beam resist is irradiated with an e-beam. (b) The exposed regions are selectively dissolved (for positive-tone resist), leaving a polymer image on the plate. (c) The polymer image is used to selectively etch the exposed Cr film, and is then removed with solvent leaving a patterned layer of Cr on the substrate.

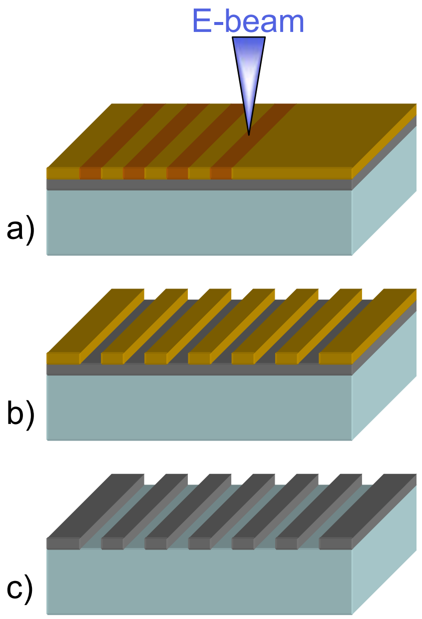

Figure 2.1: Conventional photomask process. (a) A latent image is irradiated by electron beam exposure; (b) developing the resist yields physical resist image; (c) the resist pattern is used as an etch mask to pattern the Cr, and the resist is removed.

Patterning the Cr layer, as in Figure 2.1c, may be done with liquid etchants or in a reactive ion etch (RIE) process. Liquid phase etching is known to be very isotropic, which results in Cr loss under the resist features and leads to a loss of Cr feature dimension. Because of this, liquid-phase etching is not adequate for high-resolution applications. RIE also has an isotropic component,[38,39] although it is much less pronounced than in wet processing. It is not unusual, for example to see etching of the Cr layer underneath the e-beam resist, which may result in a CD bias as large as 100 nm in standard photomask production.[38]

In modern photomask production, imperfections in equipment, processes, and processing materials may result in defects generated during the mask-making process. An entire technology has been developed around detecting and repairing such defects.[40-42] Mask inspection and repair is a very important step in delivering high quality masks. Necessitating perfect processing in the primary process flow would make masks extremely costly. The repair process generally requires some sort of charge dissipation layer, usually the patterned Cr absorber layer remaining on the photomask.

2.2 IMPRINT TEMPLATES FOR SFIL

2.2.1 Introduction to Templates Fabricated using the Chromium Process Flow

The imprint templates used in SFIL are rigid, transparent and bear topography. Templates can be made by extending the photomask process flow, as shown in Figure 2.2. (a) The Cr pattern defined in Figure 2.1 is used as an etch mask in a RIE process designed to etch into the SiO_2. This etch step is carried out until the desired etch depth is achieved, and the Cr is then removed (b), leaving a rigid, transparent imprint template.

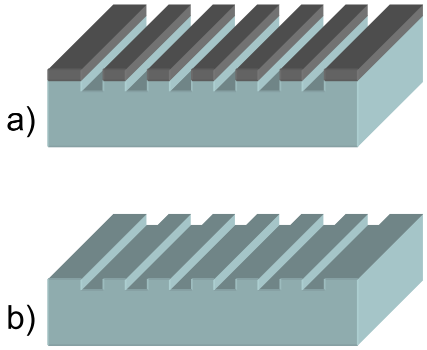

Figure 2.2: Modification of the photomask process yields SFIL imprint templates. (a) The patterned Cr layer is used as an etch mask to transfer the pattern into the quartz substrate, and then removed, yielding (b) all-quartz imprint templates bearing topography.

Most templates manufactured to date have been produced this way. This process yields templates that are comprised entirely of fused silica, and the final templates do not the possess charge dissipation capabilities required for post-processing SEM inspection. Considering that imprint lithography challenges mask-making technology by requiring 1X features, the ability to inspect and repair imprint templates is of extreme importance. The process shown in Figure 2.2 and described in detail in Section 2.2.3 results in high resolution imprint templates consisting entirely of bulk SiO_2, and therefore is not compatible with the standard, high resolution inspection and repair technology.

2.2.2 Introduction to Templates Fabricated using the Transparent Conducting Oxide Process Flow

In order to circumvent the charge dissipation problem associated with all-quartz templates, a layer of transparent, conducting material can be embedded into the final template, thereby allowing charge dissipation during both e-beam writing and CD-SEM inspection, and also allowing UV exposure through the template during the SFIL imprint process. An example process flow is shown in Figure 2.3. In this case, (a) the blank photomask substrate is coated with a thin layer of a transparent conducting oxide (TCO), commonly indium tin oxide (ITO), followed by a thin layer of SiO_2, commonly deposited via plasma-enhanced chemical vapor deposition (PECVD), followed by a layer of e-beam resist. (b) The resist is exposed with e-beam and developed, and (c) used as an RIE etch mask to pattern the SiO_2 film. (d) The final template is largely SiO_2 with an embedded layer of transparent conducting material, thus satisfying the conductivity and transparency requirements.[26]

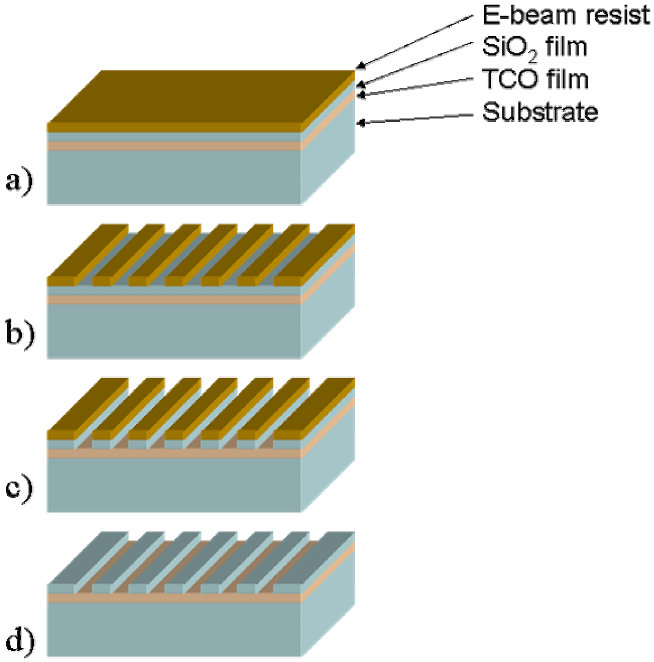

Figure 2.3: Imprint template process flow incorporating transparent conducing oxide into the final template.

There are many benefits to this type of template process in addition to the embedded charge dissipation layer. SiO_2-to-resist etch selectivities have been reported to be around 5:1.[43] As a result, it should be possible to further thin the e-beam resist and obtain even smaller features in both the resist and final template relative to the thin Cr process, which yields approximately 0.5:1 Cr-to-resist etch selectivity. The etch selectivity between PECVD oxide and ITO is roughly 125:1, and so the SiO_2 features can be clearly defined without impacting the ITO film. This results in uniform feature depth across a template.

Requirements for Transparent Conducting Oxide Layer

The TCO must possess many properties in order to enable this template scheme. Charge build-up on the substrate may lead to Coulombic e-beam deflection and result in pattern placement errors; therefore the TCO must be conductive so as to avoid charge build-up during e-beam writing. It must be transparent in the wavelength range of SFIL exposure, thus enabling polymerization of the etch barrier. The final templates are coated with a self-assembled monolayer derived from a fluoroalkyltrichlorosilane precursor, as discussed in Chapters 3-5, and the TCO must provide bonding sites to enable formation of a covalently-bound, durable release layer. The TCO must provide sufficient adhesion to both the SiO_2 substrate and the patterned SiO_2 film so as to maintain template pattern integrity. Finally, the TCO exposed at the bottom of the template features will form the top of the imprinted features, and must possess minimal roughness.

There are many transparent conducting oxides from which to choose. A review of the dominant materials is given in Ginley and Bright,[44] and the accompanying articles.[45-50] Indium tin oxide (ITO) is a transparent conducting oxide that has been used in making flat panel displays for some time,[44] and was chosen as the initial TCO for the SFIL template application. Its electrical and optical properties are discussed in Section 2.2.5, and the compatibility with the surface treatment is discussed in Chapter 5.

Indium Tin Oxide as a Transparent Conductor

Indium tin oxide (ITO) films can be formed using a variety of methods, including sputtering from a sintered target of In_2O_3/SnO_2 (usually 90%:10%),[51,52] sputtering from a metallic In/Sn target using an oxygen-rich sputtering gas feed,[53] spin- or dip-coating a solution of indium and tin compounds followed by thermal activation,[54,55] or by UV-photolysis of an ITO polymeric film.[56] The first method is most common. Studies of deposited films reveal a strong dependence of optical and electrical properties on preparation conditions, particularly related to oxidation and Sn incorporation.[57-60]

2.2.3 Experimental Method[61]

Early in process development round quartz wafers were used in place of the square photomask substrates because the chucks designed to hold photomask substrates had not yet been delivered. For the Cr process flow experiments, quartz wafers were coated with 100 Å Cr using a MRC 603 DC magnetron load-locked sputtering system at 1200 W and 35 mTorr process run in a single pass mode. The samples were coated with 180 nm NEB-22 resist, and were exposed on a Leica VB6 system operating at 100 kV with an e-beam dose ranging from 25 to 65 $\mu C/cm^2$.

Early in the SFIL ITO-template development process ITO films were obtained from Silicon Quest (SQ), and were DC sputtered at 1 kW in 100% Ar at a pressure of 8 mTorr. Subsequent development was done internally in a customized RF sputter system operating at a power of 100 W and an Ar/O_2 pressure of 6 mTorr using an In_2O_3/SnO_2 (90:10) target. Some films were annealed at various temperatures in an oven containing ambient atmosphere. Resistivity measurements were made using a Magnetron 4-point probe instrument. Ultraviolet/visible (UV/Vis) transmission spectra were obtained using a Perkin Elmer Lambda 18 UV/Vis spectrometer. For this analysis, ITO samples were prepared on smooth quartz substrates. Percent transmission curves were calculated by referencing the ITO samples to a clean quartz substrate.

Plasma-enhanced chemical vapor-deposited (PECVD) oxide was deposited in a Novellus Concept 1 system at a temperature of 250 ºC. All pattern transfer experiments were performed in a Unaxis VLR system. A chlorine and oxygen mixture was used to etch the Cr films.[39] A CHF_3 based etch was used to pattern transfer either the PECVD oxide or the quartz substrates.

Critical dimension (CD) measurements and top down micrographs were taken with a Hitachi S7800 CD-SEM equipped with a cold cathode source and an automated pattern recognition system. The repeatability of the CD-SEM is 3.5 nm (3σ) for line measurements and 1.4 nm (3σ) for pitch. Cross-sectioned images were obtained with a Hitachi S4500 SEM operating at 5 kV.

2.2.4 Imprint Templates using Thinned Chromium Process Flow[62]

Linewidths (CDs for short) were measured for 100 nm/100 nm line/space arrays after e-beam patterning, and again after Cr and quartz etch processes, after which the remaining resist and Cr were removed. In its final state the solid quartz wafer possessed no charge dissipation capabilities, which made CD measurement in the SEM very difficult; therefore the sample was coated with a 5 nm blanket Cr film to allow CD-SEM inspection, and the CDs were again measured. The resulting CD-vs.-dose curve shows an increase in CD with increasing dose. There was no observed CD bias between the resist features and the etched features. The ~10 nm increase in final CD is most likely due to the existence of the 5 nm blanket Cr film deposited following patterned Cr removal. NEB-22 is very sensitive to temperature variations, and so the noticeable deviation from a monotonic trend in Figure 2.4 was most likely caused by temperature variations across the wafer during post-exposure baking. Based on these results it was concluded that by thinning the Cr layer to ~100 Å and using a thinner e-beam resist, the CD shift normally observed in Cr mask processing using thicker Cr and resist films was essentially eliminated.

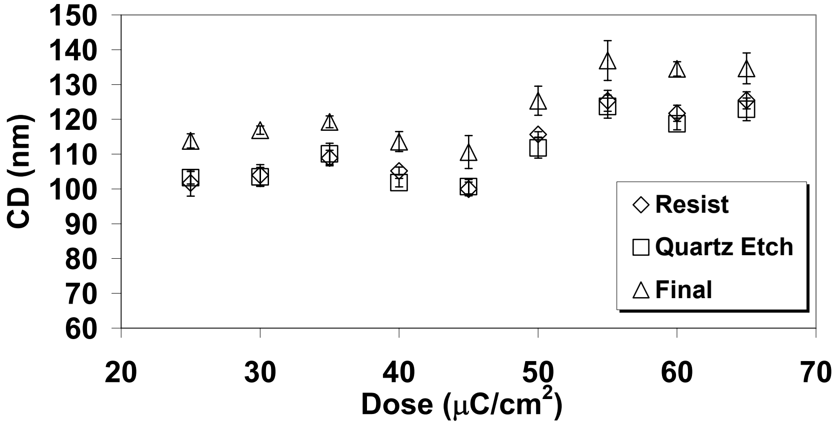

Figure 2.4: CD versus e-beam dose for thin-Cr template using NEB-22 resist.

Test templates were made using NEB-22 resist and 100 Å Cr. Features as small as 30 nm trenches and 50 nm lines were observed, as shown in Figure 2.5. Since NEB-22 is a chemically amplified resist, it is believed that the post-exposure bake steps tend to enhance acid diffusion, which can enlarge line size. For this reason, features significantly smaller than those in Figure 2.5 were not observed. ZEP-520, a non-chemically amplified positive tone resist, was used in subsequent processing. This process has yielded imprint templates with features smaller than 20 nm,[28] which have not been demonstrated using standard photomask processing techniques.

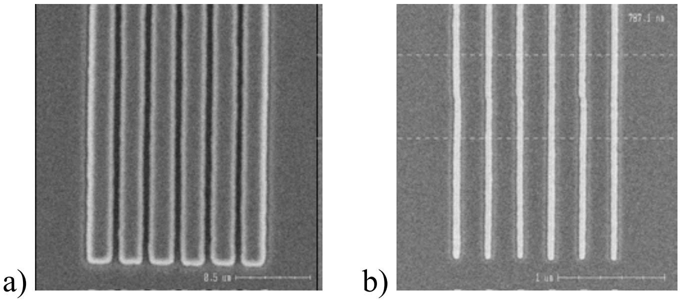

Figure 2.5: (a) 30 nm trenches and (b) 50 nm lines defined in an SFIL template.

2.2.5 Imprint Templates using a Transparent Conducting Oxide[61]

ITO Film Properties

Conductivity of ITO Films

The resistivity (ρ) of deposited ITO films was measured for films of various thicknesses, as was that of films obtained from Silicon Quest, and converted to sheet resistance (R_{sh}) according to the relation:[63]

Equation 2.1
$$R_{sh}(\Omega / sq) = \frac{\rho(\Omega \cdot cm)}{t(cm)}$$

where t is the film thickness. The 4-point probe measurement relies on some assumptions about the film conductivity and geometry,[63] and is probably not terribly accurate for the films with very high sheet resistance. The SQ films possessed much more favorable sheet resistance than the as-deposited Motorola films, as seen in Figure 2.6. The films were annealed at 300 °C for various times, after which they were again measured using the 4-point probe. The most dramatic decrease in sheet resistance was observed within the first 30 min of annealing, after which R_{sh} did not change significantly for any of the films tested. This change is most likely due to oxidation of the Sn from Sn^{+2} to Sn^{+4}.[51] Subsequent analysis of similar films revealed an amorphous-to-crystalline phase transformation, and an accompanying decrease in sheet resistance, with increasing anneal temperature.[26]

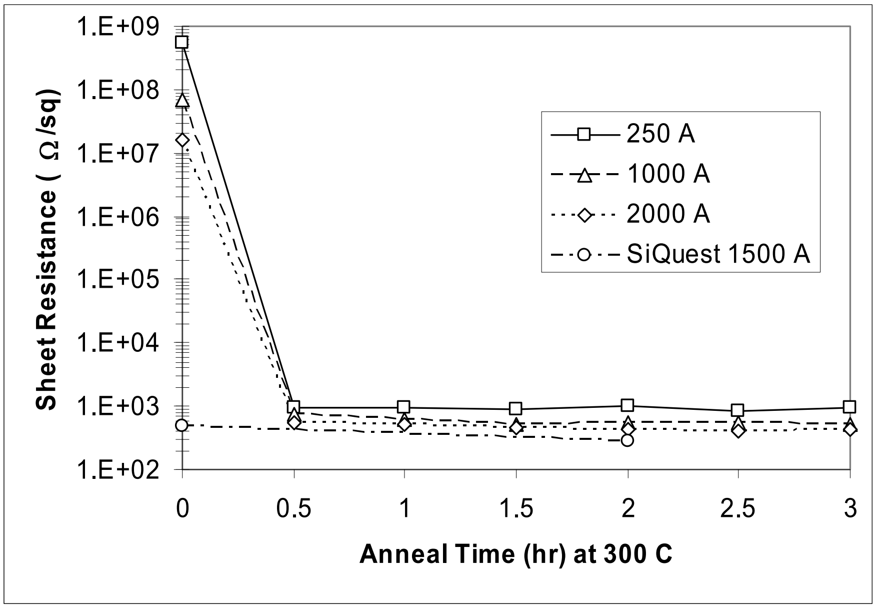

Figure 2.6: Sheet resistance of deposited ITO films of various thickness as a function of annealing time.

It can also be seen in Figure 2.6 that the sheet resistance decreases for thicker films. Shigesato found that resistivity of ITO films on glass decreases for increasing film thickness up to around 20 nm, above which resistivity was constant.[53] The films tested in the current work were all of greater thickness than 25 nm, so the normalization to film thickness as in Equation 2.1 may have caused this effect.

Films with thicknesses ranging from 250 Å to 2000 Å were annealed at 300 °C and measured on the 4-point probe. An increase in sheet resistance with decreasing film thickness is observed throughout the entire range, as shown in Figure 2.7, and is likely due to enhanced scattering at the film top and substrate interfaces.[63] In terms of utility in SFIL templates, there is likely a critical ITO sheet resistance required for sufficient charge dissipation, and thus a minimum ITO film thickness needed to achieve that target resistance. Thicknesses less than that critical thickness would result in greater sheet resistance, yielding charge build-up in the ITO film, and the resulting e-beam deflection would cause pattern placement errors. At the time of this writing that minimum thickness was not yet determined.

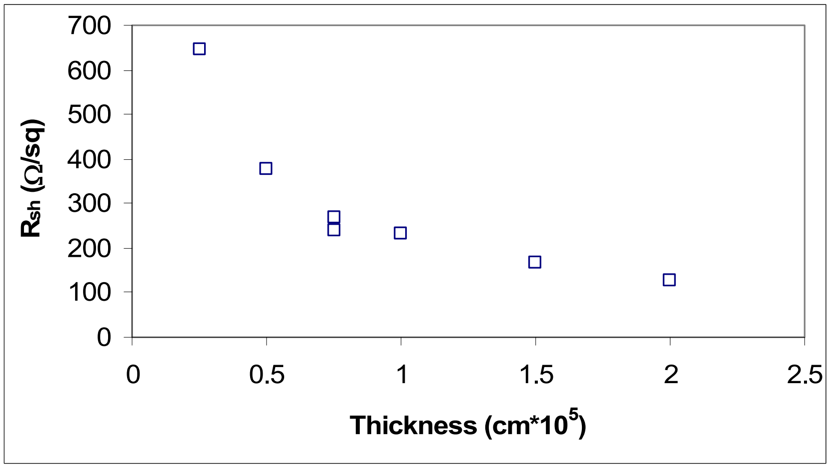

Figure 2.7: Sheet resistance as a function of Motorola ITO film thickness. Samples annealed at 300 °C for 3 hr.

Transparency of ITO

The ITO films must possess reasonable transparency at 365 nm, which is the wavelength of interest for SFIL exposure in the Hg arc spectrum. The precise definition of "reasonable" is arbitrary, but lower percent transmission results in less photons per unit time reaching the etch barrier during SFIL imprinting, which leads to slower total throughput. It was discovered that the SQ ITO films possessed less than 50% transmission at 365 nm, as shown in Figure 2.8, while early Motorola ITO films possessed nearly 80% transmission. Coupled with the nearly equal sheet resistance, as shown in Figure 2.6, it was deemed that the Motorola ITO films possessed more attractive qualities, and further work with the SQ films was halted.

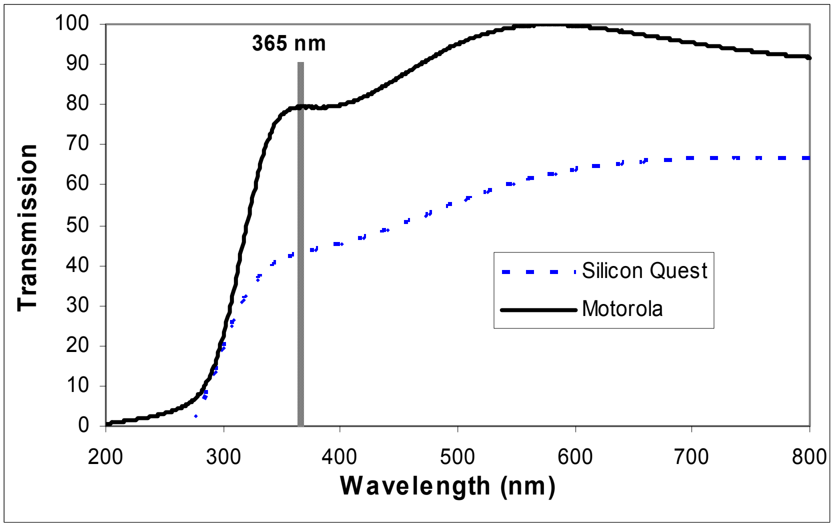

Figure 2.8: Comparison of percent transmission for 1500 Å Motorola and SQ ITO films.

Several quartz wafers were coated with ITO films of varying thickness, and annealed at 300 °C for various times. The percent transmission was seen to increase with increasing anneal time, up to about 2 hr, as seen in Figure 2.9. The curve seems to shift downscale upon annealing, the most dramatic change occurring in the first 30 min. The film stress is known to change from a compressive to a tensile regime upon annealing,[26] and this may indicate, for example, a film densification. This shift in Figure 2.9 may be caused by a change in the film density, and hence thickness, due to the amorphous-to-crystalline phase change. Film thicknesses were not measured in this experiment. Annealing of ITO is also known to cause oxidation of Sn, as described above, which is known to enhance optical transmission.[51]

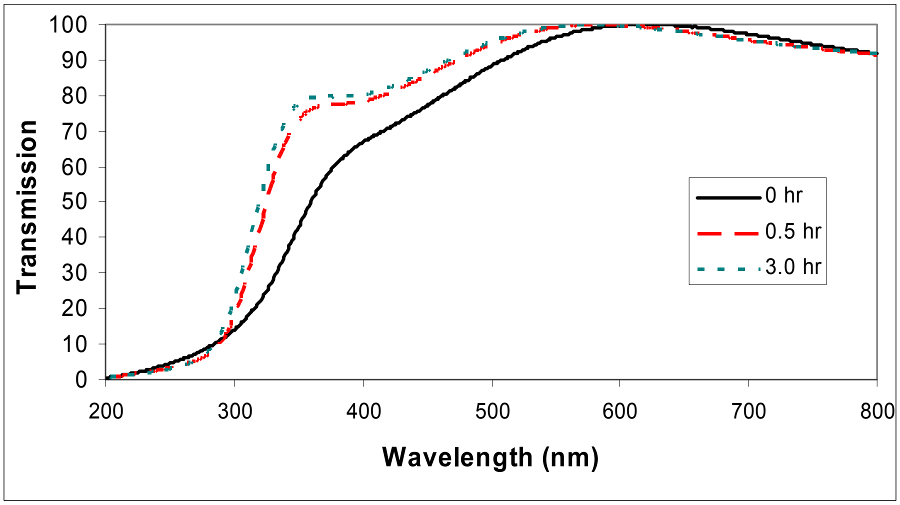

Figure 2.9: Percent transmission through 1500 Å Motorola ITO film as a function of wavelength for different annealing times at 300 °C.

A comparison of transmission through the films of various thicknesses is shown in Figure 2.10. The transmission does not appear to follow a simple Beer's Law relationship, which states that for thin films the transmission decreases exponentially with increasing film thickness. In fact, the transmission curves appear to possess artifacts of thin film interference.

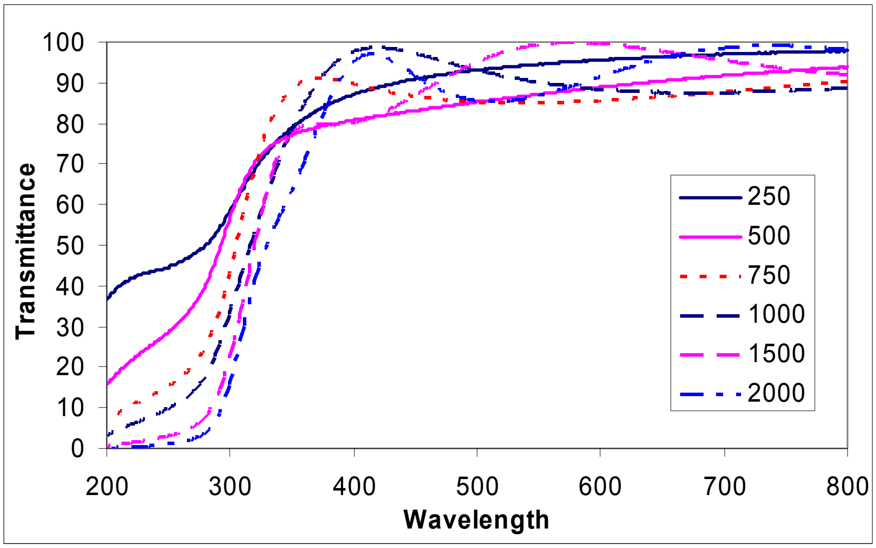

Figure 2.10: Percent transmission through ITO films of varying thicknesses (in Å). All films had been annealed at 300 °C for 3 hr.

Imprint Templates using Indium Tin Oxide Process Flow

Several iterations were necessary before the correct exposure and etch conditions were identified. After final etching and resist removal, one particular sample seemed to possess a "veil" of etch residue surrounding the features. This can be seen clearly in Figure 2.11, where the top of the feature is visually clean of resist, but there exists material on the feature sidewall that extends beyond the top of the feature. It was assumed that this "veil" was comprised of organic material from the resist plus some SiO_2 plus perhaps a small amount of ITO. A commercially available veil removal solution, EKC 265 (EKC), was used for its removal. Figure

2.12 shows line/space features possessing etch veils following etch and resist strip, and similar features after EKC treatment showing absence of such veils.

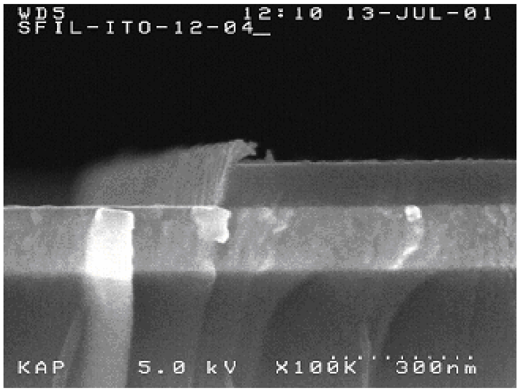

Figure 2.11: SiO_2 feature after resist strip, showing veil formation on feature sidewall.

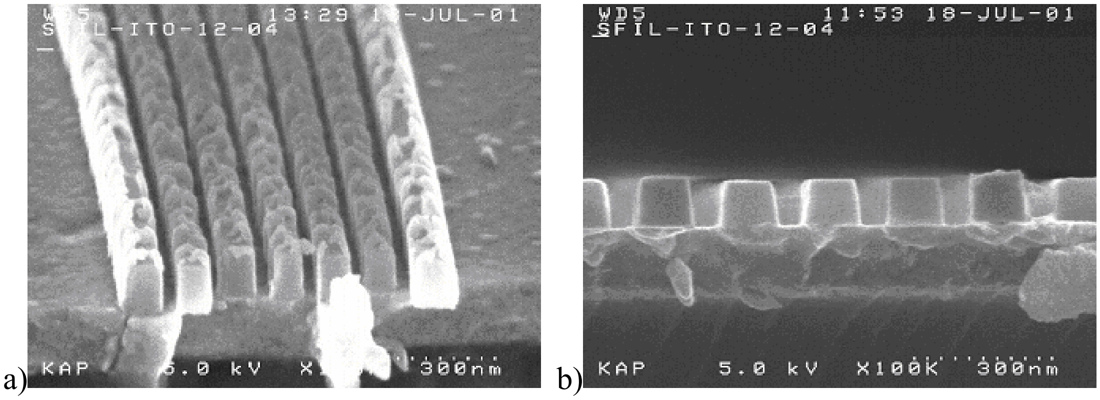

Figure 2.12: (a) As-etched patterns showing etch residue (veil), and (b) after cleaning with EKC 265 deveil solution.

Several samples were made using the process described above, and some results are shown in Figure 2.13. The SiO_2 features can be clearly delineated from the blanket ITO film. The source of the line “spreading” observed in the lines at the edge of the array is unclear, although it is assumed to be related to micro-loading during the etch process.

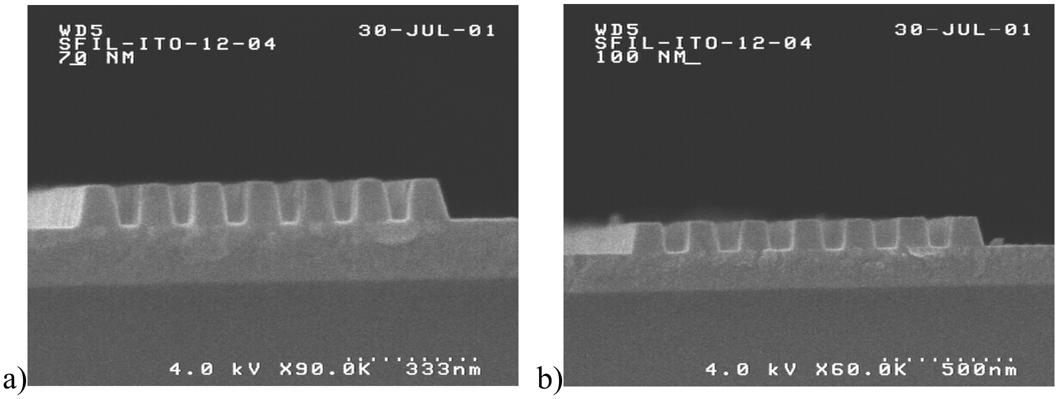

Figure 2.13: Cross section SEM images of dense 70 nm (a) and 100 nm (b) lines.

Figure 2.14 depicts SEM images from an ITO-based template (a) after resist development, and (b) after oxide etch and resist strip. No additional blanket charge dissipation layer was applied prior to obtaining the images; the ITO films also appear to be sufficiently conductive. Figure 2.14a shows 50 nm iso-dense features were well-resolved in the resist, indicating that no local beam blurring occurred during writing. Figure 2.14b depicts 100 nm dense features after oxide etch and resist strip. Line edges are well delineated and the ITO surface texture is easily observed.

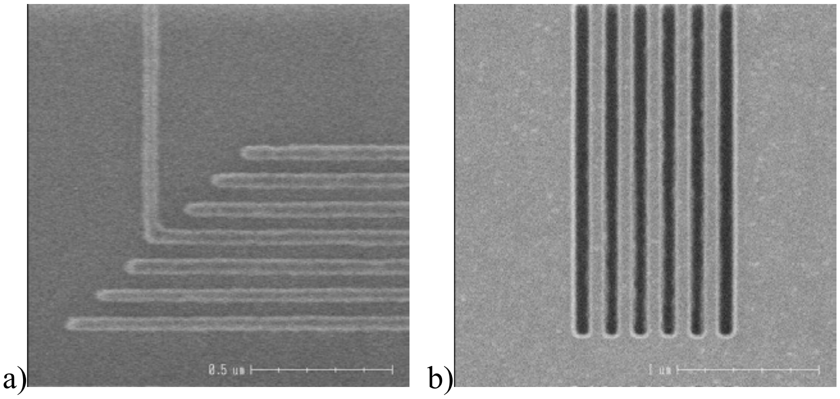

Figure 2.14: SEM micrographs of an oxide/ITO template after resist development (a) and after oxide etch and resist strip (b).

Optimization of ITO thickness

Additional factors must be taken into consideration when defining the ideal ITO thickness. The film stack of resist/PECVD oxide/ITO/quartz must be sufficiently reflective at 780 nm, which is the wavelength used by the laser height sensor in the Leica VB6 e-beam tool. This sensor detects the surface of the wafer and adjusts e-beam focus accordingly. Also, the film stack of quartz/ITO/PECVD oxide/etch barrier/transfer layer must be sufficiently transparent to 365 nm light in order to facilitate exposure for photopolymerization of the etch barrier during imprinting. These are shown pictorially in Figure 2.15. A thin film optical interference model was used to predict the effect of ITO film thickness, and also e-beam resist thickness, on these two responses. If the thicknesses and complex indices of refraction are known for each film, the reflection and transmission coefficients can be calculated using the matrix method.[64] This method is explained in some detail in Appendix A. The fluorocarbon release layer is a monolayer film of

CF_3-$(CF_2)_5$-$(CH_2)_2$- bonded to the SiO_2, and is assumed not to contribute to the optical phenomena.

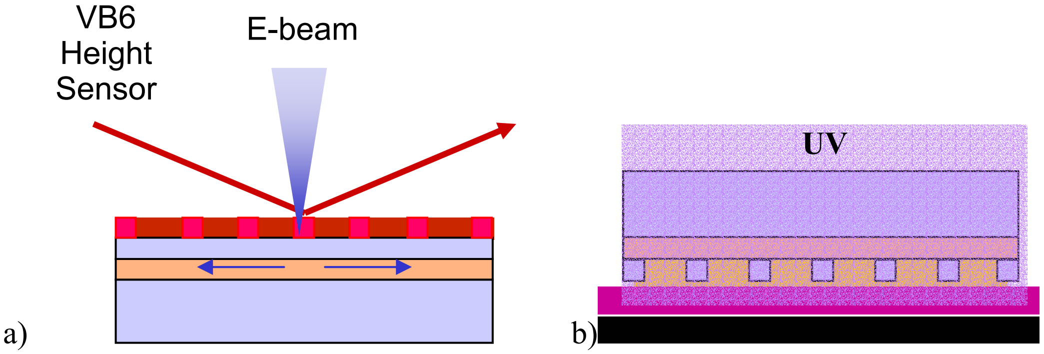

Figure 2.15: Requirements of film stacks (a) during template production and (b) during imprinting.

The optical constants for most films were fitted using Ψ and Δ data collected on a J.A. Woollam variable angle spectroscopic ellipsometer. The fitted index curves are shown in Figure 2.16 for the various materials used in the SFIL template process flow, and the optical constants for additional materials used during SIFL imprinting are shown in Figure 2.19. Optical constants and modeled layer thicknesses for all films are listed in Table 2.1 The ITO film thickness was allowed to vary from 50 nm to 300 nm.

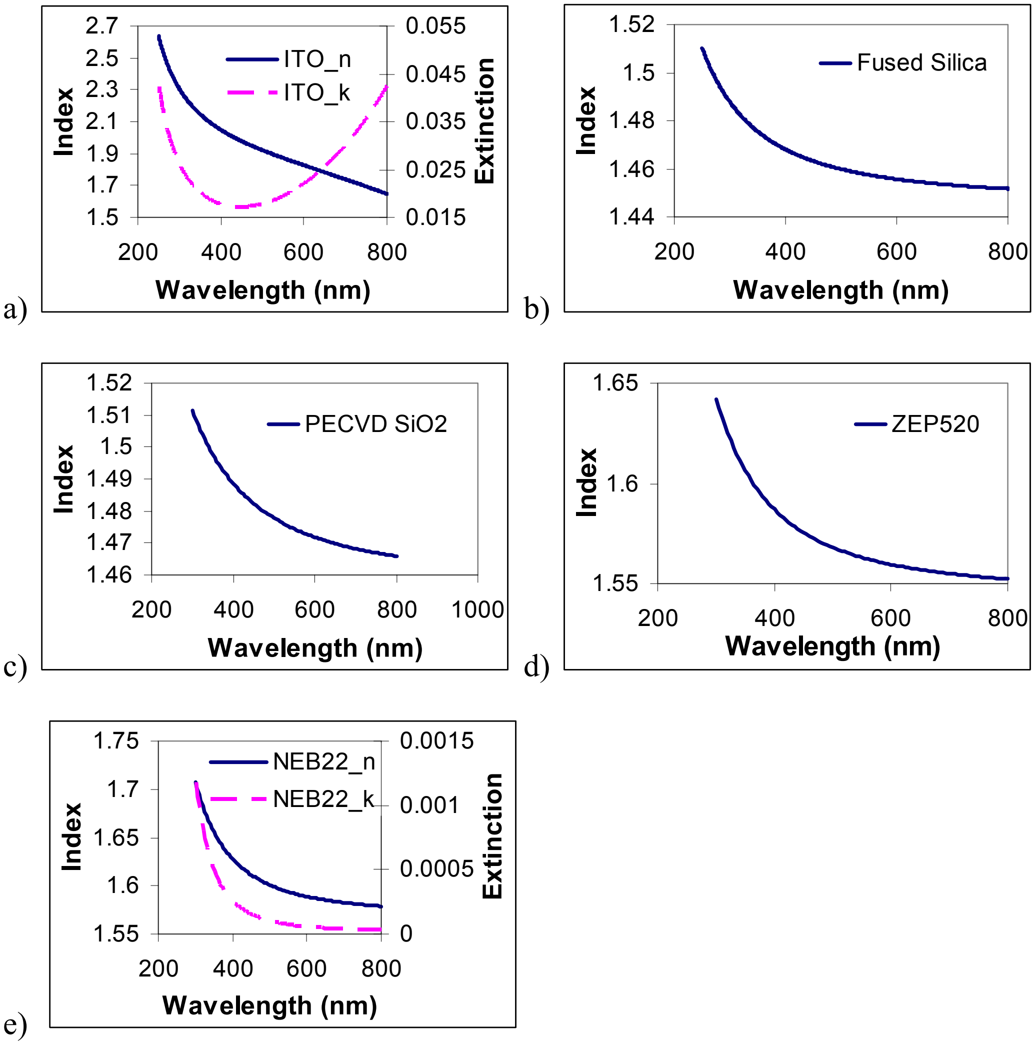

Figure 2.16: Optical constants for materials used in template fabrication. (a) ITO,[65] (b) 6.35 mm fused silica plate, (c) PECVD SiO_2, (d) ZEP520, and (e) NEB22. Extinction coefficients were calculated to be zero in the data range unless noted.

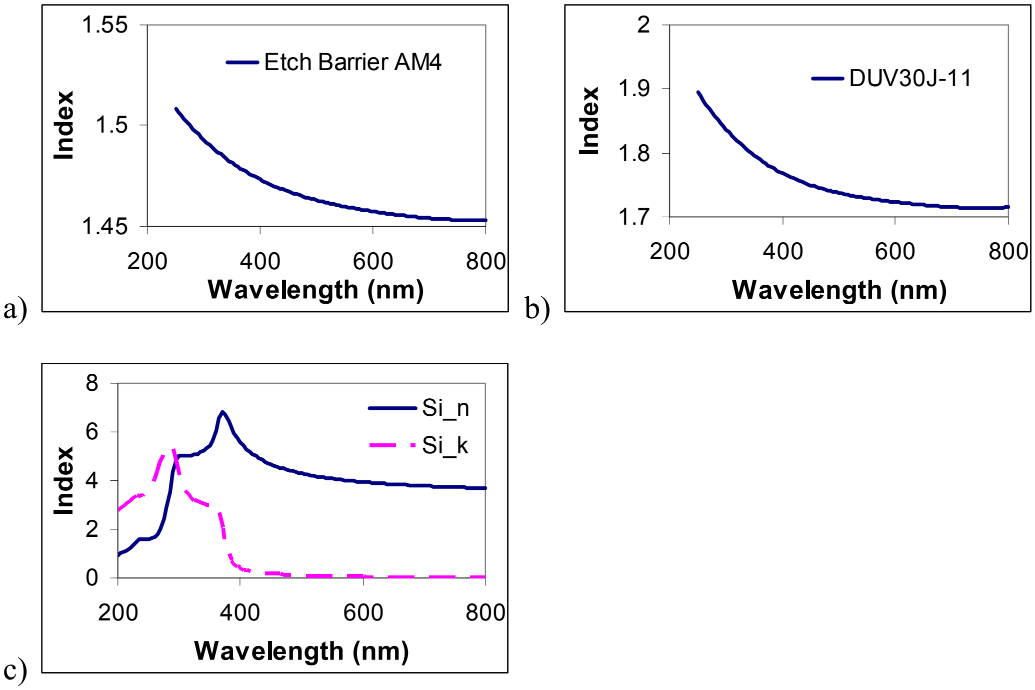

Figure 2.17: Optical constants for materials used during SFIL imprinting not listed in Figure 2.16. (a) SFIL A4 etch barrier, (b) DUV30J-11 transfer layer, and (c) Si (from reference 57).

Table 2.1: Optical constants for films in this experiment.

Material	**N at 365 nm**	**N at 780 nm**	**Thickness (nm)**
ITO	2.11+2E-002i	1.67+4E-002i	varies
Fused silica	1.47	1.45	6.35 mm
PECVD oxide	1.49	1.47	100 nm
ZEP520	1.60	1.55	180 nm
NEB22	1.65+4E-004i	1.58+2.6E-005i	180 nm
A4 Etch barrier	1.48	1.45	100 nm
DUV30J-11	1.79	1.71	250 nm
Si	6.55+2.67i	3.71+6.8E-003i	n/a

The reflectivity, transmissivity, and absorptivity for the film stack in Figure 2.15a is shown in Figure 2.18. The amplitude of the *s*-polarization reflectivity as a function of ITO thickness is much greater than that of the *p*-polarization. The VB6 laser height sensor uses only the *s*-polarization, so the effect of ITO thickness on the ability of the sensor to accurately determine sample vertical position is diminished. The reflectivity for *s*-polarization varies from ~ 44% to ~ 58%, but the signal needs only be strong enough to allow substrate positioning within the depth of focus of the electron beam. It is unclear at this point whether the change in reflectiviy with varying ITO thickness will sigificantly affect performance.

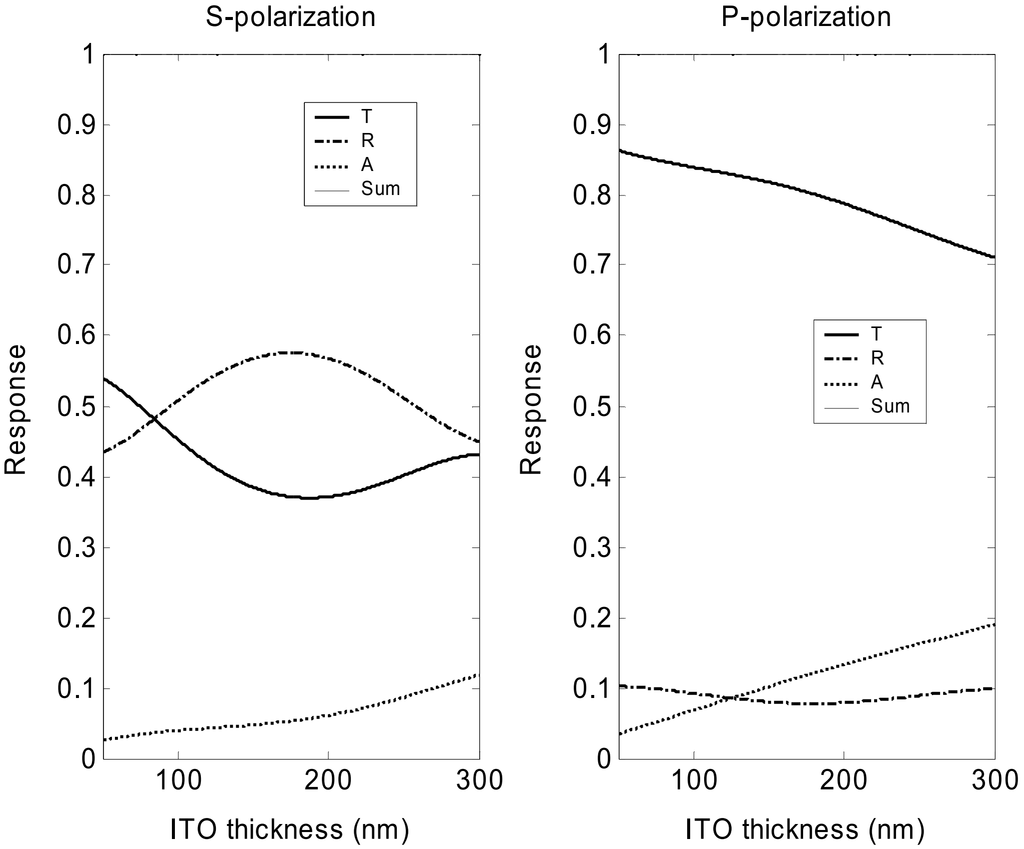

Figure 2.18: Optical coefficients for 780 nm exposure corresponding to the film stack shown in Figure 2.15b using ZEP520 as the e-beam resist. The height sensor beam is incident on the substrate at 75° from normal, hence the difference in *p*- and *s*-polarizations.

This modeling was also performed for NEB22 as the e-beam resist, but the responses were not significantly different from those shown in Figure 2.18, which were calculated assuming ZEP520 resist.

The reflectivity, transmissivity, and absorptivity for the film stack in Figure 2.15b are shown in Figure 2.19. Note the attenuation of transmission due to increase in absorption with increasing ITO thickness. The left set of plots corresponds to the areas of the template which possess SiO_2 features, and exposure proceeds through residual layer only. The right plot corresponds to the areas of the template that do not possess SiO_2 features, and exposure proceeds through the etch barrier filling the template recess plus the residual etch barrier layer. The amplitude of the *T* function is not large, and failure to optimize film thickness in this range will not cause catastrophic problems, but may diminish throughput slightly. For the purposes of the entire imprint field, both areas should be optimized, and based on these calculations the ideal ITO thickness is between 75 and 85 nm.

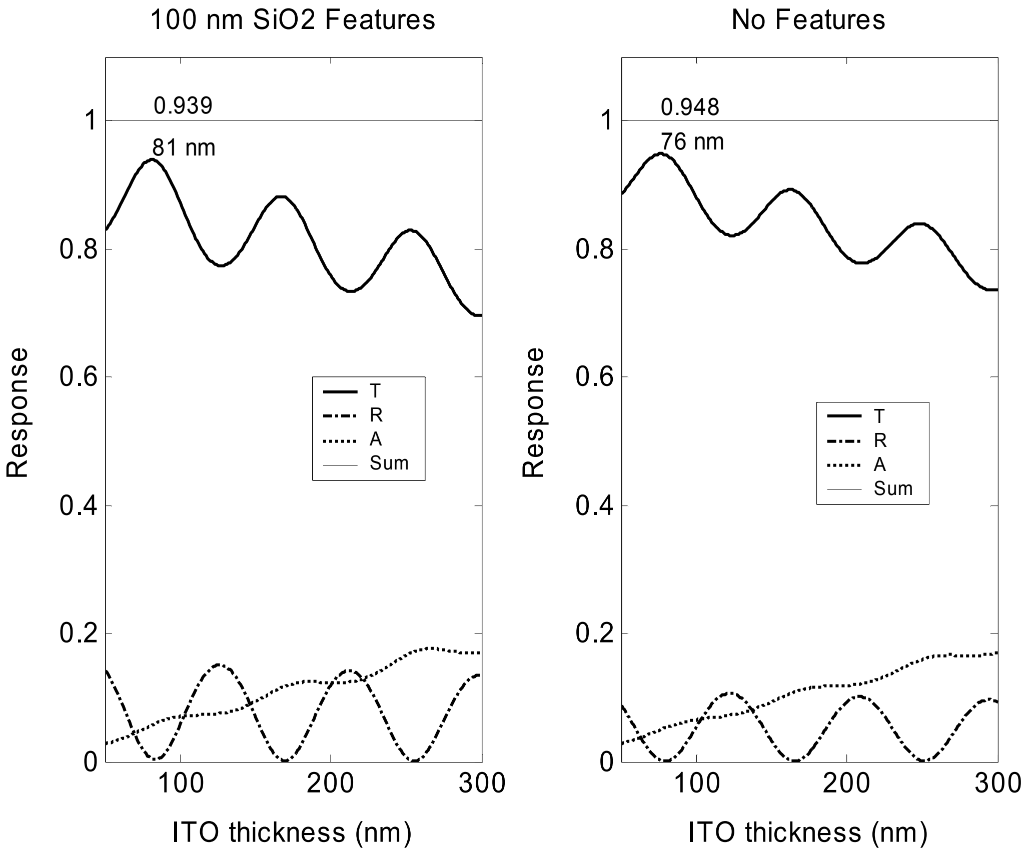

Figure 2.19: Optical coefficients for 365 nm exposure at normal incidence, corresponding to the film stack shown in Figure 2.15a. The plots are different for areas of the template that possess SiO_2 features (left) and those that do not possess features (right).

2.3 IMPRINTING RESULTS

2.3.1 Imprinting Results from Thin-Cr Templates

Early in the process development it was determined that the etch barrier did not faithfully reproduce features smaller than 100 nm, so a non-standard etch barrier was used. A more complete discussion of the etch barrier is given in Chapter 4, but it is mentioned here for context. The etch barrier used for the results in this section was 4% (w/w) 2-hydroxy-2-methyl-1-phenyl propan-1-one (Darocur 1173, Ciba) in ethylene glycol diacrylate (Aldrich). The cross-section images in Figure 2.20 demonstrate the capabilities of the thin Cr template process. Imprinted features as small as 30 nm demonstrate fairly square profiles, and 20 nm features were resolved. Further improvements in thin-Cr template processing have been made and are available in the literature along with the imprinting results,[28] but are not part of this work.

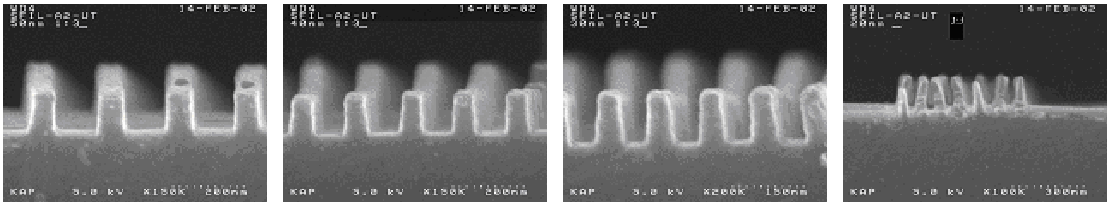

Figure 2.20: Cross-sections of imprints using Cr-based templates showing (left to right) 50, 40, 30, and 20 nm lines.

2.3.2 Imprinting Results from Indium Tin Oxide Templates

An ITO template was used in the SFIL process, and some imprint results are shown in Figure 2.21. The imprinted lines were resolved, but appear very rough. Cross-section SEMs of different areas of the same imprint field are shown in Figure 2.22. Some lines appear not to be fully intact, which may be a result of improper template processing leading to incomplete template feature definition, or perhaps a result of some etch barrier material being captured by the imprint template, thus pulling away from the imprinted feature. The tops of the imprinted features represent the area of contact between the ITO film and the etch barrier, while the sidewalls and bottom of the imprints represent area of contact between the PECVD oxide and the etch barrier. It is believed that the phenomenon seen in Figure 2.21 and Figure 2.22 is caused by failure of the release layer on ITO, and this will be discussed in detail in Chapter 5.

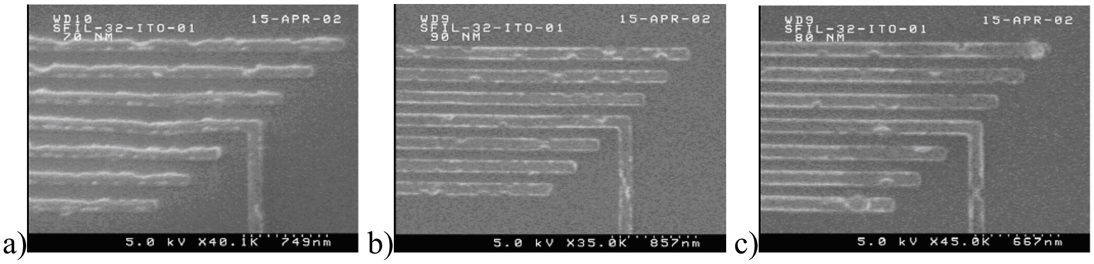

Figure 2.21: Iso-dense features imprinted with SFIL-32-ITO-01 template. a) 90 nm, b) 80 nm, c) 70 nm.

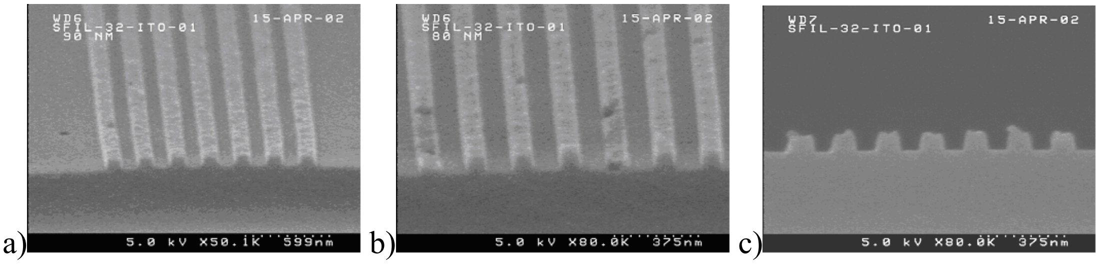

Figure 2.22: Cross-section SEMs of imprinted features. a) 90 nm, b) 80 nm, c) 70 nm.

In order to circumvent this problem, a blanket layer of PECVD oxide was deposited on a separate imprint template, thereby encapsulating any exposed ITO. This template was surface-treated according to standard procedures, and imprinted.

Some results are shown in Figure 2.23. The SiO_2 encapsulation layer apparently circumvented the etch barrier adhesion issue. A slightly different template processing procedure was discussed that involved depositing a thin layer of PECVD Si_3N_4 on the ITO prior to the PECVD SiO_2 layer. The SiO_2 etch chemistry does not attack Si_3N_4 at the same rate, and so would allow patterning the SiO_2 layer while allowing the Si_3N_4 passivating layer to remain intact.

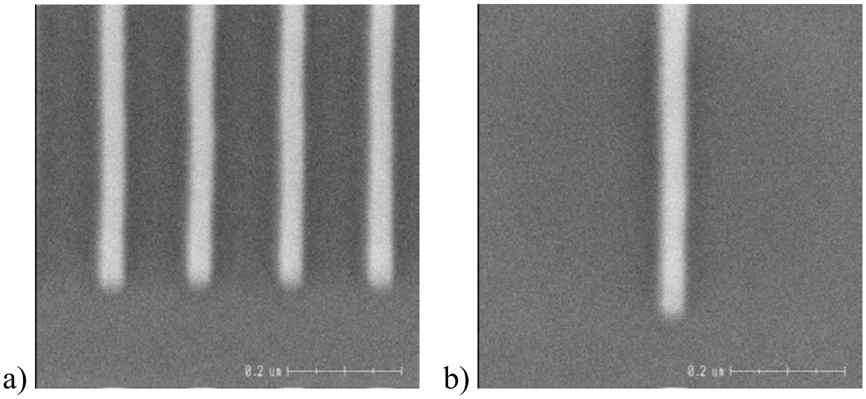

Figure 2.23: Features imprinted using a SiO_2-encapsulated ITO template. a) nested and b) isolated 20 nm lines.[26]

2.4 CONCLUSIONS

The process of making transparent imprint templates using an analogue of the traditional photomask production process flow yields imprint templates that possess most of the properties needed for the SFIL process. These templates are transparent, thereby allowing flood exposure through the template backside in order to allow photocuring of the etch barrier. They are also made of SiO_2, which is known to be a good substrate for the release layer described in Chapter 4. Using a

Cr layer that is thinner than that used in photomask manufacture maintains these qualities, and also allows features to be written in the template at higher resolution. These templates lack conductivity for post-manufacture SEM inspection, however, and must be coated with a Cr layer for inspection purposes.

Incorporating a thin, transparent conductor such as ITO in the final template circumvents this SEM inspection issue by imparting charge dissipation capabilities in the final template. The transparency of the ITO maintains the ability to expose the etch barrier through the template. Some properties of the final template change at different ITO film thicknesses, and so it may be necessary to design the final template stack around not just issues such as bulk transparency and conductivity, but to design the template in such a way as to maximize various responses. The thin film stack used in these experiments was subject to thin film interference phenomena, impacting both the reflectivity at the wavelength of the e-beam tool substrate height sensor and also the ultimate transparency of the imprint template at the SFIL exposure wavelengths. Taking into account all possible responses, and weighting those gating responses such as minimum conductivity, etc., may allow one to optimize the composite system response.

2.5 REFERENCES

1. Xia, Y. and G.M. Whitesides, Angew. Chem. Int. Ed. Engl., 1998. 37: p. 550.
2. Jackman, R.J., *et al.*, Langmuir, 1999. 15: p. 826-836.
3. Kumar, A., H.A. Biebuyeck, and G.M. Whitesides, Langmuir, 1994. 10: p. 1498-1511.
4. Wang, D., *et al.*, Appl. Phys. Lett., 1997. 70(12): p. 1593.

5. Widden, T.K., *et al.*, Nanotechnology, 1996. 7: p. 447.

6. Chou, S.Y., P.R. Krauss, and P.J. Renstrom, Appl. Phys. Lett., 1995. 67(21): p. 3114.

7. Chou, S.Y., P.R. Krauss, and P.J. Renstrom, J. Vac. Sci. Tech. B, 1996. 14(6): p. 4129.

8. Chou, S.Y., *et al.*, J. Vac. Sci. Tech. B, 1997. 15(6): p. 2897.

9. Jaszewski, R.W., *et al.*, Microelectronic Engineering, 1997. 35: p. 381.

10. Jaszewski, R.W., *et al.*, Microelectronic Engineering, 1998. 41/42: p. 575.

11. Jaszewski, R.W., *et al.*, Applied Surface Science, 1999. 143: p. 301.

12. Bendfeldt, L., *et al.*, Microelectronic Eng., 2002. 61-62: p. 455.

13. Scheer, H.-C., *et al.* in Electron, Ion and Photon Beam Technol. and Nanofabrication. 1998. Chicago.

14. Schultz, H., *et al.*, J. Vac. Sci. Tech. B, 2000. 18(4): p. 1861.

15. Zhang, W. and S.Y. Chou, J. Vac. Sci. Tech. B, 2001. 79(6): p. 845-847.

16. Colburn, M.E., Step and Flash Imprint Lithography: A Low-Pressure, Room-Temperature Nanoimprint Lithography, Ph.D. Thesis, Department of Chemical Engineering; Ph.D. Thesis, 2001, The University of Texas at Austin.

17. Bailey, T., *et al.*, J. Vac. Sci. Tech. B, 2000. 18(6): p. 3572.

18. Bailey, T., *et al.*, J. Vac. Sci. Tech. B, 2001. 19(6): p. 2806.

19. Bailey, T.C., *et al.*, J. Photopolymer Sci. Tech., 2002. 15(3): p. 481.

20. Choi, B.J., *et al.*, Proc. SPIE, 2001. 4343: p. 436-439.

21. Colburn, M., *et al.*, Proc. SPIE, 1999. 3676(I): p. 379.

22. Colburn, M., *et al.*, Proc. SPIE, 2000. 3997: p. 453.

23. Colburn, M., *et al.*, Solid State Technology, 2001. 46(7): p. 67.

24. Colburn, M., *et al.*, J. Vac. Sci. Tech. B., 2001. 19(6): p. 2685.

25. Colburn, M., *et al.*, J. Vac. Sci. Tech. B, 2001. 19(6): p. 2162.

26. Dauksher, W.J., *et al.*, J. Vac. Sci. Tech. B, 2002. 20(6): p. 2857-2861.

27. Johnson, S.C., *et al.*, Proc. SPIE: Emerging Lithographic Technologies VII, 2003. 5037: p. submitted.

28. Resnick, D.J., *et al.*, Proc. SPIE, 2002. 4688: p. 205.

29. Ruchoeft, P., *et al.*, J. Vac. Sci. Tech. B, 1999. 17(6): p. 2965.

30. Martin, C.J., *et al.*, J. Vac. Sci. Tech. B, 2002. 20(6): p. 2891-2895.

31. Bender, M., *et al.*, Microelectronic Engineering, 2002. 61-62: p. 407.

32. Hiroshima, H., *et al.*, Jpn. J. Appl. Phys., 2002. 41: p. 4173-4177.

33. Komuro, M., *et al.*, Jpn. J. Appl. Phys., 2000. 39(7075-7079).

34. Otto, M., *et al.*, Microelectronic Eng., 2001. 57-58: p. 361-366.

35. Thompson, L.F., C.G. Willson, and M.J. Bowden, Introduction to Microlithography. 2nd ed. 1994, Washington, D.C.: ACS.

36. Bailey, T.C., *et al.*, Microelectron. Eng., 2001. 61-62: p. 461.

37. Mancini, D.P., *et al.*, J. Vac. Sci. Tech. B, 2002. 20(6): p. 2896-2901.

38. Constantine, C., R. Westerman, and J. Plumhoff, Proc. SPIE, 1999. 3748: p. 153-157.

39. Smith, K.H., *et al.*, J. Vac. Sci. Tech. B, 2001. 19(6): p. 2906-2910.

40. Watanabe, H. and Y. Todokoro, J. Vac. Sci. Tech. B, 1993. 11(6): p. 2669-2674.

41. Cui, Z., P.D. Prewett, and J.G. Watson, J. Vac. Sci. Tech. B, 1996. 14(6): p. 3942-3946.

42. Wasson, J.R., *et al.*, J. Vac. Sci. Tech. B, 2001. 19(6): p. 2635-2640.

43. Dauksher, W.J., *et al.*, J. Vac. Sci. Technol. B, 1997. 15(6): p. 2232.

44. Ginley, D.S. and C. Bright, MRS Bulletin, 2000. 25(8): p. 15-18.

45. Lewis, B.G. and D.C. Paine, MRS Bulletin, 2000. 25(8): p. 22-27.

46. Kawazoe, H., *et al.*, MRS Bulletin, 2000. 25(8): p. 28-36.

47. Minami, T., MRS Bulletin, 2000. 25(8): p. 38-44.

48. Freeman, A.J., *et al.*, MRS Bulletin, 2000. 25(8): p. 45-51.

49. Gordon, R.G., MRS Bulletin, 2000. 25(8): p. 52-57.

50. Coutts, T.J., D.L. Young, and X. Li, MRS Bulletin, 2000. 25(8): p. 58-65.

51. Terzini, e., P. Thilakan, and C. Minarini, Materials Science and Engineering, 2000. B77: p. 110-114.

52. Baia, I., *et al.*, Thin Solid Films, 2001. 383: p. 244-247.

53. Shigesato, Y., *et al.*, Vacuum, 2000. 59: p. 614-621.

54. Seki, S., Y. Sawada, and T. Nishide, Thin Solid Films, 2001. 388: p. 22-26.

55. Alam, M.J. and D.C. Cameron, Thin Solid Films, 2000. 377-378: p. 455-459.

56. Wei, Q., H. Zheng, and Y. Huang, Solar Energy Mat. & Solar Cells, 2001. 68: p. 383-390.

57. Christou, V., *et al.*, J. Appl. Phys., 2000. 88(9): p. 5180-5187.

58. Mergel, D., *et al.*, J. Appl. Phys., 2000. 88(5): p. 2437-2442.

59. Milliron, D.J., *et al.*, J. Appl. Phys., 2000. 87(1): p. 572-576.

60. Omata, T., *et al.*, Appl. Phys. A, 2000. 71: p. 609-614.

61. Much of this work was carried out while at Motorola Physical Sciences Research Laboratories, Tempe, AZ, in 2001, and was performed in collaboration with D. J. Resnick, D. P. Mancini, W. J. Dauksher, and K. Nordquist.

62. Much of this work was carried out while at Motorola Physical Sciences Research Laboratories, Tempe, AZ, in 2001, and was performed in collaboration with D. J. Resnick, D. P. Mancini, W. J. Dauksher, and K. Nordquist.

63. Heavens, O.S., Thin Film Physics. 1970, London: Methuen & Co. Ltd.

64. Macleod, H.A., Thin-Film Optical Filters. 2nd Ed. ed. 1989, New York: McGraw-Hill.

65. Optical constants were not adequately determined for Motorola ITO films. Consequently, for the purposes of this excersize, optical constants for ITO in the literature were used, as found in http://www-ccd.lbl.gov/ccd_data.html.

Chapter 3: SFIL Etch Barrier Development

3.1 BACKGROUND

The successful etch barrier used in SFIL must possess certain properties. In addition to being a photocurable, low-viscosity (in liquid form), organosilicon material, the cured etch barrier must possess sufficient adhesive strength to the underlying transfer layer, minimal adhesive strength to the imprint template, and sufficient mechanical strength to maintain its integrity during the template separation step.

We formulated our first etch barrier solutions from a free radical generator dissolved in a solution of organic monomer, silylated monomer, and a dimethyl siloxane (DMS) oligimer, as described in Colburn.[1] The first-pass etch barrier formulation consisted of 47% (w/w) UMS-182, 3.5% Irgacure 184, 1.5% Irgacure 819, 24% SIA 0210.0, and 24 % butyl acrylate.

While this etch barrier formulation was useful in patterning features of modest size (> 200 nm), it did not faithfully replicate the smaller features (<100 nm) on the imprint templates from Motorola Labs described in Chapter 2. Decker[2] and Kloosterboer[3] noted that using only difunctional acrylates (crosslinker) and initiator resulted in rapid polymerization, and it was believed that this excess of crosslinker would lead to more rigid features in the SFIL process. Formulations containing 96% (w/w) SIB1402.0 (Gelest) and Darocur 1173 (CIBA) were used in the high-resolution experiments described in Chapter 2, and faithfully reproduced the vertical feature profiles that were known to exist on the templates. These formulations were too viscous, however, to be dispensed in the SFIL multi-imprint machine for automated imprinting experiments.

An effort was made to develop a formulation that provided high resolution printing capabilities while not sacrificing the other material- and process-related requirements. Different formulations were used in the various experiments described throughout this dissertation, and this chapter is presented as a guide to the various formulations.

An additional function of the etch barrier may be to aid in the post-imprinting release. Ameduri investigated fluorinated acrylate additives to weather- and graffiti-resistant coatings for sculptures and other outdoor works of art.[4] The authors found that the air/acrylate interface exhibited greater water contact angles than the substrate/acrylate interface, indicating that there may be an increased concentration of fluorinated species at the air interface.

Bender investigated using fluorinated additives to improve interfacial properties for the mold/polymer interface in UV-based imprint lithography,[5] and found a decreasing trend in fluorine concentration with polymer depth using Auger spectroscopy. This fluorine enhancement at the template/polymer interface likely modifies the interfacial properties and enhances post-imprint release.

An experiment designed around the concepts in Ameduri[4] and similar to that performed by Bender[5] was undertaken to reveal the F concentration as a function of etch barrier depth for SFIL.

3.2 EXPERIMENTAL

For the imprinting experiments, wafers were coated with a commercial bottom anti-reflection coating (BARC) (DUV30J-11, Brewer Science) to be used as the transfer layer. The BARC was spun at 3000 rpm for 60 sec and baked at 180 ºC for 60 sec, yielding films of thickness ~1250 Å. The films were double-coated, yielding thicknesses in the range of 250 nm. Etch barrier component chemicals were used as received. The formulations tested are listed in Table 3.1. After mixing, the formulations were agitated until visually well-mixed and sealed until use. Templates were manufactured in accordance with the thin-Cr process described in Chapter 2. The templates were cleaned in an acetone ultrasonic bath, followed by exposure to UV/ozone in a Jelight UVO-42 for 15 min. The clean templates were then treated with tridecafluoro-1,1,2,2-tetrahydrooctyltrichlorosilane (Geleste), by vapor exposure at 1 atm total pressure (precursor plus N_2) for 120 min, and annealed at 100 ºC for 15 min in the SFIL surface treatment chamber described in Appendix B. The template was pressed onto the etch barrier fluid on a 200 mm Si wafer, and the stack was exposed with a broadband Hg arc lamp (Oriel) operating at 450 W for 30 sec, which corresponds to an intensity of 43 mW/cm^2 at 365 nm.

Solution viscosities were measured using a Cannon-Fenske capillary viscometer using the American Societies for Testing and Materials (ASTM) method D 446, with the viscometer immersed in a water bath to minimize temperature fluctuations. SEM images were obtained on a Hitachi S-4500 field emission SEM operating at 5 kV after first coating the samples with ~5 nm Au:Pd film for charge dissipation

Table 3.1: Etch barrier formulation matrix.

Methacrylate formulations

Formulation	SIM6487.6	SIB1402.0	Darocur 1173	MMA	Si wt %
M1	45	0	4	51	11.96
M2	45	10	4	41	13.41
M3	45	20	4	31	14.86
M4	45	35	4	16	17.04
M5	45	50	4	1	19.22

Mixed acrylate/methacrylate formulations

Formulation	SIA0210.0	SIB1402.0	Darocur 1173	n-BA	Si wt %
AM1	44	0	4	52	12.09
AM2	44	10	4	42	13.55
AM3	44	20	4	32	15
AM4	44	35	4	17	17.18
AM5	44	50	4	2	19.36

Acrylate formulations

Formulation	SIA0210.0	EGDA	Darocur 1173	t-BA	Si wt %
A1	44	0	4	52	12.09
A1	44	5	4	47	12.09
A1	44	10	4	42	12.09
A1	44	15	4	37	12.09
A1	44	20	4	32	12.09

High-Si monomers:
SIM6487.6 - methacryloxypropyltris(trimethylsiloxy)silane
SIA0210.0 - (3-acryloxypropyltristrimethylsiloxy)silane
Crosslinkers:
SIB1402.0 - 1,3-bis(3-methacryloxypropyl)tetramethyldisiloxane
EGDA - ethylene glycol diacrylate
Low-MW monomers:
MMA - methyl methacrylate
n-BA - n-butyl acrylate
t-BA - t-butyl acrylate

The fluorinated additive experiments were conducted using 44% (w/w) (3-acryloxypropyltristrimethylsiloxy)silane (SIA 0210.0, Gelest), 10% 1,3-bis(3-methacryloxypropyl)tetramethyldisiloxane (SIB1402.0, Gelest), 42% *n*-butyl acrylate (Aldrich), and 4% 2-hydroxy-2-methyl-1-phenyl-propan-1-one (Darocur 1173, Ciba), which was diluted with 1% 2,2,3,3,4,4,5,5,6,6,7,7-dodecafluoroheptyl acrylate (Aldrich).

The XPS data were obtained using a Physical Electronics PHI5700 ESCA system equipped with an Al monochromatic source (Al Kα radiation at 1486.6 eV). The base pressure in the XPS UHV chamber was 1×10^{-10} Torr. Wide range (survey) scans were obtained with a step size of 1 eV and pass energy of 93.9 eV; high resolution scans were taken with a step size of 0.1 eV and pass energy of 11.75 eV. The Ag $3d_{5/2}$ XPS peak at 368.3 eV from a sputtered-clean Ag foil was used to calibrate the system. Atomic concentration data were obtained by normalizing the XPS peak area by the associated emission sensitivity factor. The work function of ESCA system is 3.3 eV, and the XPS intensity variation should be about ± 2.5 %, according to monthly calibration records.[6] Approximate sputter rate was estimated by sputtering a sample that had a blanket standard etch barrier film (no F-containing additive) on transfer layer, with thickness measured by profilometry. The sample was sputtered until no C was detected; this yielded the time to sputter through the etch barrier and transfer layer. A second sample which consisted of just the transfer layer on Si was sputtered in a similar manner. The difference in the time-to-endpoint was used to calculate a sputter rate of approximately 5 nm/min. It is important to note that no F was detected in this calibration.

3.3 RESULTS AND DISCUSSION

3.3.1 Improving Imprinting Performance[7]

All formulations were imprinted, and selected SEM cross-sections are shown in Figure 3.1. The feature integrity improves with increasing crosslinker concentration in all three sets of formulations. This improved printing fidelity comes at the expense of increased solution viscosity, as shown in Table 3.2. Both the all-methacrylate and the mixed formulations that yielded good feature profile possessed viscosities greater than 3 cP. It is important to note that we did not remove the inhibitor from the components, so we did not know what or how much inhibitor was present in the materials. It is possible that simply longer exposure times were required. The viscosities of the methacrylate and mixed acrylate/methacrylate solutions that produced reasonable profiles were determined to be too high to dispense in the current equipment. The fluid dispense system on the multi-imprint machine was not capable of projecting droplets of fluids with viscosity greater than ~2 cP. Only the acrylate formulation using ethylene glycol diacrylate as the crosslinker possessed both low viscosity (≤ 2 cP) and good feature profile. Formulation A4 was therefore chosen as the current baseline etch barrier formulation, and this formulation was used in subsequent imprinting experiments, including the defect study in Chapter 7.

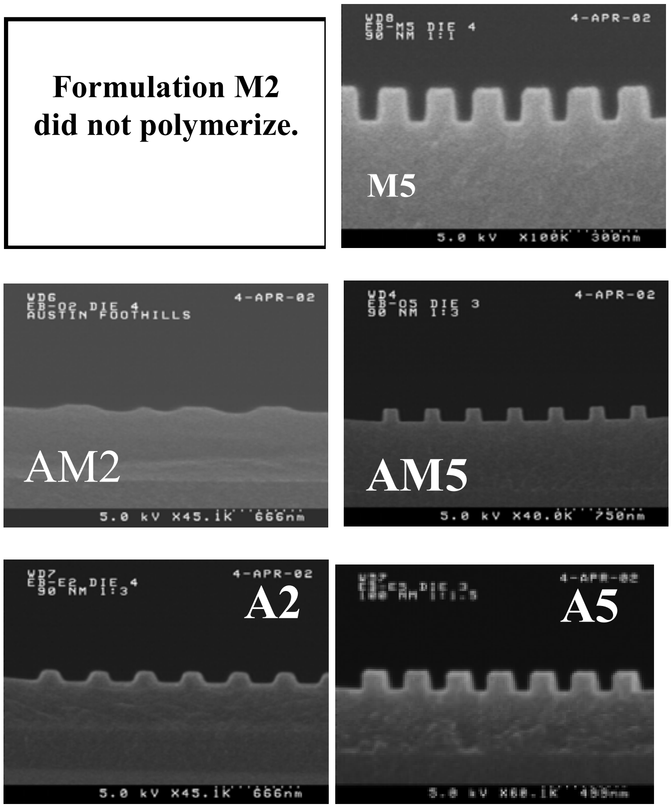

Figure 3.1: Dramatic profile improvements are observed in all etch barrier formulations with increasing crosslinker concentration. Formulation M2 did not print.

Table 3.2: Etch barrier formulation viscosities.

Formulation	Viscosity/cP
M1	1.03
M2	1.37
M3	1.86
M4	3.32
M5	6.09
AM1	1.45
AM2	1.87
AM3	2.46
AM4	4.17
AM5	6.57
A1	1.42
A2	1.52
A3	1.73
A4	1.95
A5	2.18

3.3.2 Fluorinated Etch Barrier Additive

The fluorine profile into the depth of an imprinted film was measured by XPS in terms of F 1s peak area, as shown in Figure 3.2. There appears to be an enhanced concentration of F at the etch barrier surface, represented by zero depth, followed by a region of reduced concentration within 5-15 nm of the surface. This sputtering experiment did not reach the etch barrier/transfer layer interface; the transfer layer (DUV30J-11) contains no F, and at the greatest depth sampled the F concentration is non-zero. It would be interested to investigate the effect of fluorinated acrylate concentration in the etch barrier on the F profile in the resulting imprinted film. It is possible that some F exists at the etch barrier/transfer layer interface; it would also be interesting to investigate the effect of this on the relative adhesive forces at the two interfaces, and how the addition of fluorinated acrylate modifies the relative propensity for interface fracture.

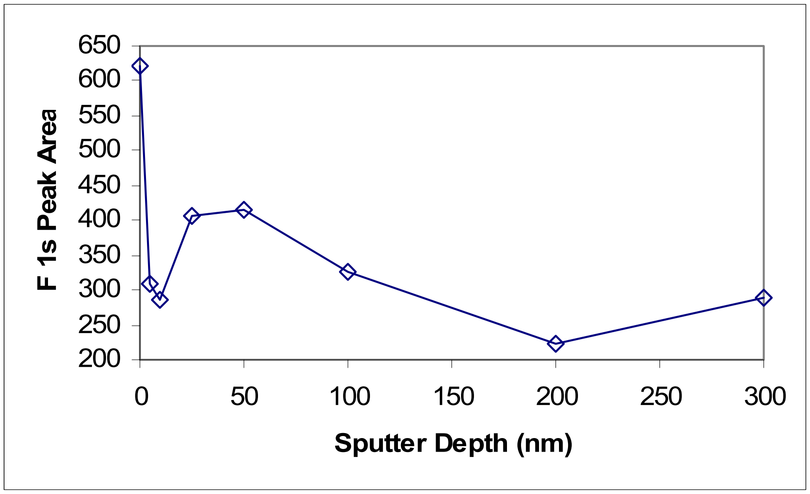

Figure 3.2: F1s XPS peak area as a function of sputter depth for imprinted film containing 1% (w/w) fluorinated acrylate.

3.4 CONCLUSIONS

The etch barrier imprinting fidelity was observed to be dependent on etch barrier material formulations. Formulations containing only methacrylate monomers did not polymerize without a significant amount of crosslinker. The amount of crosslinker required by the mixed formulations also boosted solution viscosity out of acceptable range. Imprinting performance was dramatically improved by replacing SIB1402.0 with ethylene glycol diacrylate, which is much lower in molecular weight. This monomer provides the structural stability of the silylated crosslinker, but at a greatly reduced viscosity.

One surfactant etch barrier additive was investigated, and XPS depth profiling revealed that there is an enhanced concentration of F at the etch barrier/template interface. This suggests that the F species near the interface migrate preferentially to that surface. The F concentration deep in the film is non-zero, and it remains to be seem how the potential existence of F at the transfer layer/etch barrier interface affects the overall separation performance.

3.5 REFERENCES

1. Colburn, M., *et al.*, Proc. SPIE, 1999. 3676(I): p. 379.
2. Decker, C., F. Masson, and C. Bianchi, Pol. Prepr., 2001. 42(1): p. 304-305.
3. Kloosterboer, J.G. and G.F.C.M. Lijten, Polymer, 1987. 28(7): p. 1149.
4. Ameduri, B., *et al.*, J. Polymer Sci. A, 1999. 37(1): p. 77-87.
5. Bender, M., *et al.*, Microelectronic Engineering, 2002. 61-62: p. 407.
6. Personal communication with Dr. Yangming Sun.
7. This work was performed in collaboration with Dr. Nicolas A. Stacey, Stephen C. Johnson, Britain J. Smith.

Chapter 4: Review of the Reaction of Functional Alkylsilanes on Silica

4.1 INTRODUCTION

The reaction of functional alkylsilanes on hydroxylated substrates such as silica has many applications, including reducing adhesion or friction forces, but the primary result of such a reaction is to produce a surface that is chemically different from the untreated substrate. The primary motivation for this work was to reduce the adhesive forces between the etch barrier and the imprint template during the SFIL process, and it is believed that forming a self-assembled monolayer of fluoroalkyltrichlorosilanes on the glass template is one way to achieve that goal.

It is generally accepted that functional alkylsilanes, such as alkoxysilanes and chlorosilanes, undergo hydrolysis with water adsorbed on the substrate to form silanol intermediates. These silanols undergo condensation reactions with neighboring intermediates and silanol groups on the substrate surface, liberating water and resulting in a networked film that is covalently bound to the substrate. This networking characteristic of films formed from alkyltrichlorosilanes makes trifunctional precursors appealing for applications where durability is required. These reactions are generally portrayed pictorially as two-dimensional reactions on planar substrates, such as in Figure 4.1. The primary drawbacks of portraying this reaction in such a way are that the surface is a three-dimensional structure, thus the film and its bonding network are also three-dimensional, and the surface of an amorphous solid such as silica is not planar on the atomic scale, and inferences about the reaction assuming a planar substrate must be suspect. Additionally, the amorphous nature of the substrate leads to a random distribution of silanol groups on the surface, and therefore the perfect alignment between the substrate and film bonding groups as pictured is not realistic. This figure shows complete hydrolysis of the trichlorosilanes in one step, which may not accurately represent the hydrolysis process, as described in Section 4.3.4.

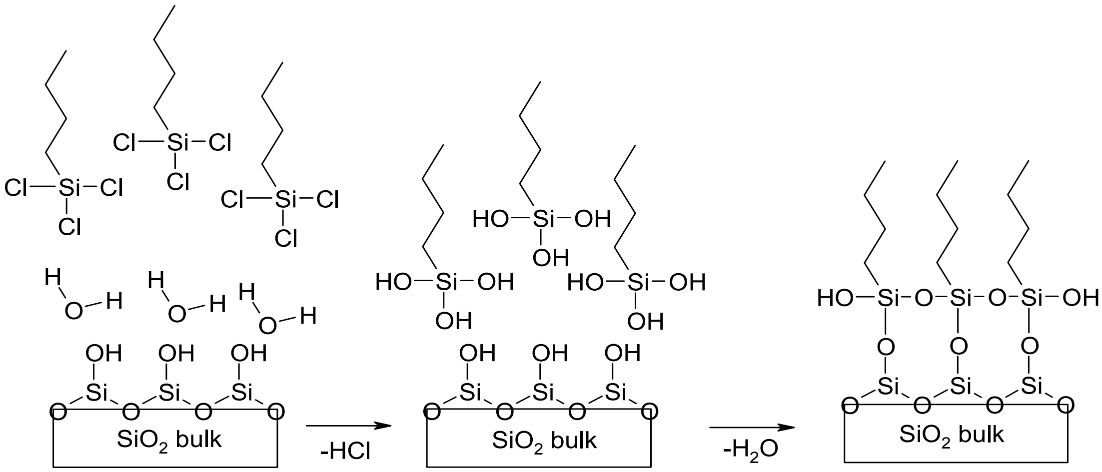

Figure 4.1: Idealized reaction of alkyltrichlorosilane on hydroxylated silica.

There are many factors that must be considered when designing experiments around this reaction or when modeling or discussing its various aspects, such as: atomic-scale substrate roughness; substrate contamination, or removal of contamination from the substrate; degree of substrate hydroxylation and distribution of those hydroxyl groups; degree of substrate hydration; desorption path for reaction byproducts; effect of reaction temperature; and the effect of post-reaction treatment such as annealing. Each of these experimental variables may have an impact on ultimate film performance, and a thorough understanding is necessary in order to fully optimize the final film.

Many research groups have investigated several of the items listed above in experimentation and modeling, but none have provided a thorough and comprehensive solution. The purpose of this chapter is to identify progress to date in the literature, and to identify areas for future work. The current work deals primarily with the reaction of alkyltrichlorosilanes on planar, solid silica used for SFIL. Much of the work in the field, however, has been done using silica gels as substrates, and so it may be necessary to draw conclusions from that body of work when applicable.

4.2 SILICA, BULK AND SURFACE CHEMISTRY

The first step toward understanding the reaction between functional alkylsilanes and silica is to understand the chemistry of the silica surface, which is likely influenced by the bulk structure of the substrate. Experiments designed around this type of reaction have used both precipitated silica gels and also bulk silicon dioxide in the form of deposited or grown films on support structures such as Si wafers and also from bulk SiO_2 melt. From the point of view of X-ray and electron diffraction analysis, noncrystalline SiO_2 films obtained by thermal oxidation are identical to fused vitreous silica.[1] Although the surface chemistry is influenced by sample thermal and processing history, it is widely believed that the surface chemistry of silica samples is largely the same from sample to sample.

Silicon dioxide, SiO_2, consists of Si atoms tetrahedrally bound to O atoms, is usually thought to be amorphous, bringing to mind a chaotic bonding structure. The phase diagram reveals a number of crystalline phases,[2] but the most common phase in commercial use is vitreous silica, which can be reached by rapid quenching of a SiO_2 melt. The resulting amorphous glass possesses many desirable properties, including its superb transparency in the visible and near-UV wavelengths. Litovchenko and coworkers have concluded that the assumption of the absence of long-range order is invalid for SiO_2 on planar Si, but instead the amorphous matrix contains microcrystalline regions.[3-5] Lisovskii and coworkers proposed a model of SiO_2 film on a Si substrate which predicts the bonding to be dominated by 4- and 6-fold Si-O rings.[3] Their films were thermally grown oxides on Si wafers, and were rapidly quenched after film growth.

Levine and Garofalini[6] used a modified Born-Mayer-Higgins potential to model a vitreous silica substrate in their work. Their silica substrate model was created by taking a cristobalite model, heated to liquid, and quenching through various intermediate temperatures to room temperature. This model has been shown to provide good structural information on the amorphous silica surface.[7] In amorphous silica the Si-O-Si bond angle is flexible and varies within a wide range (120° to 180°), while the Si-O bond length is nearly constant.[8] This bond angle range may also apply to systems of alkyl chains tethered to silica via Si-O-Si bonds.

4.2.1 Degree of Hydroxylation and Surface Silanol Distribution

Various researchers have investigated SiO_2 to determine the surface hydroxyl density. Iler provides a review of literature pertaining to hydroxyl density on colloidal silica particles.[9] He suggests that all silica surfaces are chemically similar, sharing approximately the same hydroxyl density – in the neighborhood of 4-5 hydroxyl groups per nm^2. It is widely accepted that there are three types of surface hydroxyl groups on SiO_2: geminal silanols, where two hydroxyl groups share the same silicon atom; vicinal silanols, where two adjacent hydroxyl groups are each attached to a single Si atom, the two neighboring Si atoms connected through an oxygen bridge; and isolated silanols, where the silicon atom does not have a silanol nearest neighbor. Armistead concluded that of the 4.6 hydroxyl groups per nm^2 on colloidal silica, approximately 30% are isolated silanols, while the other 70% interact with neighboring silanols, presumably consisting of either vicinal or geminal groups.[10] Bermudez used NMR techniques to study the surface of silica gels, and estimated the hydroxyl density to be nearly 4.2 groups per nm^2.[11] Morrow and McFarlan estimated 5.6 hydroxyls per nm^2 on a fully hydroxylated silica surface using IR and gravimetric techniques; of these, 1.1 per nm^2 were identified as isolated silanols.[12]

Many research groups involved in modeling the reaction of functional silanes on silica have used idealized models for the silica surface, many of which are derived from the various crystalline silica phases.[13-18] The agreement between the predicted structure and observed NMR spectra for bulk amorphous silica and those values predicted based on crystalline or semicrystalline materials in some sense validates those reaction models. Maciel and coworkers have studied the silica system using various NMR techniques.[13-18] In the analysis, they modeled the surface as comprised of regions of the 111 and 100 faces of β-cristobalite. The 111 face, as proposed by DeBoer and Vleeskins,[19] is comprised solely of isolated silanols separated by about 5 Å, corresponding to an hydroxyl concentration of 4.55 per nm^2. The 100 face of β-cristobalite, as proposed by Peri and Hensley,[20] is comprised solely of geminal silanols, yielding a surface density of 7.9 OH groups per nm^2. Neighboring geminal groups on adjacent silanols can condense under certain circumstances to form vicinal silanols and water.[20] These various bonding states yield different inter-hydroxyl distances. Chuang identified the following possibilities, shown in Figure 4.2:[16] 5.0 Å between neighboring isolated silanols; 2.7 Å between geminal groups on a shared Si, and 2.3 Å between geminal groups on neighboring geminal Si sites; and 3.3 Å between vicinal silanols. This does not exhaust all spacing possibilities, but perhaps gives a general indication of the range of inter-hydroxyl spacing for a mixed surface. Monte Carlo simulation results by Branda and coworkers[21-23] are in agreement with the mixed surface model proposed by Sindorf and Maciel.[14]

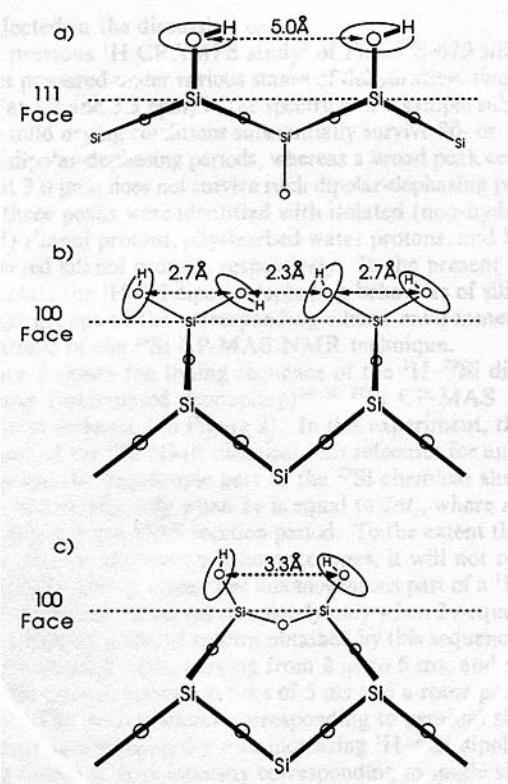

Figure 4.2: From Chuang, *et al.*[16] Side views of specific silicon planes (dashed lines representing an edge of such a plane) of β-cristobalite. Drawn approximately to scale: (a) 111-face; (b) 100-face; (c) vicinal sites from dehydration of the 100-face.

Paparazzo and coworkers' [24,25] focused on planar SiO$_2$ substrates. Using scanning Auger microprobe techniques, they concluded that the distribution of silanols is shallow with respect to the depth of the oxide, and all silanols are confined to less than 4 Å in depth. The authors provided no conclusions on the area density of hydroxyl groups, however.

Sneh and George[26] studied the surface hydroxyl groups on a SiO$_2$/Si planar system using probe molecules, specifically methanol. They found that methanol hydrogen-bonds to the hydroxyl groups on a carefully dehydrated surface, and temperature programmed desorption (TPD) could resolve multilayer methanol molecules from the molecules hydrogen-bonded to the SiO_2 silanol terminations. They estimated ~5 OH groups per nm^2, based on TPD curve analysis. This experiment relies on the assumption that methanol hydrogen bonds to silanol groups on the silica surface in a manner similar to water. Ugliengo and coworkers[27] modeled the propensity of methanol and silanol to form hydrogen bonds, although they did not draw any comparison to the hydrogen bonding of water and silanol.

Zhuravlev[28] has compiled a thorough review of the properties of the amorphous silica surface; his review of the literature revealed that most silica samples possess ~4.6 OH groups per nm^2 at room temperature, which he concluded was a physicochemical constant for silica of all types. He proposed a model similar to a phase diagram to describe the dependence of silanol density and type distribution (geminal, vicinal, isolated) as a function of sample temperature, assuming maximally hydroxylated starting point at 200 °C; according to the Zhuravlev model, the surface is comprised of 61% vicinal, 26% isolated, and 13% geminal silanol types at 200 °C.

It is widely believed that only silica that has been processed at very high temperatures and held under moisture-free conditions remains free of surface hydroxyl groups, possessing moderately hydrophobic character.[9] It has been shown that fully dehydroxylated silica samples spontaneously rehydroxylate in a humid environment.[28,29] Sneh and George[26] also studied this effect by dehydroxylation/rehydroxylation experiments. The authors subjected silica samples to 750-1000 °C, which resulted in significant dehydroxylation. Rehydroxylation was achieved by exposing the surface to H_2O plasma discharge, which resulted in a reproducible surface.

4.2.2 Degree of Hydration

The degree of hydration of silica samples has been investigated by a variety of means. Care must be taken in water desorption experiments since it is widely believed that at temperatures greater than 200 °C water evolved from the silica surface is largely from condensation of neighboring hydroxyl groups, and not from desorption of adsorbed water molecules. This motivated Sneh and George[26] to use methanol desorption, and not water desorption to probe hydroxyl coverage.

Burneau, *et al.*[30] identify key FTIR frequencies in following the hydration of silica. Ek, *et al.*[31] investigated the evolution of water from silica and concluded that the water mass loss due to desorption of water and dehydroxylation by condensation of neighboring silanol groups were distinctly different features in their TGA spectra. They concluded that all adsorbed water was removed below 130 °C, and dehydroxylation does not begin until nearly 200 °C.

Iler and Dalton[32] concluded based on viscosity data of colloidal silica solutions in water that there is a monomolecular layer of water immobilized at the hydroxylated silica surface. Sneh, Cameron, and George[33] investigated laser-induced thermal desorption of water from planar SiO_2. They found a dependence of desorption activation energy on the square root of surface coverage. Gun'ko, *et al.*[34] investigated water desorption from silica and found that approximately 7 H_2O per nm^2 evolved from the silica surface in TGA experiments, including desorption of adsorbed water and desorption by dehydroxylation, all of which desorbs below ~500 °C.

Malandrini, *et al.*[35] performed immersion calorimetry experiments using water and quartz. The authors noticed that initial water adsorption is very energetic, and the immersion enthalpy decreases with increasing water layer thickness, to about one water monolayer, after which immersion enthalpy remains constant. The reverse process may be similar, wherein water desorption activation energy is dependent on the water layer thickness, or related to hydration spheres.

Knez and Novak[36] investigated water uptake on dried silica samples and found that as the relative humidity (RH) increased, the amount of water uptake increased. The water uptake increased to 0.2 kg per kg silica at 80% RH, and then increased dramatically to 1.4 kg per kg silica at 100% RH. Given a specific surface area of ~1000 m^2/g, this converts to 120 water molecules per nm^2 at 80% RH, and 840 water molecules at 100% RH, which is vastly different from the results of Gun'ko[34] and others. Considering this large number, this may be multi-layer water rather than water that is strongly-bound to the silanol groups.

4.2.3 Removing Surface Contaminants

Removal of surface contaminants from silica substrates is essential for a complete surface reaction, and contaminants are believed to be largely organic compounds. The techniques widely used include various wet chemical washes, such as solvents, acids and bases, and dry techniques such as O_2 or H_2O plasmas or UV/ozone treatment, or a combination of any of these methods.

Cras, *et al.*[37] compared various wet cleaning methods, including various organic solvents, and acidic and basic solutions. Based on water contact angle data, they concluded that a combination of MeOH and HCl, followed by exposure to concentrated H_2SO_4 yields the best results. They also found a combination of NH_4OH and H_2O_2 to yield clean surfaces.

Mayer *et al.*[38] used in situ microwave-generated H_2O plasma to clean samples, and found that samples exposed to the plasma for 10 min displayed characteristics of a very clean surface in addition to providing maximal hydroxylaltion. Sneh and George[26] also used H_2O plasma for surface cleaning.

Ruzyllo, *et al.*[39] show that organic etch residues can be removed by UV irradiation in either wet or dry oxygen. Holländer, *et al.*[40] show that organic films can be oxidized by exposure to vacuum-ultraviolet in an O_2 ambient. Efimenko, Wallace, and Genzer[41] compare the exposure of Sylgard-184 PDMS films to UV and UV/ozone treatments. The authors conclude that the UV treatment results in chain scission in the surface region, and the UV/ozone treatment results in oxidation of the film surface and the creation of OH groups at the film surface. Ouyang, *et al.*[42] also confirm that UV/ozone can be used to oxidize the film within ~20 nm of the surface to near SiO_2 stoichiometry.

4.3 REACTION OF FUNCTIONAL ALKYLSILANES ON SILICA

4.3.1 Overview

Self-assembled monolayers (SAMs) have been studied for use in a wide variety of applications, including use as anti-stiction coatings for microelectromechanical systems,[38,43] coupling agents for protein patterning,[44] pattern transfer agents in μ-contact printing,[45,46] and release layers for imprint lithography.[47,48] Some of these applications require a durable coating, and covalent bonding to the substrate may provide that durability. Functional alkylsilanes, for example, may react in such a way as to provide a certain amount of covalent bonding to substrates possessing surface hydroxyl groups.

Functional alkylsilanes possess either alkoxy- or chloro- functionality of varying degrees (one to three functional groups), and usually require an amount of adsorbed surface water in order to undergo hydrolysis, yielding silanol intermediates as a prerequisite for substantial film organization and bonding. Tripp and Hair,[49] for example, found that alkyltrichlorosilanes react slowly on silica substrates in the absence of adsorbed surface water and rapidly in the presence of water; the fluoroalkyl- counterparts do not react in the absence of water. In the case of monofunctional alkylsilanes, the alkylsilanol intermediate can react covalently with either another alkylsilanol intermediate to form a dimer, or with a substrate hydroxyl group to be incorporated in the growing SAM. The adsorbed surface water plays a quasi-catalytic role in the reaction, as expressed in the following equations:

Equation 4.1 $R - SiR'_n X_{3-n} + (3-n)H_2O \rightarrow R - SiR'_n OH_{3-n} + (3-n)HX$

Equation 4.2 $m(R - SiR'_2 OH) \rightarrow m(R - SiR'_2 O \sim) + \frac{m}{2} H_2O$

Equation 4.3

$$m(R - SiR'_n OH_{3-n}) \rightarrow (R - SiR'_n OH_{(1-\theta)(3-n)} O \sim_{\theta(3-n)})^m + \frac{\theta}{2}(3-n)H_2O$$

where X is either an alkoxy group or a halide atom such as Cl, $O\sim$ represents bonding to neighboring alkylsilanes or to the substrate resulting from condensation reactions, and θ is the degree of condensation; Equation 4.2 applies for the case of monofunctional species and Equation 4.3 applies for the case of di- and trifunctional species. This reaction sequence does not require a solid substrate and can be performed on a water surface, as shown by Linden,[50] but as discussed by Tripp and others, the reaction on solid substrates requires surface water to reach completion. The amount of adsorbed water has been found to be related to the coverage of surface hydroxyl groups.[34]

The two general pathways to film deposition are vapor phase and liquid phase treatments. Hoffmann, Stelzle, and Rabolt[51] followed C-F stretching bands using infrared spectroscopy, and found that vapor-phase reaction conditions were more easily controlled, and therefore is preferred to solution-phase deposition. Fadeev and McCarthy[52] found that the vapor phase reaction of chlorosilanes on oxidized silicon wafers yielded films of higher quality than solvent phase reaction, as measured by liquid contact angles.

4.3.2 Effect of Degree and Type of Functionalization

It has been shown that trifunctional alkylsilanes yield films of higher quality than their mono- and di-functional counterparts. Monde, *et al.*[53] found that trifunctional semifluorinated silanes yield less gas adsorption than the mono- and difunctional silanes in Brunauer-Emmett-Teller (BET) adsorption experiments, indicating more complete surface coverage by the monolayer film.

Genzer, Efimenko, and Fischer[54] used near-edge X-ray absorption fine structure (NEXAFS) spectroscopy to investigate films from semifluorinated mono-, di-, and tri-chlorosilanes. The authors found that the tilt angle of the bonded molecules increased with decreasing degree of functionalization, with trichlorosilanes yielding the least tilt at 10°. The grafting density also varied with differing degrees of functionalization, with the monofunctional silanes yielding roughly half the density of the trifunctional films. Geer, *et al.*[55] found that the tilt of the molecules in the resulting SAM film was strongly dependent on the degree of functionality of the chlorosilane precursor. The authors conclude that the fluoroalkyltrichlorosilane precursor yielded films with little or no molecular tilt from the substrate normal, while fluoroalkyldimethylchlorosilane precursor yielded films with molecular tilt approaching 40°.

Angst and Simmons[56] found that monolayer coverage for octadecyldimethylchlorosilane was significantly less than its trichloro- counterpart, as measured by contact angle, ellipsometry, and ATR-IR. The authors observed this phenomenon under a variety of substrate hydration conditions. Bierbaum, *et al.*[57] suggest that SAMs from alkyltrichlorosilane precursors result in a higher molecular density than those from their trimethoxy- counterparts, arising from incomplete lateral polymerization of the trimethoxy end groups.

4.3.3 Effect of Reaction Temperature

Rondelez and coworkers[58-60] have reported that some self-assembling monolayer precursors form complete, tightly-packed monolayers up to some critical substrate temperature, above which the surface energy of the resulting film increases with increasing temperature. They attribute this to increased entropy in the forming film, and more rapid substrate bonding, which may decrease surface mobility that would normally lead to more organized films. The authors find this T_{crit} is different for precursors of different alkyl chain length. Davidovits and coworkers[61,62] studied the formation of OTS films at reaction temperatures of 12 and 43 °C, and found that the films formed at 12 °C transitioned from a disordered phase early in film growth to a more ordered phase at growth completion, whereas the films formed at 43 °C resulted in films of lower density, suggesting that these films remain in the less ordered phase.

Mayer, *et al*.[38] investigated the effect of reaction temperature on film quality for FOTS on planar silicon dioxide, and found that film quality decreased monotonically with increasing reaction temperature over the tested range of 25 to 90 °C, as measured by water contact angle. Gao[63] investigated the deposition of OTS on silica monospheres using ^{13}C cross polarization and magic angle spinning (CPMAS) NMR, and found that lower deposition temperatures yielded a more ordered film, with maximal ordering at 0 °C reaction temperature.

4.3.4 Precursor Hydrolysis: The Effect of Water Adsorbed and in the Bulk Phase

Alkyltrichlorosilanes react with surface bound water to form networks derived from the formation of bonds between adjacent molecules, as described above. The water adsorbed on the glass surface reacts with the alkyltrichlorosilane to form a silanol intermediate and acid in an irreversible reaction:[64]

Equation 4.4 $R\text{-}SiCl_3 + 3H_2O \Rightarrow R\text{-}Si(OH)_3 + 3HCl$

Wieber, *et al.*[65] used an infrared apparatus to follow the partial hydrolysis products, $RSiCl_3$, $RSiOHCl_2$, $RSi(OH)_2Cl$, and $RSi(OH)_3$ during hydrolysis of various alkyltrichlorosilanes. They found that for phenyltrichlorosilane, methylchlorosilane, and hydridotrichlorosilane, the length of the R group affects the stability of the intermediates. The authors observed the non-hydrolyzed and fully-hydrolyzed species to be highest in concentration, but that there were low concentrations of partially hydrolyzed species as well. They found the progression of singly-hydrolyzed to fully-hydrolyzed to be very rapid.

McGovern, Kallury, and Thompson[66] studied the reaction of OTS on glass substrates in the liquid phase using a variety of solvents. Those solvents that possess moisture-extracting properties, such as benzene and toluene, yielded the highest quality films, as determined by XPS and water contact angle. The authors conclude that the extraction of water from the surface allows precursor hydrolysis in the bulk phase, and the enhanced hydrolylsis in the bulk phase is the dominant factor in the improved film quality. They do not, however, discuss the possibility that the removal of excess surface water may expose substrate silanol groups to condensation reactions with the silanol intermediates. Their post-reaction agitation in chloroform of the treated samples may in fact remove loosely-bound molecules on the surface, and the film actually probed is made of a combination of molecules bound to the substrate through Si-O-Si linkages, and those molecules networked to the surface-bound molecules. Abstraction of excess water by solvents may yield a more ideal amount of surface hydration. Cao *et al.*[67] investigated SAM deposition from liquid and supercritical CO_2. The authors noted that although the CO_2 extracts water from the silica surface, using substrates that had not been rigorously dried allows the extracted water to remain in the bulk CO_2, thus providing a means for the chlorosilane hydrolysis, and resulting in monolayer film formation.

Wang and Wunder[68] studied the effect of hydration on the formation of SAMs on fumed silica, and found that saturating the surface with adsorbed water by bubbling argon through a water bubbler resulted in silica samples that contained more alkylsilane chains per unit silica area than the similar reaction on as-received silica. Wang, *et al.*[69] found that reaction of OTS on dehydrated and dehydroxylated silica yielded disordered structure, but reaction of OTS on increasingly-hydrated silica yielded an increase in lateral packing of the SAM.

Mayer, *et al.*[38] studied the reaction of fluorinated octyltrichlorosilane (FOTS) from the vapor phase on dehydrated Si, and noted that the adsorbed chlorosilane precursors tend to desorb rather than react with the substrate silanol groups. By introducing water vapor following adsorption of the FOTS molecules allows precursor hydrolysis, and subsequent condensation reactions, resulting in a more stable film.

Rye[70] used the XPS peak area ratio of the C to SiO_2 peaks as a metric for film coverage in experiments of alkylchlorosilanes on Si wafers. The authors found that the reaction of alkyltrichlorosilane on dehydrated substrates yields incomplete coverage, but that exposure to water followed by a second reaction cycle enhances the film coverage. Experiments by Angst and Simmons[56] agree with these results. The authors found that monolayers formed from OTS were denser on a hydrated substrate, as measured by contact angle, ellipsometry, and ATR-FTIR, as compared to dehydrated substrate.

Water in the bulk phase during the deposition of trifunctional silanes may allow hydrolysis of the precursor before it reaches the substrate, but it may also have undesired consequences. Bunker[71] found that water in the bulk phase cause the formation of inverse micelle spheres in the bulk, and hence oligimer deposition on the substrate, leading to films of inferior quality. Vallant[72] shows that increased water content in the bulk phase has the causes the film to grow in a more island-growth mode, and also that deposition rates are enhanced by oligimer deposition.

Zhao[73] suggests that the most probable formation mechanism is the deposition of precursor onto an adsorbed water layer, followed by hydrolysis and network bonding and surface bonding. Le Grange[74] found that film coverage increases with substrate hydration state, and that a fully hydrated substrate is not necessary for complete film formation, suggesting that only a fraction of the adsorbed molecules are bonded to the surface. Silberzan[75] found that the roughness of a silanated substrate is lower than that of an unsilanated substrate, suggesting that the molecules do not all attach to the substrate. It is instead argued that the SAM forms on a layer of adsorbed water, and that there are bonds distributed throughout the film that anchor the film to the substrate.

The degree of hydration has an effect on the ability of a film to bond to the substrate. It has been shown that films of alkyltrichlorosilanes can form on the surface of water, and that the films network to some extent.[76] It has also been shown that excess surface water allows stable adsorption and network bonding even on hydrated Au substrates,[77] which possess no silanol bonding sites for the hydrolyzed intermediates. These results may indicate that while water is an essential reagent in forming the reactive silanol intermediates, excess surface water may in fact inhibit the surface condensation reactions that are necessary for an anchored film, and may therefore limit the film durability in imprint lithography release layer applications.

4.3.5 Effect of Adsorbed Reaction Products on Surface Chemistry

The hydrolysis of functional silanes yields products such as HCl for chlorosilanes and alcohols for alkoxysilanes. A key to the complete surface reaction may be the removal of those products from potential surface reaction sites. Kopylov, *et al.*[78] indicate that the HCl produced during the reaction may, in fact, result in reverse hydrolysis. For the case of alkoxysilanes, the hydrolysis reaction may not be completely irreversible,[79] and so the removal of alcohol products from the reacting surface is imperative to ensuring complete reaction. Evans, Jones, and Overstreet modeled HCl evaporation from aqueous solutions using ALOHA in studying hazard assessment in materials spills.[80] Although it is likely that the behavior of HCl desorption from semi-hydrated silica is different than evaporation from aqueous solution, this data may give insight to the phenomenon.

Lindén, Slotte, and Rosenholm[81] studied the hydrolysis and condensation of monolayers of octadecyltrimethoxysilane (ODTMS), and found that highly condensed monolayers formed below pH 3 and above pH 12. Solutions with intermediate pH yielded films that were not maximally condensed. Additionally, the authors found the point of zero charge to be 3, and concluded that the hydrolysis and subsequent condensation of the ODTMS is both acid- and base-catalyzed.

Reymond and Kolenda[82] investigated the point of zero charge of SiO_2 samples, and found the value to vary from 3.5 to 10.7, depending on the sample. Duval, et al.[83] proposed a two-step deprotonation model to describe the protonation of the quartz surface. Their model is based on XPS data revealing shifts in the Si 2p and O 1s peaks, and proposes relative surface densities of $>SiOH^0$, $>SiOH_2^+$, and $>SiO^-$ species as a function of solution pH.

4.3.6 Effect of Chain Length and Composition

The chain length of the SAM precursor may impact surface properties and long-term film performance. For vapor-deposited films, larger molecules tend to have lower vapor pressures, which would impact the reaction cycle time. This may be offset, however, if there is significant improvement in film quality.

Fadeev and McCarthy[84] found that vapor deposition of trichlorosilanes with alkyl groups shorter than 7 carbon groups resulted in film thicknesses that were greater than the length of the alkyl chain, as measured by ellipsometry, suggesting a mechanism other than self-limiting film growth. Fadeev also found a trend of increasing water contact angle with increasing alkyl chain length. It is worth noting that the vapor reactions were not carried out in dry conditions, rather in a beaker that likely possessed a significant amount of water in the gas phase, which, it is suggested by other authors,[66] can lead to oligimer formation in the gas phase, and hence oligimer deposition.

Ohtake, Mino, and Ogawa[85] found that SAM films formed from *n*-aklyltrichlorosilanes with alkyl chains less than 8 carbon units long resulted in multilayer film growth, whereas films with longer alkyl chains resulted in self-limiting film thickness. This is in agreement with the results of Fadeev and McCarthy.[84]

Sugimura, Ushiyama, and Hozumi[86] investigated the deposition of fluoroalkyltrichlorosilanes of 8 and 10 carbon units in length on SiO_2, and found that the longer chain precursor yielded higher quality films, as measured by water contact angle, XPS, and lateral force microscopy (LFM). Mayer, *et al.*[38] indicate that the longer-chain fluoroalkyltrichlorosilane precursors may possess vapor pressure significantly lower than that of their shorter-chain counterparts, which may impact the reaction time necessary for complete film formation.

Stevens[87] argues that the large CF_3 end groups on fluorinated trichlorosilanes impart enough steric hinderence that complete networking at the silane end is not possible. This was confirmed experimentally by Blaudez, *et al.*[76] through monitoring Langmuir films of perfluorodecyltriethoxysilane on an acidic water subphase. The authors did not see the appearance of Si-O-Si infrared absorption bands indicative of film networking and crosslinking, and concluded that the lack of this bonding is a result of the increase in intermolecular distance to 5.8 Å from 4.8 Å for octadecyltrimethoxysilane, which does form networking bonds. The authors show, however, that the non-fluorinated counterparts are able to form networking bonds.

In experiments of alkyltrimethoxysilanes on a water subphase, Fontaine[88] found that the 2-D cross-linking can occur. The steric hindrance effects of the alkyl chain compression in forming a dense film was overcome by the energetics of forming the Si-O-Si network bonds. The authors observed hexagonal head group structure using grazing angle X-ray diffraction.

4.3.7 Effect of Annealing

Following the SAM formation, there may be uncondensed hydroxyl groups distributed throughout the interface. Tripp and Hair[89] showed that post-deposition annealing enhances the incorporation of these groups to form a more highly networked and highly bonded film.

Calistri-Yeh[90] showed that annealing can effect the wetting characteristics of SAMs from OTS and UTS (11 carbons). The advancing water contact angle did not change after 2 h anneal at temperatures ranging from 25 to 200 °C, but that the contact angle (CA) hysteresis (advancing minus receding) did change. The CA hysteresis increased in the OTS films after annealing at about 100 °C, and in the UTS films at about 120 °C. They also found the hexadecane advancing contact angle to decrease in the UTS films after annealing at 60 °C, and in the OTS films at 100 °C.

Angst and Simmons[56] found that curing overnight at 150 °C reduced the water contact angle, but also decreased the water adsorption relative to uncured films. They conclude that the curing is believed to enhance network and surface bond formation, and this enhanced bonding restricts access to surface sites by water molecules.

Maboudian[43] suggests that the condensation/polymerization reaction is spontaneous, and can achieve completion at room temperature in a few days, but can also be achieved by baking the sample at 100-120 °C for a few hours.

Fontaine, *et al.*[91] used a film of octadecyltrichlorosilane on native SiO_2 as the ultrathin insulating films in a metal-insulator-semiconductor (MIS) device. The authors observed a decrease in the positive charge states at the oxide interface after annealing at 350 °C in He for 30 min; these charge states may be indicative of unbonded hydroxyl groups.

4.3.8 Film Growth Models

Several groups have used a Langmuir model of irreversible adsorption to describe the growth of SAMs,[92-95] in which the rate of adsorption is proportional to the fraction of available adsorption sites. Hertl[96] investigated the reaction of functional alkoxysilanes on silica, and found the reaction order depended on the number of functional groups on the precursor; the growth of a film from trimethoxysilane followed third order kinetics. Each time a precursor molecule adsorbed on the surface, three potential surface sites were removed from the reaction system.

Richter, *et al.*[97] use X-ray reflectivity to probe growing films of OTS on Si(111), presumably with a native oxide, and concluded that the thickness of the growing film remains constant, at around 25 Å, and that the electron density of the film increases monotonically with increasing reaction time. The authors concluded that this indicates a film growth mode in which there are islands of film in which the alkyl chains are oriented normal to the substrate, and that these islands grow in size throughout the course of the reaction. This island-growth model is in agreement with previous work in this area by Banga[98] and others.

4.3.9 Surface Retreatment

It may be necessary, in the course of experiments or manufacturing, to remove a degraded surface treatment and reapply a new coating in its place. It is imperative in such a case that the new film possesses the same high quality and release characteristics as a release film on a virgin substrate. The concerns are as follows: (i) complete removal of the existing surface treatment; (ii) resurrection of the substrate initial state with respect to hydroxyl concentration and distribution, and degree of hydration; and (iii) verification of resulting film quality equivalent to the previous film.

Several groups have shown that SAMs can be removed from the substrate via oxidizing and other dissociative reactions. Sugimura[99,100] and Dressick[101] demonstrated that films from alkylsilanes could be patterned with selective exposure to short wavelength UV light. Sugimura reported a decrease in water contact angle as a function of UV exposure time, reaching a minimum of ~0° after 400 s. Ruzyllo, *et al.*[39] show that organic etch residues can be removed by UV irradiation in either wet or dry oxygen. Holländer, *et al.*[40] show that organic films can be oxidized by exposure to vacuum-ultraviolet in an O_2 ambient. Werst and Vinokur[102] similarly showed decomposition of alkoxy and siloxy ligands using e-beam irradiation.

Brunner[103] showed in experiments of cyclic SAM growth and UV/oxidation that the oxidized SAM film leaves behind its Si-O component, and this leads to a process of step-wise SiO_2 film growth. This may indicate that the removal of the alkyl chain by UV/ozone oxidation yields substrates that are of sufficient reactivity to form SAM films of at least moderate quality upon subsequent exposure to the SAM precursors.

The concept of removing a SAM film has been demonstrated, but the precise correlation between the virgin substrate and the reclaimed substrate has yet to be concretely established.

4.3.10 Probing Film Durability

Many different techniques have been used to probe the quality of SAMs, including various forms of spectroscopy and forms of wear testing. It is imperitive to understand not only the quality of the as-deposited films, but also how that film quality changes over time under various use and storage conditions. Pellerite, Wood, and Jones[104] note that storage conditions may affect the long-term stability of SAMs from trichlorosilanes precursors. Films stored in high humidity conditions for 12 weeks yielded decreases in water contact angle up to 15°, while samples stored in dry conditions showed no such change.

Perhaps the ultimate test for films that will be exposed to mechanical forces is mechanical wear testing. Srinivasan[105] investigated the friction wear characteristics using a lateral friction test structure, and observed a 1300% increase in the friction coefficient after 2100 cycles. Preliminary imprint durability results for SFIL are presented in Chapter 5.

4.4 SUMMARY

There is a large body of experimental work around the reaction of functional alkylsilanes on hydroxylated surfaces, especially various forms of SiO_2. Taken together, the data suggest that the substrate must be maximally hydroxylated, possess at least some adsorbed water, and be free of contaminants. The alkylsilane precursors that yield the best films are trifunctional, and possess at least some critical alkyl chain length. The highest quality films appear to be deposited through vapor precursor delivery, and annealing plays a crucial role in the ultimate film organization and performance, although precisely the best annealing conditions have not been identified. Considering the ongoing effort in this field, and the widely varying potential applications, there seems to be a large driving force to optimize all aspects of this reaction scheme.

Most attempts at modeling this type of reaction do not encompass all of the various parameters in the reaction sequence. It is unclear, for instance, whether the adsorbed water must be precisely controlled, or whether it is best to saturate the surface prior to film deposition, and drive excess water off in an anneal step. Silica gel literature suggests that condensation reactions are aided in an acidic environment, but it is unclear exactly what role the HCl (for chlorosilanes) plays in the adsorbed state. The condensation reaction kinetics in a film deposited from alkoxysilanes is likely to be at least somewhat different than that deposited from chlorosilanes.

It may be possible to develop a universal model for SAM deposition based on fundamental equations for each step in the reaction sequence, and derive from that the optimal conditions in each substep. Such a model could apply for vapor-, liquid-, and potentially supercritical-phase deposition, and account for the different reaction kinetics observed in different reaction systems, using precursors with different chain lengths or functional type and number. Additionally, a model that was able to predict the networking and surface bonding density may help predict the ultimate durability in various applications. This remains an open problem.

4.5 REFERENCES

1. Coleman, M.V. and D.J.D. Thomas, Phys. Status Solidi, 1967. 22(2): p. 593-602.
2. Boyd, F.R. and J.L. England, J. Geophys. Res., 1960. 65: p. 749.
3. Lisovskii, I.P., *et al.*, Thin Solid Films, 1992. 213: p. 164-169.
4. Litovchenko, V.G. and V.P. Kostylev, Semiconductor Films and Layered Structures. 1977, Kiev: Naukova Dumka.
5. Litovchenko, V.G. and G.P. Romanova, Thin Solid Films, 1981. 81: p. 27-34.
6. Levine, S.M. and S.H. Garofalini, Surf. Sci., 1985. 163: p. 59-66.
7. Mitra, S.A., Phil. Mag., 1982. B45: p. 529.
8. Pantelides, S.T. and W.A. Harrison, Phys. Rev. B, 1976. 13: p. 2667.
9. Iler, R.K., The Chemistry of Silica. 1979, New York: John Wiley & Sons.
10. Armistead, C.G., *et al.*, J. Phys. Chem., 1969. 73(11): p. 3947-4161.
11. Bermudez, V.M., J. Phys. Chem., 1970. 74(23): p. 4160.
12. Morrow, B.A. and A.J. McFarlan, Langmuir, 1991. 7: p. 1695.
13. Sindorf, D.W. and G.E. Maciel, J. Phys. Chem., 1982. 86: p. 5208.
14. Sindorf, D.W. and G.E. Maciel, J. Am. Chem. Soc., 1983. 105: p. 1487.
15. Bronnimann, C.E., R.C. Zeigler, and G.E. Maciel, J. Am. Chem. Soc., 1988. 110(7): p. 2023.
16. Chuang, I.-S., *et al.*, J. Phys. Chem., 1992. 96: p. 4027.
17. Kinney, D.R., I.-S. Chuang, and G.E. Maciel, J. Am. Chem. Soc., 1993. 115: p. 6786.

18. Chuang, I.-S. and G.E. Maciel, J. Am. Chem. Soc., 1996. 118: p. 401.

19. DeBoer, J.H. and J.M. Vleeskins, Proc. K. Ned. Akad. Wet., Ser. B: Palaentol., Geol., Phys., Chem., 1958. B61: p. 2-11.

20. Peri, J.B. and A.L. Hensley, J. Phys. Chem., 1968. 72: p. 2926.

21. Branda, M.M., R.A. Montani, and N.J. Castellani, Surface Science, 1995. 341: p. 295.

22. Branda, M.M. and N.J. Castellani, Surface Science, 1997. 393: p. 171.

23. Branda, M.M., R.A. Montani, and N.J. Castellani, Surface Science, 2000. 446: p. L89-L94.

24. Paparazzo, E., *et al.*, J. Vac. Sci. Tech. A, 1992. 10(4): p. 2892.

25. Paparazzo, E., Appl. Surf. Sci., 1993. 72: p. 313.

26. Sneh, O. and M. George, J. Phys. Chem., 1995. 99: p. 4639.

27. Ugliengo, P., *et al.*, Chem. Phys. Lett., 1992. 191: p. 537.

28. Zhuravlev, L.T., Coll. Surf. A, 2000. 173: p. 1-38.

29. Shioji, S., *et al.*, Adv. Powder Tech., 2001. 12(3): p. 331-342.

30. Burneau, A., *et al.*, Langmuir, 1990. 6: p. 1364.

31. Ek, S., *et al.*, Thermochimica Acta, 2001. 379(201-212).

32. Iler, R.K. and R.L. Dalton, 1956: p. 955-963.

33. Sneh, O., M.A.Cameron, and S.M. George, Surf. Sci., 1996. 364: p. 61-78.

34. Gun'ko, V.M., *et al.*, Inter. J. Mass Spec. Ion Proc., 1998. 172: p. 161-179.

35. Malandrini, H., *et al.*, Langmuir, 1997. 13: p. 1337-1341.

36. Knez, Z. and Z. Novak, J. Chem. Eng. Data, 2001. 46: p. 858-860.

37. Cras, J.J., *et al.*, Biosensors and Bioelectronics, 1999. 14(8-9): p. 683-688.

38. Mayer, T.M., *et al.*, J. Vac. Sci. Tech. B, 2000. 48(5): p. 2433-2440.

39. Ruzyllo, J., *et al.*, Proc. Electrochem Soc., 1987. 87-11: p. 281-289.

40. Holländer, A., J.E. Klemberg-Sapieha, and M.R. Wertheimer, Macromolecules, 1994. 27(10): p. 2893-2895.

41. Efimenko, K., W.E. Wallace, and J. Genzer, J. Coll. Int. Sci., 2002. 254: p. 306-315.

42. Ouyang, M., *et al.*, Chem. Mater., 2000. 12(6): p. 1591-1596.

43. Maboudian, R., W.R. Ashurst, and C. Carraro, Sensors and Actuators, 2000. 82: p. 219-223.

44. Veiseh, M., M.H. Zareie, and M. Zhang, Langmuir, 2002. 18(17): p. 6671-6678.

45. Loo, Y.-L., *et al.*, Appl. Phys. Lett., 2002. 81(3): p. 562-564.

46. Kumar, A., H.A. Biebuyeck, and G.M. Whitesides, Langmuir, 1994. 10: p. 1498-1511.

47. Bailey, T., *et al.*, J. Vac. Sci. Tech. B, 2000. 18(6): p. 3572.

48. Resnick, D.J., *et al.*, Semiconductor International, 2002(June 1).

49. Tripp, C.P., R.P.N. Veregin, and M.L. Hair, Langmuir, 1993. 9: p. 3518.

50. Lindén, M., J.P. Slotte, and J.B. Rosenholm, Langmuir, 1996. 12(18): p. 4449-4454.

51. Hoffmann, P.W., M. Stelzle, and J.F. Rabolt, Langmuir, 1997. 13: p. 1887-1880.

52. Fadeev, A.Y. and T.J. McCarthy, Langmuir, 1999. 15(11): p. 3759-3766.

53. Monde, T., *et al.*, J. Coll. Int. Sci., 1997. 185: p. 111-118.

54. Genzer, J., K. Efimenko, and D.A. Fischer, Langmuir, 2002. 18(24): p. 9307-9311.

55. Geer, R.E., *et al.*, Langmuir, 1994. 10: p. 1171-1176.

56. Angst, D.L. and G.W. Simmons, Langmuir, 1991. 7(10): p. 2236-2242.

57. Bierbaum, K., *et al.*, Langmuir, 1995. 11(2): p. 512-518.

58. Parikh, A.N., *et al.*, J. Phys. Chem., 1994. 98: p. 7577.

59. Brzoska, J.B., N. Shahidzadeh, and F. Rondelez, Nature, 1992. 360: p. 719.

60. Brzoska, J.B., I.B. Azouz, and F. Rondelez, Langmuir, 1994. 10(11): p. 4367.

61. Davidovits, J.V., *et al.*, Surf. Sci., 1996. 352-354: p. 369-373.

62. Goldmann, M., J.V. Davidovits, and P. Silberzan, Thin Solid Films, 1998. 327-329: p. 166-171.

63. Gao, W. and L. Reven, Langmuir, 1995. 11(6): p. 1860-1863.

64. Tripp, C.P. and M.L. Hair, Langmuir, 1995. 11: p. 1215.

65. Wieber, G., *et al.* in Organic-Inorganic Hybrids Conference. 2000. University of Surrey, Guilford, UK.

66. McGovern, M.E., K.M.R. Kallury, and M. Thompson, Langmuir, 1994. 10: p. 3607-3614.

67. Cao, C., A.Y. Fadeev, and T.J. McCarthy, Langmuir, 2001. 17(3): p. 757-761.

68. Wang, R. and S.L. Wunder, Langmuir, 2000. 16(11): p. 5008-5016.

69. Wang, R., *et al.*, Langmuir, 2000. 16(2): p. 568-576.

70. Rye, R.R., G.C. Nelson, and M.T. Dugger, Langmuir, 1997. 13: p. 2965-2972.

71. Bunker, B.C., *et al.*, Langmuir, 2000. 16: p. 7742.

72. Vallant, T., *et al.*, J. Phys. Chem. B, 1998. 102: p. 7190-7197.

73. Zhao, X. and R. Kopelman, J. Phys. Chem., 1996. 100: p. 11014.

74. Le Grange, J.D. and J.L. Markham, Langmuir, 1993. 9: p. 1749.

75. Silberzan, P., *et al.*, Langmuir, 1991. 7: p. 1647.

76. Blaudez, D., *et al.*, Langmuir, 2002. 18(24): p. 9158-9163.

77. Allara, D., A.N. Parikh, and F. Rondelez, Langmuir, 1995. 11(7): p. 2357-2360.

78. Kopylov, V.M., *et al.*, Pol. Sci. A, 1995. 37(3): p. 242-265.

79. Rankin, S.E. and A.V. McCormick, Chem. Eng. Sci., 2000. 55: p. 1955-1967.

80. Evans, M., R. Jones, and R. Overstreet, Modeling Hydrochloric Acid Evaporation in ALOHATM. 1993, National Oceanic and Atmospheric Administration: Seattle. p. 3-6.

81. Linden, M., J.P. Slotte, and J.B. Rosenholm, Langmuir, 1996. 12(18): p. 4449-4454.

82. Reymond, J.P. and F. Kolenda, Powder Tech., 1999. 103: p. 30-36.

83. Duval, Y., *et al.*, J. Phys. Chem. B, 2002. 106: p. 2937-2945.

84. Fadeev, A.Y. and T.J. McCarthy, Langmuir, 2000. 16(18): p. 7268-7274.

85. Ohtake, T., N. Mino, and K. Ogawa, Langmuir, 1992. 8(9): p. 2081.

86. Sugimura, H., *et al.*, J. Vac. Sci. Tech. B, 2002. 20(1): p. 393-395.

87. Stevens, M.J., Langmuir, 1999. 15: p. 2773-2778.

88. Fontaine, P., M. Goldmann, and F. Rondelez, Langmuir, 1999. 15: p. 1348.

89. Tripp, C.P. and M.L. Hair, Langmuir, 1995. 11: p. 149.

90. Calistri-Yeh, M., *et al.*, Langmuir, 1996. 12(11): p. 2747-2755.

91. Fontaine, P., *et al.*, Appl. Phys. Lett., 1993. 62: p. 2256.

92. Vallant, T., *et al.*, Langmuir, 1999. 15: p. 5339-5346.

93. Richter, A.G., *et al.*, Phys. Rev. E, 2000. 61(1): p. 607-615.

94. Brunner, H., *et al.*, Langmuir, 1999. 15: p. 1899-1901.

95. Schreiber, F., Prog. Surf. Sci., 2000. 65: p. 151-256.

96. Hertl, W., J. Phys Chem., 1968. 72(4): p. 1248-1253.

97. Rihter, A.G., *et al.*, Langmuir, 1998. 14(21): p. 5980-5983.

98. Banga, R., *et al.*, Langmuir, 1995. 11: p. 4393-4399.

99. Sugimura, H., *et al.*, Langmuir, 2000. 16: p. 885.

100. Sugimura, H. and N. Makagiri, Jpn. J. Appl. Phys., 1997. 36: p. L968.

101. Dressick, W.J. and J.M. Calvert, Jpn. J. Appl. Phys., 1993. 32: p. 5829.

102. Werst, D.W. and E.I. Vinokur, J. Phys. Chem. B, 2001. 105(8): p. 1587-1593.

103. Brunner, H., *et al.*, Langmuir, 1996. 12: p. 4614.

104. Pellerite, M.J., E.J. Wood, and V.W. Jones, Journal of Physical Chemistry B, 2002. 106(18): p. 4746-4754.

105. Srinivasan, U., *et al.* in Proc. Solid-State Sens. Act. Workshop. 1998. Hilyon Head.

Chapter 5: SFIL Imprint Template Release Layer

5.1 IMPRINT TEMPLATE SURFACE TREATMENT TECHNOLOGY

5.1.1 Introduction

The complete separation of the imprint template from the imprinted material is essential for the success of imprint lithography. Any imprint material retained on the imprint template will result in pattern defects on at least the following imprint, and the potential exists for a far worse outcome. Figure 5.1 illustrates perfect separation as compared to two modes of imperfect separation, partial or complete delamination of the imprint layer from the substrate, and internal feature failure, both of which result in imprint material being retained on the template.

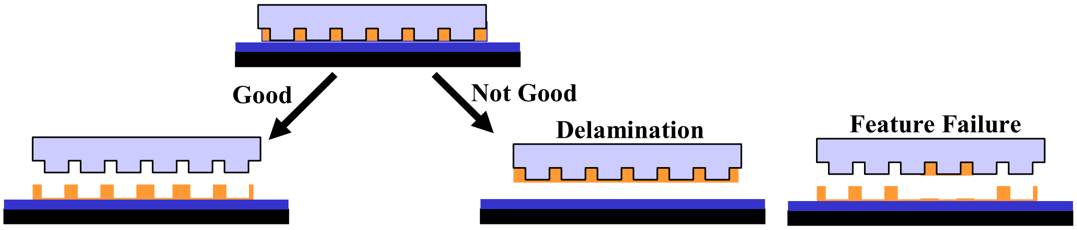

Figure 5.1: Illustration of perfect and imperfect separation of imprint template from substrate.

The act of separation is governed by interface fracture mechanics and is related to the surface properties of the imprint template and substrate, and the surface and bulk material properties of the imprint polymer.[1] Various authors have attempted to change the material interactions at the template/polymer interface by, for example, adding fluorinated additives into the photopolymer which preferentially migrate to the template/polymer interface,[2] CVD or PECVD fluoropolymer films[3-6] or self-assembled monolayer films[7-11] applied to the template to reduce adhesion effects, or by using exotic imprint template materials such as sapphire.[12] More broadly, anti-sticking layers have been investigated for use in contact lithography for many years.[13-15]

5.1.2 PVD, CVD and PECVD Fluoropolymer Release Layers

Perhaps the most widely known material used for release or non-stick applications is polytetrafluoroethylene (PTFE), or Teflon®. Matsui used a few nm of evaporated PTFE on the imprint mold in imprint experiments with PMMA and spin-on-glass (SOG) as the imprint polymer.[3] The authors found that the PTFE mold coating exhibited no noticeable degradation through ten imprint cycles, as evidenced by the absence of visible defects.

Jaszewski and coworkers have studied the reliability of deposited fluorocarbon films for use in hot embossing lithography.[5,6] The authors conclude that functional fluorocarbon material in the mold release layer becomes entrained in the imprinted material, thus limiting the lifetime of its mold release function.[6]

Hirai compared evaporated fluorinated ethylene-propylene copolymer (FEP) to a new perfluoropolyether-trimethoxysilane (PEPE-S), using water contact angle to probe release film durability.[4] The authors observed a slight decrease in water contact angle for the FEP-coated sample after six imprints, and accelerated wear testing using an abrasion testing machine caused significant FEP film degradation. In comparison, the PEPE-S films demonstrated good durability in both tests.

5.1.3 Self-Assembled Monolayer Release Layers

Perhaps the most commonly used release layers in imprint lithography are those resulting from the reaction between functional alkyl- or fluoroalkylsilanes with the template or mold, most commonly fused silica or oxidized silicon wafers, which both possess the surface hydroxyl groups needed to allow covalent film-surface bonding.

Taniguchi compared the durability of FOTS versus KP-801M (Shin-Etsu), which is a fluoroalkyl oligimer,[8] using glass slides as the imprint mold and PAK01 resin (Toyo Gosei). The authors found that the FOTS-treated slide demonstrated less degradation in release performance than the KP-801M-treated slide.

In the fabrication of T-gate devices using nanoimprint lithography, Chen used DC20 (Dow Corning), a dilutable PDMS material, and OTS in separate imprinting experiments.[11] The authors found that the DC20 film survived only one or two imprint runs, but the vapor-deposited OTS film survived “many” imprint sessions, although no quantification of durability was presented.

Beck investigated the performance of FOTS deposited from both liquid and vapor phases in imprint experiments using Si imprint molds and MR-I 8000 imprint resist (micro resist technologies).[9] The authors found that non-patterned areas are reproduced well using both treatment methods, but that the patterned areas of the mold are reproduced faithfully in the imprint material using only the vapor-treated mold. Various other groups have also used fluoroalkyl functional silanes as release agents in UV-curing imprint lithography.[2,16]

Based on these results and others, it was decided to pursue a fluoroalkyltrichlorosilane as the primary release agent for SFIL templates.

Considering the discussions outlined in Chapter 2, there are potentially a wide variety of materials used in imprint template manufacture. It is necessary, therefore, that any such material that comes into intimate contact with the etch barrier possess surface hydroxyl groups of sufficient number and distribution to which the silane can bond. This chapter presents some introductory experiments into evaluating the effectiveness of the FOTS surface treatment on various materials that may be used in template manufacture, including preliminary data on imprinting durability of the template surface treatment. Indium tin oxide (ITO), deposited silicon dioxide (PETEOS), silicon nitride (correctly Si_3N_4, but abbreviated here as SiN), and silicon oxynitride (correctly SiO_xN_y, but abbreviated here as SiON) are also investigated for their potential as substrates for the FOTS surface treatment.

5.2 EXPERIMENTAL

Experimental fused silica sample substrates were cut from 5-in by 0.125-in photomask substrates (HOYA) to 1 cm squares. For the substrates which contained ITO, the ITO films themselves were deposited in a Motorola-designed three cathode sputtering system equipped with both radio frequency and direct current sputter capabilities. In this system, the substrate holder is located above the cathodes, and the system base pressure is 5.0×10^{-7} Torr. No pre-sputter surface preparation was performed on the substrates. All depositions were conducted at 3 mTorr and 100 W. In order to maximize optical transmission at 365 nm (the current ideal SFIL exposure wavelength) and to lower resistivity, the ITO films were annealed on a hot plate at 350 °C, as discussed in Chapter 2. Silicon wafer samples of various films on Si wafers were received from Motorola Labs. Each wafer was coated with 600 Å

ITO, followed by plasma-enhanced chemical vapor deposition (PECVD) of either SiO_2, SiO_xN_y, or Si_3N_4 at a thickness of 1000 Å. The samples were cleaned in an ultrasonic acetone bath for 15 min, followed by UV-ozone exposure in a Jelight UVO-42 system for 15 min.

The samples were treated by vapor exposure to tridecafluoro-1,1,2,2-tetrahydrooctyl trichlorosilane (Gelest) at 760 Torr (precursor plus N_2) for 2 hrs, followed by annealing at 100 ºC for 15 min, unless otherwise noted. The reaction sequence, including purging and annealing steps, was performed in a specially-designed surface treatment chamber that is described in Appendix B. For the rinsing experiments, samples were rinsed in alternating IPA and acetone ultrasonic baths. For the buffing experiments, samples were lightly buffed with a Kimwipe that was saturated with IPA.

The etch barrier in the imprinting experiments was comprised of 44% (w/w) (3-acryloxypropyltristrimethylsiloxy)silane (SIA 0210.0, Gelest), 10% 1,3-bis(3-methacryloxypropyl)tetramethyldisiloxane (SIB1402.0, Gelest), 42% *n*-butyl acrylate (Aldrich), and 4% 2-hydroxy-2-methyl-1-phenyl-propan-1-one (Darocur 1173, Ciba), which was diluted with 1% 2,2,3,3,4,4,5,5,6,6,7,7-dodecafluoroheptyl acrylate (Aldrich). Approximately 100 nl of this solution was dispensed on a Si wafer substrate that was previously coated with commercial bottom anti-reflection coating (BARC) (DUV30J-11, Brewer Science) to be used as the transfer layer. The BARC was spun at 3000 rpm for 60 sec and baked at 180 ºC for 60 sec, yielding films of thickness ~1250 Å. The films were double-coated, yielding thicknesses in the range of 250 nm.

Contact angles were measured on a Rame Hart m100 Contact Angle Goniometer. The RH-100 consists of a goniometer, a manually operated micropipette that is held in position above the gimbaled sample stage, an optics rail to align the diffuse light illumination system with a CCD camera that feeds the image to the computer for image analysis. There is disagreement in the literature as to the best method of determining surface free energy of a solid surface, as discussed in Appendix C. For the purposes of this work, contact angles using only deionized water were measured.

The XPS data were obtained using a Physical Electronics PHI5700 ESCA system equipped with an Al monochromatic source (Al Kα radiation at 1486.6 eV). The base pressure in the XPS UHV chamber was 1×10^{-10} Torr. Wide range (survey) scans were obtained with a step size of 1 eV and pass energy of 93.9 eV; high resolution scans were taken with a step size of 0.1 eV and pass energy of 11.75 eV. The Ag $3d_{5/2}$ XPS peak at 368.3 eV from a sputtered-clean Ag foil was used to calibrate the system. Atomic concentration data were obtained by normalizing the XPS peak area by the associated emission sensitivity factor. The work function of ESCA system is 3.3 eV, and the XPS intensity variation should be about ± 2.5 %, according to monthly calibration records.[17]

5.3 RESULTS AND DISCUSSION

5.3.1 Fused Silica Substrates

Deposition of FOTS on Fused Silica

Traditional SFIL imprint templates are comprised of patterned fused silica. As was discussed in Chapter 3, there are many parameters that can affect the resulting film. In an initial investigation it was desired to determine both the reaction time necessary to ensure a complete reaction, and also to determine the critical temperature for film deposition, as defined by Rondelez and coworkers.[18,19]

A series of samples were generated using two different reaction temperatures, and over various reaction times from zero to 120 min. The films were probed with water contact angle and XPS, and the results are shown in Figure 5.2. Contact angle in this case is defined as the interior angle the droplet makes with the surface, which yields a zero angle for complete wetting, and 180° for complete hydrophobicity. It appears that the reaction is nearly complete after only a few minutes, but that the film coverage may continue to increase through the entire time range. The contact angle data are less noisy than the XPS data. The probe areas for these two measurement techniques is vastly different – the water droplet contact area is on the order of mm^2, while the X-ray spot size used in XPS is on the order of μm^2. Contamination of exposed SiO_2 by organic compounds is known to reduce the surface energy of silica, and any untreated areas are likely to attract such contamination. This change in surface energy of unreacted regions would likely mitigate sample-to-sample coverage estimate variations based on water contact angle. It is expected that the fluorine XPS signal would not be affected by such contamination, and thus the XPS data shown in Figure 5.2b may more accurately represent the fluorocarbon coverage. Interestingly, both measurement techniques indicate that the film quality is better at the higher reaction temperature, which is in direct disagreement with the results for equivalent films published by Rondelez and coworkers.[18,19]

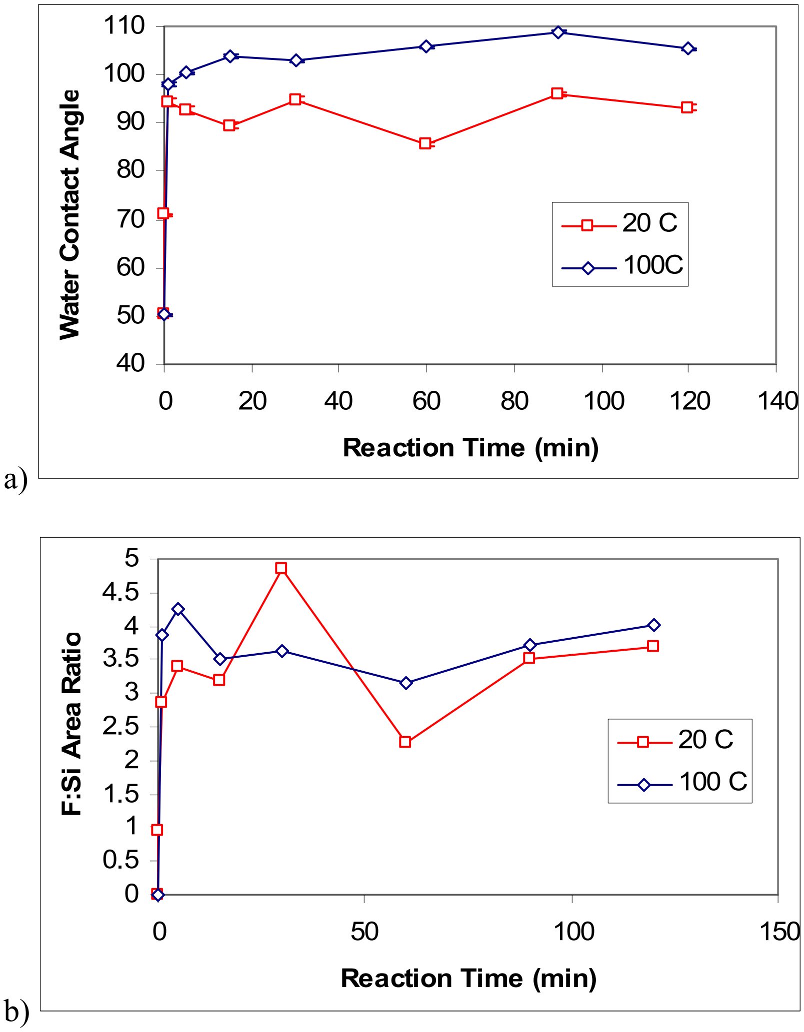

Figure 5.2: Comparison of (a) water contact angle and (b) F:Si XPS peak area ratio for samples treates at 20 °C for various reaction times.

In order to probe this further, a series of samples were generated at various reaction temperatures, and the film quality was assessed by water contact angle and XPS, as shown in Figure 5.3. There appears to be no obvious trend to the data. The experiments of Rondelez and coworkers[18,19] indicate that the critical surface tension of these types of films is constant below some critical temperature, and increases monotonically above that temperature. The contact angle of water, for example, would increase for films of higher quality, and conversely for films or poorer quality. No such trend exists in these data.

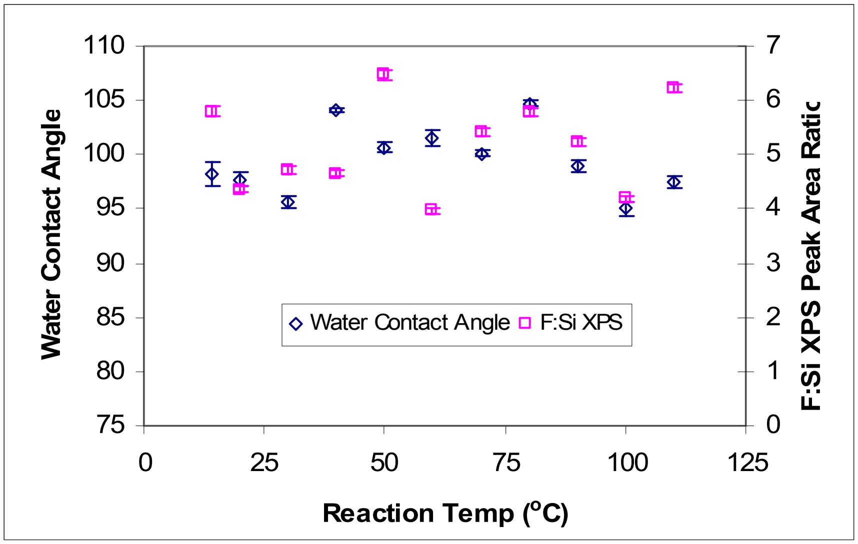

Figure 5.3: Water contact angle and F:Si XPS peak area ratio for samples prepared at various reaction temperatures for 120 min reaction time.

It is possible that the increase in substrate temperature causes a change in the degree of surface hydration, which could impact the final film. New procedures were implemented designed to provide better surface hydration control. The new reaction sequence steps include surface dehydration by baking at ~100 °C in a N_2 stream, followed by controlled rehydration using N_2 flow through a water bubbler. The liquid in the water bubbler can be changed to various salt solutions to allow more fine control over total water exposure. Experiments were designed around these new additions to the sequence, and this is discussed in more detail in Chapter 5.

Imprinting Durability of FOTS on Fused Silica

Two fused silica samples were surface treated according to the standard procedure, and used as blank imprint templates in this imprinting experiment. One such sample was imprinted only once, and then analyzed with XPS. A second sample was imprinted five times, and it and all imprinted samples were also analyzed with XPS. The resulting F:Si peak area ratios are shown in Figure 5.4, with different scales for the template and etch barrier signals. The template shows mild loss of F between the first and fifth imprints, and the etch barrier shows the existence of F through the first three imprints. It was thought that loosely-bound hydrolyzed FOTS monomers or oligimers were being removed in the initial imprints, after which the more durably-bound film would remain. The imprint templates that were used for 256 and 320 imprints in the defect study discussed in Chapter 6 were analyzed with XPS, and significant loss of F from the template was observed, as shown in Figure 5.5. It appears that very little F remains on the template, as revealed by the relatively small F signal. This indicates that the F species retained in the imprinted etch barrier is non-zero. This also suggests that this particular film does not appear to possess the imprinting durability required for hundreds or thousands of imprints.

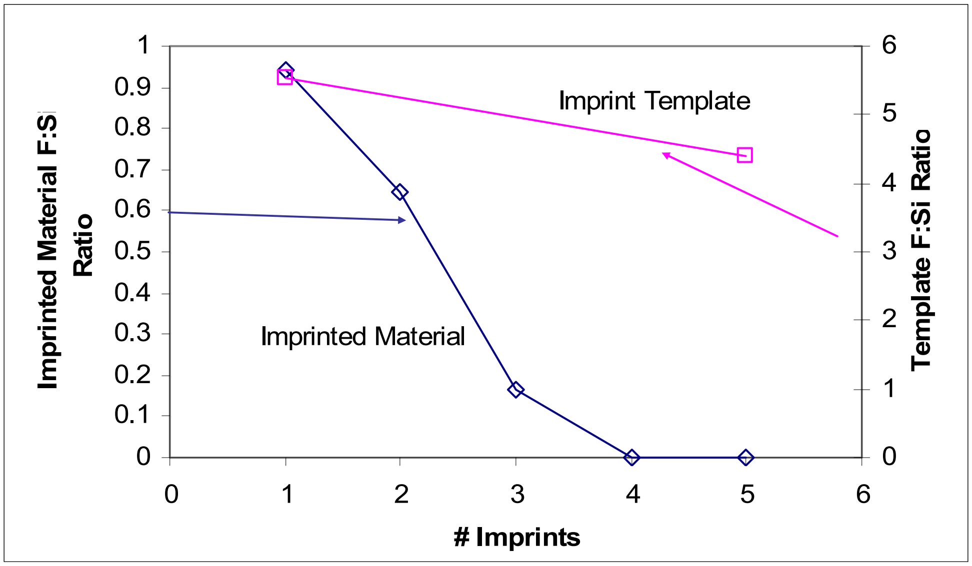

Figure 5.4: F:Si XPS peak area ratios for imprinted etch barrier and imprint templates. Note the two different ordinate scales.

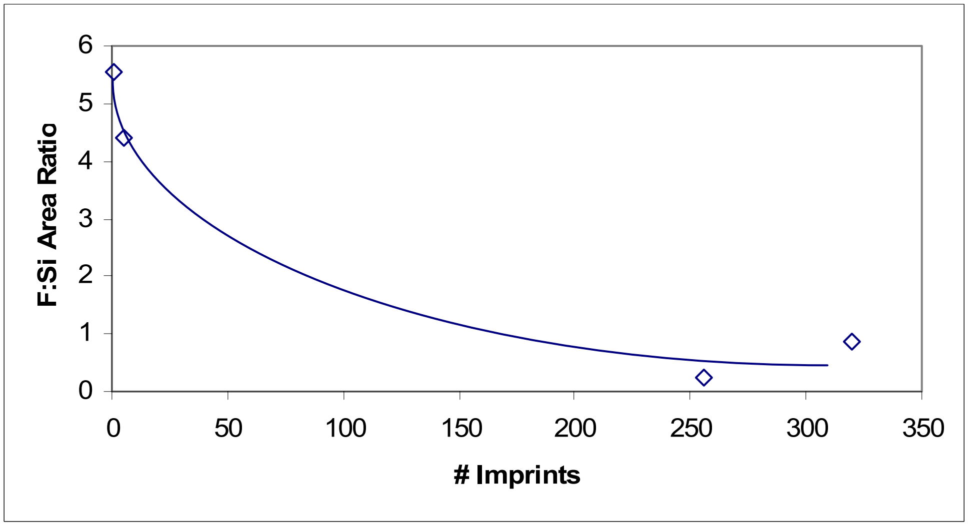

Figure 5.5: Comparison of template surface treatment F:Si XPS peak area ratios after various numbers of imprints. The trend line was added to guide the eye, and is not meant to accurately represent the precise degradation function.

At the time of this writing, no other literature was found which presents imprint template surface treatment durability results after so many imprints. It has been suggested that the FOTS monomer may not be able to optimally self-organize relative to its non-fluorinated counterparts, as was discussed in Chapter 3. The improvement in surface energy of these films may come at the expense of the two-dimensional networking and density of bonds to the substrate, as well as possibly lower film density, and these factors may contribute to the observed inadequate film durability. It is important to note that no aspect of this reaction is assumed optimized. Optimizing various factors such as surface hydroxylation and hydration state, reaction temperature, and anneal conditions, among others, may prove to enhance the resulting film characteristics. Further work in identifying the optimal degree of hydration for FOTS films is presented and discussed in Chapter 5.

5.3.2 Indium Tin Oxide Substrates[20]

Indium tin oxide is currently being used in some imprint lithography templates, and any ITO that is exposed to the etch barrier must possess release characteristics. Several groups have shown that alkyl trichlorosilanes monolayers form on ITO substrates,[21-23] but none have demonstrated the durability of such films in imprint applications.

The surface treatment reaction on one ITO template resulted in a very cloudy film formation, which was assumed to be excess film and was removed by wiping the template with a cleanroom wiper soaked with acetone and IPA. Imprinting with the template resulted in catastrophic release failure, and nearly the entire imprint field of polymerized etch barrier adhered to the template and was released from the transfer layer. It was thought that wiping the template removed most of the release layer, which may indicate very limited durability of the surface treatment on ITO, as formed under those conditions. Interestingly, Schondelmaier[23] observed that wiping a similar SAM film deposited on ITO resulted in loss of F, but not complete loss.

In order for an effective and durable surface treatment reaction of FOTS on ITO, the substrate must possess surface hydroxyl groups, and there must be water adsorbed on the substrate to hydrolyze the FOTS monomers. Previous literature suggests the existence of hydroxyl groups on ITO,[24,25] although no titration experiments similar to those used to probe hydroxyl groups on SiO_2[26] have been found in the literature. The following experiment was designed to compare the hydroxyl groups on ITO and SiO_2.

Probing the Hydroxyl Concentration on ITO

Methanol (CH_3OH) can be used as a probe molecule to determine the surface concentration of hydroxyl (-OH) functional groups on SiO_2.[26] When CH_3OH is adsorbed onto SiO_2 at 130 K, it forms hydrogen bonds with the -OH groups, and the amount of CH_3OH desorbing during a temperature programmed heating ramp titrates the -OH group density. TPD analyses presented by Sneh and George show multilayer CH_3OH desorption from SiO_2 at 150 K followed by a broad desorption feature from 150 to 220 K, which is attributed to hydrogen-bonded CH_3OH. The integrated peak area of this broad feature is a measure of the density of -OH groups on the surface. This titration technique was applied in this study to ITO film surfaces for comparison to SiO_2 films deposited by chemical vapor deposition.

Methanol adsorption below 130 K followed by TPD to 423 K was performed for the ITO and SiO_2 surfaces. The mass-to-charge ratio (m/z) 31 (for the CH_3O^+ ionization fragment) was measured by a quadrupole mass spectrometer and used to detect CH_3OH. The samples were annealed at 423 K for 30 min in UHV to desorb water prior to adsorption and TPD procedures. TPD was performed for 0.2, 0.6, and 1.0 L (1 L = 10^{-6} T·s) CH_3OH exposures for each sample (Figure 5.6), and the TPD spectra for the ITO surface were similar to spectra for CH_3OH desorption from SiO_2, indicating that this titration method is suitable for detecting -OH groups on ITO. These exposures do not saturate the -OH groups; to do this would require at least 100 L exposure[26] and is beyond the system capability. Hydrogen-bonded CH_3OH on the ITO sample desorbed about 15 K lower than on the SiO_2 sample, which suggests that CH_3OH was more strongly bound to the hydroxyls on the SiO_2 surface. Relative comparison of TPD peak areas, based upon the average peak area ratio from the exposures examined, showed that the ITO surface had 13 ± 4 % more -OH groups than the SiO_2 surface. This data suggests that -OH groups on the ITO surface bind H_2O less strongly than on the SiO_2 surface.

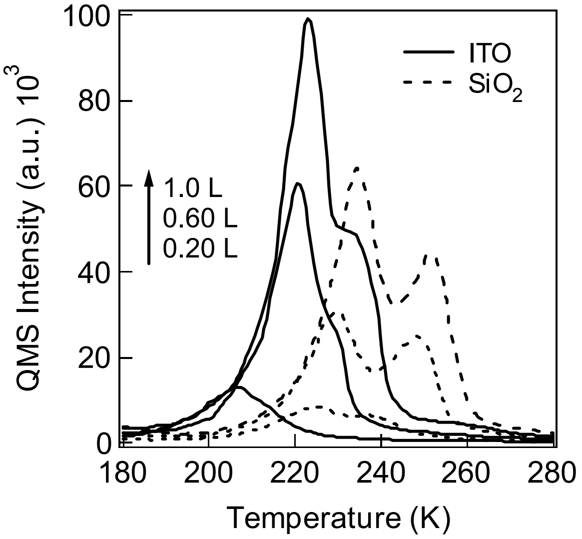

Figure 5.6: TPD spectra of the broad desorption feature attributed to hydrogen-bonded CH_3OH for 0.2, 0.6, and 1.0 L exposures on the ITO and SiO_2 surfaces.

Although proof of concept of the use of ITO-based templates has been demonstrated, as shown here are in Chapter 2, future work will focus on better tailoring the release layer and/or the release layer preparation sequence to the ITO films.

5.3.3 Silicon Nitride and Silicon Oxynitride Substrates[27]

At the time of this writing, the best known method for depositing FOTS on ITO resulted in a film with very poor imprinting durability, as discussed above. A potential work-around is to add a buffer layer between the blanket ITO film and the patterned oxide features; the buffer layer would then need to be compatible with the surface treatment. Silicon nitride (Si_3N_4) and silicon oxynitride (SiO_xN_y) are two candidates. It was believed that the difference in film composition between the SiO_2 film and the underlying buffer layer (SiN or SiON) would allow dry etch patterning of the SiO_2 layer to define the template features without significantly etching the buffer material. Also, depositing a buffer layer that is sufficiently thin would not impair the ability of the underlying ITO to dissipate charge during e-beam pattern definition or SEM inspection.

It has been shown that alkylsiloxane monolayers can be formed on HF-treated Si_3N_4 substrates,[28] which are deficient in oxygen. The current treatment procedure involves exposure of the substrate to air and UV-ozone treatment. The surface of a Si_3N_4 film is known to undergo oxidation on exposure to air[29] even at room temperature.[30] The effect of the UV-ozone treatment on film composition was investigated by XPS, as shown in Figure 5.7. Figure 5.7a-c are the results from the SiN films, and Figure 5.7d-f are those from the SiON films; (a) there is a noticeable increase in the Si-O peak at ~104 eV, but no significant change in the Si-N peak at ~103 eV; (b) an increase in the O 1s peak corresponding to the increased Si-O signal in (a); (c) no significant change in the N 1s peak; no significant change in any of the peaks for the SiON film, perhaps because the film was already O-rich. This composition can be tuned during deposition to achieve an optimal etch selectivity to the SiO_2 film.

The surface oxidation in this case is not expected to impact the process in a negative way. The nitrogen-rich SiON and SiN films can provide the etch selectivity to SiO_2 needed for patterning the template features. The surface oxidation of the SiN and SiON films may yield a film surface that is chemically similar to that of SiO_2 which, in turn, may enhance the surface treatment reaction.

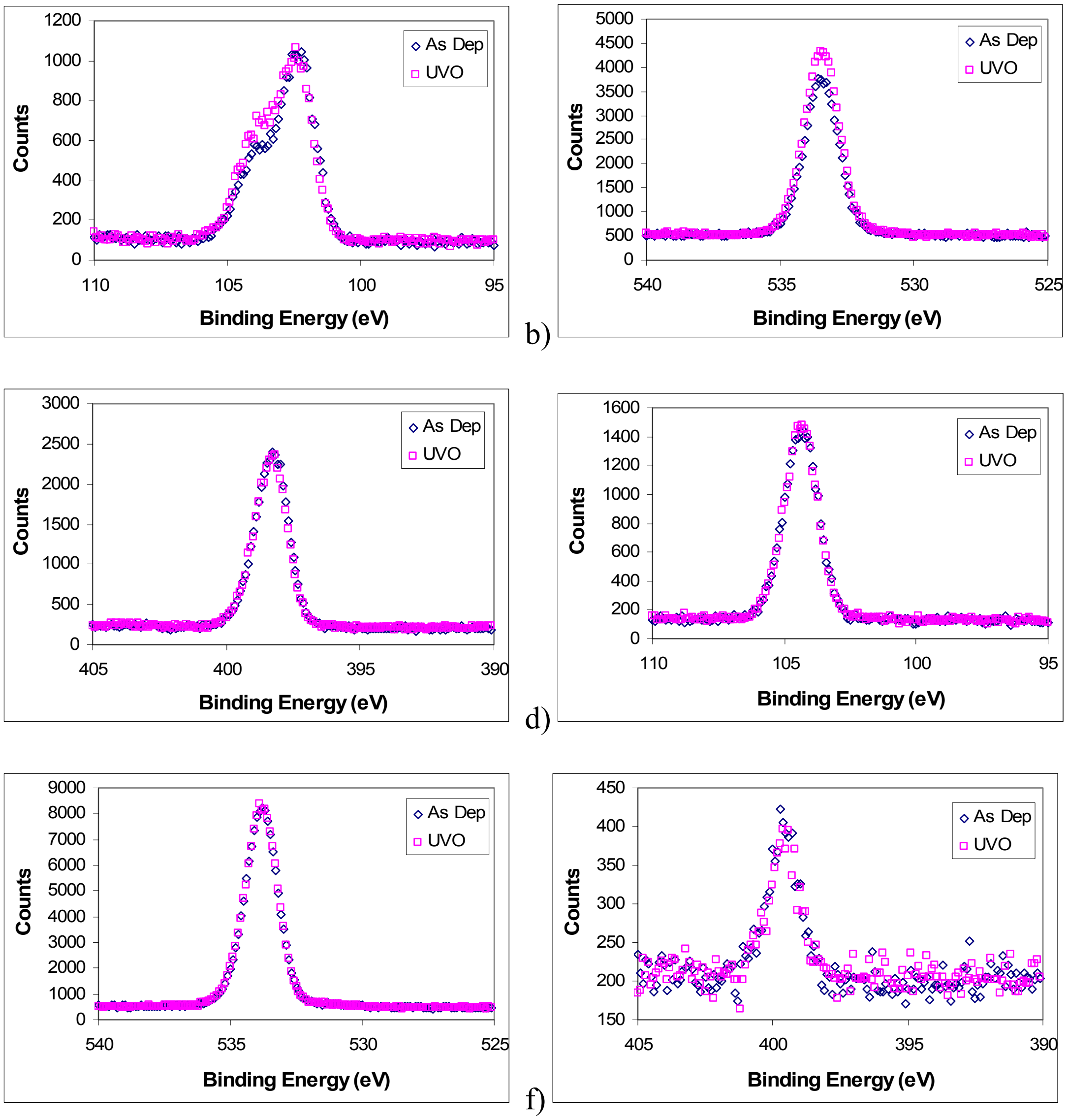

Figure 5.7: XPS investigation of films exposed to UV-ozone treatment for 15 min.

All samples analyzed retain F species following both the solvent-rinse procedure and the buffing procedure. Drawing an analogy to the ITO investigation, these results indicate that the reaction of tridecafluoro-1,1,2,2-tetrahydrooctyltrichlorosilane on SiO_2, SiO_xN_y, and Si_3N_4 would yield surface treatment films of at least modest durability. The SiN films appear to retain less F species than the others, perhaps due to the lack of a fully oxidized surface. In light of these results, it may be necessary to allow longer UV-ozone treatment for the SiN film, or to use SiON films of a certain composition which possess the surface chemistry needed for the FOTS reaction while also maintaining the required etch selectiviy.

Further enhancements could possibly be made to the films following oxide etch (feature definition) and prior to the surface treatment, such as increasing the surface silanol concentration using, e.g., H_2O plasma. Further process development would most likely be needed to yield optimal surface treatment film quality.

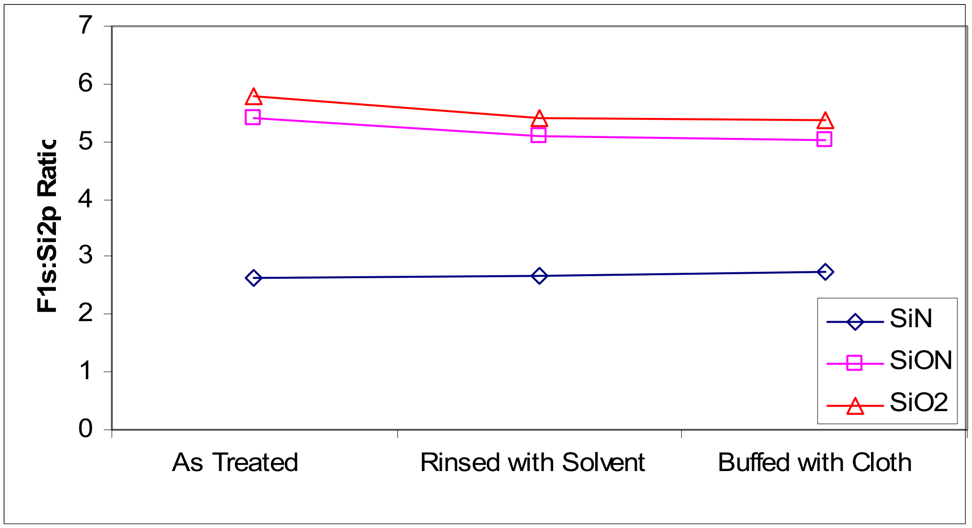

Figure 5.8: F 1s:Si 2p XPS peak area ratios comparing various stages in the initial evaluation of buffer films.

5.4 CONCLUSIONS

Investigation into the critical reaction temperature for FOTS on fused silica was inconclusive. The reaction appears largely complete within the first few minutes, but more data are needed for a complete kinetics study. The reaction of FOTS on fused silica imprint templates yielded films of modest durability, and a steady decrease in F species on the template was observed with increasing numbers of imprints. Further work is needed to optimize this reaction in order to extend imprinting durability.

Imprinting with an FOTS-treated ITO template revealed a potentially severe lack of imprinting durability. Methanol TPD was used to probe for the existence of hydroxyl groups on the ITO surface, which are necessary for FOTS to bond covalently to the substrate. Hydrogen-bonded methanol desorbed about 15K lower than that from SiO_2; it was concluded that the methanol is less strongly hydrogen-bound to the ITO hydroxyl groups than to the SiO_2 silanol groups. This suggests that H_2O may also be less strongly bound to the surface hydroxyl groups. More work is needed in order to quantify the surface hydroxyl coverage on ITO, and also to determine the adsorption and desorption kinetics of water on ITO.

The treatment of Si_3N_4 films with UV-ozone was observed to oxidize the film slightly, while no significant change was observed for the O-rich SiO_xN_y films. XPS analysis revealed a lower F concentration on the Si_3N_4 substrate, which may indicate lower film density; the FOTS film on SiO_xN_y was comparable in XPS signal to that on SiO_2. Preliminary tests of FOTS film durability on these films revealed an equivalent loss of F after solvent rinse and buffing treatments as compared to SiO_2, which suggests that they may possess a similar level of imprinting durability. Due to the reduced F concentration on the Si_3N_4 films tested, it was concluded that either the Si_3N_4 films required longer UV-ozone treatment in order to oxidize the exposed surface prior to FOTS treatment, or that SiO_xN_y films should be used as the buffer layer of choice.

5.5 REFERENCES

1. Swadener, J.G., K.M. Liechti, and A.L. de Lozanne, J. Mech. Phys. Sol., 1999. 47: p. 223-258.
2. Bender, M., *et al.*, Microelectronic Engineering, 2002. 61-62: p. 407.
3. Matsui, S., *et al.*, J. Vac. Sci. Tech. B, 2001. 19(6): p. 2801-2805.
4. Hirai, Y., *et al.*, J. Photopolym. Sci. Tech., 2001. 14(3): p. 457.
5. Jaszewski, R.W., *et al.*, Microelectronic Engineering, 1997. 35: p. 381.
6. Jaszewski, R.W., *et al.*, Applied Surface Science, 1999. 143: p. 301.
7. Bailey, T., *et al.*, J. Vac. Sci. Tech. B, 2000. 18(6): p. 3572.
8. Taniguchi, J., *et al.*, Jpn. J. Appl. Phys., 2002. 41: p. 4194-4197.
9. Beck, M., *et al.*, Microelectronic Eng., 2002. 61-62: p. 441-448.
10. Loo, Y.-L., *et al.*, J. Am. Chem. Soc., 2002. 124: p. 7654-7655.
11. Chen, Y., *et al.*, J. Vac. Sci. Tech. B, 2002. 20(6): p. 2887-2890.
12. Komuro, M., *et al.*, Jpn. J. Appl. Phys., 2002. 41: p. 4182-4185.
13. Matsuzawa, T., *et al.*, J. Electrochem. Soc., 1981. 128(1): p. 184-187.
14. Mancini, D.P., *et al.*, Proc. SPIE: 21st Annual BACUS Symposium on Photomask Technology, 2001. 4562: p. 593-599.
15. Resnick, D.J., *et al.*, Semiconductor International, 2002(June 1).
16. Hiroshima, H., *et al.*, Jpn. J. Appl. Phys., 2002. 41: p. 4173-4177.

17. Personal communication with Dr. Yangming Sun.

18. Brzoska, J.B., N. Shahidzadeh, and F. Rondelez, Nature, 1992. 360: p. 719.

19. Parikh, A.N., *et al.*, J. Phys. Chem., 1994. 98: p. 7577.

20. This work was performed in collaboration with Andrew Lemonds in the Department of Chemical Engineering at the University of Texas at Austin, and also with William J. Dauksher at Motorola Physical Sciences Research Laboratories.

21. Kim, S., H.K. Christenson, and J.E. Curry, Langmuir, 2002. 18(6): p. 2125-2129.

22. Hillebrandt, H. and M. Tanaka, J. Phys. Chem. B, 2001. 105(19): p. 4270-4276.

23. Schondelmaier, D., *et al.*, Langmuir, 2002. 18: p. 6242-6245.

24. Milliron, D.J., *et al.*, J. Appl. Phys., 2000. 87(1): p. 572-576.

25. Donley, C., *et al.*, Langmuir, 2002. 18(2): p. 450-457.

26. Sneh, O. and M. George, J. Phys. Chem., 1995. 99: p. 4639.

27. Part of this section was submitted as an invention to Motorola Labs while under Motorola employ during the year 2001.

28. Sung, M.M., G.J. Kluth, and R. Maboudian, J. Vac. Sci. Tech. A, 1998. 17(2): p. 540-544.

29. Raider, S.I., *et al.*, J. Electrochem. Soc., 1976. 123: p. 560.

30. Jo, Y.-S., *et al.*, J. Appl. Phys., 1986. 60(7): p. 2564.

Chapter 6: Effect of Substrate Hydration on the Reaction of Tridecafluoro-1,1,2,2-Tetrahydrooctyl Trichlorosilane on SiO_2

6.1 INTRODUCTION

The literature review and discussion given in Chapter 4 suggest that the amount of water adsorbed on the SiO_2 substrate can have a major impact on the quality of the self-assembled, tridecafluoro-1,1,2,2-tetrahydrooctyl siloxane film. The goal of this chapter was to investigate the conditions necessary to ensure a known hydration state of the surfaces of the fused silica samples, and then to observe the change in FOTS film formation with varying states of hydration. This required complete desorption of surface water, followed by controlled exposure to water, and finally exposure to the SAM precursor. This work was motivated by the need to optimize the conditions for depositing high-quality SAM films that exhibit a high degree of durability for use as template release layers in SFIL.

6.2 EXPERIMENTAL

Fused silica substrates (EQZ 5009 2C AR3, Hoya) were stripped of Cr and diced into 1 cm^2 samples for deposition experiments, ground with mortar and pestle, moistened with deionized water (DIW) and allowed to equilibrate at ambient prior to use for TGA experiments. Fumed silica (Cab-O-Sil HS-5, Cabot) was moistened with DIW and allowed to equilibrate at ambient prior to use. Thermogravimetric analysis was performed on the fumed and ground fused silica samples using a

Perkin Elmer TGA 7 Thermogravimetric Analyzer and a 5.0 °C/min programmed temperature ramp.

Samples designated for film deposition were rinsed in an acetone ultrasonic bath for 15 min, followed by UV-ozone treatment in a Jelight UVO-42 system for 15 min. The samples were loaded into a custom-built film deposition system that is described in Appendix B. The samples were baked under N_2 for the prescribed time in order to remove at least 99% of the adsorbed water, and then exposed to a humid flow stream from a bubbler containing either pure DIW or a saturated LiBr solution. The samples were then exposed to tridecafluoro-1,1,2,2-tetrahydrooctyltrichlorosilane (FOTS) vapor at 1 atm (N_2 plus FOTS) for the prescribed time, and annealed at 100 °C for 15 min.

Film samples were analyzed using water contact angle, X-ray photoelectron spectroscopy (XPS), spectroscopic ellipsometry (SE), and atomic force microscopy (AFM) in both tapping and friction mode. Contact angles were measured on a Rame Hart m100 Contact Angle Goniometer. The RH-100 consists of a goniometer, a manually operated micropipette that is held in position above the gimbaled sample stage, an optics rail to align the diffuse light illumination system with a CCD camera that feeds the image to the computer for image analysis. The XPS data were obtained using a Physical Electronics PHI5700 ESCA system equipped with an Al monochromatic source (Al Kα radiation at 1486.6 eV). The base pressure in the XPS UHV chamber was 1×10^{-10} Torr. Wide range (survey) scans were obtained with a step size of 1 eV and pass energy of 93.9 eV; high resolution scans were taken with a step size of 0.1 eV and pass energy of 11.75 eV.

The Ag $3d_{5/2}$ XPS peak at 368.3 eV from a sputtered-clean Ag foil was used to calibrate the system.

6.3 WATER DESORPTION MODEL

Guided by the literature, a model was developed to describe the observed TGA curves for the fumed silica and ground fused silica samples, and also to predict under what bake conditions >99% of the adsorbed water is desorbed without significant loss of silanols by condensation reactions. Multilayer water desorption was assumed to occur under different kinetic parameters than the more tightly-bound adsorbed water layer. According to Gun'ko,[10] the desorption of water can be modeled using the following equations, where $\theta_i = C_i/C_{0,i}$:

Equation 6.1

$$\frac{d\theta_{adsorbed}}{dt} = -k_{adsorbed}\exp\left(\frac{E_{adsorbed}}{RT}\right)\theta_{adsorbed}$$

Equation 6.2

$$\frac{d\theta_2}{dt} = -k_2\exp\left(\frac{E_2}{RT}\right)\left(\theta_{OH,2}\right)^2$$

Equation 6.3

$$\frac{d\theta_3}{dt} = -k_3\exp\left(\frac{E_3}{RT}\right)\left(\theta_{OH,3}\right)^2$$

Equation 6.4

$$\frac{d\theta_4}{dt} = -k_4\exp\left(\frac{E_4}{RT}\right)\left(\theta_{OH,4}\right)^2$$

where the adsorbed water corresponds to the first layer, $\theta_{OH,2}$, etc. is the evolution of water from condensation reactions, and the numerical subscripts 2, 3, and 4 refer to the silanol coverages corresponding to densely-populated, sparsely-populated, and isolated distributions. In the Zhuravlev context, the first two surface states would be comprised of all types of silanols, and the third state would be comprised of only isolated groups. The rate of disappearance of silanol groups is simply double the rate of water evolution for Equation 6.2 and Equation 6.3. For each vicinal or geminal silanol lost, two hydroxyl groups are lost and one isolated group is created. Therefore, the rate of isolated silanol loss is double the water loss in Equation 6.4 minus half the sum of silanol loss from Equation 6.2 and Equation 6.3. This assumes that most isolated silanols are lost at higher temperatures according to Equation 6.4, and very few are lost according to Equation 6.2 and Equation 6.3. Further, an additional equation was added to the system to account for multilayer water, which is expected to desorb at lower temperatures than the other species. The following set of equations was used in this model, with the model parameters listed in Table 6.1.

Equation 6.5

$$\frac{d\theta_{multi}}{dt} = -k_{multi}\exp\left(\frac{E_{multi}}{RT}\right)\theta_{multi}$$

Equation 6.6

$$\frac{d\theta_{adsorbed}}{dt} = -k_{adsorbed}\exp\left(\frac{E_{adsorbed}}{RT}\right)\theta_{adsorbed}$$

Equation 6.7

$$\frac{d\theta_{OH,2}}{dt} = -k_2\exp\left(\frac{E_2}{RT}\right)\left(\theta_{OH,2}\right)^2$$

Equation 6.8

$$\frac{d\theta_{OH,3}}{dt} = -k_3 \exp\left(\frac{E_3}{RT}\right)\left(\theta_{OH,3}\right)^2$$

Equation 6.9

$$\frac{d\theta_{OH,4}}{dt} = -k_4 \exp\left(\frac{E_4}{RT}\right)\left(\theta_{OH,4}\right)^2 + \frac{1}{2}k_2 \exp\left(\frac{E_2}{RT}\right)\left(\theta_{OH,2}\right)^2 + \frac{1}{2}k_3 \exp\left(\frac{E_3}{RT}\right)\left(\theta_{OH,3}\right)^2$$

Table 6.1: Model Parameters (Adapted from Gun'ko[10] unless noted)

Species	E_A (kJ/mol)	k (s^{-1})	C_0 (nm^{-2})
Multi-layer H_2O	model fit	model fit	model fit
Adsorbed H_2O	66	1.6×10^{6}	0.25
OH Type 2 (densely-populated)	106	9.5×10^{7}	0.74
OH Type 3 (sparsely-populated)	171	4.9×10^{10}	1.84
OH Type 4 (isolated)	252	5.2×10^{14}	1.60

6.4 RESULTS AND DISCUSSION

6.4.1 Silica Dehydration

The ultimate goal of the TGA experiments was to determine the time and temperature required to desorb most or all of the adsorbed water without any significant dehydroxylation, and to use those parameters to optimize the reaction sequence of FOTS with quartz substrates. Mass loss by dehydration of Cab-O-Sil and ground fused silica (quartz, for short) samples was analyzed by TGA, and the results are shown in Figure 6.1. The samples were analyzed only in the temperature range of 25 – 400 °C, since the ultimate goal is surface dehydration and not dehydroxylation. The mass loss by the quartz sample is more rapid than by the fumed silica, and the % mass loss is less; both are likely due to the dramatically different surface areas of the samples. Cab-O-Sil HS-5 consists of 70 nm spheres of SiO_2 and has a total area of 325 m^2/g. The ground fused silica area was not measured; it is likely more than a factor of 10^3 more than the HS-5. It is clear, however, that the mass loss features are similar.

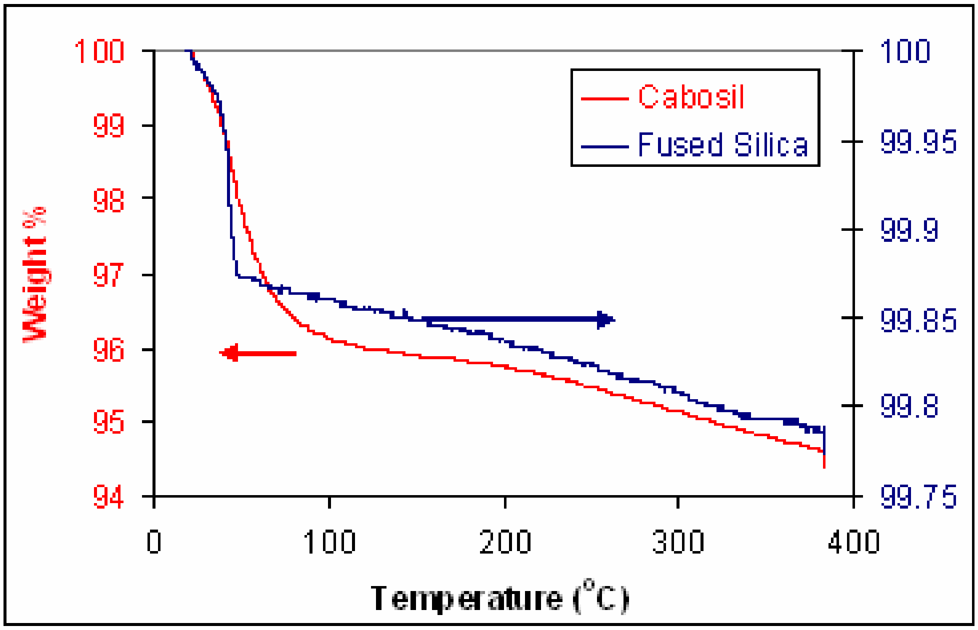

Figure 6.1: Comparison of mass loss by TGA for fumed silica and ground fused silica samples. The sample was held at ~380 °C for 30 min, leading to the additional mass loss.

The loss of adsorbed water and silanol groups for a silica sample was predicted using the model outlined above, and is shown in Figure 6.2. According to the model results, all adsorbed water desorbs below 200 °C, and little silanol loss is predicted in that range. Note that multilayer water desorption was not modeled for this plot.

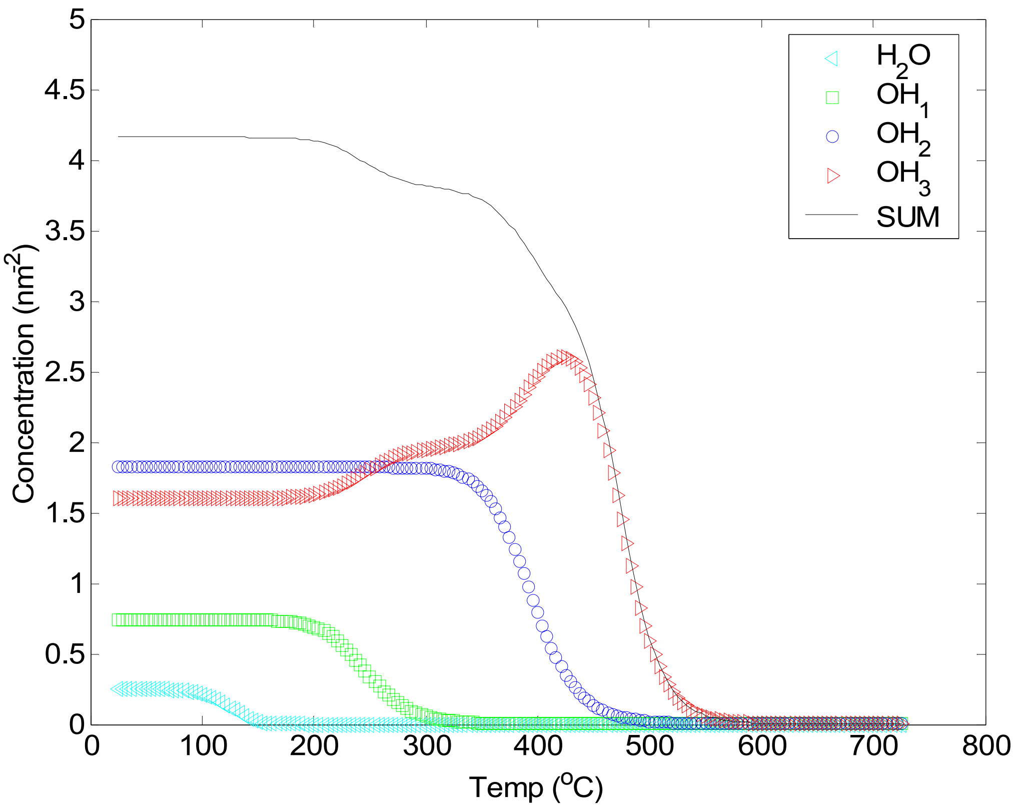

Figure 6.2: Model results for hydroxyl coverage as a function of temperature for ramp rate of 5 °C/min including only the first layer of adsorbed water.

The leading mass loss feature in the TGA spectra of both the fused silica and fumed silica samples was fitted in order to determine E_{multi}, k_{multi}, and C_{multi}, as defined in Equation 6.5. Only the data up to 200 °C were used to fit these parameters, since it is predicted in Figure 6.2 that the adsorbed water is removed below that temperature. The parameters were estimated based on least-sum-of-squared-errors in that temperature range, and the results are shown in Figure 6.3 and Figure 6.4. As can be seen in the figures, the leading weight loss feature is described well by the model, and yields the parameters listed in Table 6.2. The fitted parameters are in reasonable agreement considering the vastly different types of the two samples. It is expected that the parameters obtained by fitting the fused silica data may more accurately represent the parameters for water desorption from the substrates to be used in the film deposition experiments.

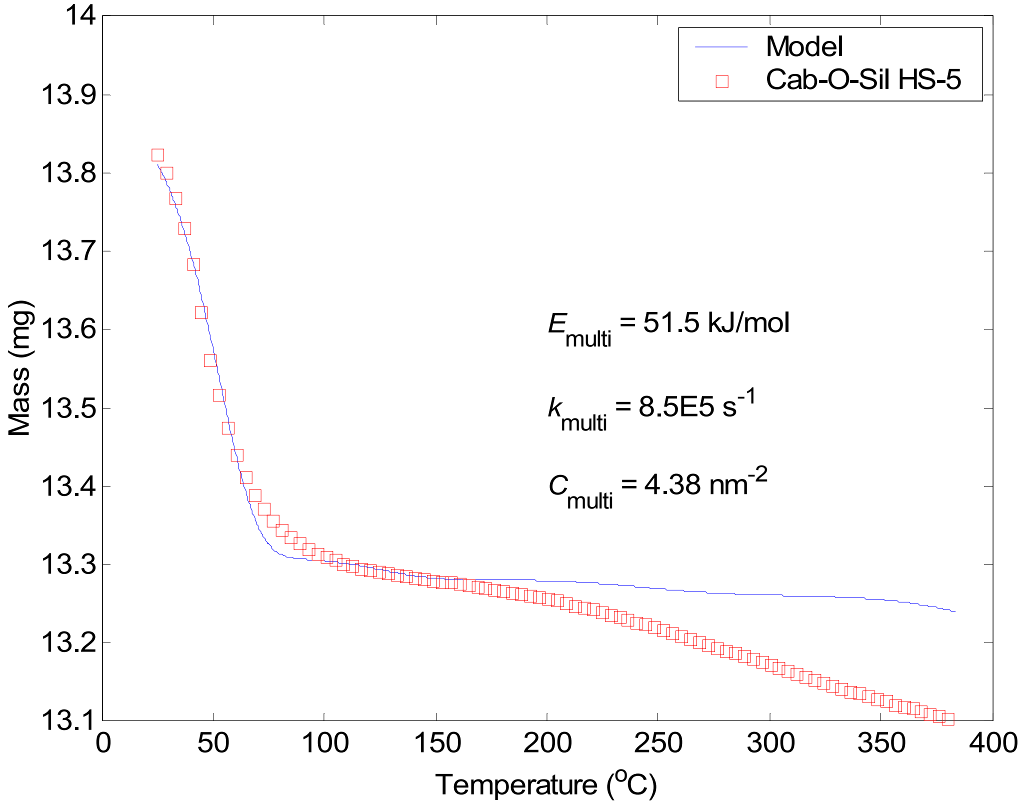

Figure 6.3: Comparison of predicted and experimental TGA curves for fumed silica.

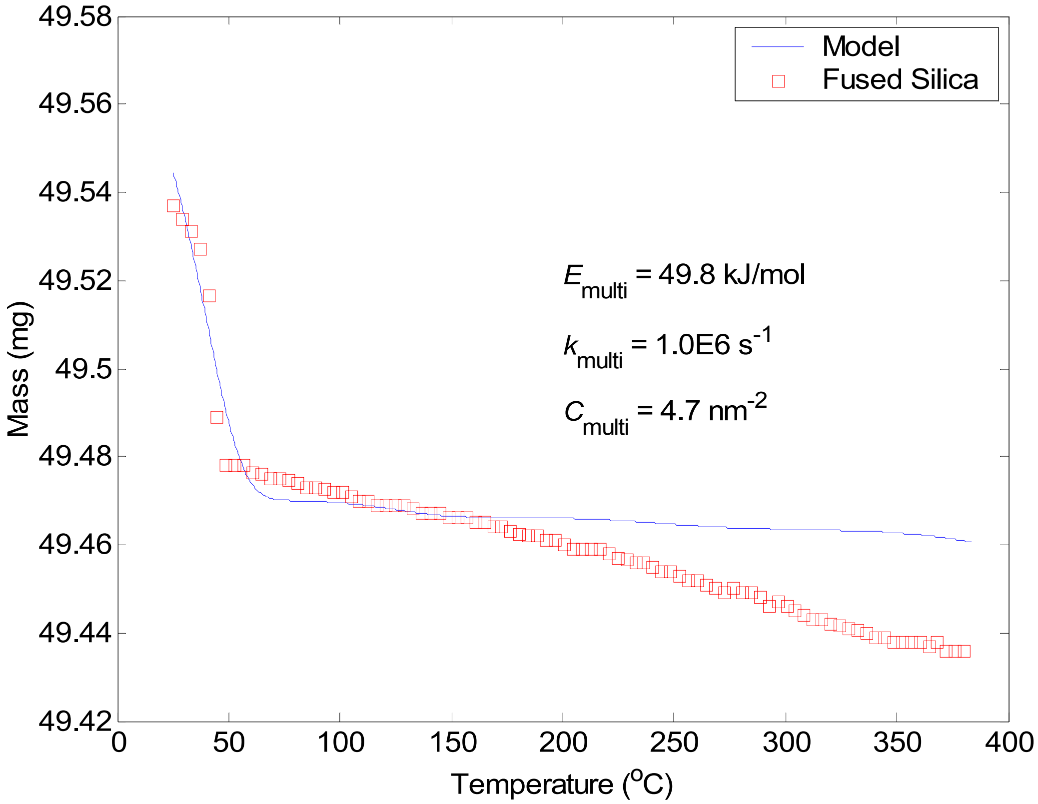

Figure 6.4: Comparison of predicted and experimental TGA curves for fused silica.

Table 6.2: Fitted multilayer water desorption parameters.

Substrate	E_{multi} (kJ/mol)	k_{multi} (s^{-1})	$C_{0,multi}$ (nm^{-2})
Fumed Silica	51.5	8.5E5	4.4
Fused Silica	49.8	1.0E6	4.7

There are a few features worth noting in comparing Figure 6.2 to the silanol distribution diagram in Zhuravlev.[30] According to this model, the initial silanol coverage is ~4.2 per nm^2; hydroxyl loss begins at ~200 °C; and at 400 °C there are approximately 3 silanol groups per nm^2. The Zhuravlev model does not predict silanol coverage for temperatures below 200 °C, and the author predicted no significant loss in that temperature range; the initial silanol coverage is 4.6 nm^2, which is said to be a constant for maximally-hydroxylated silica; and the silanol coverage at 400 °C is between 2.4 and 3 per nm^2. The loss of silanol groups at temperatures greater than 400 °C as predicted by this model does not agree with the Zhuravlev model; this may be because at low coverages the desorption of water is limited by surface diffusion of H· and HO· species, and this model does not take that into account. The experiments in this paper involve treating SiO_2 surfaces at temperatures less than 400 °C, and so this model is assumed to be adequate in this temperature range.

The parameters for fused silica in Table 6.2 were used in predicting the time to remove > 99% of the adsorbed water various temperatures, and also to estimate the amount of silanol loss under those conditions. Figure 6.5 shows that the model predicts less than 0.1% silanol loss even at a 140 °C bake temperature. The current equipment is capable of heating samples to a maximum temperature of 100 °C; samples baked at that temperature for 90 min should experience ~0.02% silanol loss, which is negligible. Based on these results, it was decided to bake substrates prior to film deposition for 90 min at 100 °C.

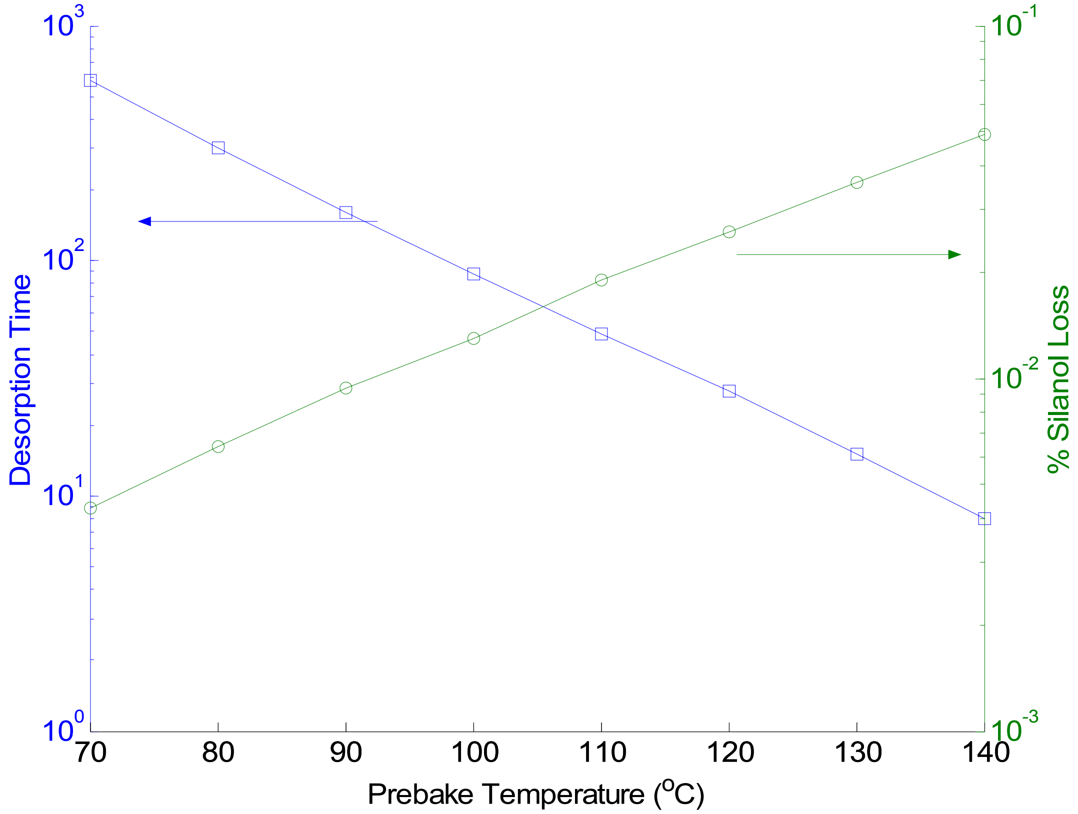

Figure 6.5: Predicted time in minutes to desorb >99% of adsorbed water at various bake temperatures, and the associated % silanol loss.

6.4.2 Effect of Silica Hydration on Film Growth

Dehydrated fused silica substrates were exposed to a stream of water vapor from a bubbler containing pure DIW for various lengths of time, and then exposed to FOTS for 120 min. Water contact angle and XPS results indicate that the deposition of FOTS on the substrate increases with increasing water exposure, as shown in Figure 6.6. There appears to be asymptotic behavior, suggesting that even at long water exposure times, the film growth is self-limiting. This trend of increasing film density with increasing water exposure is consistent with results presented by Wang.[35] The self-limiting growth, even at high hydration conditions, is consistent with Fadeev,[36] who found that SAMs deposited from precurors possessing alkyl chains less than 7 carbon units in length resulted in multilayer growth, but longer chains resulted in self-limiting film growth.

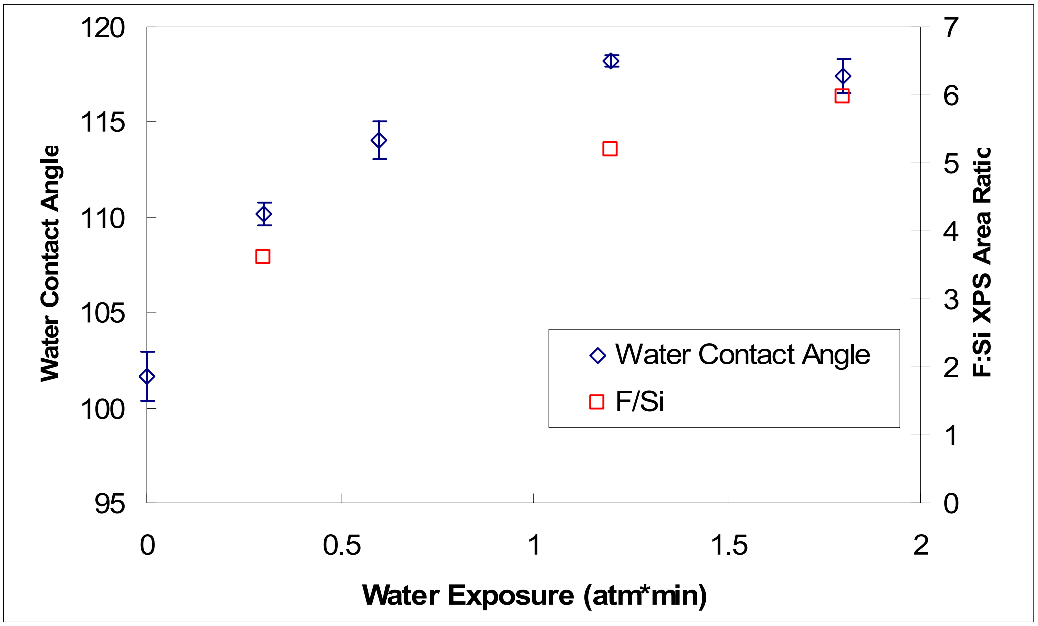

Figure 6.6: Water contact angle and F 1s:Si 2p XPS peak area ratios for FOTS films deposited on fused silica substrates that were exposed to varying doses of water vapor.

For durable imprint template release layers, however, film quality cannot be measured simply by water conatact angle or XPS peak area. There is likely a combination of optimal substrate hydration state coupled with SAM precursor type and reaction time, plus anneal conditions, which result in high-density films that possess good mechanical wear properties. Investigation into the amount of water remaining on the substrate after the reaction, or the density of film/substrate bonding or film network bonding remains to be done.

6.5 CONCLUSIONS

Guided by the literature, a model was developed to predict the conditions necessary to desorb all of the adsorbed water on a fused silica surface without significantly altering the concentration of surface hydroxyl groups. Based on this model, fused silica samples were baked under N_2 stream at 100 °C for 90 min, followed by exposure to a water vapor stream for various times. The samples were then exposed to FOTS vapor for 120 mins. Water contact angle and XPS data reveal that film deposition improves with increasing water exposure, which is consistent with the literature. Results also indicate that film growth is self-limiting, even at high water exposures. Future work should be targeted at identifying the optimal combination of water exposure and post-SAM-deposition annealing conditions that result in films that possess both high-density and mechanical durability.

6.6 REFERENCES

1. Gun'ko, V.M., *et al.*, Inter. J. Mass Spec. Ion Proc., 1998. **172**: p. 161-179.
2. Zhuravlev, L.T., Coll. Surf. A, 2000. **173**: p. 1-38.

DEFECT ANALYSIS FOR SFIL

Chapter 7: Defect Analysis for SFIL

7.1 INTRODUCTION

The motivation for measuring defects introduced at each process step in the manufacture of integrated circuits and other such devices is driven by profit. For a manufacturing process flow to generate profitable product, the yield, or percent good chips, for each wafer must exceed some break-even point. If the break-even point for a process containing 30 steps (combined deposition, etching, and lithography) is 90%, then the yield at each process step must be at least $x = 0.9^{1/30}$, or 99.6%, with some give and take between defect-prone and defect-resistant steps. Determination of yield at each step is unique, since the gate level for a 90 nm gate MOSFET product is less tolerant of 100 nm defects than a 1 μm gate MOSFET product. Similarly, the front-end processes such as the gate patterning steps are generally less tolerant of small defects than back-end processes such as the top interconnect levels, which possess much larger features. For this reason each process step generally has a unique acceptable operating space, and an acceptable defect size and density boundary, which results in the appropriate yield for that step. For example, the ITRS Roadmap calls for the Litho Stepper process step to induce no more than 113 defects/in^2 of size 75 nm and greater for the 90 nm node.[1] If SFIL is to be used to manufacture products addressed by the ITRS Roadmap, then it will ultimately have to conform to the defect and yield requirements outlined therein.

The SFIL process is very immature, and so the goal of this work is to establish a baseline by which the performance of process and materials changes can be measured.

Skeptics of SFIL and other imprint techniques claim that the problems plaguing defect generation and propagation in contact lithography described in Chapter 1 may be common to all forms of lithography where there is intimate contact between the master pattern (mask, reticle, or imprint template) and the imaging layer (resist, etch barrier). The goal of this chapter is to determine the trend in defects over time (number of imprints), and determine whether there exists any gating pathology. Two potential results are shown in Figure 7.1, where there may be a relatively constant level of defects (left), as is the case with current processing technology, or perhaps an increasing trend in defects over time (right). The former trend would be acceptable if the number of defects is small, and the latter trend would be unacceptable in a mature process for almost any application.

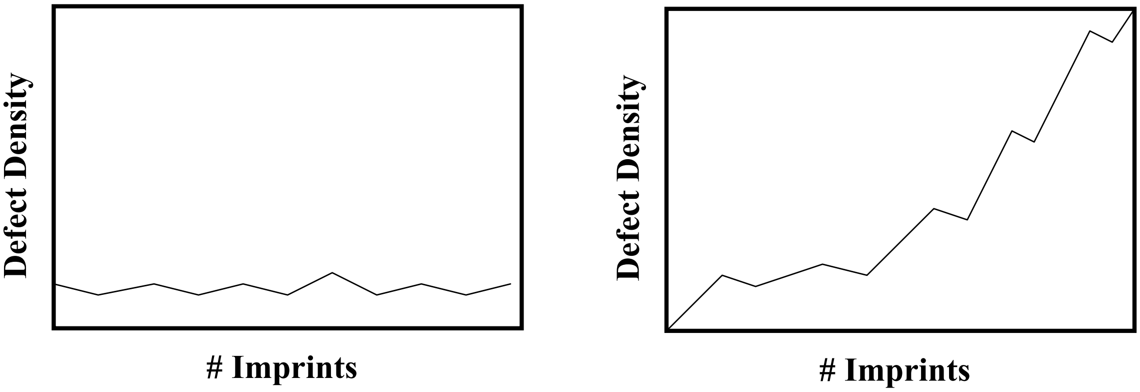

Figure 7.1: Two of the potential defect trends.

The fundamental question to be answered is whether the imprint process creates and/or propagates defects simply by its contact nature. There are three extreme hypotheses illustrated in Figure 7.2. Figure 7.2a shows the case in which no defects are generated and there are no defects that can propagate, which defines the perfect imprint process. Figure 7.2b shows the case in which some defects are generated during an imprint cycle, but the defects do not propagate through multiple imprints. These defects may exist for a few imprints, but they eventually disappear, regenerating the original defect-free imprint pattern. This case may be acceptable if the number of generated defects is very small and the number of steps required to clean the template is very few. The third case (Figure 7.2c) is that in which defects are generated, and most of these new defects propagate through multiple imprints, possibly even for the lifetime of the template, leading to catastrophic loss of pattern transfer fidelity. The initial investigation is based on the effect of multiple imprints on the transfer fidelity using patterns comprised of features with dimensions on the order of 1 μm. If catastrophic defect generation processes exist, they should appear in patterns of such features.

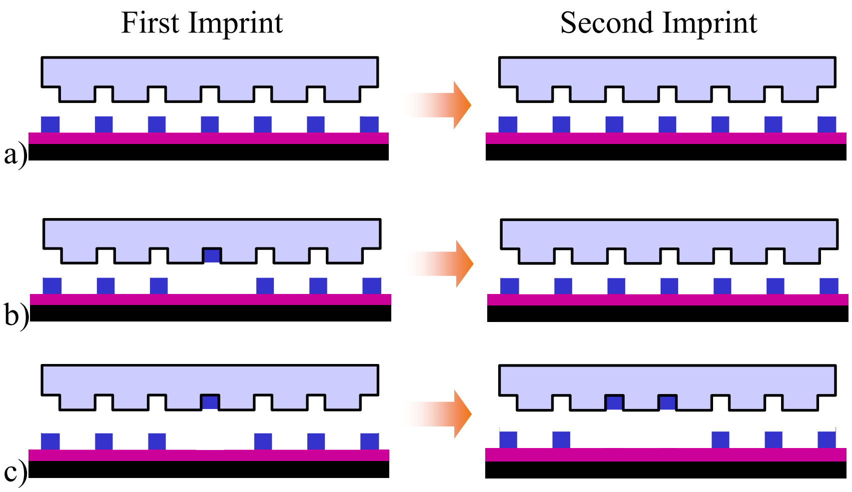

Figure 7.2: Three hypothetical scenarios governing defect generation and propagation. a) No defect generation, and hence perfect imprinting; b) defect generation and rapid recovery of desired pattern; and c) defect generation and propagation.

Essential to a project of this nature is the ability to remove as much as possible of the human component from the experimental procedure. It is therefore necessary to have an imprint tool that provides reproducible, hands-free production of imprinted wafers that are of sufficient imprint quality as to be inspectable by an industry-standard wafer inspection tool. The intent is that the industry-standard inspection tool will provide defect data that is accepted as legitimate by the majority of the academic and industrial community.

The definition of sufficient wafer quality includes issues of both individual pattern design and also the layout of imprint patterns in an array on the wafer. The pattern must possess features designed to elucidate defect generation and propagation modes in SFIL, and also features used by the inspection tool for alignment purposes, which are usually of different geometries. The variation in die placement in the die array must be sufficiently small so as to fall within the capture range of the alignment algorithm of the inspection tool; the die must be arranged in a rectilinear array along axes that are orthogonal, to within the error-capture range of the inspection tool; and finally the orthogonal die array must be sufficiently aligned to the wafer notch as to fall within the wafer rotational error capture range of the inspection tool.

Progress to date has been largely cyclical, involving repeated imprinting-inspection efforts. This activity revealed errors in experimental design early in the process, and necessitated changes to equipment, processes, and materials. As an example, the method of securing imprint templates in the SFIL Multi-Imprint Machine (MIM) does not allow for template rotational correction, and therefore necessarily imparts some rotational error to the imprinted pattern. It was determined that a large number of alignment marks must be embedded in the die pattern to allow for alignment and flexible definition of inspection area within the pattern. It was also determined that the as-built MIM did not provide die arrays that were sufficiently orthogonal, and, in fact, imbued the resulting imprinted array with significant die placement noise as to render the wafers unrecognizable as valid die arrays by the inspection tool. These issues are discussed in detail in Section 7.3. Finally, it was demonstrated that solving these equipment-related problems allows automated inspection of SFIL-patterned wafers. This chapter represents the first automated inspection of such patterns.

7.2 EXPERIMENTAL PROCEDURE

Various areas within the SFIL cleanroom were monitored using a Met One 200L laser particle counter, equipped with an isokinetic probe. The raw data from the air sampler, in the form of total particles in the sampling time, was normalized to reflect the number of particles per cubic foot of sampled air. The flow rate of the air sampled by the isokinetic probe is 1.0 +/- 0.1 ft^3/min.[2]

The number of particles added on the wafers during handling and transportation was measured using a Tencor 6200 bare wafer surface scanner. Twenty-five wafers were measured on the Tencor 6200 at International Sematech (ISMT), transported to the UT cleanroom, loaded onto the SFIL stepper and "stepped," but without imprinting, transported back to ISMT, and scanned again on the 6200. The data sets were subtracted, giving the number of defects added to the bare wafers during handling and transportation.

Imprinting was performed on an imprint stepper that was built on an UltraTech stepper platform, and is shown in Figure 7.3. The major machine components include the following: (i) a micro-resolution Z-stage that controls the average distance between the template and the substrate and the imprinting force; (ii) an automated X-Y stage for step and repeat positioning; (iii) a pre-calibration stage that enables attainment of parallel alignment between the template and substrate by compensating for orientation errors introduced during template installation; (iv) a fine-orientation flexure stage that provides a highly accurate, automatic parallel alignment of the template and wafer to the order of tens of nanometers across an inch; (v) a flexure-based wafer calibration stage that orients the top of the wafer surface parallel with respect to the plane of the XY-stage; (vi) an exposure source that is used to cure the etch barrier; (vii) an automated fluid delivery system that accurately dispenses known amounts of the liquid etch barrier; and (viii) load cells that provide both imprinting and separation force data.

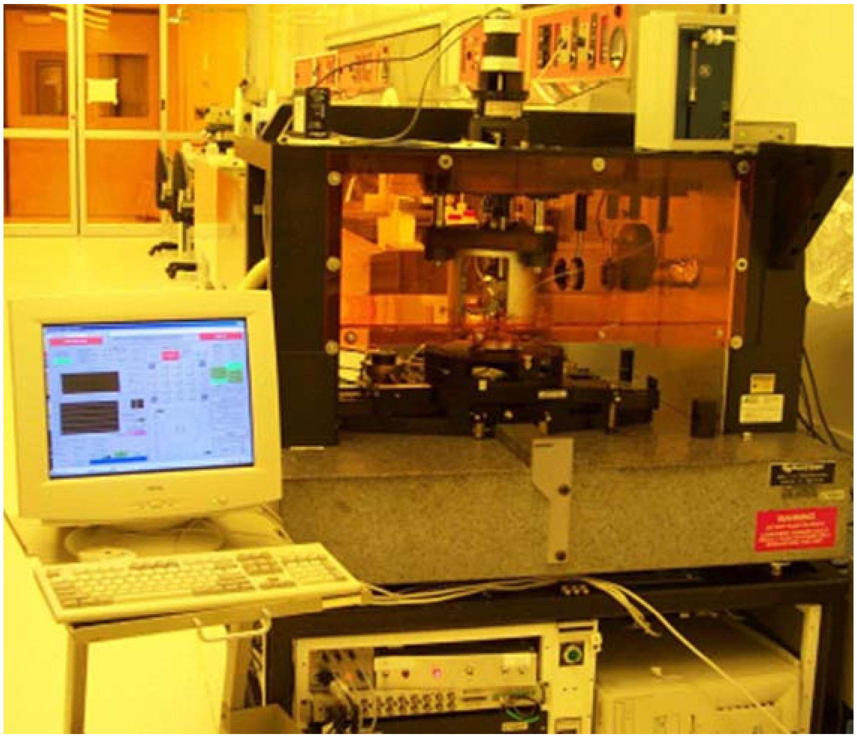

Figure 7.3: SFIL Imprint Stepper at the University of Texas at Austin.

The template flexure stage, shown in Figure 7.4, accepts 1-in by 1-in templates, and these templates are held in place by eight set screws. Experience has shown that this is not the best method for holding templates, since it is difficult to install the templates so that the pattern is ultimately aligned to the wafer notch during imprinting. The template stage apparatus does not have the capability to measure and correct for template installation errors that result in pattern rotation. This and other potential alignment-related issues are discussed in Section 7.3. In addition, the method of securing the template by applying lateral force results in template distortion (bowing), which imparts imprint film thickness non-uniformity that manifests itself as color fringes. This effect has been modeled and is discussed in Chapter 7. We believe it is manageable, but there is no way to correct this problem on the current imprint tool.

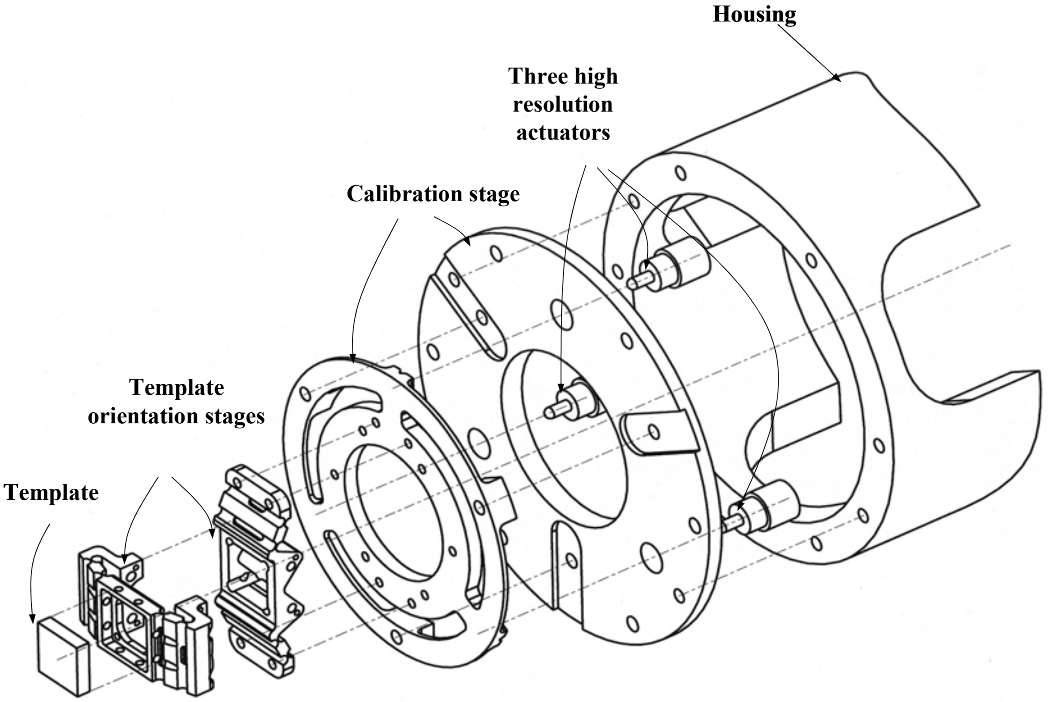

Figure 7.4: Template orientation stage design.[3]

For the imprinting experiments, wafers were coated with a commercial bottom anti-reflection coating (BARC) (DUV30J-11, Brewer Science) to be used as the transfer layer. The BARC was spun at 3000 rpm for 60 sec and baked at 180 ºC for 60 sec, yielding films of thickness ~1250 Å. The films were double-coated, yielding thicknesses in the range of 250 nm. Approximately 100 nl SFIL etch barrier, consisting of 15%(w/w) ethylene glycol diacrylate (Aldrich), 44% (3-acryloxypropyl)tris(trimethylsiloxy)silane (SIA0210.0, Gelest), 37% t-butyl acrylate (Lancaster), and 4% 2-hydroxy-2-methyl-1-phenyl-propan-1-one (Darocur 1173, Ciba), which is etch barrier "A4" as defined in Chapter 3, was dispensed for each imprint.

Templates were manufactured in accordance with the thin-Cr process described in Chapter 2. The templates were cleaned in an acetone ultrasonic bath, followed by exposure to UV/ozone in a Jelight UVO-42 for 15 min. The clean templates were then treated with a release agent, tridecafluoro-1,1,2,2-tetrahydrooctyltrichlorosilane (Geleste), by vapor exposure at 1 atm total pressure (precursor plus N_2) for 120 min, and annealed at 100 ºC for 15 min in the SFIL surface treatment chamber described in Appendix B. The template was pressed onto the etch barrier fluid on a 200 mm Si wafer, and the stack was exposed with a broadband Hg arc lamp (Oriel) operating at 450 W for 30 sec.

Die placement accuracy was estimated by logging the die coordinates on an imprinted wafer using a Leica INS2000 inspection microscope at ISMT. The stage accuracy of the microscope was estimated by repeated measurement of the 16 die locations on a single wafer, and was determined to be ± 1 μm (1σ).

Pattern defect data were obtained on KLA ILP-2139 wafer inspection tools located at KLA-Tencor in San Jose and Milpitas, CA. The 2139 uses a broadband Xe illumination source and a Sony DXC 9000 camera. The camera is equipped with a Sony ICX074AL CCD image sensor to detect reflected light, which contains 659 (H) × 494 (V) effective square pixels.[4] The inspection recipe parameters were adjusted where necessary, and the effect of inspection parameters on detection of defects is discussed in Section 7.4.3.

Distillation of the KLA inspection tool data files was necessary to convert the data into the format "defects detected per sequential imprint," and also to standardize the defect size bins across all wafers. This data analysis was performed using MatLab with the program code listed in the Appendix. Some analysis was performed using SAS in collaboration with Dr. David Dickey at North Carolina State University.

7.3 ENABLING DEFECT INSPECTION

7.3.1 Cleanroom Class Characterization

The cleanroom area was divided into subsections in order to identify any areas of concern. Areas sampled include the pre-gowning room, the gowning room, the cleanroom entrance (east), the middle section of the cleanroom (middle), and the back portion of the cleanroom (west). Figure 7.5 is a diagram of the sampled locations in the cleanroom area.

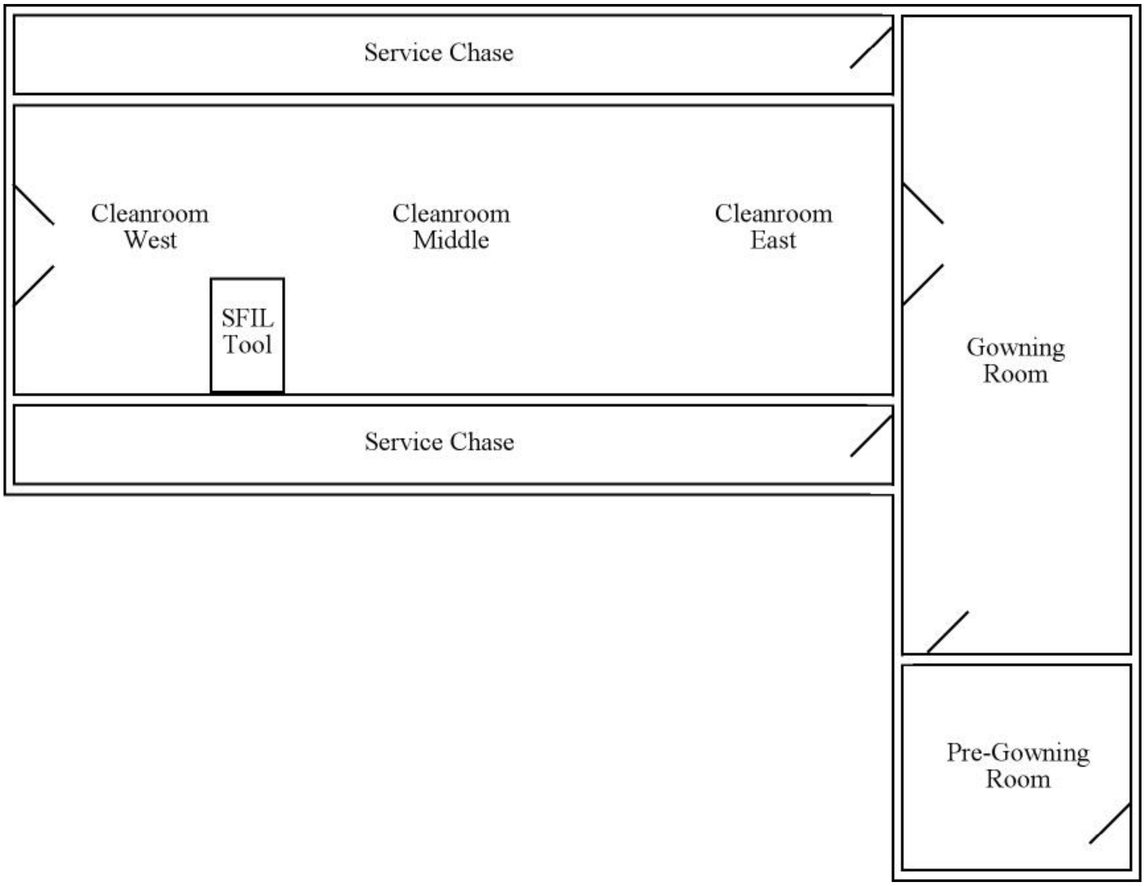

Figure 7.5: UT MER South cleanroom layout showing locations of particle detection.

During preliminary experiments, it was discovered that the number of particles recorded in a particular area varied with the placement of the isokinetic probe relative to the particle counter. When the isokinetic probe was placed in close proximity with the particle counter, a noticeable increase in the particle density was observed. This increase was thought to be a result of the fan located on the back of the particle counter, which serves for ventilation and cooling. To verify the impact of the fan, an experiment was conducted to sample the area in close proximity of the fan, and compare it to an area a reasonable distance from the fan. Figure 7.6

illustrates that the particle counts are greatly increased when the isokinetic probe is placed in close proximity to the ventilation fan. This would suggest that the most accurate data may be obtained by placing the isokinetic probe the maximum distance from the particle counter and with the particle counter exhaust fan aimed towards a ventilation grate on the walls of the cleanroom.

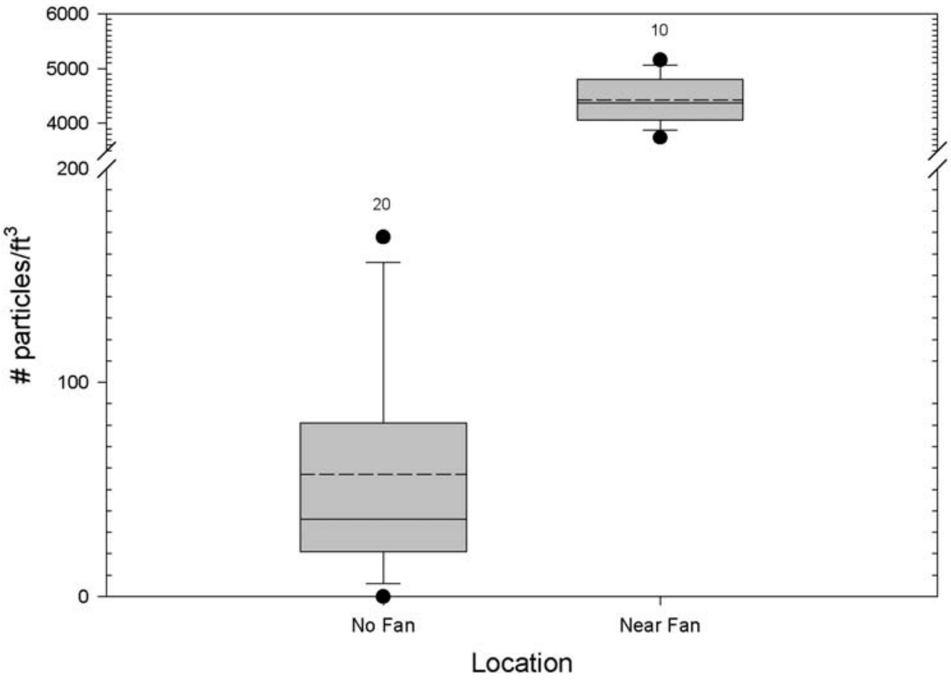

Figure 7.6: Effect of the particle sniffer fan on the placement of the isokinetic probe. The solid line, dashed line, shaded box, and line extensions represent the sample mean, sample median, the 50th percentile, and the 75th percentile, respectively.

Airborne Particulate Cleanliness Standards

Cleanrooms are classified based on unoccupied environments, and reflect the number of particles of a specific size or larger in a specified volume of air. The

English rating denotes the number of particles 0.5 μm or larger allowed per ft^3 of air. This rating enables one to understand the effects standardization of clean environments. The maximum numbers of particles of various sizes allowed in a particular cleanroom environment defines the class of the cleanroom. These numbers are generated using the following equation:

Equation 7.1
$$\frac{particles}{ft^3} = N_c\left(\frac{0.5}{d}\right)^{2.2}$$

where, N_c is the numerical designation of the class based on English Units, and d is the particle size in microns.

The cleanroom at the UT Microelectronics and Engineering Research Center in which this study is being conducted was designed to conform to a class 100 rating (English units). According to Equation 7.1, this would imply that a maximum of 100 particles 0.5 μm and larger are allowed per cubic foot. This would also correspond to a maximum of 300 particles 0.3 μm and larger per cubic foot. This study reports particles 0.3 μm and larger, due to the strict particle constraints of the SFIL process.

After verifying the reliability of the data from the particle sniffer, a complete analysis of different areas of the cleanroom was performed. Each area shown in Figure 7.5 was analyzed separately using the particle counter in the optimized configuration as previously discussed. The particle counts in each area listed is displayed in Figure 7.7. The box plots used to portray the results throughout this study effectively display the statistical information of each sample taken. For each sample location, the shaded area represents the first 50% of the data, while the solid and dashed line within the shaded rectangle represent the median and mean, respectively. The brackets above and below the shaded rectangle define 75% of the data, and the black dots show the outliers in each data set. The number above each set of data gives the sample size at each location.

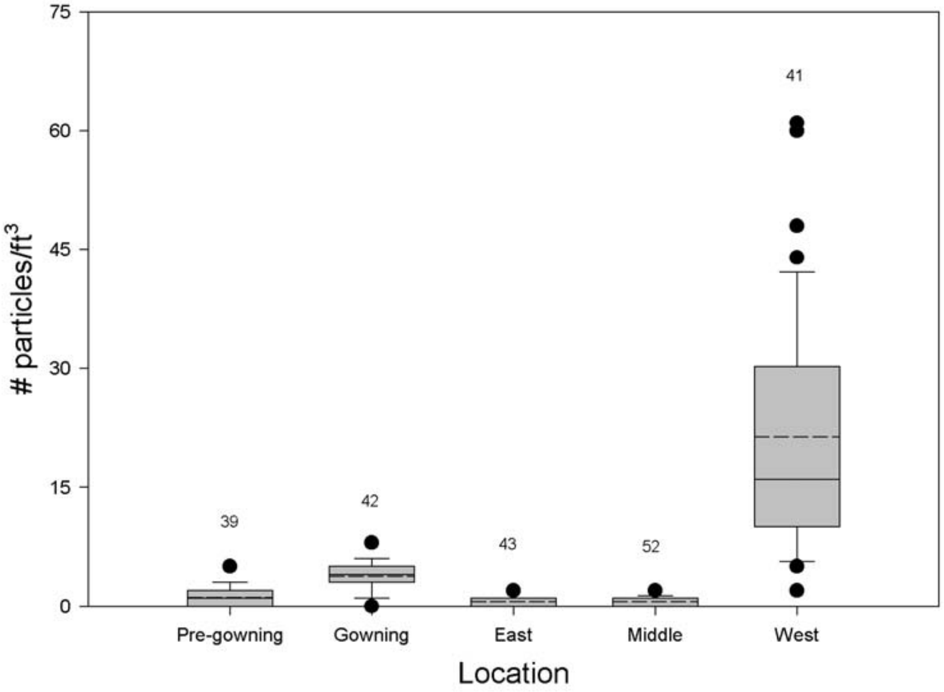

Figure 7.7: Initial cleanroom overview before the air balancing was corrected in the west section

It can be seen that the pre-gowning room, gowning room, east side and middle section of the cleanroom are much lower than the target guidelines. The west side is also within the guidelines, but there is a dramatic increase in the particle density in that area. This raised some concerns about analyzing SFIL process defects, since the SFIL tool is currently located on the west side of the cleanroom. Further investigation revealed that a set of large metal doors located on the back wall of the cleanroom was a large contributor to this data, as shown in Figure 7.8. The "West Door-Neg" data reveal that the area of the cleanroom nearest the doors was not within specification.

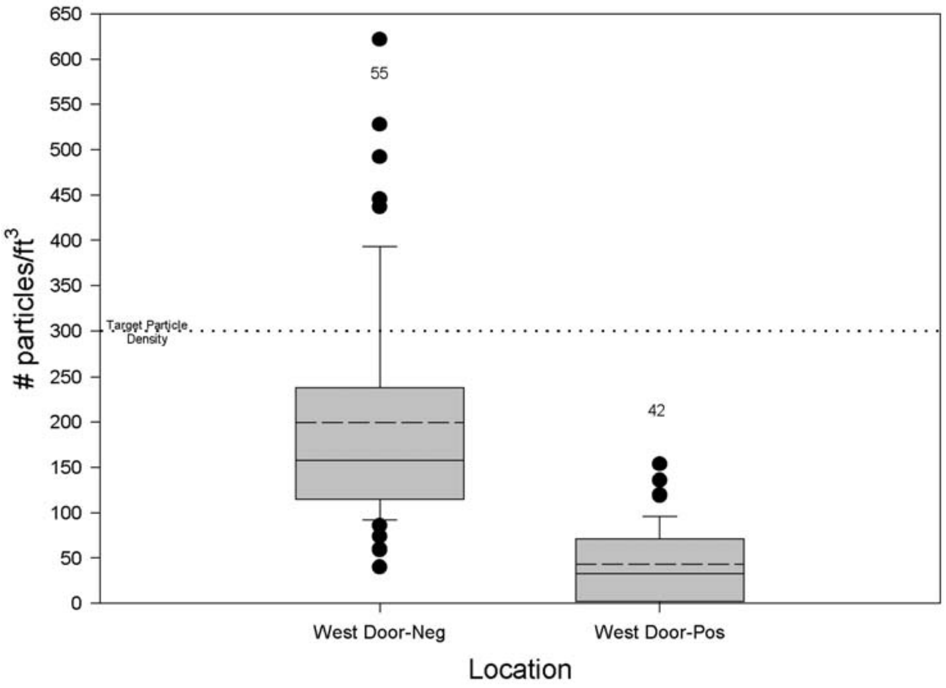

Figure 7.8: Particle sniffer in close proximity with the metal doors in the west section of the cleanroom

After careful evaluation, it was discovered that the air make-up unit, used to increase the pressure in this section of the cleanroom above the pressure outside the cleanroom, was not operating correctly. Without proper air balancing, the negative pressure inside the cleanroom relative to outside the cleanroom allowed particles from the adjacent room, which is not supplied with clean, filtered air, to migrate through cracks in the doorframe and contaminate the cleanroom. Some adjustments were made to this unit to reverse the air flow through the door frame, and data were again collected for the area in close proximity to the metal doors. This location titled “West Door-Pos” clearly shows a decrease in total number of particles; the air in this area is still “dirtier” than the air in the rest of the cleanroom, but conforms to Class 100 specifications.

Following the repairs to the make-up air system, every area within the SFIL cleanroom meets or exceeds the standards for the airborne particulate cleanliness for a class 100 cleanroom. All the data collected in this report correspond to an unoccupied cleanroom as stated in the classification guidelines for classifying a cleanroom. The introduction of people into the analysis presents an entire new set of variables, since the movements of people are random and hard to characterize. It is predicted that the introduction of people at our cleanroom will increase the total particle counts, but the extent of the increase is unknown and nearly impossible to measure with the current equipment.

7.3.2 SFIL Multi-Imprint Machine Class Characterization

This portion of the study focused the SFIL tool and evaluated the number of particles generated by both the materials used in the construction of the SFIL tool and the operation of the tool. Air sampling was performed at the entrance of the tool while idle, inside the tool while idle, inside the tool with only the air table on, and inside the tool with the X-Y table and the air table on. The sample of the X-Y table includes random motions of the wafer stage under the template, while the air table sample consist of a constant flow of air through an air bearing on the wafer stage.

The results of the particles generated by the SFIL tool are shown in Figure 7.9. Fortunately, all the samples taken were well within the classification of the cleanroom, as described in Section 7.2.1. It can be seen that the sample which includes both the X-Y table and the air table emitted the most particles, and this is presumably because it involved the most movement within the SFIL tool.

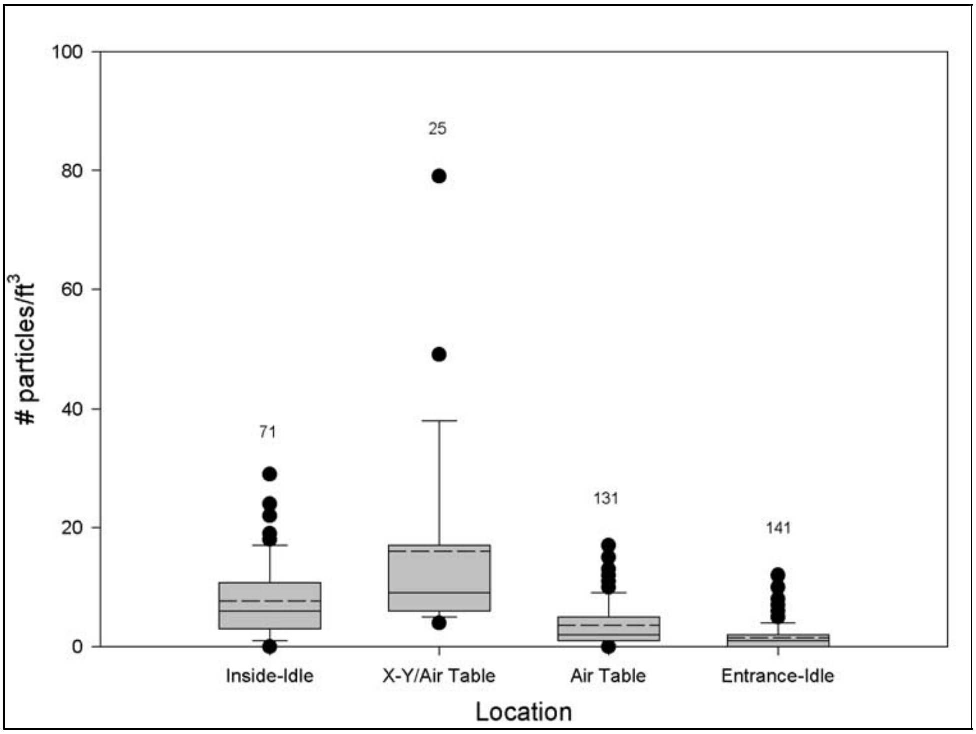

Figure 7.9: Overview of the Number of Particles Generated By Various Components in the SFIL Tool

Another interesting note is the difference in particles between the inside of the tool and the entrance of the tool while the tool sat idle. (The tool entrance is the area where an operator stands to loads wafers.) This would indicate that either the air within the tool is being disturbed, possibly increasing the total particle count, or that another particle source is present within the tool components.

The complete operation of the SFIL stepper, including a combination of the X-Y table and the air bearings, produces the most particles. All the samples taken had relatively low number of particles present, and were actually within the cleanroom classification.

7.3.3 Bare Wafer Particle Test

Twenty-five wafers were scanned on a Tencor 6200 bare wafer scanner, as described in Section 7.2. The number of particles added between the initial scan and the final scan varied for each wafer, and the average was 8.5 +/- 5.9 particles 0.25 μm or larger in size. This relatively small number of particles was not expected to impair the imprinted wafer inspection, since this represents less than 1 particle per imprint for a wafer with 16 imprints. It was concluded that no further modifications to the handling and transportation protocols were needed.

7.3.4 MIM Tool Modifications

There have been a number of iterations in this process, resulting in modifications to the stepper software and some of the hardware components. One major challenge was overcoming the die and pattern placement errors in order to produce wafers that are acceptable in the defect inspection tool. Some example placement errors we have observed are shown in Figure 7.10. Non-orthogonal die array error, shown in Figure 7.10a is caused by X-Y stage rail non-orthogonality. Figure 7.10b shows wafer rotation error caused by improper wafer orientation on the wafer chuck, and we have attempted to optimize the wafer chuck alignment pin placement to reduce this effect. Figure 7.10c shows the effect of an error in template installation, which manifests itself as die pattern rotation It is not possible to eliminate this effect. The final placement error (not shown) is random placement error associated with imprint tool compliance and X-Y stage accuracy, and is not correctable.

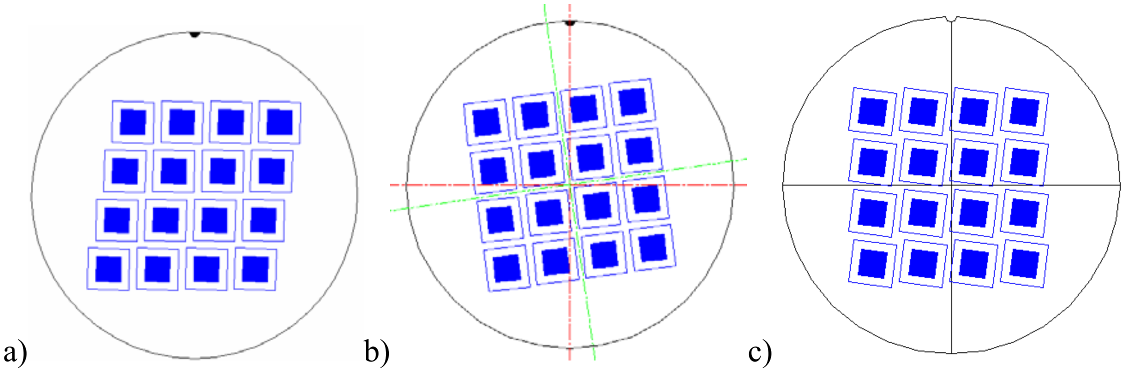

Figure 7.10: Potential pattern placement errors. (a) Die array not orthogonal; (b) die array not aligned to wafer notch; and (c) imprint template rotated in template stage.

In order to help correct for some of these errors, linear encoders were installed on the X-Y MIM stage. Die placement was measured, and die array non-orthogonality was corrected by adding trigonometric terms in the stepper software. As can be seen in Figure 7.11, this modification helped to reduce the systematic errors caused by the non-orthogonality of the X and Y rails, and also helped to mitigate the random die placement errors. After this modification the largest deviation from ideal die placement was reduced from 315 μm to less than 6 μm.

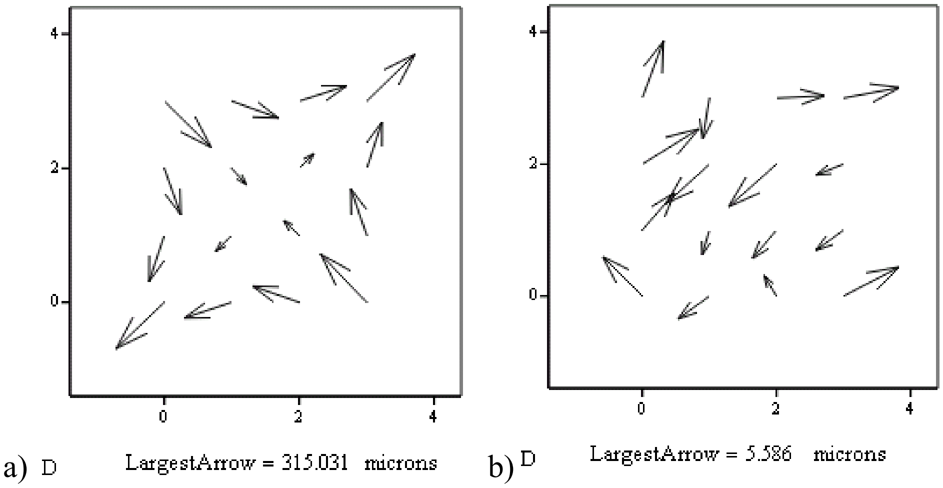

Figure 7.11: Vector plots showing die placement errors a) before, and b) after installation of the linear encoders and subsequent axes angular correction.

7.3.5 Imprint Template Design and Modifications

It was determined early in the process that the pattern rotation shown in Figure 7.10c presents complications in inspection recipe setup. In order to compensate for this, and provide “unique” alignment marks for automatic wafer alignment in the inspection tool, a new template pattern was designed. The new template patterns were designed with alignment marks arrayed throughout the active area, to allow flexibility in aligning the die array in the inspection tool. This is discussed in Section 7.3.3.

7.4 RESULTS & DISCUSSION

7.4.1 Template Self-cleaning

Wafers with multiple imprints were carefully analyzed for defects. One region of the imprint field was tracked through multiple imprints starting with the first imprint using an Olympus Vanox-T microscope. The sizes of the defects were estimated and tracked. Figure 7.12 shows a field with defects, some of which are identified. These defects were followed through consecutive imprints. After eight imprints, the region was free of defects, as seen in Figure 7.13. We believe that these defects were an artifact of contamination on the template that was removed by entrainment in the etch barrier, thus cleaning the template for the following imprints. Based on these results, it appears that the process is self-cleaning for contaminants of this sort on the template.

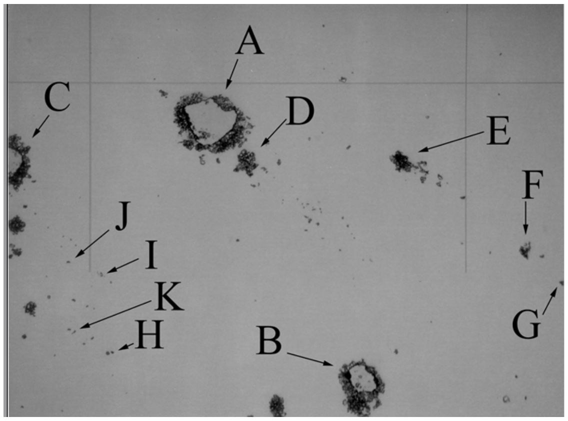

Figure 7.12: Detailed Defect Region. The defects tracked in the following images are labeled here. Note the cross pattern; this was the reference point used to find the defect region on each imprint, since only one such feature exists on this imprint template.

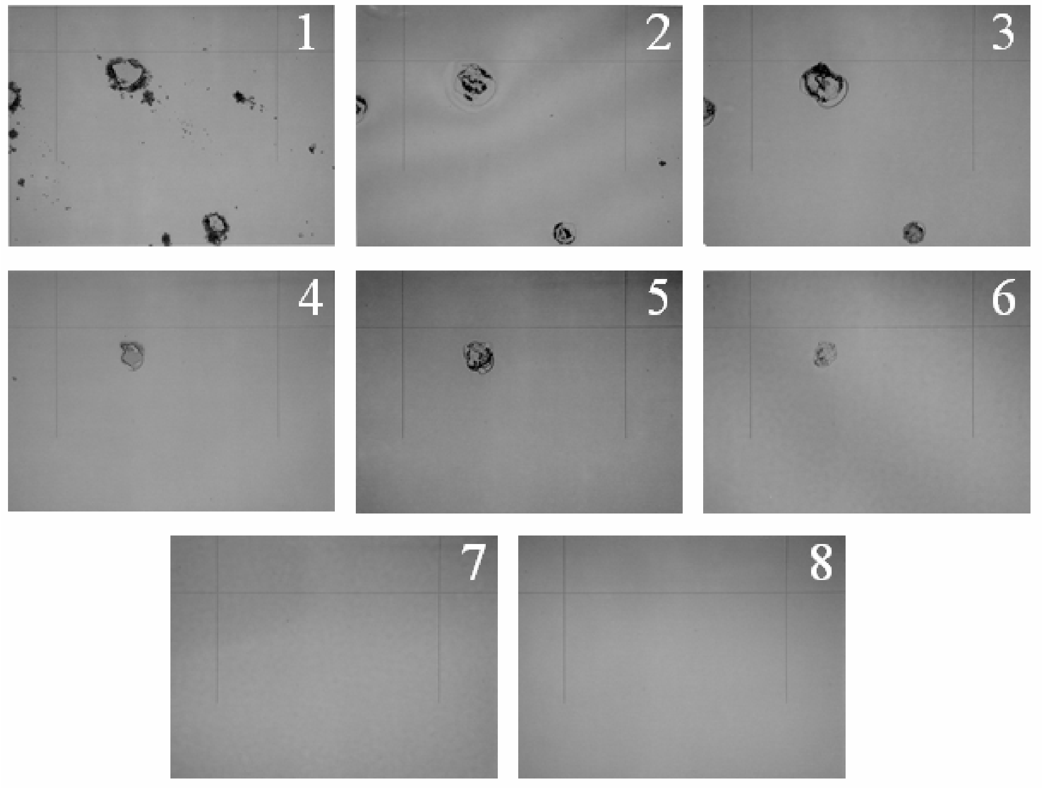

Figure 7.13: The disappearance of template-bound contamination can be seen in these images. Image 1 is a micrograph of the first imprint, etc. Note the rapid disappearance of small defects. Even the very large defects shrink upon successive imprinting and are visually absent after the eighth imprint.

In order to confirm this self-cleaning hypothesis, a separate experiment was performed in which an imprint template was inspected prior to installation, and again after imprinting. The template possessed surface-bound contamination prior to imprinting, as shown in Figure 7.14a. After two imprints, an area of contamination on the template is visually clean (Figure 7.14b). While it is unlikely that every sort of contamination is removed by the imprinting process, it is clear that the sorts of contamination introduced by normal storage and handling are removed quite efficiently. Thus, while SFIL does not incorporate an analog of the pellicle that protects the master from contamination, contamination does not necessarily result in producing repeated defects in every die.

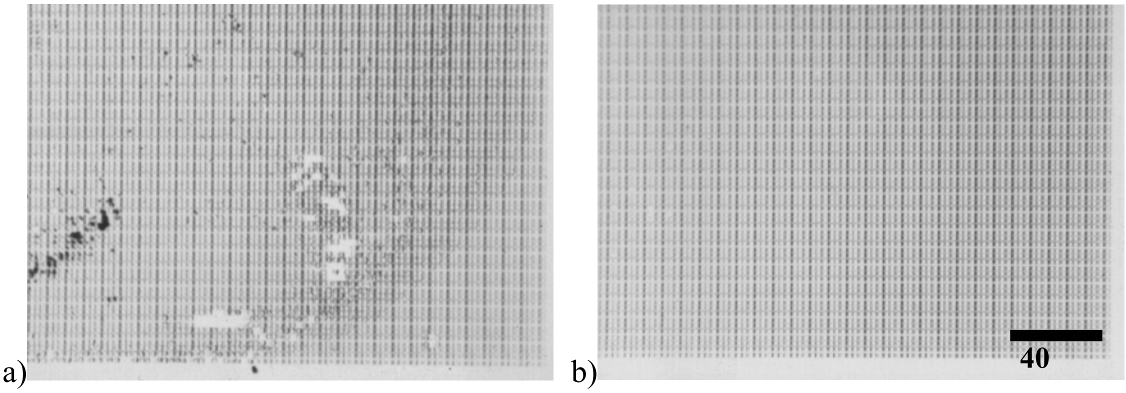

Figure 7.14: Images of an imprint template before (a) and after (b) two imprints. This confirms our conclusion that the template contamination is removed during imprinting.

7.4.2 Visual Inspection of Multiple Imprints

Initial inspections of multiple imprints using a Leica INS2000 inspection station were encouraging. Figure 7.15a shows the first imprint on a sample wafer, Figure 7.15b the fifth, and Figure 7.15c the tenth imprint. The features are 1 μm by 4 μm by 0.25 μm, and there are approximately 1100 bricks per image. No defect generation is visually observed through the ten imprints. It is important to note, however, that these fields represent only a small fraction of the imprint area. It should be noted that while the template surface treatment or release layer is not presented as an integral part of this study, imprinting with untreated templates results in catastrophic loss of pattern fidelity. The effect of template surface treatment conditions on release layer durability through multiple imprints is still under investigation.

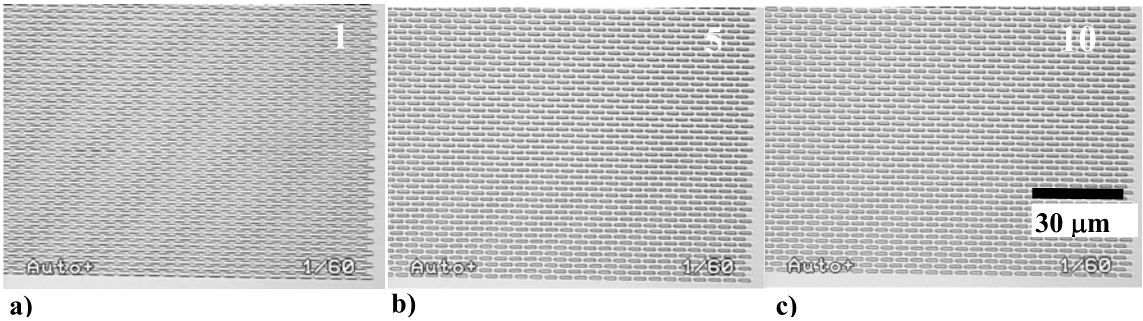

Figure 7.15: Visual inspection of multiple imprints. The same area of an imprint field was visually inspected through ten imprints. No generation of defects can be seen. The diagonal fringes are a Moiré effect manifested by the pattern regularity. Any observed difference in the pattern sharpness is due to manual focusing on the Leica INS2000 microscope, and not due to pattern transfer fidelity issues.

7.4.3 Automated Inspection of Multiple Imprints on Test Wafer Set

Introduction

The defect detection algorithm used by the KLA ILP-2139 is proprietary KLA-Tencor information, but certain non-proprietary aspects of the algorithm have become available from various KLA-Tencor sources. The two available inspection modes are Array mode and Random mode. Both modes generally compare three adjacent image fields captured by the camera, and common differences between one field and the other two are deemed to be defects at that site. This algorithm involves image subtraction, conversion of the resulting grayscale field to an image contrast histogram, and application of certain filters to the histogram. These filters include contrast threshold, pixel merge radius, image stack tolerance, and others. Threshold determines the absolute value of contrast (positive and negative) below which is considered image noise. Merge determines the search radius in pixels from a defective pixel, within which other defective pixels would be considered part of the same defect. Stack tolerance allows overlay correction, in microns, of images in the comparison algorithm to correct for image non-orthogonality in Array mode, or die placement errors in Random mode.

Array mode compares adjacent image capture fields within a single imprinted die when detecting defects. This mode is used only for regular arrays of features such as test structures and memory cells. The template pattern used in this study was designed specifically to be a regular repeating array of rectangles, to allow facile ocular detection of defects under a microscope and also to enable both defect detection modes. Random mode compares equivalent image areas on adjacent imprint dies, and can be used to inspect patterns with features of any geometry.

Array mode inspection by its nature will detect any irregularities in the regular array, which may include pattern errors caused during the template manufacture and also template damage caused by handling and installation or other events, in addition to errors caused by the imprint process. Random mode inspection detects differences in adjacent imprint fields, which may be the result of the appearance of defects, but also may be the result of the disappearance of defects. Additionally, defects that appear and persist for many imprints are lost in this analysis, and are only counted as defects when they appear or disappear. After lengthy consideration it was decided to use Array mode inspection for this analysis. This will result in a trend of defects over time that is a combination of pattern defects on the template plus those defects created by the imprint process and materials.

Imprint Template Pattern for Automated Inspection

Any die pattern intended for automated inspection must possess at least low-magnification alignment marks and high-magnification alignment marks, which may be the same features if designed properly. Patterns intended for Array mode inspection must possess at least one area which consists of a regular array of features of the same type and size. Patterns for imprint templates must additionally possess some capability to specify an inspection area that is aligned orthogonal to the wafer axes in a die that is improperly aligned, which may exist due to the inability to align the template during installation in the current imprint machine.

After consultation with personnel at Sematech and KLA-Tencor, it was decided to use a brick-and-mortar pattern as the main array on the imprint templates for this study. This pattern consists of 1 μm × 4 μm rectangles that are recessed in the template, separated by 1 μm on all sides and the array area is 0.25 in × 0.25 in. Versatile alignment marks were also developed and were placed at a 500 μm perimeter around the array area at a pitch of 1000 μm. Figure 7.16 shows e-beam resist images of the array pattern and the alignment marks captures during template manufacture.

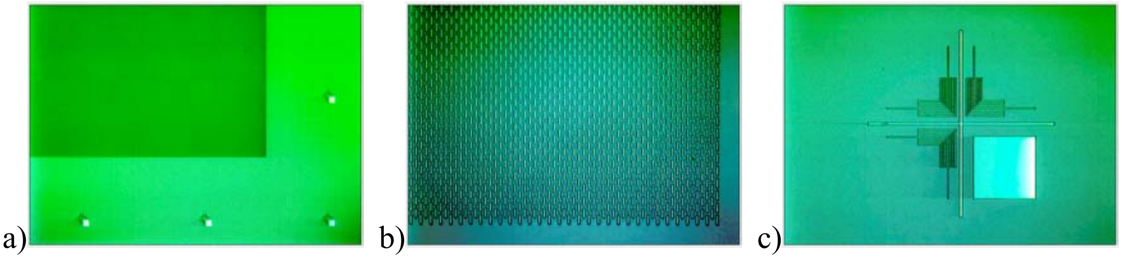

Figure 7.16: Resist images of defect template during manufacture. (a) Relation between main pattern area and alignment marks, (b) close-up of brick-and-mortar pattern, and (c) close-up of alignment mark.

Test Wafer Set and Data Analysis

Six wafers were printed using a new imprint template with a freshly-deposited release layer, according to standard processing conditions. The wafers were inspected at KLA-Tencor on the 2139 using the following inspection parameters: 0.391 μm pixel size, 50% coverage, threshold 30, 5 micron stack tolerance, 5 pixel merge, and 1 μm size sieve, a setting which filters out smaller defects.

Total defect data from the Array Mode inspection of six wafers are presented in Figure 7.17. This plot is obviously noisy, and perhaps the ultimate question is: What is the best logical function that can describe these data? Or more importantly: Is the data set large enough to conclude anything about defect trends in SFIL?

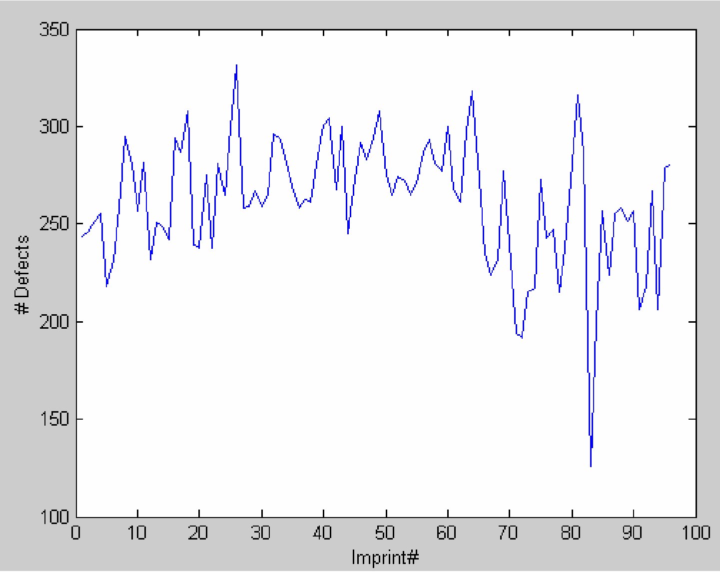

Figure 7.17: Sum of all defects detected in Array mode.

Assuming a linear model, the evolution of slope and its confidence with increasing inclusion of imprints is shown in Figure 7.18. The slope is established to be greater than zero by the 25th imprint, and remains relatively constant through the 64th imprint, after which the slope shifts downward. The slope of the entire data set, shown at point #96, are not included in the confidence limits of slope of the 64th data point. There seems to be evidence of some "event" at imprint 65 or 66 that drastically shifts the slope of the sample data. If a linear fit is truly representative of this data set, then it would be expected that the slope would evolve toward a single value. There appears to have been some event, either in the imprinting process or in the inspection process, which caused a sudden shift in the linear slope at the 65th imprint. If this is the case, the data can be broken into two lines rather than one, or perhaps there is a more complicated function to describe the data.

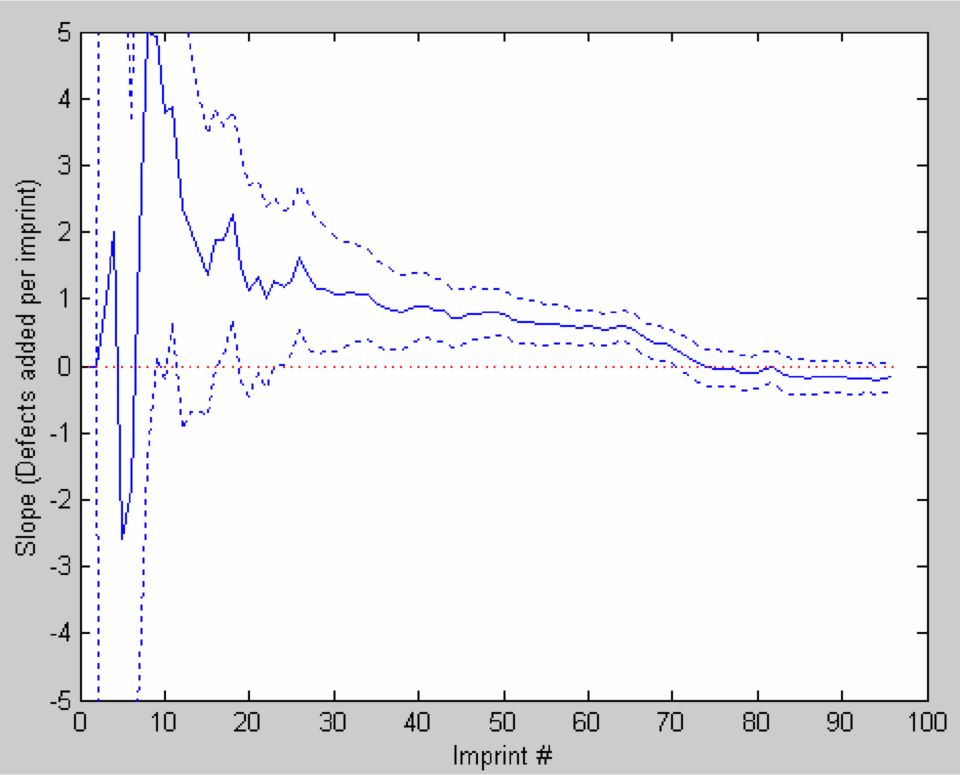

Figure 7.18: Evolution of slope (solid line) and its 95% confidence limits (dotted line) with increasing data set size for the data in Figure 7.17.

The data in Figure 7.17 were split into two regimes, each possessing its own linear parameters, and regressed as outlined below. Multiple linear regression was performed in MATLAB using the `regress` command, with the split occurring between points *m-1* and *m*:

$$y = bX + \varepsilon$$

$$where$$

Equation 7.2

$$X = \begin{pmatrix} 1 & 1 & 0 & 0 \\ 1 & 2 & 0 & 0 \\ \vdots & \vdots & \vdots & \vdots \\ 1 & m-1 & 0 & 0 \\ 0 & 0 & 1 & 1 \\ \vdots & \vdots & \vdots & \vdots \\ 0 & 0 & 1 & n-m-1 \\ 0 & 0 & 1 & n-m \end{pmatrix}, b = \begin{pmatrix} b_1 & b_2 & b_3 & b_4 \end{pmatrix}$$

where y is the observed data set, b_1 and b_3 are the intercepts of the segments before and after the break, respectively, b_2 and b_4 are the slopes of the segments before and after the break, respectively, and ε is the residual data set. The optimal location of the split was determined by allowing the split at every data point, and calculating the error sum of squares (SSE) for each split possibility. The global minimum of the SSE function (Figure 7.19) was taken to be the optimal split location, which in this case is between the 65th and 66th imprints. Multiple linear regression of the data allowing for this split was performed, and the results are shown in Figure 7.20. In order to test for the significance of the two-line model over the one-line model, an F-test was invoked.

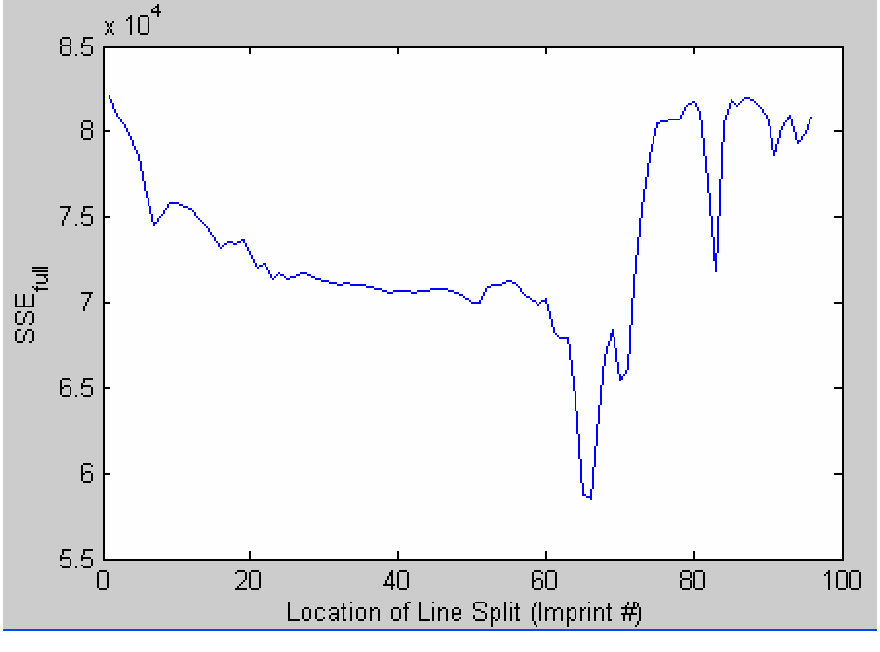

Figure 7.19: SSE for the data in Figure 7.17 modeled as two lines.

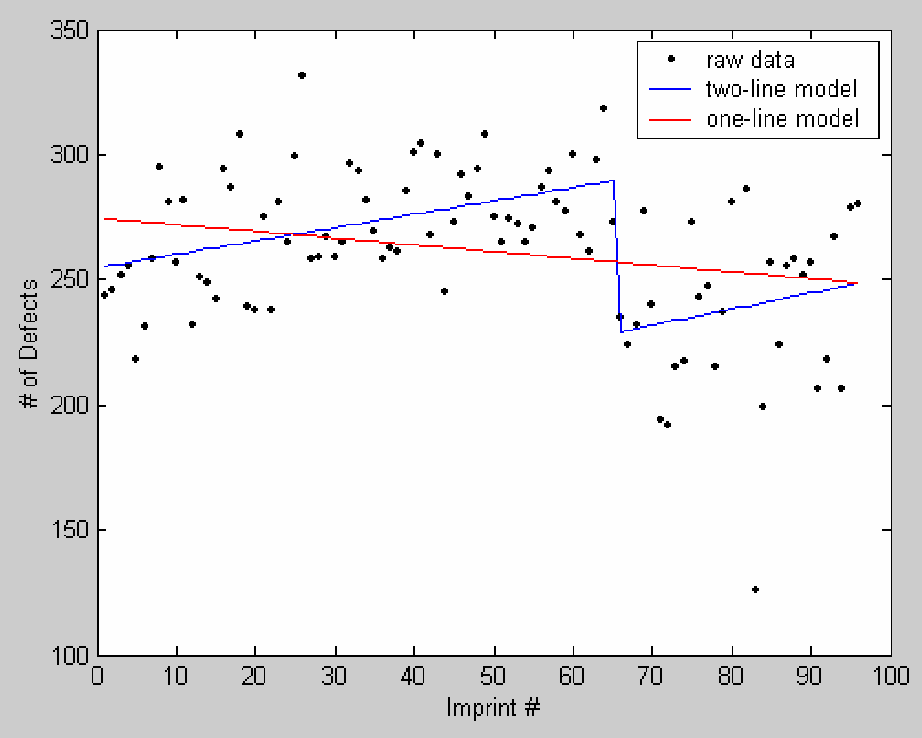

Figure 7.20: Multiple linear regression and simple linear regression of the data.

The F-test compares the ratio of variance from both models to an F probability distribution. The specific ratio used in this analysis compares a simplified model (the simple linear model) to the more complex model (the multiple linear model):

Equation 7.3
$$F = \frac{\left(SSE_{one-line} - SSE_{two-line}\right)/2}{\left(MSE_{two-line}\right)}$$

where SSE is the error sum of squares and MSE is the mean square error. In this case, $SSE_{one\text{-}line}$ = 9.33E4, $SSE_{two\text{-}line}$ = 6.76E4, and $MSE_{two\text{-}line}$ = 734, yielding F = 17.5. The probability in an F table with $\alpha = 0.05$ allowing 2 DOF in the numerator and 92 in the denominator is 3.95;[5] since $F_{\text{experiment}} > F_{\text{table}}$, we can say with 95% certainty that there is statistical basis for the two-line model for this data set. The implications of this are unclear at present, and it may be that a larger data set is required to clarify the model. The regression also yielded 95% confidence windows for the slopes of both line segments, as shown in Figure 7.21.

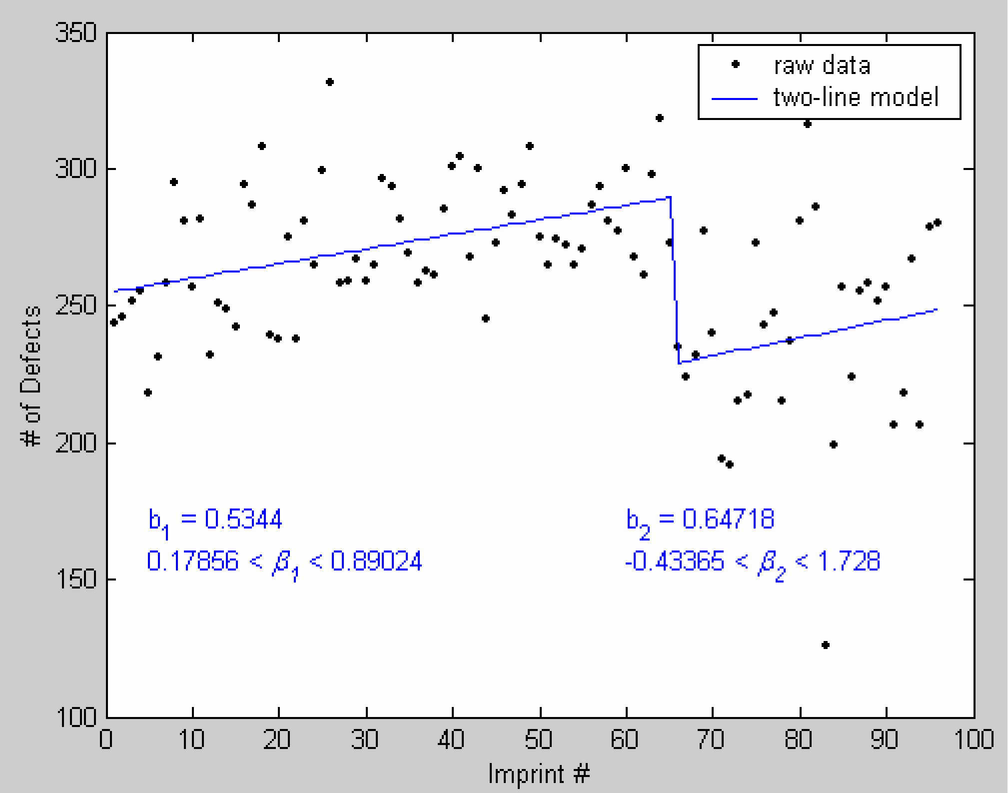

Figure 7.21: Estimated slopes and their associated 95% confidence windows for the two-segment model.

It appears, based on this regression, that the first segment of the data possesses a positive slope, and that some significant event occurred either in the imprinting process or in the inspection process that yielded a step discontinuity in the data at point 65. If this event occurred in the imprinting process, was it an event that is part of some regular process during the imprinting cycle such as, for example, sudden removal of built-up contamination? If that is the case, is it reasonable to expect such an event to occur on a regular basis throughout a longer imprint cycle, or was this part of a “seasoning” process for the template that occurs once early in the repeated imprinting process? Perhaps the answer lies in some other case not yet considered. Visual inspection using an Olympus microscope of the imprints surrounding this apparent event revealed no obvious cause for the observed trend discontinuity.

Randomly-captured images of detected defects indicate that the recipe is capable of detecting real pattern defects. There also appeared to be areas designated as defects that did not appear to possess any pattern irregularities other than color variations likely resulting from residual film thickness variation. This effect is discussed in more detail in Chapter 7. Two images of detected defects are shown in Figure 7.22, one which is obviously a pattern irregularity, and one that appears to be a non-defect, but could be detected as a result of within-die color variations. One contributor to this apparent false defect detection may be a low threshold setting in the inspection recipe. A thorough investigation of the effect of the threshold setting on defect detection was not undertaken, but later inspections using a setting of 60 seemed to mitigate the detection of false defects.

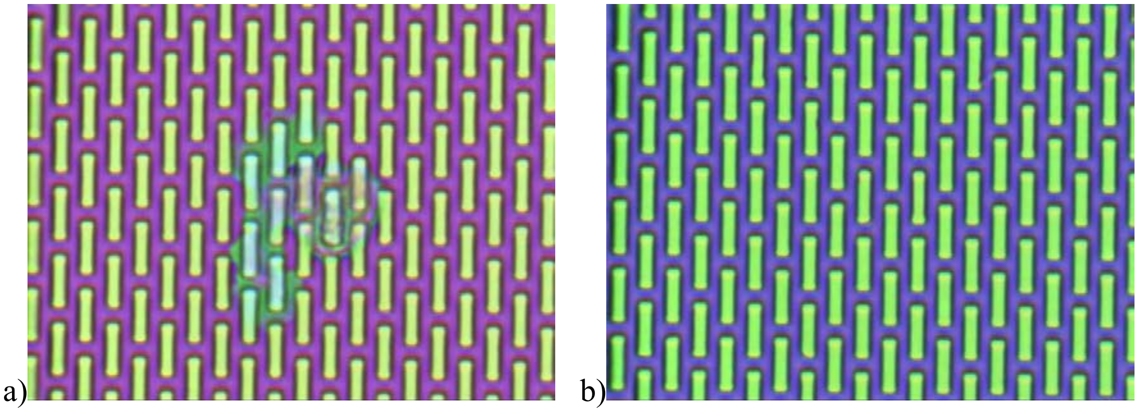

Figure 7.22: (a) Obvious pattern defect, and (b) apparent false defect detected using the inspection settings described in this section.

Estimation of Measurement Error in Defect Detection of SFIL Imprints

These six wafers were inspected three times using these settings: 0.625 µm pixel size, 100% coverage, threshold 60, 5 micron stack tolerance, 25 pixel merge, and 1 µm size sieve. The reason for choosing this merge setting is discussed in the next section. Figure 7.23 shows the three data sets. It is likely that any error is a result of variations in wafer alignment and the automatic light adjustment and focusing steps the 2139 performs at the beginning of each inspection.

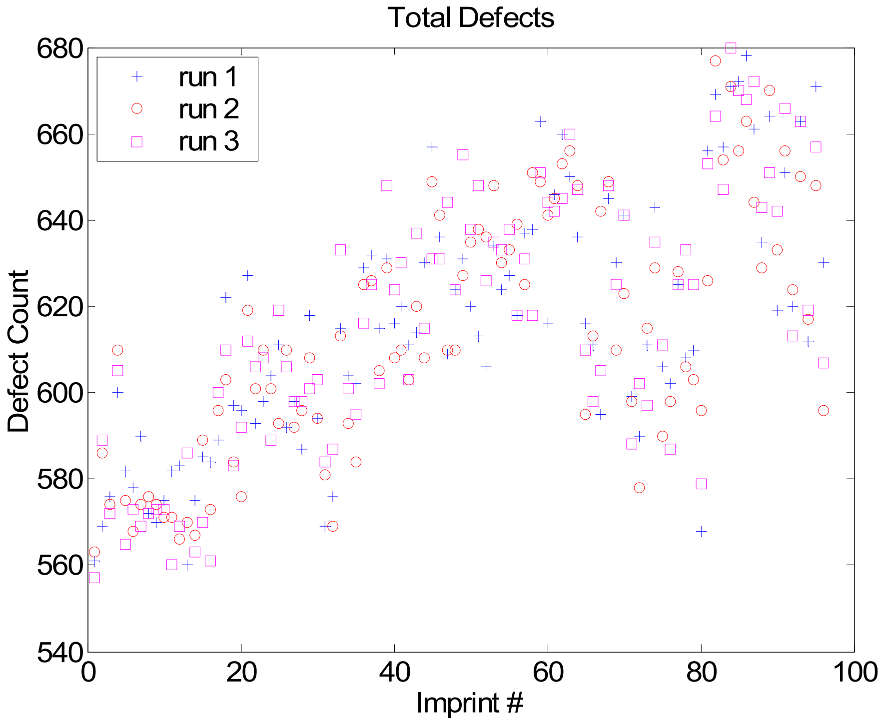

Figure 7.23: Results of three consecutive inspections of the same wafers using the same inspection recipe.

The defects for each imprint were binned according to size, and the standard deviation of the defect counts for each size bin and the total defect count were calculated for each imprint. The standard deviation ($s_{\bar{x}},_i$) was normalized by the mean number of defects ($\bar{x}$) detected in each category (i) with the assumption that errors in detecting defects is proportional to the number of defects detected, and this is shown in Table 7.1.

Equation 7.4 $$\%E_i = \frac{s_{\bar{x}},_i}{\bar{x}_i} \cdot 100\%$$

Table 7.1: Percent standard error in detecting SFIL defects of various sizes.

Defect Size (μm)	% Error
< 1.5	4.7%
1.5 - 2.25	9.6%
2.25 - 5	6.4%
5 - 10	3.3%
10 - 25	3.7%
> 25	3.4%
Total Defects	1.4%

Effect of Merge Setting on Defect Detection

Sixteen wafers were imprinted using a new template and freshly deposited release layer according to standard processing conditions. The wafers were inspected on the 2139 using the following inspection parameters: 0.625 μm pixel size, 100% coverage, threshold 60, 5 micron stack tolerance, 1 μm size sieve, and merge settings of 10, 15, 20, 25, and 50 pixels. Only 10, 25, and 50 were initially used, and 15 and 20 were used later in order to fill in the parameter space.

Results for defects of various sizes are shown in Figure 7.24. There is clearly a difference between how the inspection algorithm groups defects with changing merge setting. There is a marked difference in the trend for 10 pixel merge and the rest of the trials. It is interesting that the trend for the largest defect bin appears not to change significantly with different merge settings. Review of the detected defects on the wafers indicated that some large area defects were counted as many small defects using merge set to 10. Setting merge to 25 seemed to result in the categorization of those types of defects as single, large defects, which seemed to be more accurate. To illustrate this, a comparison of image captures from inspections using various merge settings of 5 and 25 pixels is shown in Figure 7.25, where the blue box is the rectangular boundary of the assigned defect. There did not appear to be a noticeable difference during the defect review process between the assignment of defects using merge 25 and 50. For this reason, it was decided to use 25 pixel merge setting, in order to minimize false inclusion of separate defects.

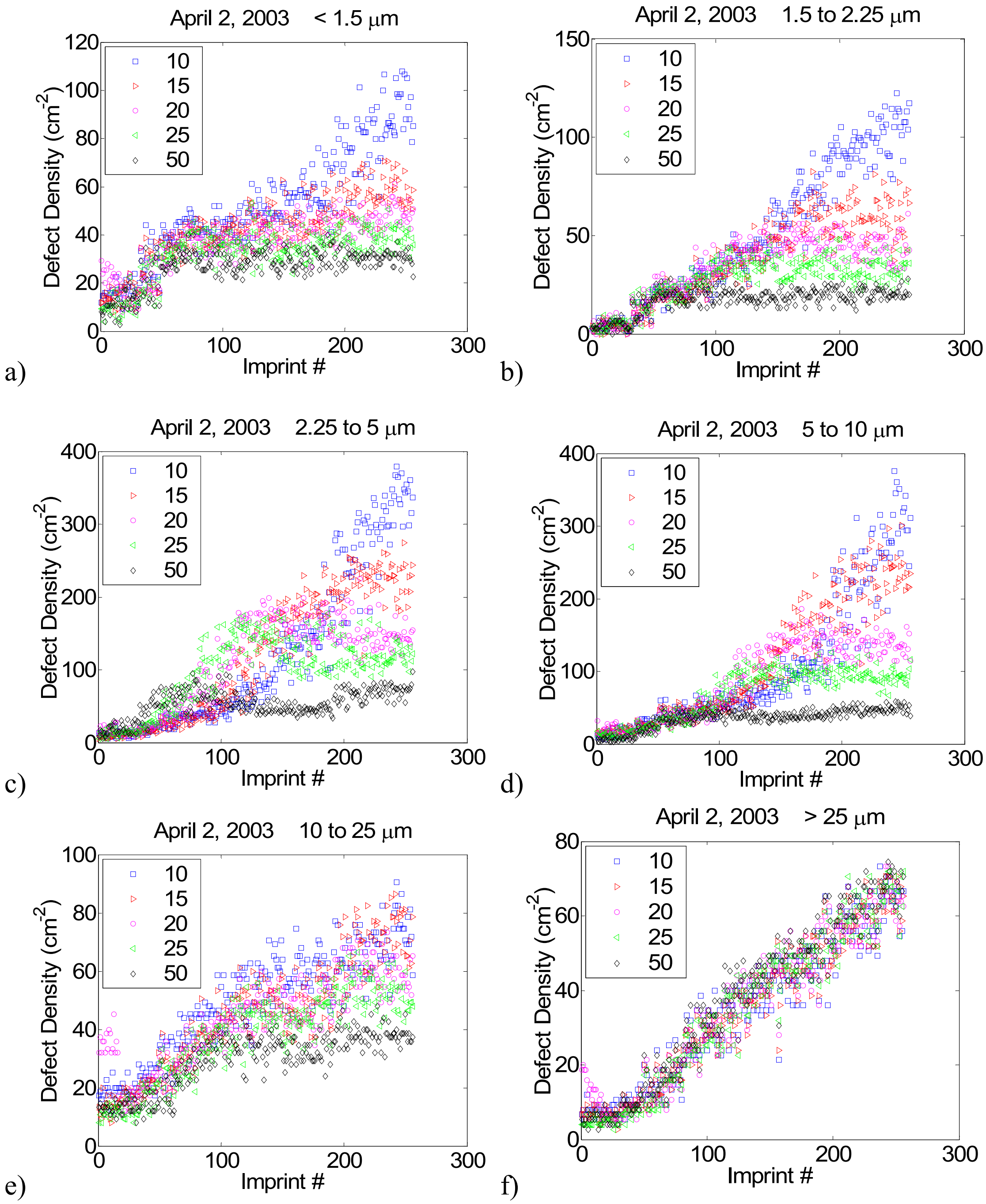

Figure 7.24: Comparison of defects of various sizes detected as a function of merge setting in pixels. Defect size range is labeled at the top of each plot.

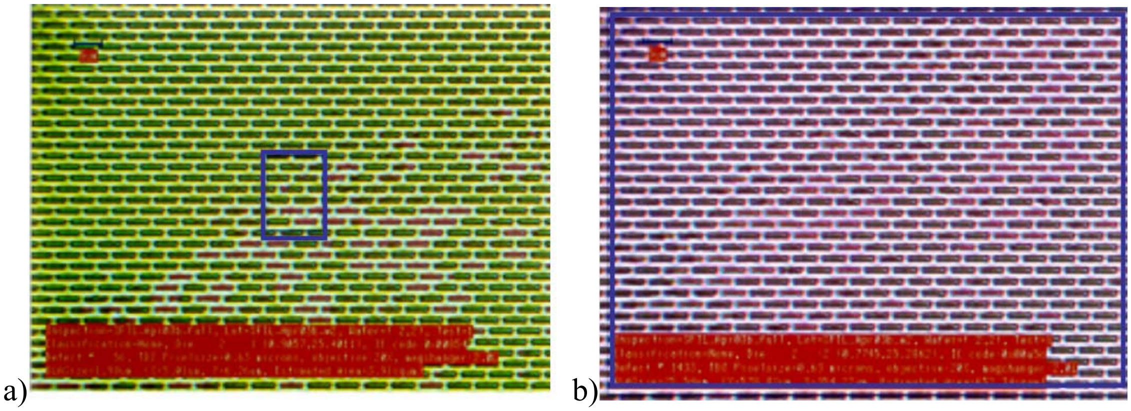

Figure 7.25: Images captured during review of wafers inspected using (a) merge 5, and (b) merge 25 pixels. The defective features in (b) are subtle, but the rectangular border groups them into one large defect.

As was mentioned previously, the data for 15 and 20 pixel merge settings were collected near the end of the window of availability for the 2139, and so a detailed review of defects between those and the other settings was not possible. There is likely some ideal setting which allows the most accurate data collection, but significantly more time and effort will need to be expended to identify it.

Marathon Wafer Sets and Data Analysis

After the inspection parameters were identified, the data files were manipulated according to the procedure outlined in Appendix D in order to establish a baseline trend of defect density as a function of imprint number. Figure 7.26 shows such a plot for these 16 wafers, including error bars as defined in Table 7.1. Figure 7.26a suggests that there may be an induction period in which there is little increase in the defect density, followed by a period of increasing defect density over time, followed by asymptotic behavior. Figure 7.26b shows these data in terms of defect size, with the appropriate error bars. The data show that the smallest two defect bins reveal an increase in defect density through roughly 100 imprints, followed by a period where there appears to be no increase. The defects of size 2.25 to 10 microns appear to increase in number to about 100 imprints, and then decrease slowly over time, and the defects larger than 10 microns appear to steadily increase over time.

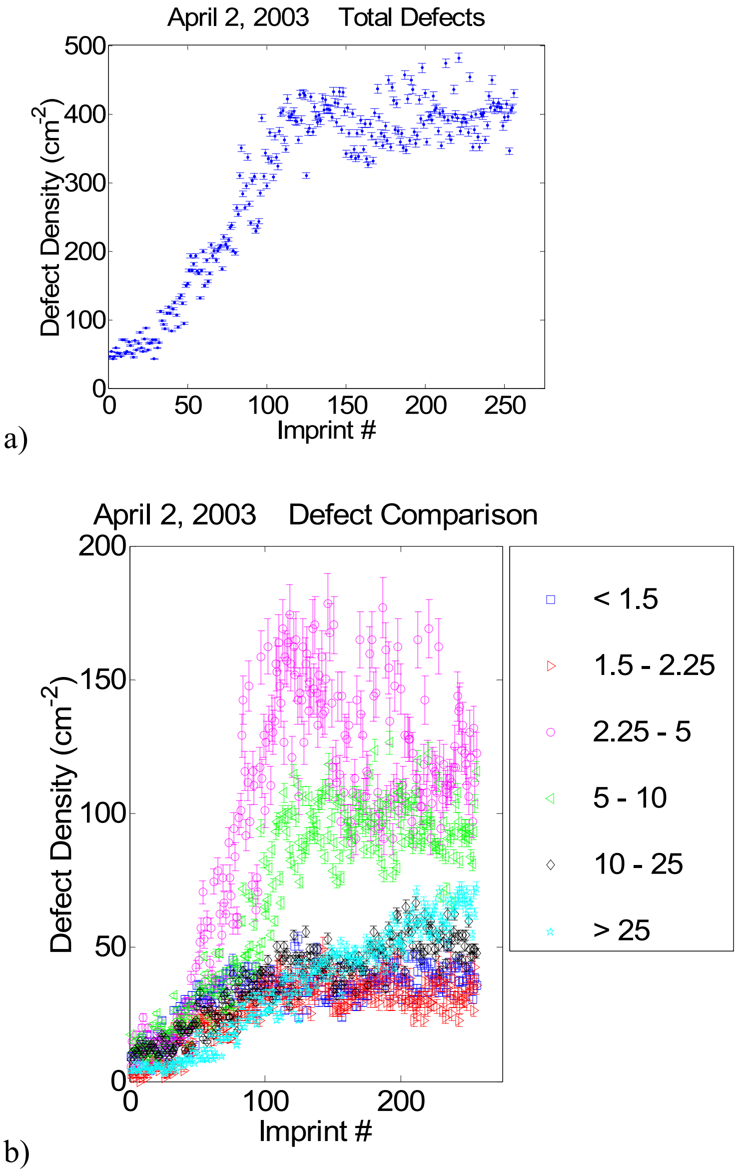

Figure 7.26: Defect data for 16 wafers imprinted on April 2, 2003. (a) Total of all defects, and (b) comparison of different defect sizes.

There are a multitude of possible explanations for this behavior. It may be that there are essentially a certain number of sites prone to defect generation, and that some of these defects gradually grow in size over time. An example map of detected defects in one particular imprint is shown in Figure 7.27. The defect density may be such that there is a probability that randomly-added defects appear within the merge radius of existing defects, which would result in growth of defect size, and not growth of defect counts.

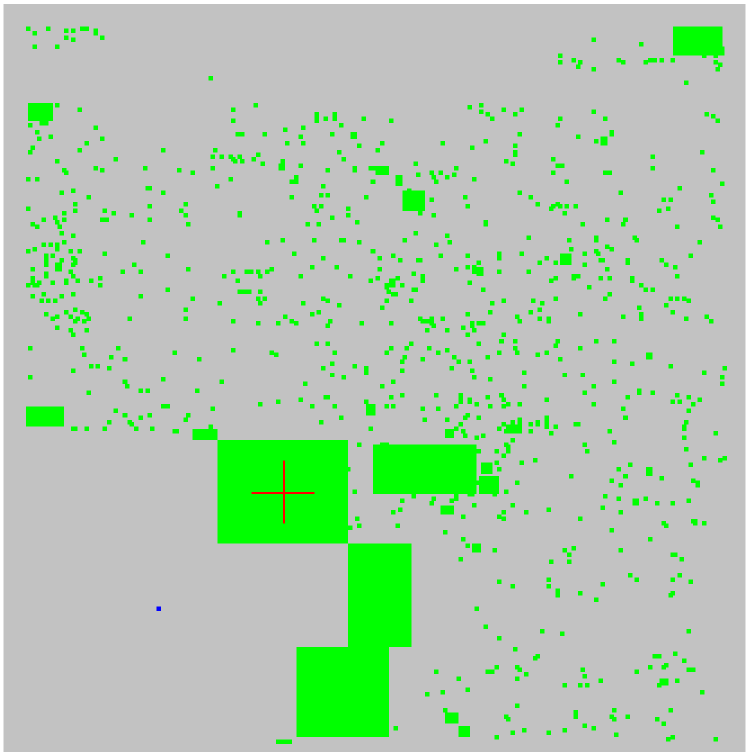

Figure 7.27: Map of detected defects in a 1 cm × 1 cm imprint field. The lower left corner of the pattern field was not replicated during the imprint process.

A second set of wafers was imprinted using a template that had been used previously, but otherwise standard imprinting procedures. Removal and subsequent redeposition of SAM films is possible, as discussed in Chapter 4, but the effect of this recycling process on the quality of the SAM film has not been ascertained. The wafers were inspected using the same inspection parameters, and the resulting data are shown in Figure 7.28.

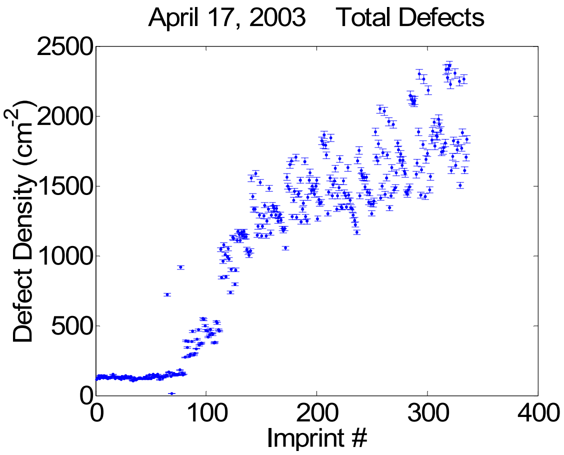

a)

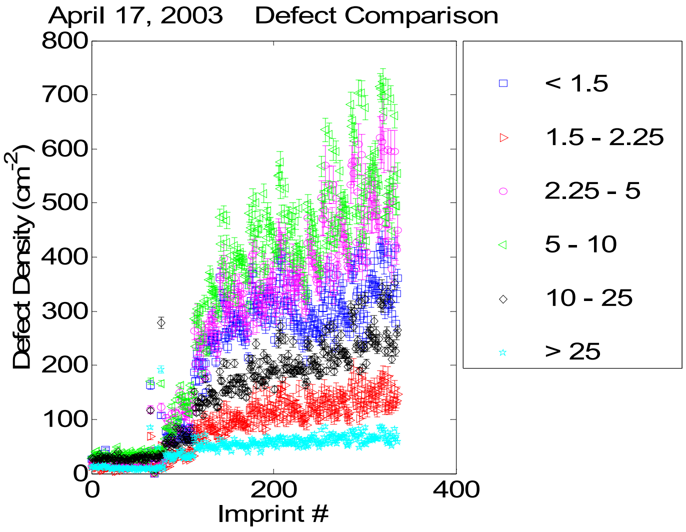

b)

Figure 7.28: Defect data for 21 wafers imprinted on April 17, 2003. (a) Total of all defects, and (b) comparison of different defect sizes.

There are some glaring features in these data, not the least of which is the dramatic increase in raw defect density as compared to Figure 7.26. The first 76 imprints show little or no increase in defect density, and the 77th imprint shows a spike. Shortly thereafter, the defect density increases very rapidly for all defect sizes. During the imprinting process, the 77th imprint failed to print properly. Apparently there was a large object wedged between the template and wafer which preventing the template from making intimate contact, and the object remained adhered to the template, thereby preventing template-wafer contact in the following four imprints. This type of defect has become known as a "tilter," because the result is that the template can tilt relative to the wafer and generally results in a failure of pattern transfer. The 80th imprint was the last imprint on the wafer, and this defect was observed. Figure 7.29 shows an optical micrograph of the resulting imprint, where a residue of the tilter can be seen, but no pattern is seen.

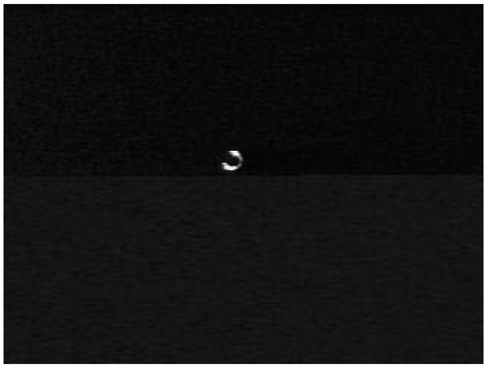

Figure 7.29: Optical micrograph of the 77th imprint, showing residue of a very large particle. The total image size is roughly 1 cm, so the particle appears to be ~ 500 microns.

It was concluded that the possibility of continuing the imprint experiment was unlikely without some intervention to remove this object. The template removed from the imprint machine, wiped vigorously with an acetone-soaked cleanroom wipe, and immersed in an acetone ultrasonic bath for 5 min. This removed the object, and the template was reinstalled in the imprint machine, after which the experiment was continued. It is at this point, the 81st imprint, that the defect trend rose sharply. It seems logical that the change in behavior in defect trend was caused by the handling and cleaning of the imprint template. It is unclear how the individual factors, such as wiping versus solvent, affected the outcome. It is also unclear how the durability of the reclaimed template, vis-à-vis the stripped and redeposited release layer, differs from that of a fresh release layer on a new template.

The three data sets analyzed in this work are presented together in Figure 7.30, which compares the total defect densities for the three experiments. The complete data sets are shown in Figure 7.30a, and the first 76 imprints are shown in Figure 7.30b, which is a comparison of the defect trends prior to the catastrophic event in the April 17 wafer set. It is interesting that the Nov 2002 wafers possess such a large number of defects initially, but it is worth pointing out that the imprint templates for that experiment were manufactured using a less mature template process, which likely resulted in a less pristine feature array. It is likely that the further refinement of the template process resulted in more regular features, which would then lead to reduced template-related pattern defects.

Some example defects are shown in the next section, but it is important to note that complete understanding of the causes of the features in this trend will only result from a significant amount of additional investigation.

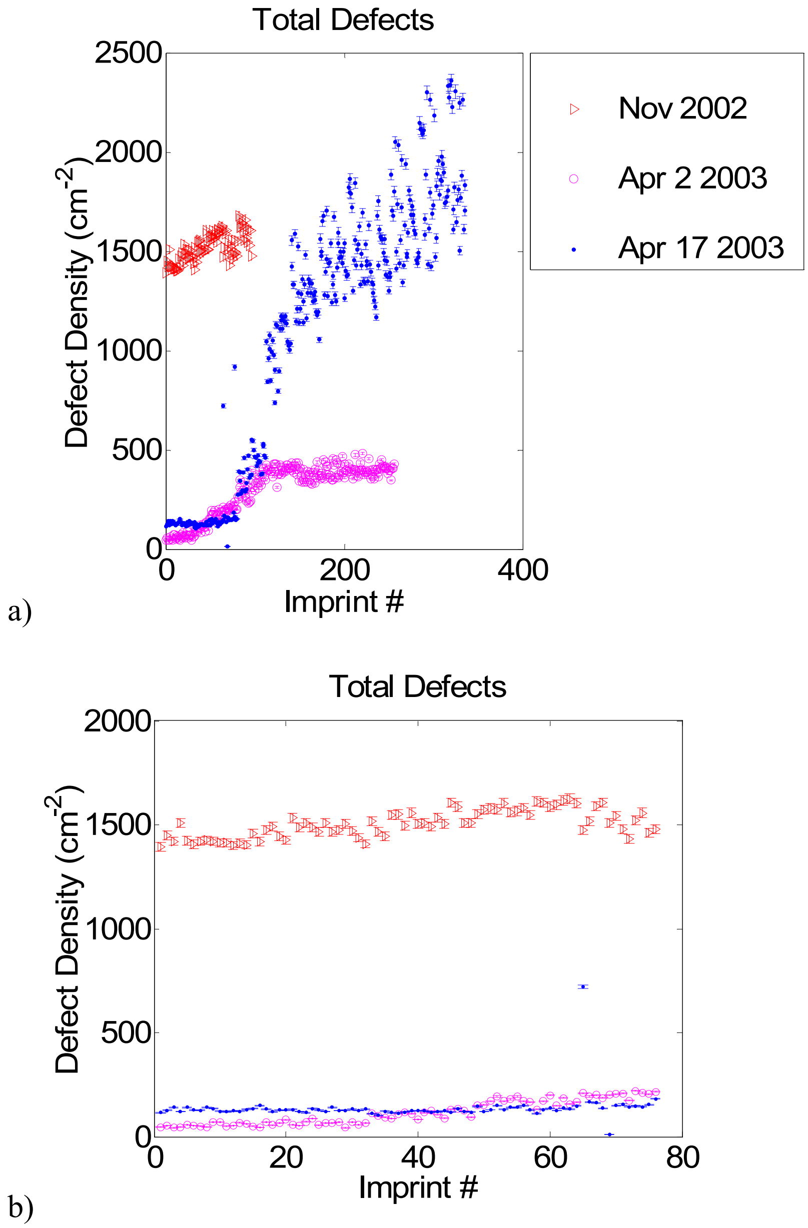

Figure 7.30: Comparison of the three data sets in this work. (a) Entire data set, and (b) the first 76 imprints of each set.

Example Defects

Certain types of defects appear regularly, and may be indicative of process or materials issues that need attention. Figure 7.31 shows one such defect which appears to be a mass of material, but it is difficult to tell in these images whether the topography in the defect is positive or negative. It is also interesting that it appears as though these sometimes heal themselves (a), and other times seem to persist (b).

Figure 7.32 shows the type of defect that appears to be the largest contributor in the April 2003 wafer sets. The defect appears suddenly (b), and then indefinitely persists as a shadow of the original. SEM inspection reveals that there is material missing from the imprinted field (e-i), and that there is actually material on the imprint template (j-k). One hypothesis that has been discussed is shown in Figure 7.33. The etch barrier may not be entirely stable in its current formulation, and there may be some oligimerization in the dispense system prior to dispense. In that case, (a) oligimers of various sizes that are likely deficient in initiator are dispensed into the imprint field. These oligimers adhere to the template, completely disrupting pattern transfer in the imprint in which they first appear. The defects are gradually removed over time (b-d), finally revealing the template in its clean state. The various snapshots of these steps are seen in Figure 7.32 and Figure 7.33. Figure 7.34 shows a defect which is similar to the Type 2 defect in that there appears to be a transition from good features to poor features, but the transition is much less abrupt. This may be an indication of component segregation in the etch barrier while in the liquid phase. It is important to note that at present no investigation into the temporal stability of the etch barrier liquid has been performed.

Figure 7.35 shows a defect composed of feature edge roughness, which appears to be largely confined to the top corners of the features. Template SEMs (e-f) reveal that there is some material in the corners of the features in the imprint template, but it is unclear whether this material is a result of template manufacture or adhesion of etch barrier to the template. It is important to note that there have been many experiments that do not reveal this edge roughness (cf. Chapter 2), and so it is unlikely that this is inherent in the SFIL imprint process, but more likely that it is a solvable materials issue.

There were a large number of defects such as that shown in Figure 7.33e-f in which the defect appeared to be caused by cohesive failure of the etch barrier. The etch barrier appeared torn rather than separating cleanly from the template. If this is truly the case, then it may be possible to reduce or eliminate this defect mode simply by using an etch barrier material that is more resistant to cohesive failure.

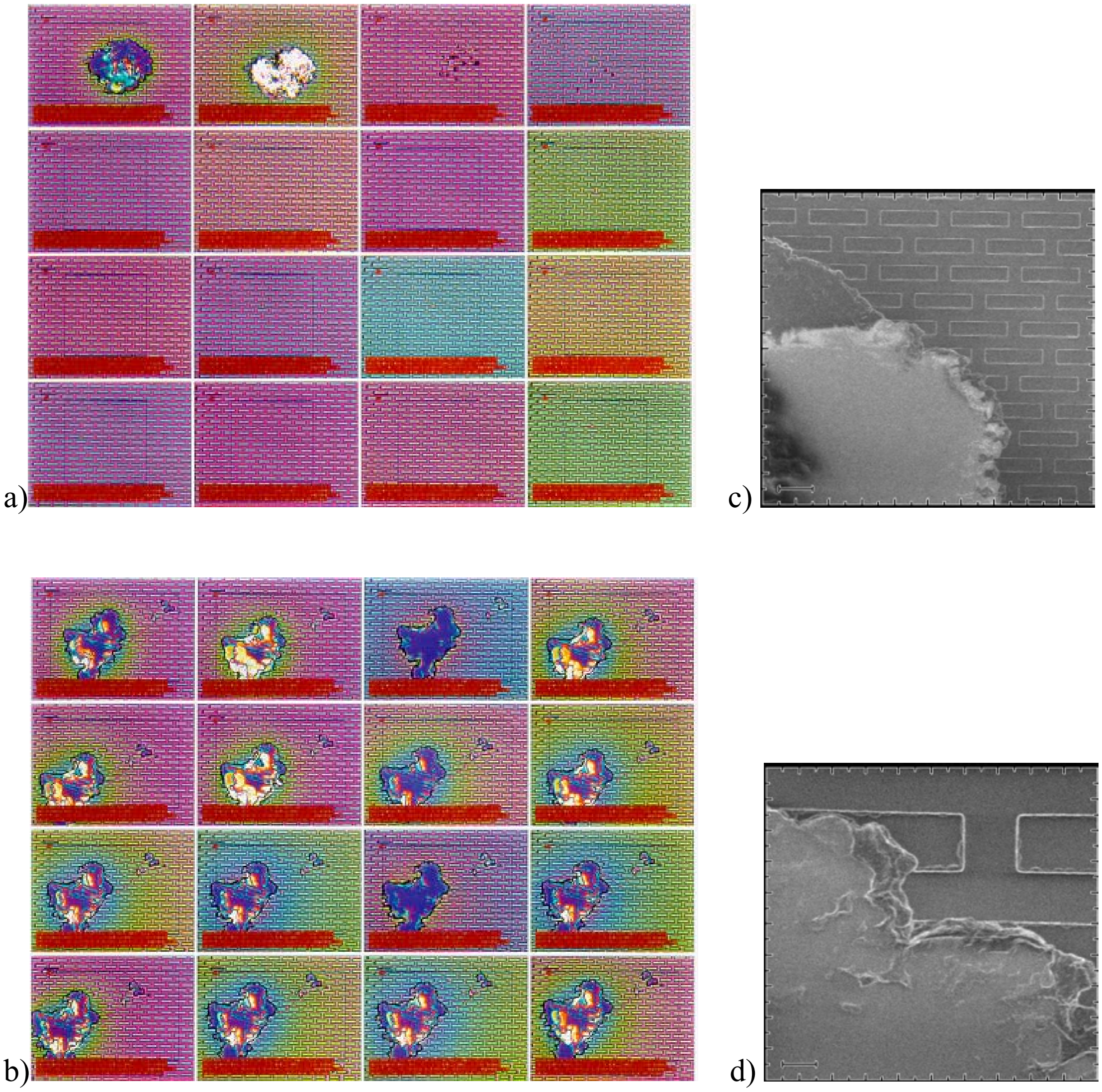

Figure 7.31: Example defect of Type 1. These appear to be the same type of defect. (a) Microscope image captures of the same region of 16 consecutive imprints in which the defect appears to be removed in the imprint process. (b) Images of 16 consecutive imprints in which the defect persists. (c-d) SEM images of this type of defect.

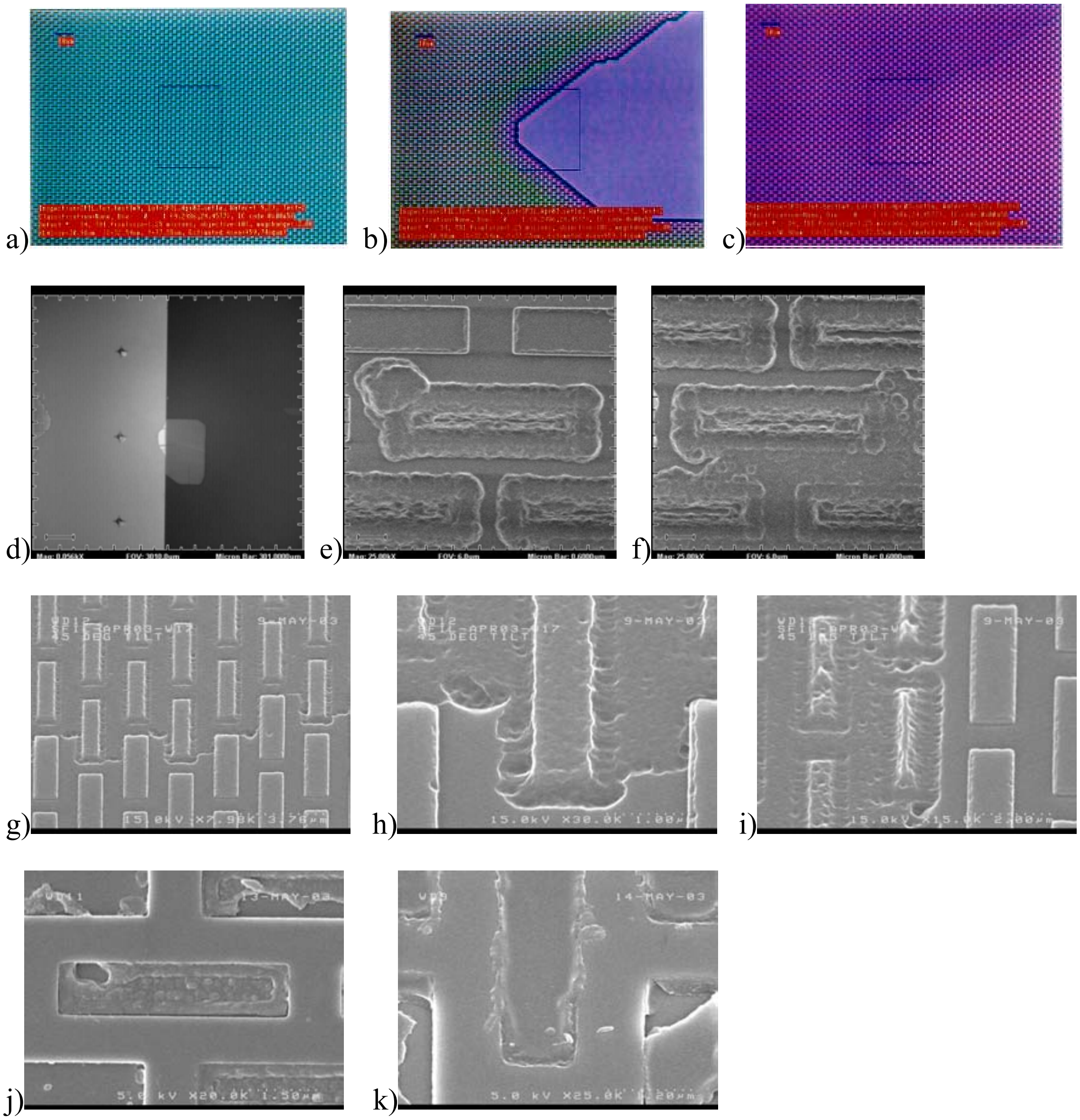

Figure 7.32: Example defect of Type 2. (a-d) Optical micrographs of imprints (a) before defect appears, (b) its first appearance, and (c) the following imprint; (d-f) top-down and (g-i) 30° tilt SEMs of imprints showing more detail; (j) top-down and (k) tilt SEMs of template in a region likely to cause this type of defect.

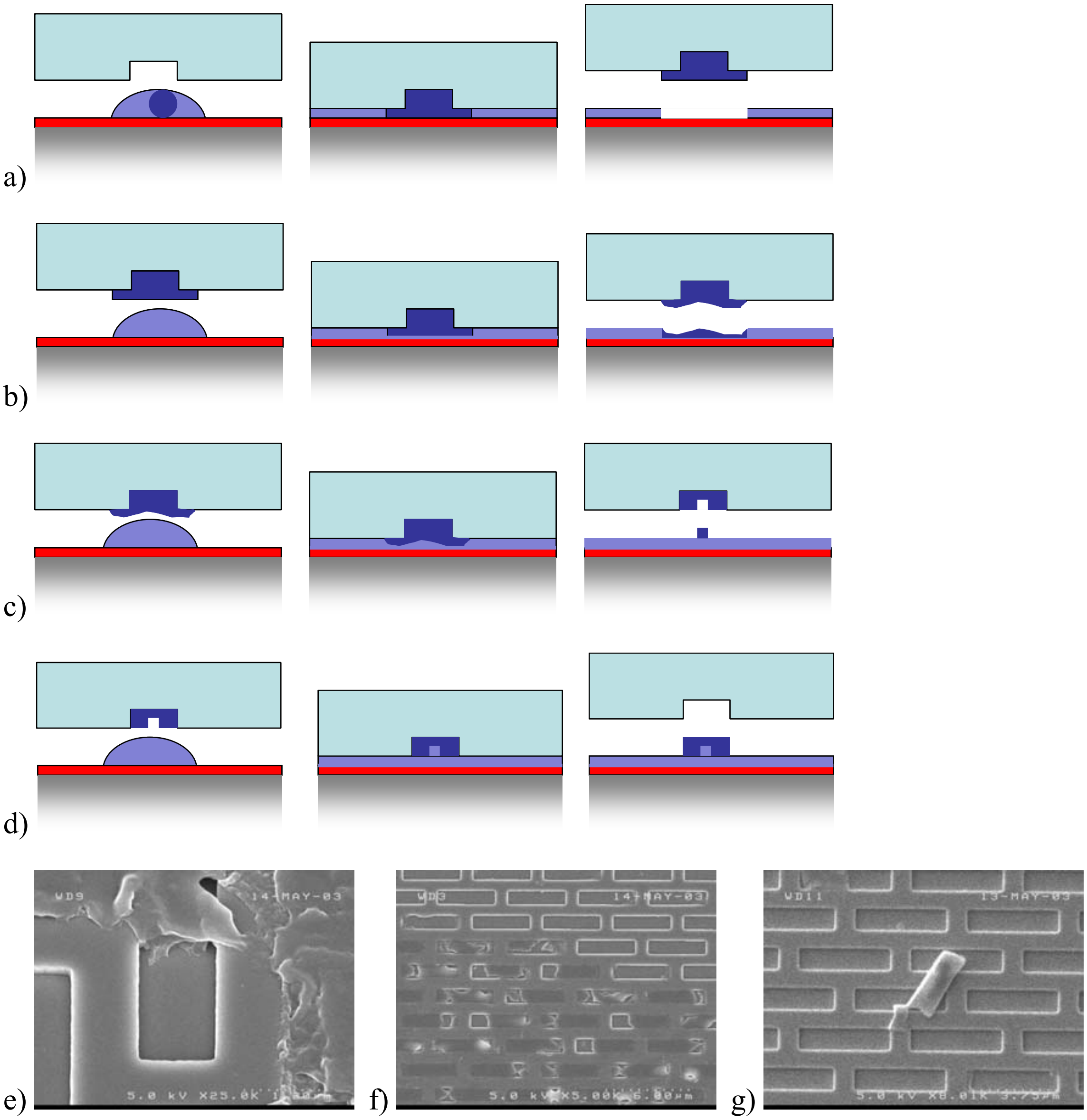

Figure 7.33: An elaborate hypothesis for the cause and result of the defects of Type 2. (a-d) Pictorial representation of oligimers in the etch barrier adhere to the template and are gradually removed over the course of many imprints. (e-g) Some SEM snapshots of these steps.

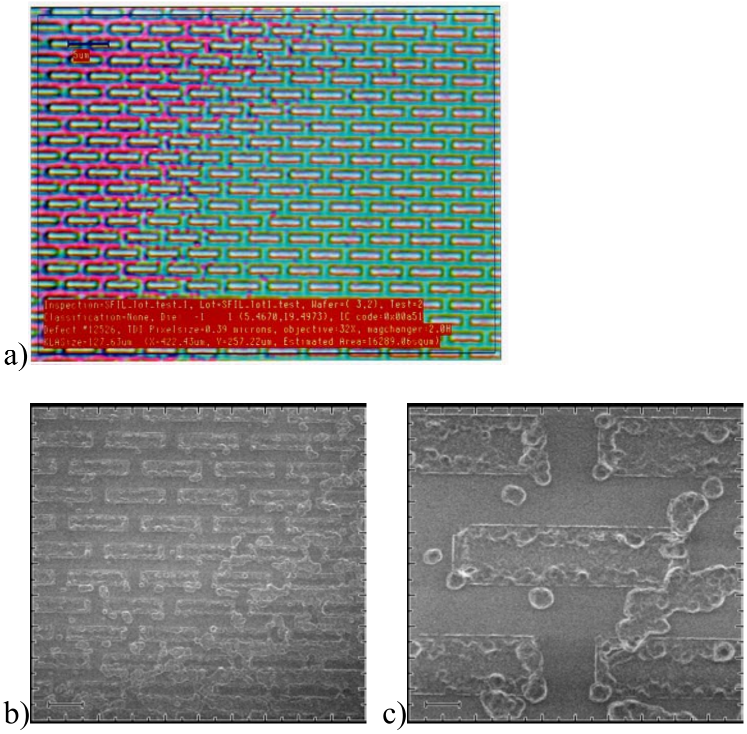

```
Inspection=SFIL_lot_test_1, Lot=SFIL_lot1_test, Wafer=( 3,2), Test=2
Classification=None, Die   -1    1 (5.4670,19.4973), IC code:0x00a51
Defect *12526, TD1 Pixelsize=0.39 microns, objective:32X, magchanger:2.0H
KLASize=127.63um  (X=422.43um, Y=257.22um, Estimated Area=16289.0bsqum)
```

Figure 7.34: Example defect of Type 3. (a) Optical micrograph of imprint showing some local variations in film thickness, as represented by the color differences; (b-c) tilt-SEMs showing more detail.

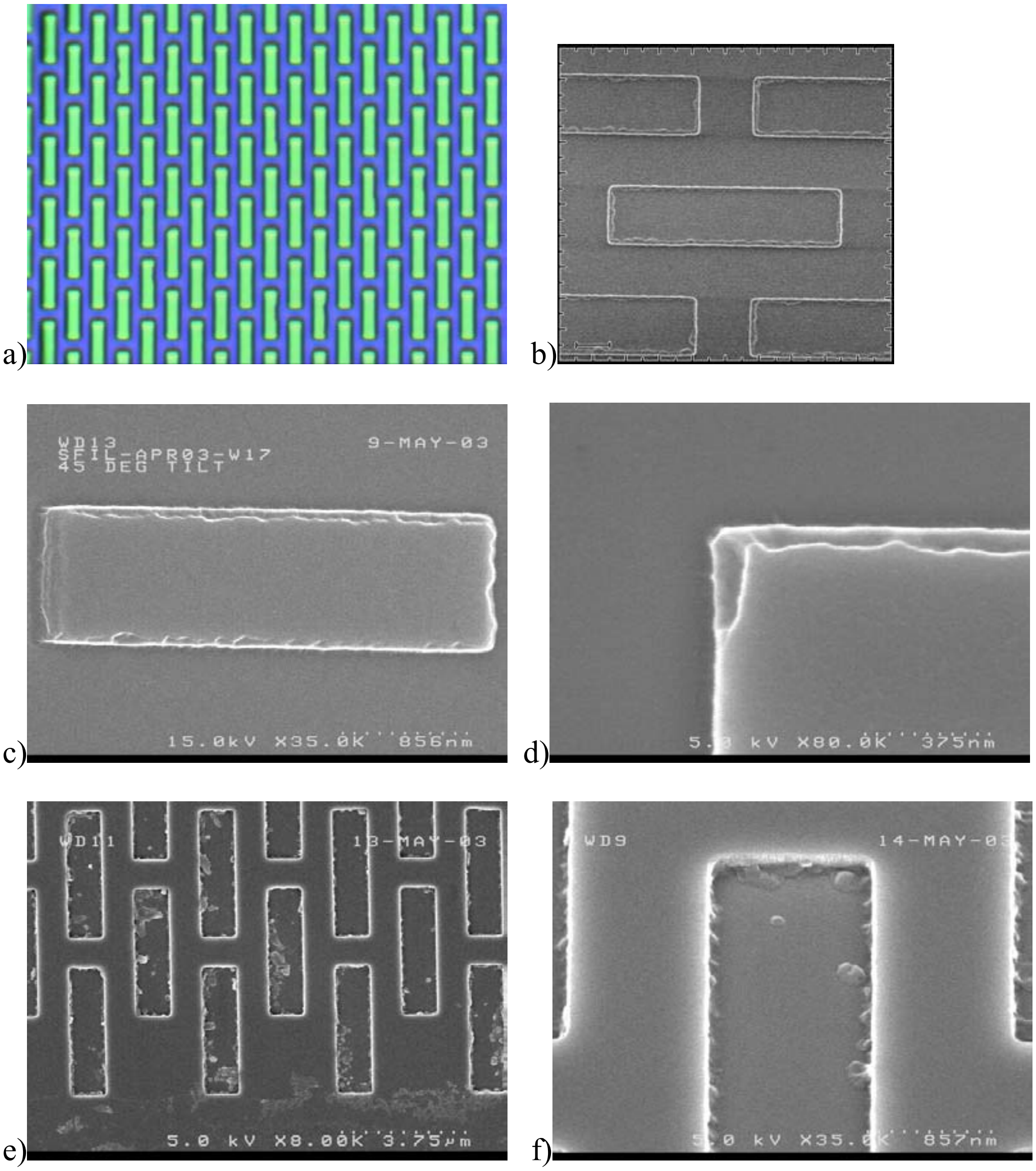

Figure 7.35: Example defect of Type 4. (a) Optical micrograph of imprint showing no obvious defect; (b) top-down and (c-d) 30° tilt SEMs of imprint showing detail of the edge roughness; (e) top-down and (f) 30° tilt SEM of imprint template showing the likely cause of this edge roughness.

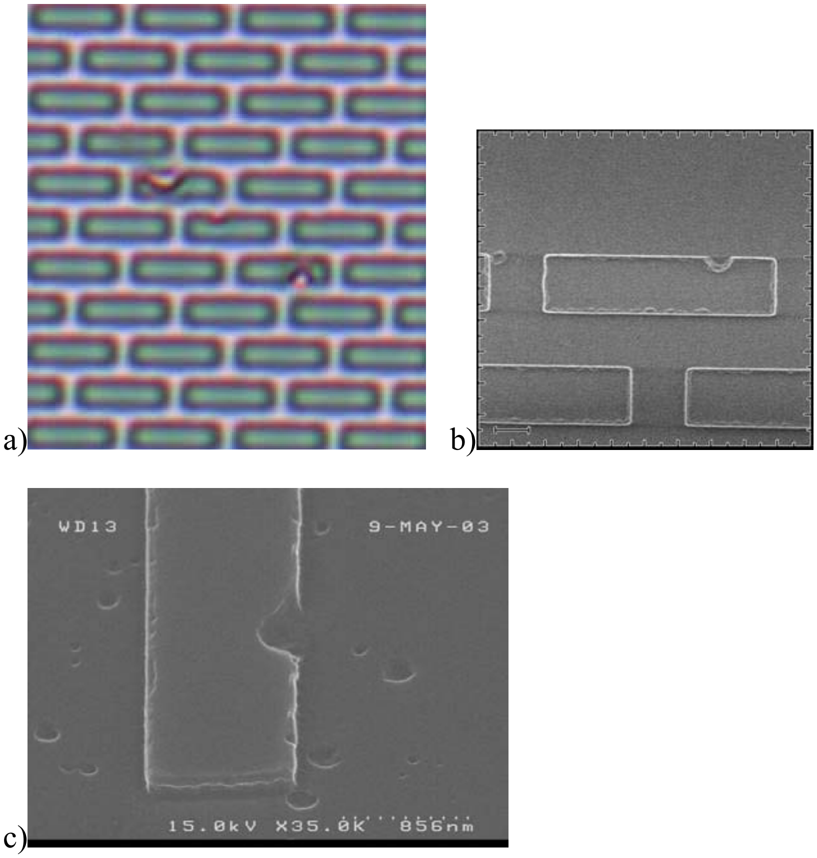

Figure 7.36: Example defect of Type 5. (a) Optical micrograph, and (b) top-down and (c) tilt SEMs of imprints showing this defect, which appears to be large missing portions of the features. This may be simply an enlarged Type 4 defect.

7.5 IMPROVEMENTS IN ETCH BARRIER MECHANICAL PROPERTIES[7]

Motivated by these defect results, we tested various etch barrier formulations using different components. This section is meant to acquaint the reader with more recent work in relation to the effect of etch barrier mechanical properties on the generation of cohesive failure defects. Precise formulations of the new etch barriers are lot disclosed, since at the time of this writing the formulations were the intellectual property of Molecular Imprints, Inc., with whom some joint efforts have been made.

Several formulations that did not contain Si were tested for their mechanical strength using a testing apparatus that yields typical stress (σ) – strain (ε) curves. A formulation was eventually selected that possessed greater Young's modulus (σ/ε) and greater overall stress- and elongation-to-break, as compared to the standard A4 etch barrier defined in Chapter 3, and the results are shown in Figure 7.37. The A4 etch barrier tested was modified slightly in that *t*-butyl acrylate was omitted.

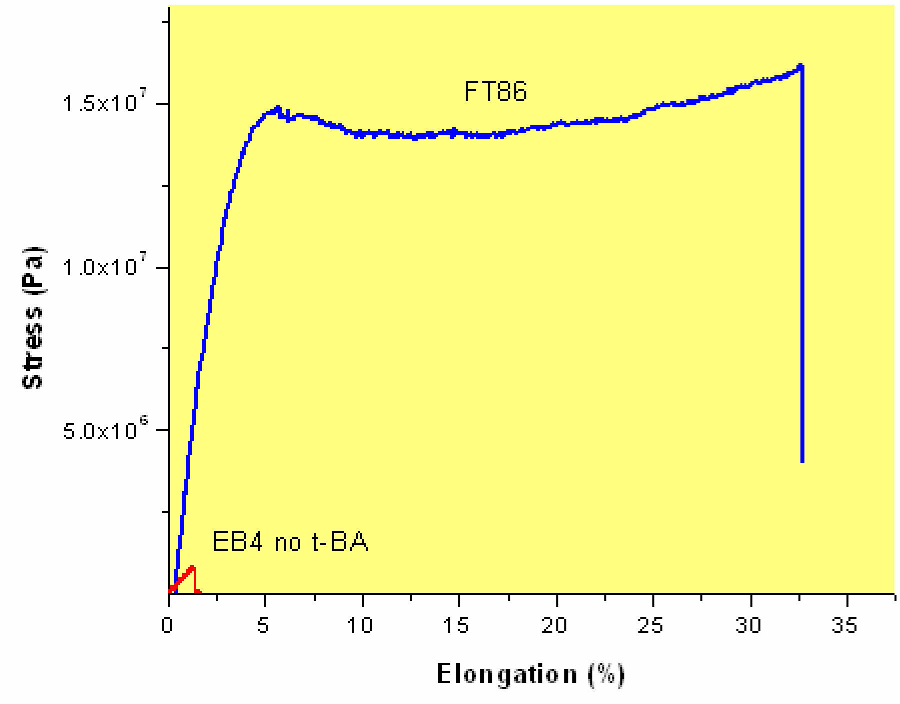

Figure 7.37: Stress-strain comparison for FT86 (Molecular Imprints, Inc. proprietary) and A4 etch barrier (labeled here as EB4).

It was believed that the greatly enhanced mechanical properties would mitigate the cohesive failure defect mode, and this particular formulation was used to imprint several wafers using the same template. Some SEM images of imprinted patterns are shown in Figures 7.38 and 7.39. The difference between the results shown in Section 7.4.3 and these imprinting results is dramatic, and is believed to be primarily a result of the change in the cohesive strength of the photopolymer.

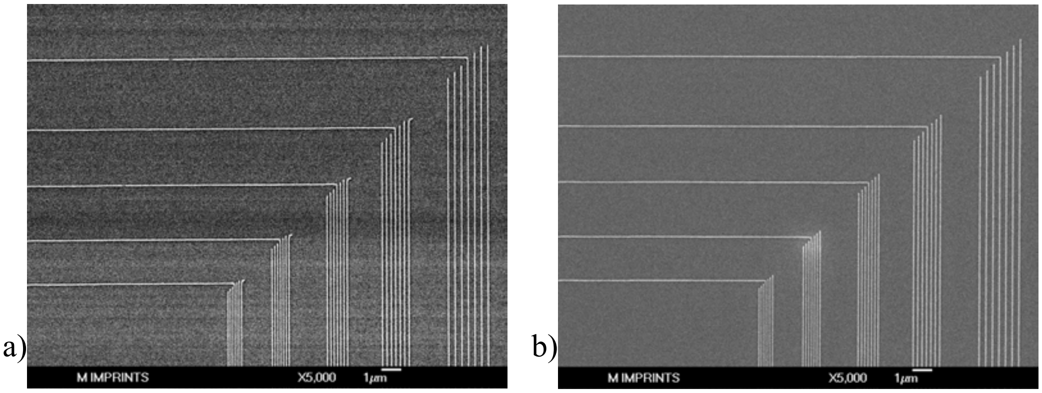

Figure 7.38: SEM images of the same 50 nm isolated/dense line set after (a) one and (b) 440 imprints using the same template.

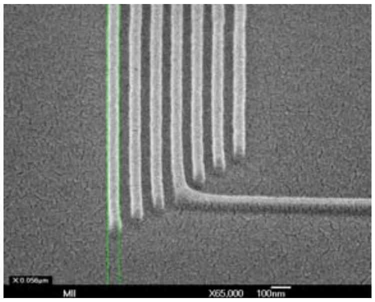

Figure 7.39: Close-up SEM of a 50 nm iso/dense feature after 440 imprints.

While work remains to be done to incoporate Si into the new formulation without dramatically reducing the mechanical strength, this set of experiments demonstrates proof of concept that imprint performance with respect to generation of defects can be vastly improved simply by changing the materials used during imprinting. Future work should include incorporating Si into this or a similar formulation, and performing an imprinting and defect inspection experiment similar to the one described in this chapter.

7.6 CONCLUSIONS

The SFIL cleanroom operates at near Class 10 conditions. The number of particles added during handling and transportation of the wafers, and due to the motion of the SFIL machinery was measured to be approximately 8 particles per wafer. This number of particles was not expected to limit the ability to characterize generation and propagation of process-related defects.

Contamination from storage and handling of the template prior to imprinting was efficiently removed during imprinting. This greatly reduces concern that the imprint fidelity would diminish over time, resulting from contaminants irreversibly adhering to the template.

Automated inspection of two sets of wafers generally revealed an inexplicable rise in the defect density over time, and the precise cause of these defects is not yet known. The Array mode inspection is known to detect pattern defects induced during the template manufacturing process. This behavior would result in a baseline defect density which should be insensitive to process conditions and SFIL materials. A thorough investigation of the cause of the increasing defect density is required, but initial investigation and hypotheses suggests that the dominant defect modes are predominantly caused not by the imprint nature of the SFIL process, but by the materials used in the process. A thorough analysis of such issues as etch barrier shelf life, mixture homogeneity, and even etch barrier/transfer layer and etch barrier/release layer interactions is necessary, and will likely lead to vastly improved performance.

One new etch barrier formulation was tested that possessed a greater Young's modulus, stress- and elongation-to-break than a formulation similar to the one used in the sefect study described in this chapter. This new formulation was used in an imprinting experiment, and SEM inspection revealed no loss of imprint fidelity through 440 imprints. A defect inspection experiment similar to that used to gain the statistical data using the A4 etch barrier remains to be done with the new formulation, but the SEM images from the new formulation are very promising.

7.7 REFERENCES

1. International Technology Roadmap for Semiconductors: 2002 Update. 2002, Semiconductor Industry Association. p. 119.
2. Met One 200L User Manual
3. Choi, B.J., *et al.*, Precision Engineering, 2001. 25(3): p. 192.
4. Personal communication with Mike Mortensen at SONY Corporation (Mike.Mortensen@am.sony.com).
5. Discussions with Dr. David Dickey at North Carolina State University were invaluable in this analysis.
6. Box, G.E.P., W.G. Hunter, and J.S. Hunter, Statistics for Experimenters: An Introduction to Design, Data Analysis, and Model Building. 1st ed. 1978, New York: John Wiley & Sons.
7. This work was performed by Nick Stacey, and E.K. Kim at The University of Texas at Austin, and Frank Xu at Molecular Imprints, Inc..

Chapter 8: Effect of Film thickness Variation on Defect Inspection for Imprint Lithography

8.1 INTRODUCTION

Inspection of imprint patterns for defects is ideally performed after imprinting/exposure, rather than after the associated etching steps, so that the true measure of defects added during the imprinting process can be reconciled. Since the imprinted pattern consists of polymer features on a layer of the same polymer, image contrast is provided by the difference in film thickness alone, as shown in Figure 8.1. Film thickness variations in the residual imprinted material manifest themselves visibly as color fringes, and monochromatically as intensity fringes. These variations in film thickness may arise from, for example, compliance in the template or wafer chuck during imprinting, or from the distortion of the wafer from the vacuum chuck. Une[1] has developed a new pin-type wafer chuck that yields ±30 nm flatness across an 8-in. wafer. Even this low level of flatness variation can potentially contribute to thin film interference effects that may confound defect inspection routines. These thin film effects may result in variations in image contrast across an imprint, or across a wafer, as in Figure 8.2. This chapter explores the effect of film thickness variation on image contrast for a bilayer imprint lithography scheme.

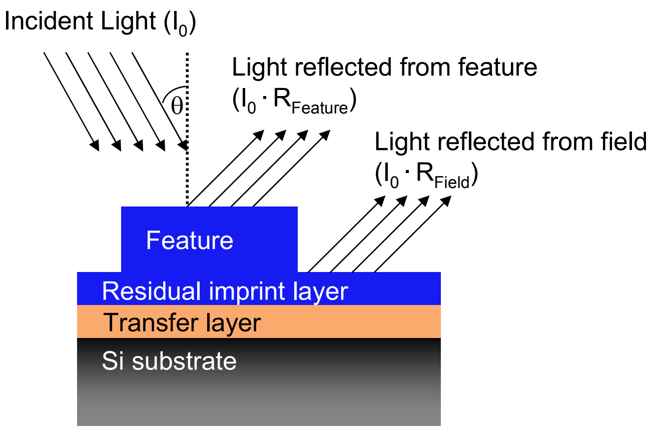

Figure 8.1. Schematic of light reflection from an imprinted pattern.

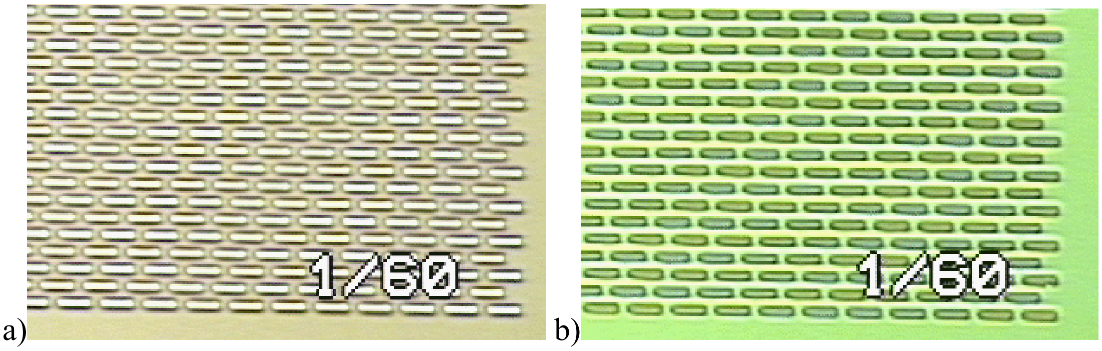

Figure 8.2. Micrographs of imprinted pattern. These images were taken from the same area of two imprints on the same wafer, demonstrating the variation of intensity of reflected light from the feature relative to that reflected from the field. (a) Imprinted features appear brighter than the field, and (b) imprinted features appear darker than the field. This intensity variation is likely caused by residual layer film thickness variations.

8.2 EXPERIMENTAL

A Woollam M-2000 spectral ellipsometer was used to extract *n*(λ) and *k*(λ) for bare silicon, the organosilicon photocurable material (etch barrier), which has been described previously,[2] and DUV30J-11 (Brewer Science), which was used a the model organic film (transfer layer).[3] Optical constants for these films are shown in Figure 8.3.

A KLA-Tencor 2139 was chosen as the model optical inspection tool. The 2139 uses a broadband Xe illumination source, and a Sony camera with a Sony ICX074AL CCD image sensor to detect reflected light; these components were considered in the model because their performance has spectral dependence. The irradiance spectrum for a medium power Oriel Xe lamp is shown in Figure 8.4a, and the response curve for the CCD image sensor is shown in Figure 8.4b.

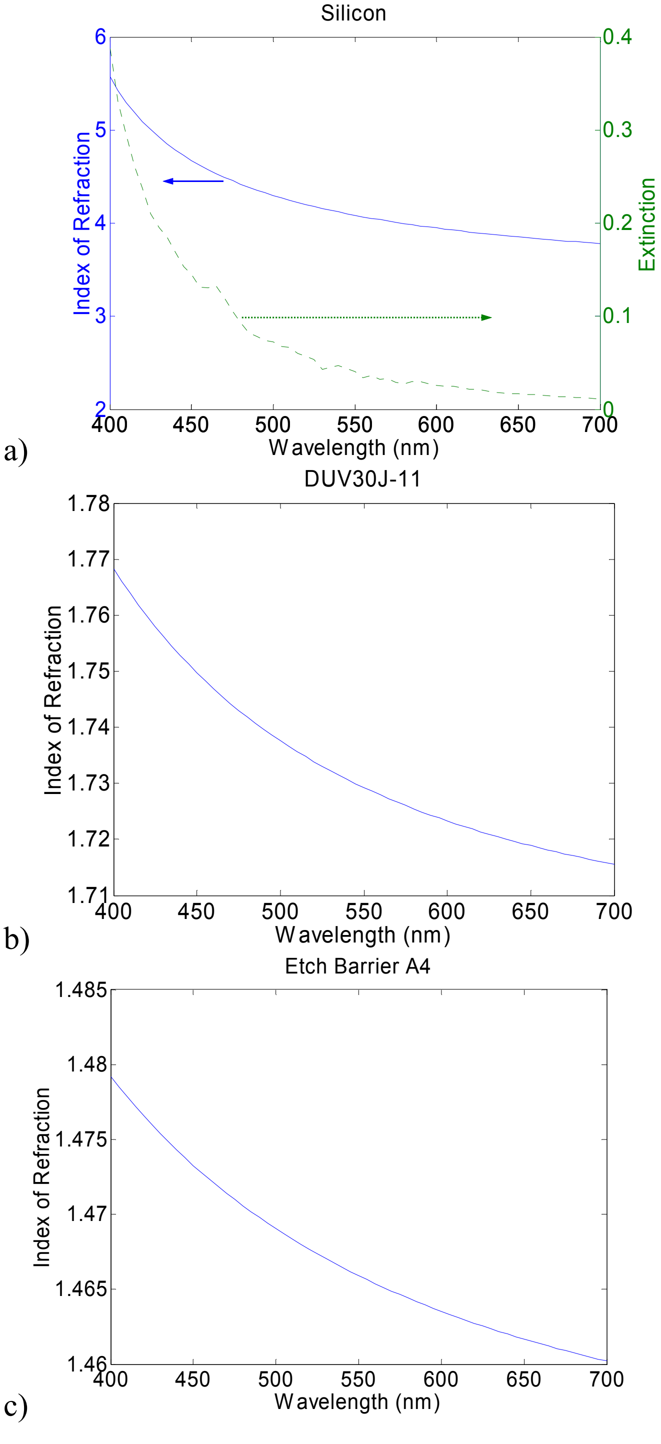

Figure 8.3. Optical constants used for (a) Si, (b) DUV30J-11, and (c) etch barrier.

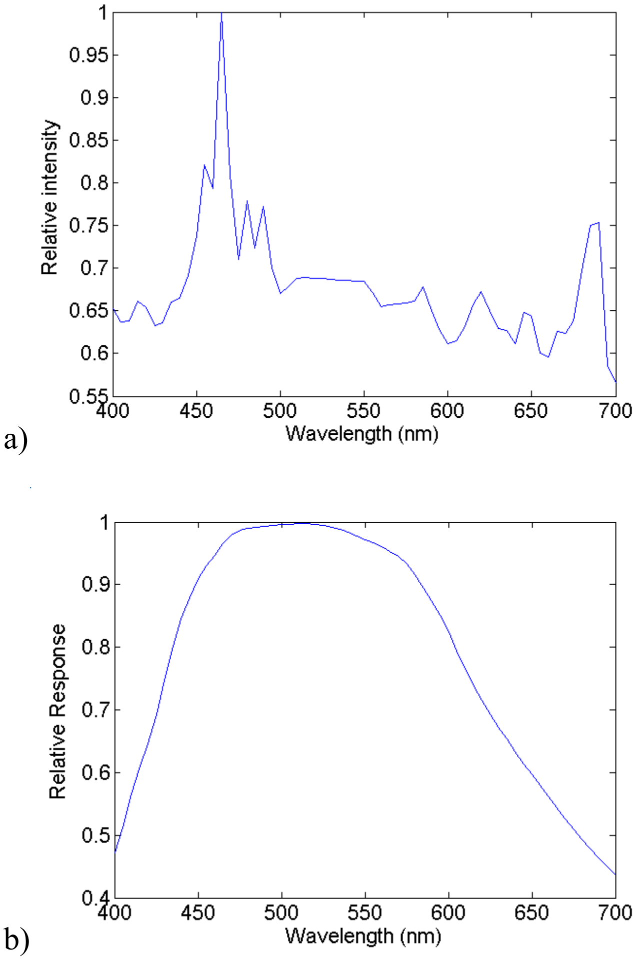

Figure 8.4. (a) Irradiance spectrum for a Xe arc lamp. The KLA 2139 uses a similar lamp for its illumination source. (b) Response curve for the Sony ICX074AL CCD image sensor.

As a practical consideration, successful etch transfer of the imprinted image requires residual layers thinner than the feature step height, and the imprinted step height is limited to some extent by feature aspect ratio. Organic transfer layer, imprint material residual thickness, and feature step height were allowed to vary from 0 to 600 nm, 0 to 250 nm, and 30 to 250 nm, respectively.

For simplicity of the model, the light was assumed at normal incidence, the substrate used was bare Si, and the aerial geometry of the feature was assumed much greater than the wavelengths of inspection light. These assumptions allowed a preliminary look into the effect of film thickness variation on reflected intensity without regard to the effects of underlying patterns on the substrate or scattering from sub-λ features.

8.3 METHOD OF CALCULATION

If the complex index of refraction and film thickness are known for each layer, as well as the angle of incidence on the surface, the reflection (*R*) coefficient of a system can be calculated, as shown in Appendix A. Image contrast at a particular wavelength derives to an extent from the relative magnitudes of *R* from the feature and the surrounding field. This ratio, coupled with the illumination irradiance spectrum and the CCD response curve and integrated over all pertinent wavelengths, may determine the level of contrast for a particular set of film parameters:

Equation 8.1

$$C_1 = \int_{\lambda} \frac{R_{feature}(\lambda)}{R_{field}(\lambda)} I(\lambda) Rsp_{CCD}(\lambda) d\lambda$$

Equation 8.2

$$C_2 = \int_{\lambda} \frac{R_{field}(\lambda)}{R_{feature}(\lambda)} I(\lambda) Rsp_{CCD}(\lambda) d\lambda$$

where $R_{feature}$ is the reflection coefficient from the patterned feature, R_{field} is the reflection coefficient from the background field, *I* is the normalized irradiance intensity of the Xe lamp, and Rsp_{CCD} is the CCD relative response, all at some particular wavelength. This assumes the detection algorithm sums the voltages from the three color detectors on the CCD. Where the ratio $R_{feature}/R_{field} > 1$, the reflected light from the feature is more intense than the reflected light from the field at a particular wavelength. Where $R_{feature}/R_{field} < 1$, the opposite is true. This give rise to the existence of two “tones,” one in which the feature appears “brighter” than the field, and the other where the inverse is true. When $C_1 = C_2$, contrast arises only from scattering at the feature edge.

8.4 RESULTS

Example model results are given in Figure 8.5, showing A, T, and R for both the imprinted residual layer (left) and the imprinted feature (right), where the organic layer, residual layer, and feature step height are 330 nm, 100 nm, and 100 nm, respectively. The absorbance in the Si does not contribute because the Si wafer is the exit medium in the model. Absorbance, transmittance, and reflectance sum to 1, which should be the case. The reflectance ratio $R_{feature}/R_{field}$ coupled with the Xe irradiance and CCD response curves is shown in Figure 8.6a. The effect of variations in residual layer thickness on the system contrast can be seen by integrating over all pertinent wavelengths for each thickness, as in Equation 8.1, yielding Figure 8.6b.

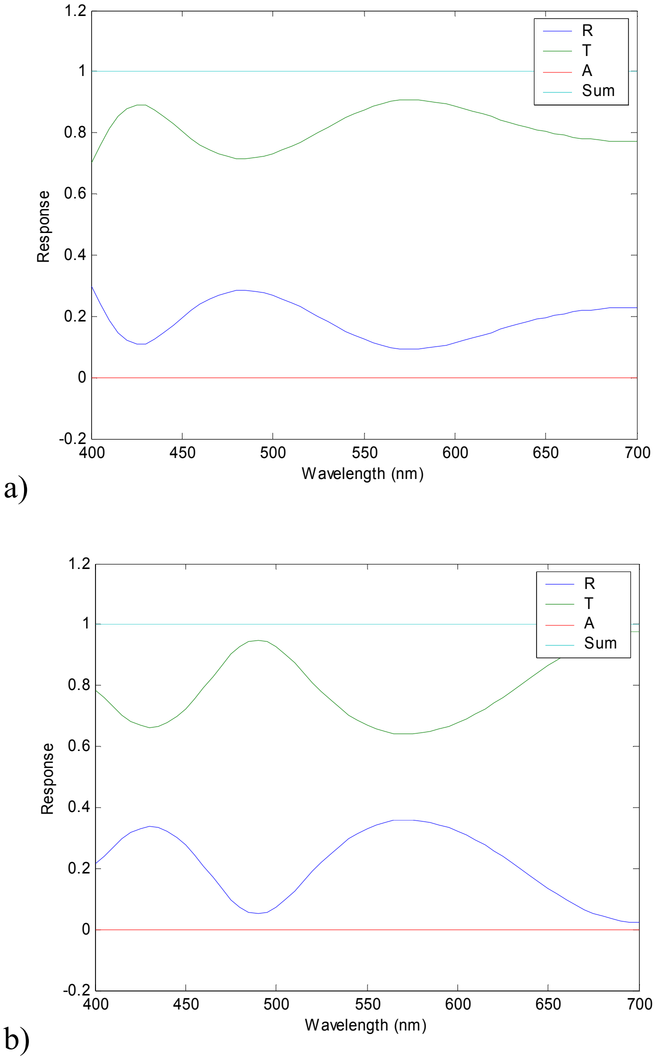

Figure 8.5. Model output for residual layer (a) and feature (b), assuming 330 nm transfer layer, 100 nm residual layer, and 100 nm feature step height.

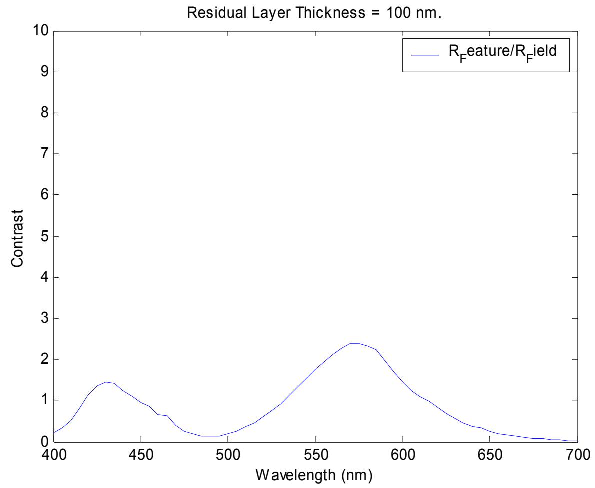

a)

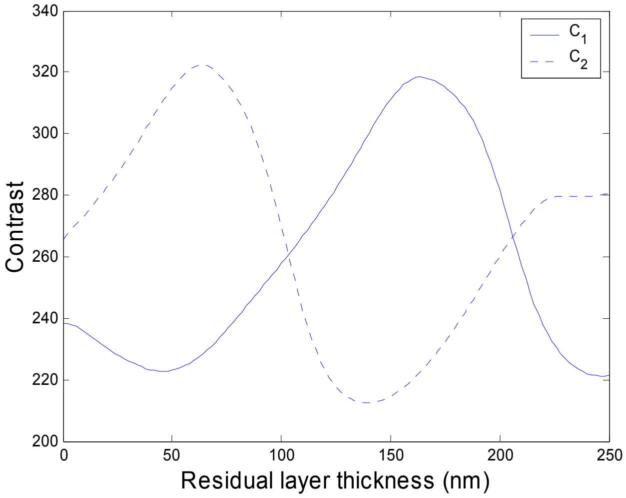

b)

Figure 8.6. (a) Ratio of reflectivities coupled with the Xe irradiance and CCD response for the case in Figure 8.5a. (b) Total contrast integrated over all pertinent wavelengths for varying residual layer thicknesses.

The overall contrast of the system is also dependent on the thickness of the transfer layer. Expansion of transfer layer thickness through the range 0 to 600 nm yields a pair of surfaces such as in Figure 8.7. The left surface represents image contrast based on Eq. (1a), while the right surface is based on Eq. (1b). Where these surfaces intersect, the system has no intensity contrast. For comparison, normal photoresist processes result in polymer features on bare silicon or on a thin anti-reflection coating, analogous to the case with zero residual layer and zero or very thin transfer layer. Note that the reflectivity at certain wavelengths may be different for the feature and field, and so the pattern may have a visible color tone, but the total intensity calculated from each surface will be identical. Figure 8.8 shows the boundaries between the different contrast regions for the case where the feature step height is 100 nm. The light regions represent parameter space where the field appears brighter than the feature, and conversely for the dark regions. The interfaces between light and dark regions represent those parameter sets where the intensities are equal. The process for applying transfer layer films on the substrate is well characterized, and produces very good uniformity across the wafer. The thickness variation in the imprinted residual layer, however, is a function of the compliance of the imprint system, as discussed above. The effect of system compliance on film thickness variation can presumably be characterized, giving the experimenter a target residual layer thickness range. This allows one to choose a transfer layer thickness for a given target residual layer thickness range so that the intensity in only one plane, feature or field, will dominate.

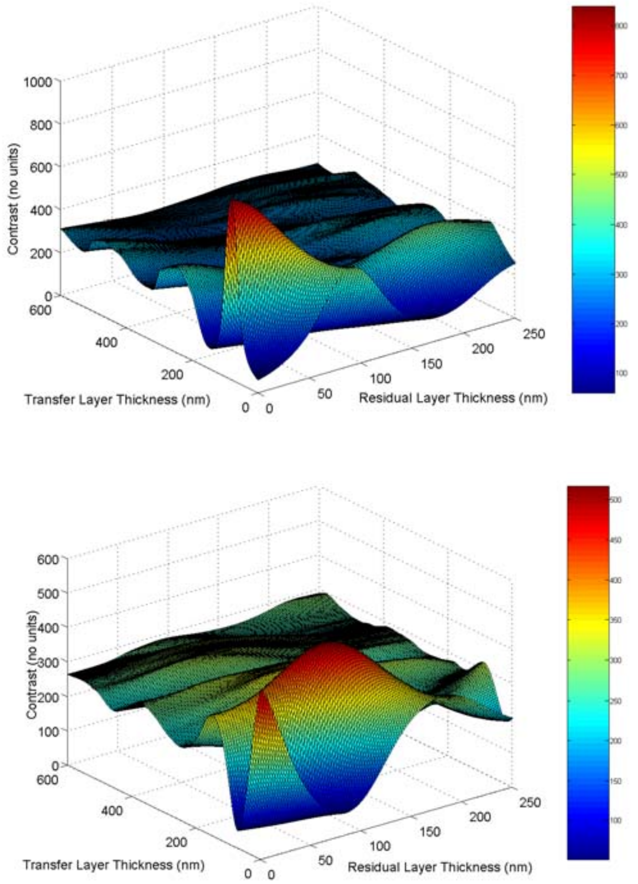

Figure 8.7. Contrast response curves for (a) $R_{feature}/R_{field}$, and (b) $R_{field}/R_{feature}$ for 100 nm feature step height.

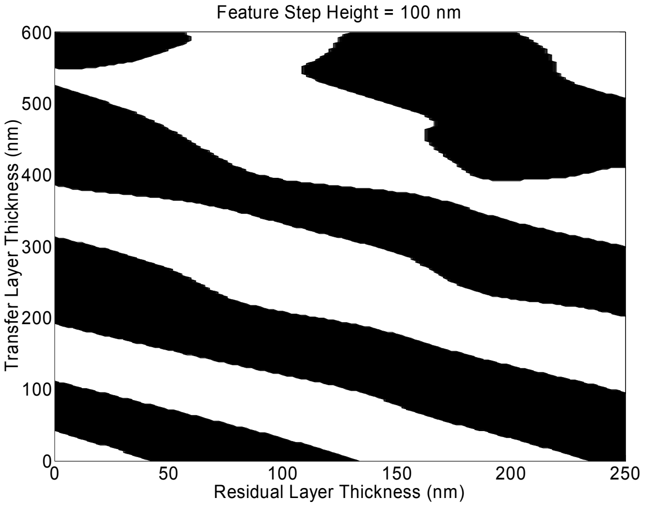

Figure 8.8. Image contrast plot for varying transfer layer and residual etch barrier layer thicknesses. The light regions represent parameter space where the field appears brighter than the feature, and conversely for the dark regions. The interfaces between light and dark regions represent those parameter sets where the intensities are equal.

Varying feature height affects image contrast as well, as shown in Figure 8.9. Feature height was allowed to vary from 30 nm to 250 nm. The size and location of regions of constant tone changes with increasing feature height, indicating a process window specific for each parameter set. Given, for example, a target feature step height of 100 nm, a target transfer layer thickness of 350 nm, and a residual layer thickness range of 50-150 nm accounting for all system compliance, the transfer layer thicknesses that result in constant tone are 270-290 nm, 365-375 nm, and 464-496 nm, as shown in Figure 8.10.

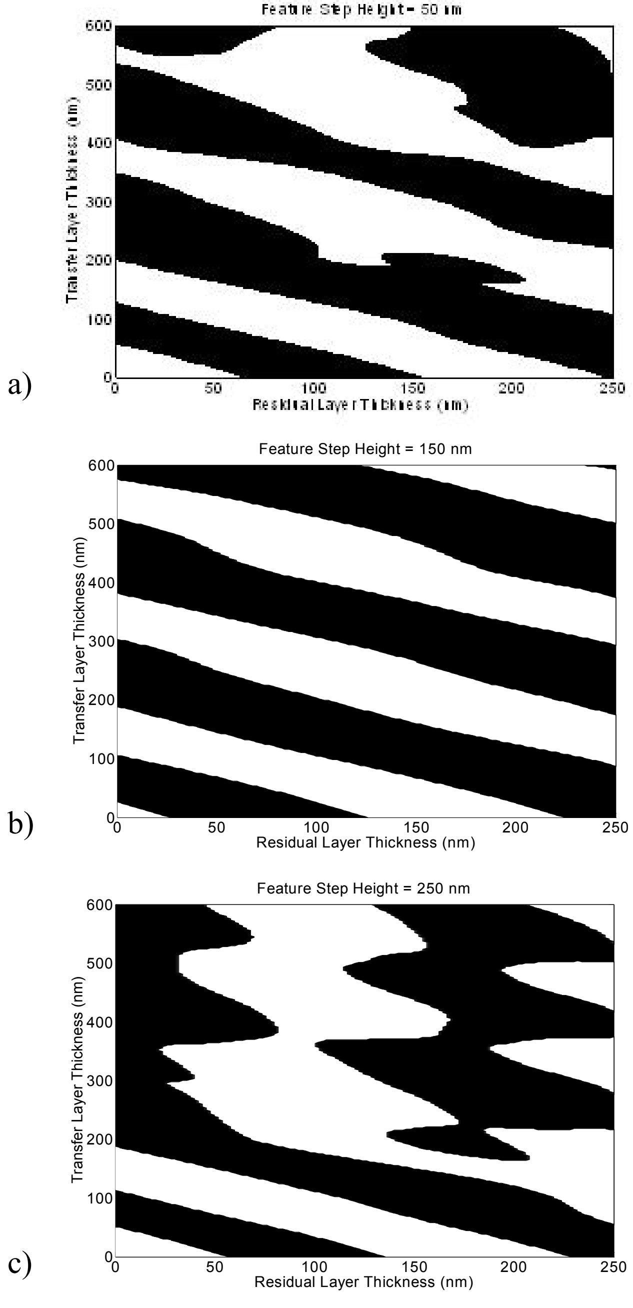

Figure 8.9. Tone plots as in Fuigure 8.8 with varying feature step height. The size and shape of constant-tone regions differs tremendously as feature step height increases from (a) 50 nm, (b) to 150 nm, and (c) to 250 nm.

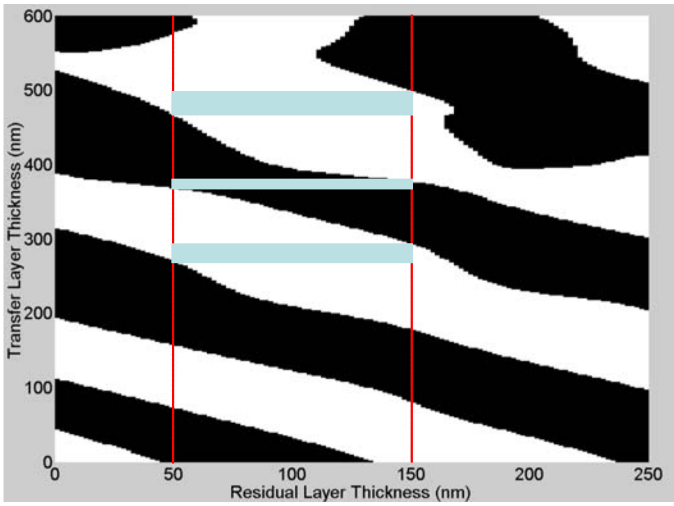

Figure 8.10. Process window for 100 nm feature step height, given a residual layer thickness range of 50 - 150 nm. The rectangular regions are the transfer layer thicknesses that would yield constant tone across the entire range of possible residual layer, thus most likely yielding the best parameter set for accurate defect detection.

These results allow one to design an imprint parameter set to yield the optimal contrast between the imprinted feature and the surrounding field. Enhancement of this contrast will likely yield more accurate defect inspection results. A more rigorous analysis is needed for studying the effect of film thickness variations on optical image contrast for features smaller than optical wavelengths, and for investigating the effect of specific pattern geometries.

8.5 CONCLUSIONS

Lithography by imprinting results in a thin residual layer of imprinted material underneath the desired imprinted pattern. This results in zero material contrast prior to subsequent etching steps, which has the potential to confound optical inspection for defects. For the case of bilayer imprint schemes, the thicknesses of both films impact the image contrast. Film thickness variations arising from imprint system compliance and other factors result in contrast variations across a patterned area. These contrast variations can lead to detection of false defects, or potentially to non-detection of real defects. The current modeling work has demonstrated that residual layer thickness variations can result in image tone reversal within a die, or across a wafer. This leads to the idea that the variability of residual layer thickness should be well characterized for a particular imprint system, and that the optical contrast window must be taken into account when specifying the underlying transfer layer thickness.

8.6 REFERENCES

1. Une, A., *et al.*, Microelectronic Eng., 2002. 61-62: p. 113.
2. Colburn, M., *et al.*, Solid State Technology, 2001. 46(7): p. 67.
3. Bailey, T., *et al.*, J. Vac. Sci. Tech. B, 2001. 19(6): p. 2806.

CONCLUSIONS

Chapter 9: Conclusions and Recommendations for Future Work

The process of making transparent imprint templates using an analogue of the traditional photomask production process flow yields imprint templates that possess most of the properties needed for the SFIL process. These templates are transparent, thereby allowing flood exposure through the template backside in order to allow photocuring of the etch barrier. They are also made of SiO_2, which is known to be a good substrate for the release layer described in Chapter 4. Using a Cr layer that is thinner than that used in photomask manufacture maintains these qualities, and also allows features to be written in the template at higher resolution. Replacing the Cr film with ITO and a film of deposited SiO_2 allows the final template to posses charge dissipation capabilities needed for end-of-line SEM inspection. The transparency of the ITO maintains the ability to expose the etch barrier through the template. Some properties of the final template change at different ITO film thicknesses, and so it may be necessary to design the final template stack around not just issues such as bulk transparency and conductivity, but to design the template in such a way as to maximize various responses. Further imprint template process development is taking place largely at Motorola Labs, but there may be some integration issues to be solved related to surface treatment compatibility with some of the template materials currently being considered.

The etch barrier imprinting fidelity was observed to be dependent on the acrylate functionality. Formulations tested that contained only methacrylate monomers did not polymerize without a significant amount of crosslinker. The amount of crosslinker required by the mixed formulations also boosted solution viscosity out range for use in the current fluid dispensing system. Imprinting performance was dramatically improved by replacing the silylated diacrylate with ethylene glycol diacrylate, which is much lower in molecular weight. This monomer provides the structural stability of the silylated crosslinker, but at a greatly reduced viscosity. There are likely many surfactants that can be added to the etch barrier to alter the interfacial properties at both the template/etch barrier interface and the etch barrier/transfer layer interface, including both reactive and non-reactive surfactants. One reactive surfactant was investigated as an etch barrier additive, and XPS depth profiling revealed that there is an enhanced concentration of F at the etch barrier/template interface. This suggests that the F species near the interface migrate preferentially to that surface. The F concentration deep in the film is non-zero, and it remains to be seen how the potential existence of F at the transfer layer/etch barrier interface affects the overall separation performance. Further work around these types of reactive surfactants, and other non-reactive surfactants may result in improved interfacial properties.

Based on a literature review of the field, the final quality of films derived from functional alkylsilanes on SiO_2 is dependent on a variety of factors, including substrate preparation conditions that impact hydroxyl density, degree of hydration, and surface cleanliness. The type and number of silane functionalities also contribute to film quality, as does reaction temperature, reaction time, and annealing conditions. The reaction of FOTS on fused silica imprint templates yielded films of modest durability, and a steady decrease in F species on the template was observed with increasing numbers of imprints. Imprinting with an FOTS-treated ITO template revealed a potentially severe lack of imprinting durability. Methanol TPD from ITO confirmed the existence of hydroxyl groups on the ITO surface, and suggests that H_2O may be less strongly bound to the surface hydroxyl groups. More work is needed in order to quantify the surface hydroxyl coverage on ITO, and also to determine the adsorption and desorption kinetics of water on ITO. The FOTS-treatment of Si_3N_4 and SiO_xN_y films demonstrated at least modest compatibility and film durability. XPS analysis revealed a lower F concentration on the Si_3N_4 substrate, which may indicate lower film density perhaps arising from a decreased hydroxyl concentration relative to the O-rich films; the FOTS film on SiO_xN_y was comparable in XPS signal to that on SiO_2. Preliminary tests of FOTS film durability on these films revealed an equivalent loss of F after solvent rinse and buffing treatments as compared to SiO_2, which suggests that they may possess a similar level of imprinting durability. The desorption of multilayer and adsorbed water from SiO_2 was modeled in order to determine the baking conditions necessary to dehydrate a SiO_2 template without significant dehydroxylation. These model results were used in rehydration experiments in which water was exposed to the SiO_2 surface for various times, followed by reaction of FOTS. It was determined that the SAM film coverage increases monotonically with increasing water exposure to some asymptotic value, as measured by water contact angle and F 1s XPS. Future work should include an investigation of the effect of various annealing conditions on film mechanical wear resistance. A combined parameter space evaluation needs to be undertaken to determine the optimal conditions in the hydration/reaction/anneal space that yields high-quality, dense films with extended wear resistance. Additionally, a comparison of film qualities for films derived from fluorinated and hydrogenated alkylsilanes may reveal differences in film durability, resulting from the different networking efficiencies.

Automated inspection of two sets of wafers generally revealed an inexplicable rise in the defect density over time, and the precise cause of these defects is not yet known. The Array mode inspection is known to detect pattern defects induced during the template manufacturing process. This behavior would result in a baseline defect density which should be insensitive to process conditions and SFIL materials. A thorough investigation of the cause of the increasing defect density is required, but initial investigation and hypotheses suggests that the dominant defect modes are predominantly caused not by the imprint nature of the SFIL process, but by the materials used in the process. A thorough analysis of such issues as etch barrier shelf life, mixture homogeneity, and even etch barrier/transfer layer and etch barrier/release layer interactions is necessary, and will likely lead to vastly improved performance.

One new etch barrier formulation was tested that possessed a greater Young's modulus, stress- and elongation-to-break than a formulation similar to the one used in the sefect study described in this chapter. This new formulation was used in an imprinting experiment, and SEM inspection revealed no loss of imprint fidelity through 440 imprints. A defect inspection experiment similar to that used to gain the statistical data using the A4 etch barrier remains to be done with the new formulation, but the SEM images from the new formulation are very promising.

APPENDICES

Appendix A: Thin Film Interference Modeling

GOVERNING EQUATIONS

Given indices of refraction at an interface, Snell's Law can be used to calculate the angle of refraction for the light transmitted through that interface:[1]

Equation A.1
$$N_1 \sin\theta_1 = N_2 \sin\theta_2$$

where N_1 is the complex index of refraction of the incident medium given by n_1+ik_1, etc., and θ_1 and θ_2 are the angles of incidence and transmission at the interface, respectively. Following the method of Macleod,[2] if the complex indices of refraction N are known for a stack of thin films, the absorption (A), transmission (T), and reflection (R) coefficients can be calculated for a stack of thin films:

Equation A.2
$$A = \frac{4\eta_0 \operatorname{Re}(B\overline{C} - \eta_m)}{(\eta_0 B + C)\overline{(\eta_0 B + C)}}$$

Equation A.3
$$T = \frac{4\eta_0 \operatorname{Re}(\eta_m)}{(\eta_0 B + C)\overline{(\eta_0 B + C)}}$$

Equation A.4
$$R = \frac{(\eta_0 B - C)\overline{(\eta_0 B - C)}}{(\eta_0 B + C)\overline{(\eta_0 B + C)}}$$

where η_0 and η_m are the optical admittance of free space and the substrate, given by:

Equation A.5 $$\eta_s = Y_0 N \cos\theta \qquad \text{for } s\text{-polarization}$$

Equation A.6 $$\eta_p = \frac{Y_0 N}{\cos\theta} \qquad \text{for } p\text{-polarization}$$

Y_0 is the optical admittance of free space ($\sqrt{\varepsilon_0 / \mu_0}$), and η_s and η_p are equal for light at normal incidence. Re(~) denotes the real part of the quantity in parentheses, $\overline{(\sim)}$ is the complex conjugate of (~), etc., and B and C are elements of the characteristic matrix of the film stack calculated using Equation A.7:

Equation A.7 $$\begin{bmatrix} B \\ C \end{bmatrix} = \left(\prod_{r=1}^{q} \begin{bmatrix} \cos\delta_r & (i \sin\delta_r)/\eta_r \\ i\eta_r \sin\delta_r & \cos\delta_r \end{bmatrix} \right) \begin{bmatrix} 1 \\ \eta_m \end{bmatrix}$$

where $r = 1$ is the topmost layer and $r = q$ is the film nearest the substrate. The term δ_r is film phase factor given by:

Equation A.8 $$\delta_r = \frac{2\pi N_r d_r \cos\theta_r}{\lambda}$$

where d_r is the film thickness, θ_r is the angle of transmission through the film, and λ is the wavelength in the incident medium.

EXAMPLE MATLAB CODE

The file Leica_VB6_780 calculates the coefficients A, R, and T for a 780 nm laser at 75° incident angle on the surface of an ITO template stack. The template consists of e-beam resist (NEB22 in this case), PECVD SiO_2, and ITO on a fused silica substrate.

<u>Leica_VB6_780.m</u>

```
global Y0
eps_0 = 8.854187817 * 1e-12;
mu_0 = 4 * pi * 1e-7;
Y0 = sqrt(eps_0/mu_0); % admittance of free space

% read in all pertinent data

lambda = 780;
Theta = 75 * pi / 180; % incident angle from normal

% read in film data. These data files are
     [lambda,index,extinction]
quartz = dlmread('quartz index 365 780.txt',' ');
N_qz = quartz(2,2:3);
air = dlmread('air index 365 780.txt',' ');
N_air = air(2,2:3);
ITO = dlmread('ITO index 365 780.txt',' ');
N_ITO = ITO(2,2:3);
t_ITO = 50:300; % thickness in nm
[dummy sizethickness] = size(t_ITO);
SiO2 = dlmread('PECVD SiO2 index 365 780.txt',' ');
```

```
N_SiO2 = SiO2(2,2:3);
t_SiO2 = 100;
ZEP520 = dlmread('ZEP520 index 365 780.txt',' ');
N_ZEP520 = ZEP520(2,2:3);
t_ZEP520 = 180;
NEB22 = dlmread('NEB22 index 365 780.txt',' ');
N_NEB22 = NEB22(2,2:3);
t_NEB22 = 180;

% set up index matrix
N = [N_air ; N_NEB22 ; N_SiO2 ; N_ITO ; N_qz];
N = N(:,1) - i * N(:,2); % set up complex indices

%Invoke Snell's Law
theta = zeros(length(N),1);
theta(1) = Theta;
for m0 = 1:length(N)-1
    theta(m0+1) = asin((N(m0)/N(m0+1)) *
     sin(theta(m0)));
end

thickness = zeros(5,sizethickness);
thickness(1,:) = 0;
thickness(2,:) = t_NEB22;
thickness(3,:) = t_SiO2;
thickness(4,:) = t_ITO;
thickness(5,:) = 0;

data = SFILcalc(lambda,N,thickness,theta);
```

```
subplot(1,2,1)

plot(thickness(4,:),data(1,:),'-r')

hold

plot(thickness(4,:),data(2,:),'-.b')

plot(thickness(4,:),data(3,:),':g')

plot(thickness(4,:),data(1,:)+data(2,:)+data(3,:),'-
     k')

legend('T','R','A','Sum',0)

xlabel('ITO thickness (nm)','FontSize',14)

ylabel('Response','FontSize',14)

Title('S-polarization','FontSize',14)

axis([50 300 0 1])

set(gca,'FontSize',14)

hold


subplot(1,2,2)

plot(thickness(4,:),data(4,:),'-r')

hold

plot(thickness(4,:),data(5,:),'-.b')

plot(thickness(4,:),data(6,:),':g')

plot(thickness(4,:),data(4,:)+data(5,:)+data(6,:),'-
     k')

legend('T','R','A','Sum',0)

xlabel('ITO thickness (nm)','FontSize',14)

ylabel('Response','FontSize',14)

Title('P-polarization','FontSize',14)

axis([50 300 0 1])

set(gca,'FontSize',14)

hold
```

SFILCalc.m

```
function data = SFILcalc(lambda,n,thickness,theta)
global Y0
layers = length(n);
sizethickness = length(thickness);
for m1 = 1:sizethickness
    c_s = eye(2,2);
    c_p = eye(2,2);
    for m2 = 2:layers-1
        H_s = eta_s(n(m2),theta(m2));
        H_p = eta_p(n(m2),theta(m2));
        a_s =
     phase(lambda,n(m2),H_s,thickness(m2,m1),theta(m2)
     );
        a_p =
     phase(lambda,n(m2),H_p,thickness(m2,m1),theta(m2)
     );
        c_s = c_s * a_s;
        c_p = c_p * a_p;
    end
    b_s = [1;eta_s(n(end),theta(end))];
    b_p = [1;eta_p(n(end),theta(end))];
    E_s =  c_s * b_s;
    E_p =  c_p * b_p;
    B_s(m1) = E_s(1);
    B_p(m1) = E_p(1);
    C_s(m1) = E_s(2);
    C_p(m1) = E_p(2);
T_s(m1) = (4 .* eta_s(n(1),theta(1)) .*
     real(eta_s(n(end),theta(end)))) ./ ...
```

```
    ((eta_s(n(1),theta(1)).* B_s(m1) + C_s(m1)) .*
     conj(eta_s(n(1),theta(1)).* B_s(m1) + C_s(m1)));
R_s(m1) = ((eta_s(n(1),theta(1))*B_s(m1) - C_s(m1)) *
     conj(eta_s(n(1),theta(1))*B_s(m1) - C_s(m1))) ./
     ...
    ((eta_s(n(1),theta(1)).* B_s(m1) + C_s(m1)) .*
     conj(eta_s(n(1),theta(1)).*B_s(m1) + C_s(m1)));
A_s(m1) = (4 * eta_s(n(1),theta(1)) * real(B_s(m1) *
     conj(C_s(m1)) - eta_s(n(end),theta(end)))) / ...
    ((eta_s(n(1),theta(1)).* B_s(m1) + C_s(m1)) .*
     conj(eta_s(n(1),theta(1)).*B_s(m1) + C_s(m1)));
T_p(m1) = (4 .* eta_p(n(1),theta(1)) .*
     real(eta_p(n(end),theta(end)))) ./ ...
    ((eta_p(n(1),theta(1)).* B_p(m1) + C_p(m1)) .*
     conj(eta_p(n(1),theta(1)).* B_p(m1) + C_p(m1)));
R_p(m1) = ((eta_p(n(1),theta(1))*B_p(m1) - C_p(m1)) *
     conj(eta_p(n(1),theta(1))*B_p(m1) - C_p(m1))) ./
     ...
    ((eta_p(n(1),theta(1)).* B_p(m1) + C_p(m1)) .*
     conj(eta_p(n(1),theta(1)).* B_p(m1) + C_p(m1)));
A_p(m1) = (4 * eta_p(n(1),theta(1)) * real(B_p(m1) *
     conj(C_p(m1)) - eta_p(n(end),theta(end)))) / ...
    ((eta_p(n(1),theta(1)).* B_p(m1) + C_p(m1)) .*
     conj(eta_p(n(1),theta(1)).*B_p(m1) + C_p(m1)));
end
data = [T_s ; R_s ; A_s ; T_p ; R_p ; A_p];
```

index.m

```
function N = index(n)
N = n(1) - i * n(2);
```

phase`.m`

```
function [a] = phase(lambda,N,H,thickness,theta)
beta = 2*pi* (thickness/lambda) .* N .* cos(theta) ;
a = [ cos(beta) , i*sin(beta)/H ; ...
      i*H*sin(beta) , cos(beta) ];
```

eta_p.m

```
function H = eta_p(N,theta)
global Y0
H = Y0 .* N ./ cos(theta);
```

eta_s.m

```
function H = eta_s(N,theta)
global Y0
H = Y0 .* N .* cos(theta);
```

beta.m

```
function [b] = beta(lambda,N,thickness,theta)
b = 2*pi* (thickness/lambda).* N .* cos(theta);
```

REFERENCES

1. Serway, R.A., Physics for Scientists and Engineers. 3rd ed. 1990, Philadelphia: Saunders College Publishing.

2. Macleod, H.A., Thin-Film Optical Filters. 2nd Ed. ed. 1989, New York: McGraw-Hill.

Appendix B: Surface Treatment Apparatus

INTRODUCTION

The surface treatment chamber described in this Manual was designed with two concepts in mind: Facile experimentation with little user input, which was intended to ensure run-to-run consistency, and ease of use for various operators. The system was constructed to handle imprint templates and other samples of 1-in by 1-in by ¼-in and smaller. LabVIEW software was used for the control system and graphical user interface. This Manual is comprised of various flowcharts, LabVIEW excerpts, and equipment diagrams with appropriate explanations to aid further equipment development and repair, and an operating guide for the average user in the Appendix.

A picture of the machine is shown in Figure B.1; not shown are the roughing pump and the recirculating chiller, which reside in the maintenance chase. The general operating guidelines are given in the file "`Operating Instructions for the SFIL Surface Treatment Chamber.doc`" on the Windows desktop, and the control program can be executed by double-clicking on the "`FSAMSuto.vi`" icon also on the desktop.

Figure B.1: Picture of the surface treatment chamber and control computer (left), and the Jelight UVO42 UV-Ozone cleaner (right), both of which reside in the MER South cleanroom.

DESCRIPTION OF APPARATUS

A diagram of the equipment is given in Figure B.2. The NI 6025E data acquisition card is installed in a PCI slot in the Gateway computer, and has 100 pin output. The NI R1005050 ribbon cable routs pins 1-50 to jack J1 on the NI SC-2051 cable adapter, and pins 51-100 to the CB-50LP terminal block connector. Digital I/O Ports A and B on the SC-2051 cable adapter are connected via NI NB7 ribbon cables to two ER-8 relay pods for solenoid control and chamber heater control, respectively.

The power supplied to the ER-8 pod through Port A of the SC2051 from the 6025E card is sufficient for switching all relays. The maximum rated switching current for each relay is 3A at 250 VAC, and the maximum working voltage is 250 Vrms [ref]. Each MS-SOL-2K-BN solenoid valve requires 4.2 VA power for switching and 3.0 VA for holding state [ref]. The maximum current draw for switching on the ER-8 pod attached to Port A is:

$$(5\ \text{solenoids}) * (4.2\ \text{VA/solenoid}) / (110\ \text{V}) = 0.19\ \text{A}$$

which is well below the maximum rated switching current. The maximum current draw for holding all five solenoids open is slightly less. The SOL-2K-BN solenoid valves operate at 110 VAC, which is within the specified range of the ER-8. The solenoid valves control flow of house clean dry air (CDA) at an upstream pressure of 80 psig, which is below the maximum solenoid operating pressure of 100 psig. The SS-BNVCR4-C valves are actuated at 45 psig to 120 psig, and so the 60 psig supplied is sufficient for actuation. The system has been built so that all valves will fail closed. The SS-BNVCR4-C valves are set in the "Normally Closed" position, and the power to the SOL-2K-BN solenoids is routed through the COM ("common") and NO ("normally open") terminals on the ER-8 relay pod. The SS-BNVCR4-C valves are rated to a maximum pressure of 125 psig for "Normally Closed" configuration, and the N_2 supply regulator for process inert gas has been set to 40 psig.

The Omega CSH-102150/120 cartridge heaters attached to the ER-8 pod through Port B draw ~0.45 A, which is well within the operating specifications of the ER-8 relay pod. The system has been built so that the heaters will fail off. The power to the cartridge heaters is routed through the COM ("common") and NO ("normally open") terminals on the ER-8 relay pod.

110 V wall supply is routed through both ER-8 relay pods to the solenoids and heaters via a wiring block enclosed in an aluminum box, which is grounded to the equipment chassis.

An Omega type K thermocouple is connected to ACH0 and ACH8 on the NI CB-50LP wiring block, and provides the temperature of the chamber interior surface closest to the sample. This is not, of course, actual sample surface temperature, but there is an offset that can be estimated through simple heat transfer calculations.

The MKS 1479A12CR1BM mass flow controller and the MKS 640A13TW1M12D electronic pressure controller are connected to “F” cards installed in the MKS type 146 controller, which in turn is connected to the Gateway computer via RS232 connections. The control algorithm is set to closed loop operation within the 146 controller. This means that the LabVIEW code needs only to address the appropriate channel in the 146 and provide the setpoint for either unit. Additionally, the 146 can be queried to determine the state of each unit. Vacuum is provided by an Edwards-18 mechanical pump.

The substrate cooling was installed both to allow sub-ambient processing, and also to serve as a thermal sink to help stabilize chamber temperature. The sub-chamber cooling unit was constructed with flow channels to allow efficient heat transfer. Cooling is achieved via flow supply from a VWR model 1166 recirculating chiller loaded with 25% Polyscience HC-50 heat transfer fluid in deionized water. The addition of HC-50 depresses the freezing point of the cooling fluid, allowing sub-0 °C temperatures.

The precursor bubbler was fabricated by Bob Lewandowski of the UT Department of Chemistry and Biochemistry glassblowing shop, and includes stopcocks to seal the bubbler during handling, and a sparger to aid in bubbling activity. The bubbler must be loaded in a dry environment such as a dry box, but the precursor usage is relatively slow due to its low vapor pressure. There is a large head space in the bubbling chamber that was designed to dissipate the foaming observed during bubbling. Failure to include this head space resulted in loss of liquid precursor into the downstream flow lines.

Sample precleaning is achieved via acetone ultrasonic bath, followed by exposure to UV light and ozone in the Jelight UVO-42 UV-ozone cleaner. The UVO-42 has been outfitted with an exhaust blower assembly and ozone-quenching catalyst unit.

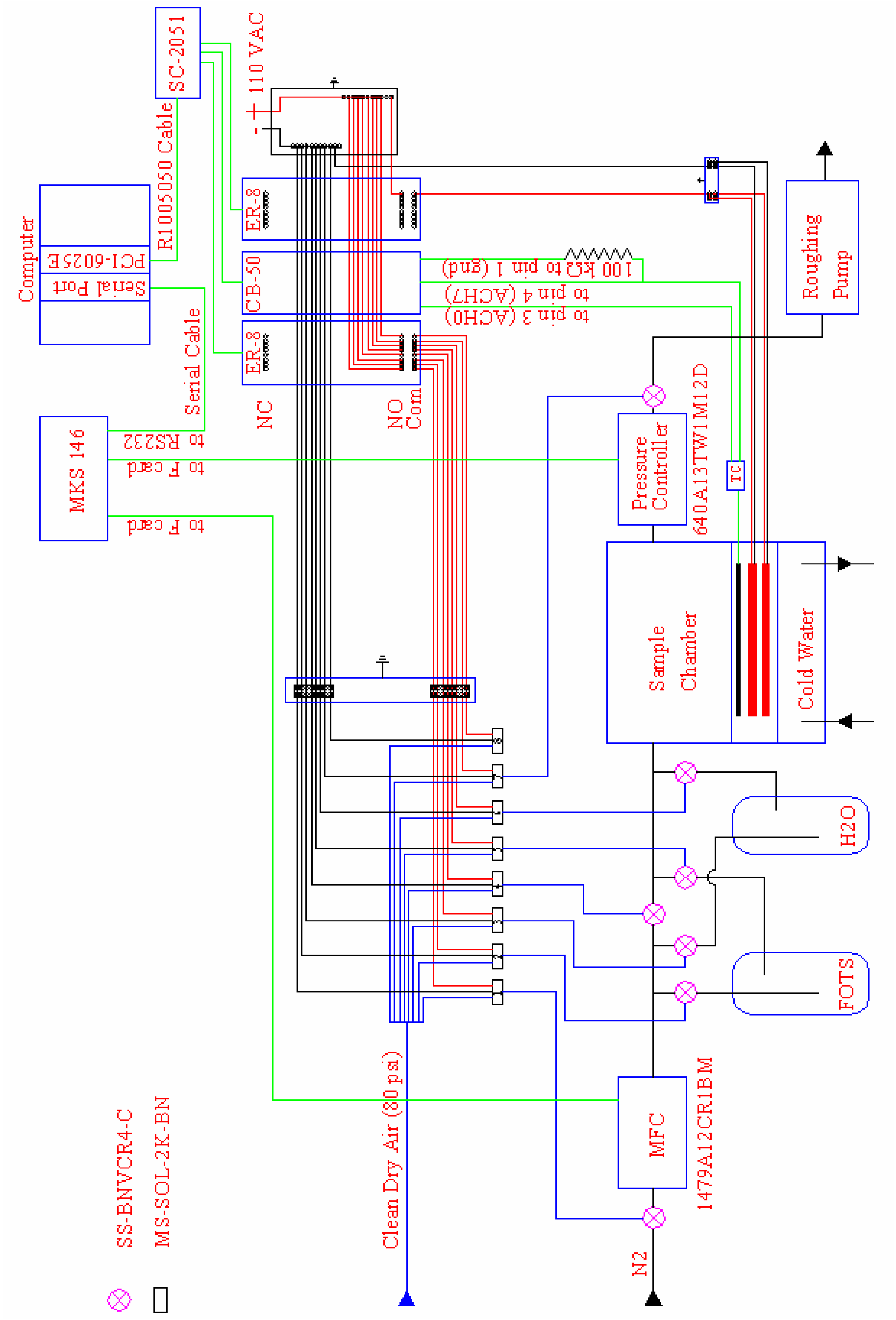

Figure B.2: Diagram of surface treatment apparatus.

FLOWCHARTS AND LABVIEW DIAGRAMS

There are two LabVIEW programs for use with this machine. The `FSAM_Manual.vi` program is designed for more manual operation, allowing equipment troubleshooting and more flexible program control. The `FSAMAuto.vi` uses the same communication sub-VIs as the `Manual` program, but the reaction steps are arranged in an automatic sequence. The user interfaces for Manual and Auto programs are shown in Figure B.3 and Figure B.4. Valves in operation are shown with a bright green indicator and valves not in operation with a dull red indicator; lines in use are bright green and dull green otherwise. The chamber cartridge heaters are shown as dark blue indicators when off, and bright red indicators when on, and the thermocouple temperature, MFC flowrate, and chamber pressure are also given in the appropriate places in the schematic. There are various System Indicators, conveying to the user the current state of the system, such as the current step in the process, various setpoints, miscellaneous replies from the 146 unit, and elapsed reaction and anneal times.

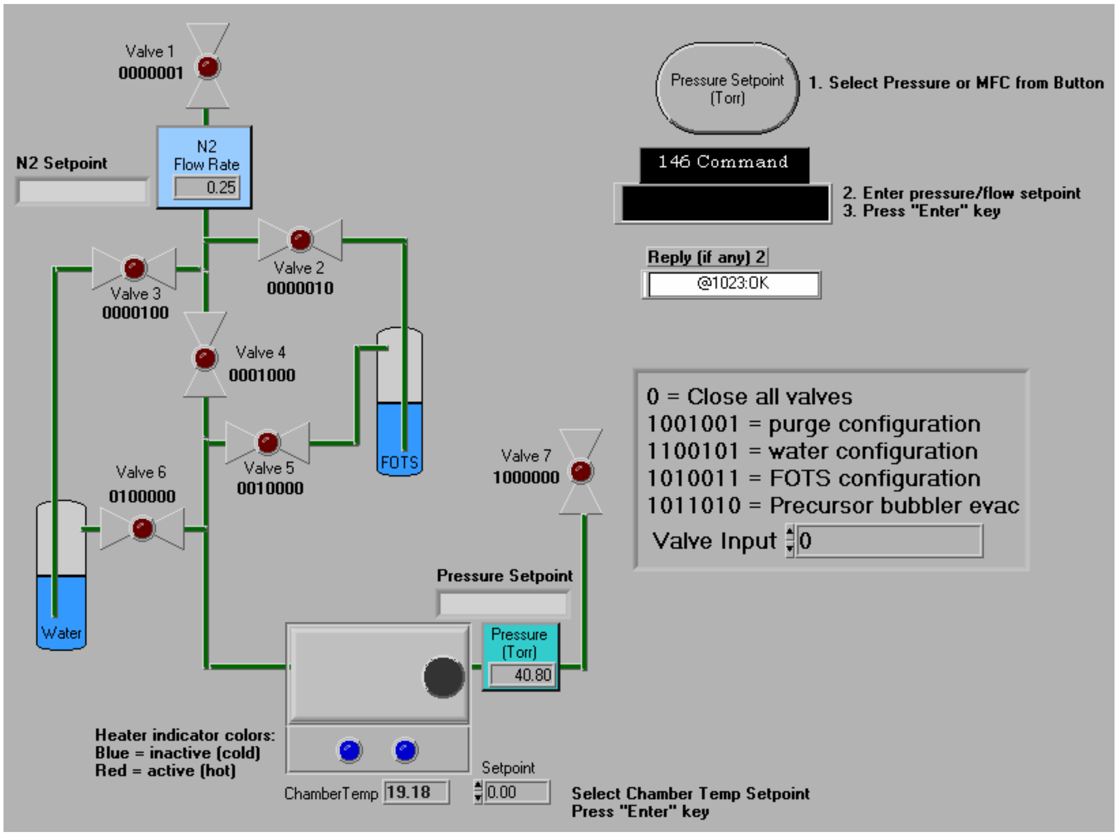

N2 Setpoint

N2 Flow Rate 0.25

1. Select Pressure or MFC from Button
2. Enter pressure/flow setpoint
3. Press "Enter" key

Reply (if any) 2 @1023:0K

0 = Close all valves
1001001 = purge configuration
1100101 = water configuration
1010011 = FOTS configuration
1011010 = Precursor bubbler evac

Valve Input 0

Pressure Setpoint

Pressure (Torr) 40.80

ChamberTemp 19.18

Setpoint 0.00

Select Chamber Temp Setpoint
Press "Enter" key

Figure B.3: User interface for the `FSAM_Manual.vi` program.

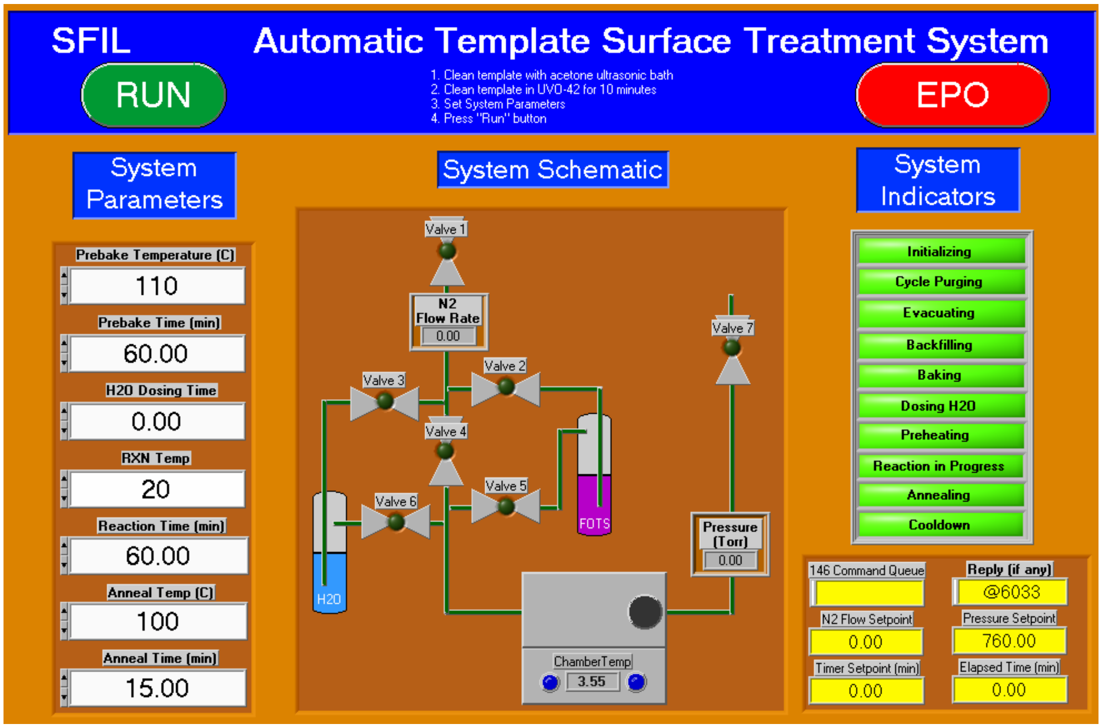
SFIL Automatic Template Surface Treatment System

1. Clean template with acetone ultrasonic bath
2. Clean template in UVO-42 for 10 minutes
3. Set System Parameters
4. Press "Run" button

Prebake Temperature (C): 110
Prebake Time (min): 60.00
H20 Dosing Time: 0.00
RXN Temp: 20
Reaction Time (min): 60.00
Anneal Temp (C): 100
Anneal Time (min): 15.00

N2 Flow Rate: 0.00
Pressure (Torr): 0.00
ChamberTemp: 3.55

146 Command Queue:
Reply (if any): @6033
N2 Flow Setpoint: 0.00
Pressure Setpoint: 760.00
Timer Setpoint (min): 0.00
Elapsed Time (min): 0.00

Figure B.4: User interface for the `FSAM_Auto.vi` program.

The Manual program is divided into a few sections. In parallel are various processes for reading from and writing to the units attached to the 146 controller, and sub-VIs that operate the ER-8 relays and calculate chamber temperature. There are also windows that read user-defined values into the program, and optionally write system data to a data file. These are described below.

Figure B.5 shows the LabVIEW code for the initialization routine, which executes once when the program is run. This initializes the various communication channels from the computer to the equipment, and defines local variables. The routine for writing data to a data file is shown in Figure B.6, where the user has the option when the program is started whether or not to record a data file. If recording a data file is selected, the first step in the sequence (not shown) writes text column headings to the designated file, and then the second step opens the file again to append the data; this second step requires the user to select the same filename as was designated for writing the column headings.

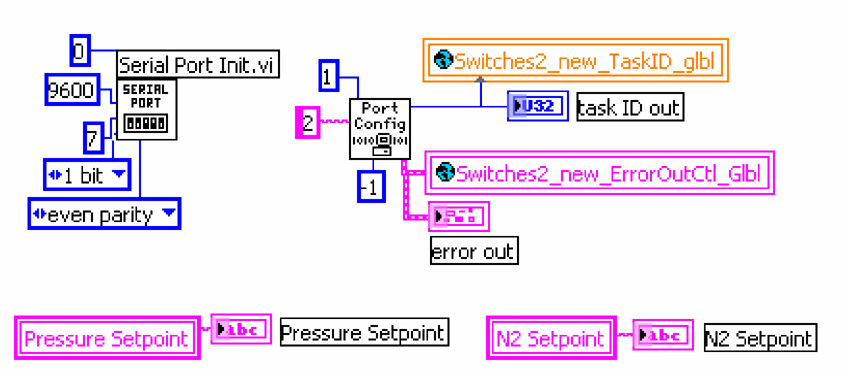

Figure B.5: Initialization routine at start of program.

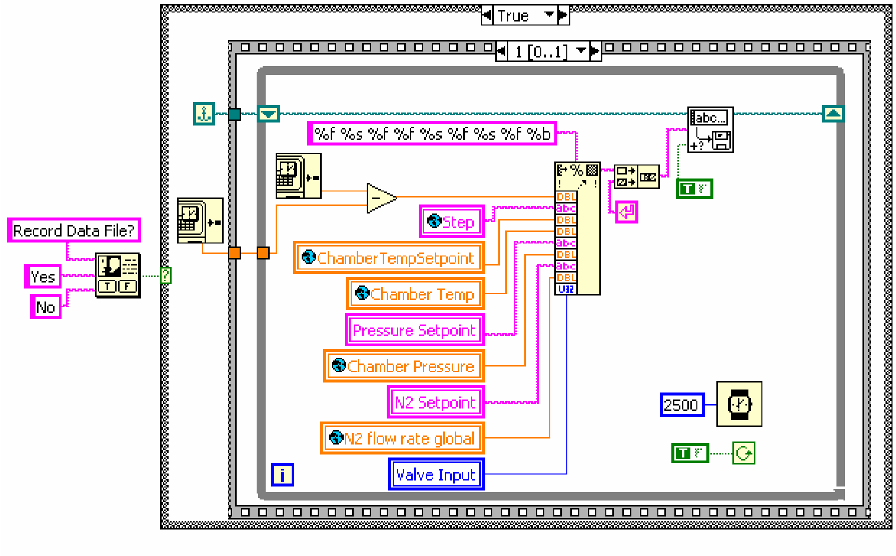

Figure B.6: Data file routine.

Several subVIs are called by the program to calculate chamber temperature, operate the heaters, and change output to the valve solenoids based on user input, as shown in Figure B.7. Also included in this `while` loop are the Boolean operators for displaying the flow line states. The diagrams for the three subVIs are shown in Figures B.8 – B.10.

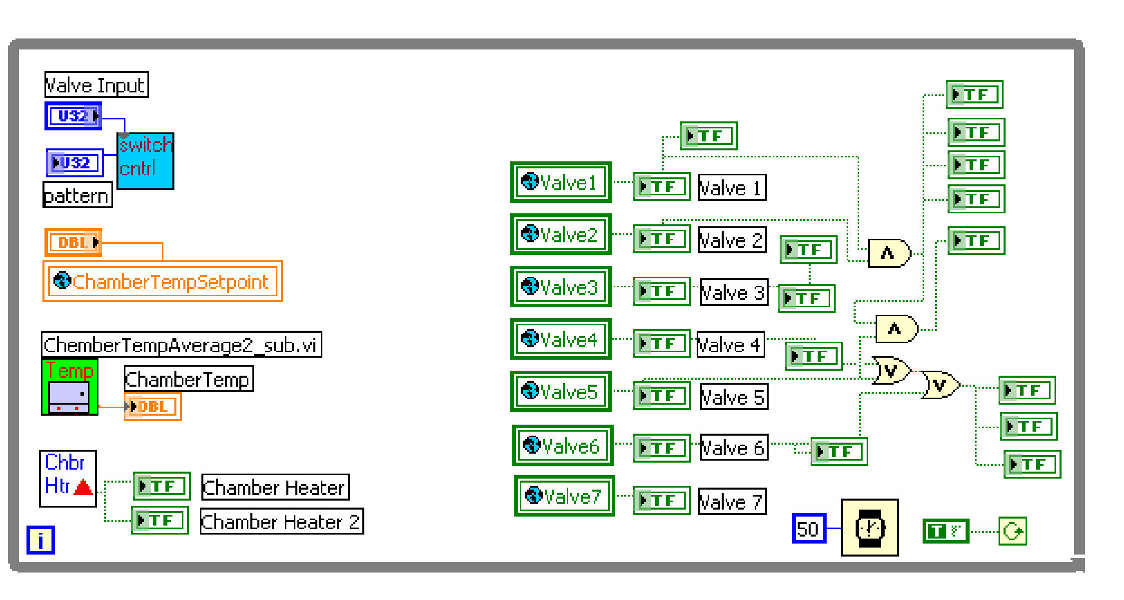

Figure B.7: Various subVIs called by this program (left side), and the Boolean operations used for the flow line indicators (right).

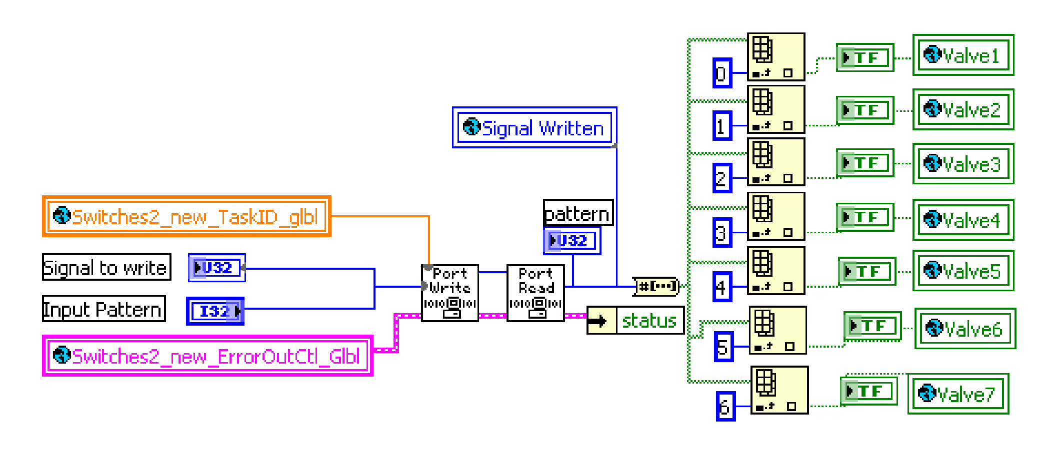

Figure B.8: Program diagram for `Switches3.vi`, labeled as "switch control" in Figure B.7.

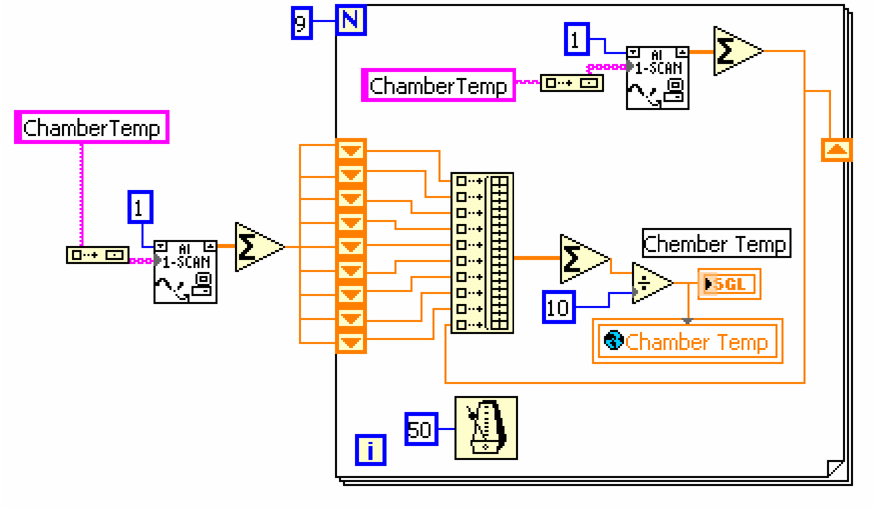

Figure B.9: Program diagram for `ChamberTempAverage2_sub.vi`.

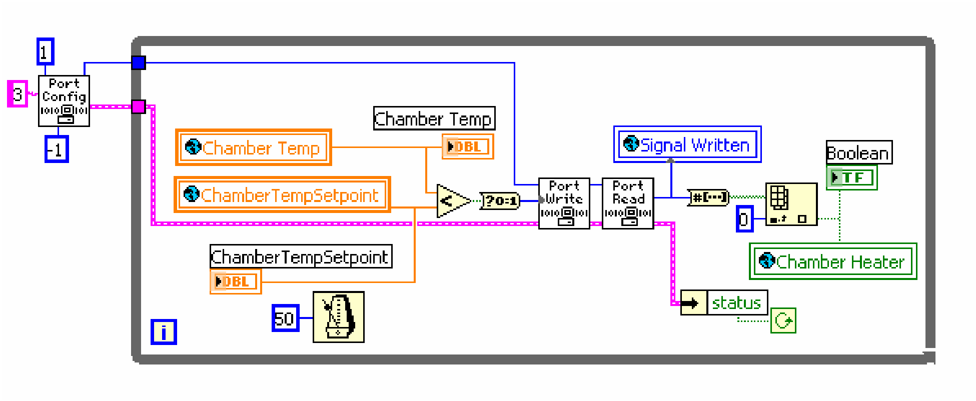

Figure B.10: Program diagram for `ChmbrHtr_sub.vi`.

The `while` loop that governs communication with the MKS Type 146 controller is shown in Figure B.11. The loop can be divided into three sections: The upper left sequence loops through pinging the pressure and MFC channels for states (pressure and flowrate), and then writes any queued commands to the 146 unit. The upper right sequence reads the response from the 146 ping in reverse order one character at a time for the appropriate number of characters, and then flushes the 146 buffer. It is important to note that this sequence may take up to 1000 ms to complete, and for that reason any consecutive 146 commands sent from other `while` loops must be delayed by at least 1000 ms. Failure to delay the commands may result in lost commands. The bottom section reverses the order of the 146 response, and scans for a pattern that would identify the response as a flowrate, pressure, or other response, and writes those values to the appropriate global or local variables.

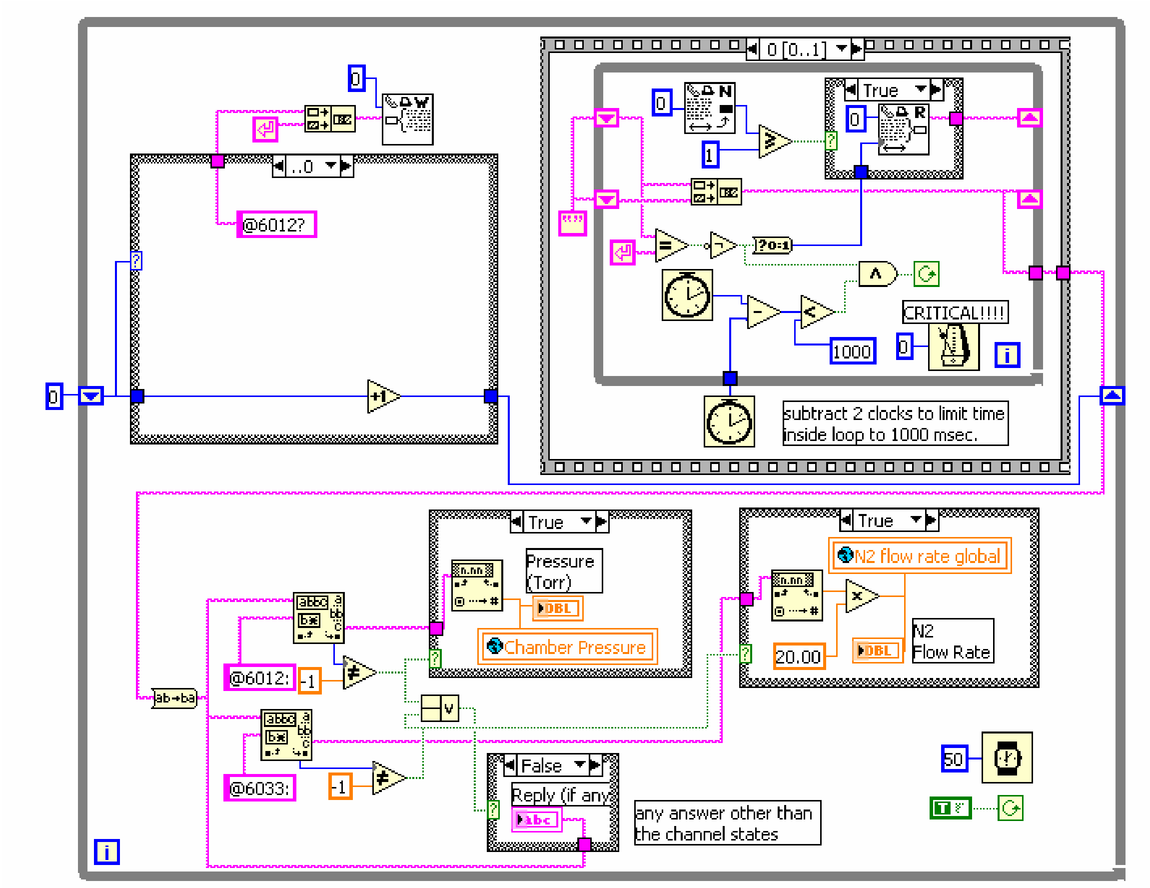

Figure B.11: Communication with the MKS Type 146 controller is achieved with this `while` loop.

The Auto program uses these same subVIs and while loops to operate the surface treatment system, but does so in a automated, sequential manner. The flowchart for this process is shown in Figure B.12.

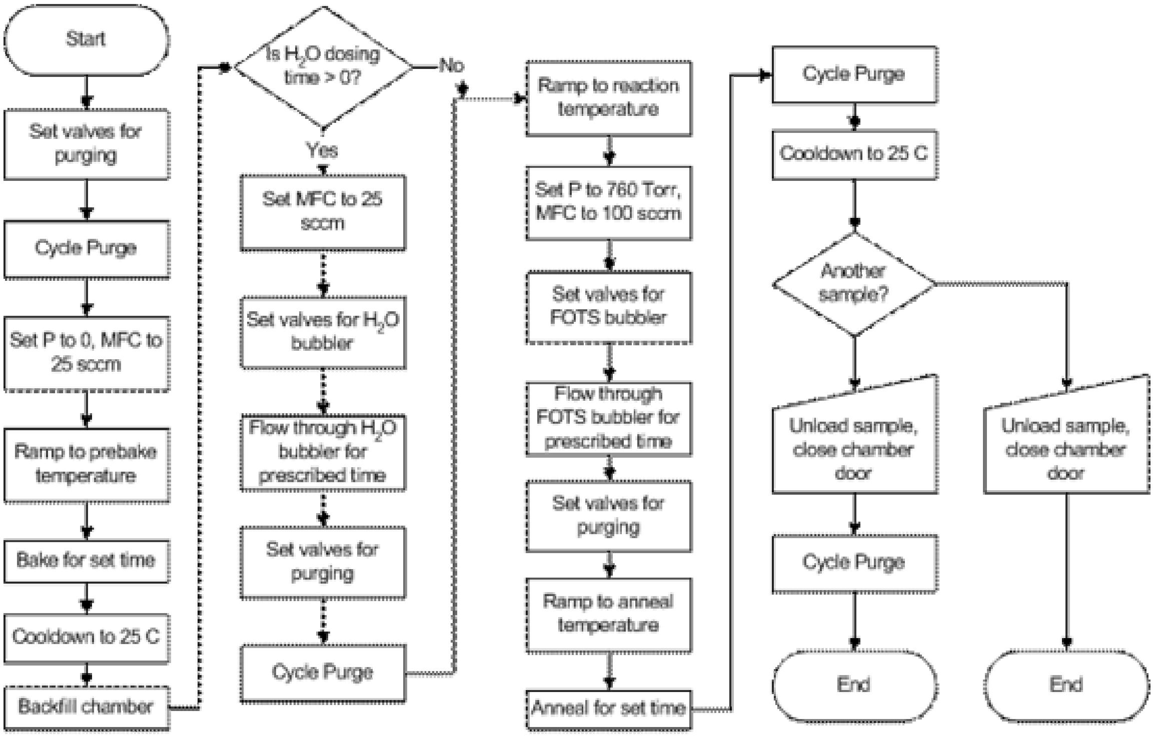

Figure B.12: Flowchart describing the `FSAMAuto.vi main` operating sequence

Appendix C: Evaluation of Methods for Determining Solid Surface Energy from Contact Angle Measurements

INTRODUCTION

Thomas Young, in 1805, described verbally the relation to the angle of contact of a liquid drop on a solid surface to the surface energies of the liquid, solid, and interface.[1] This idea was later expressed in equation form by Bangham and Razouk:[2]

Equation C.1 $$\gamma_{lv}\cos\theta + \gamma_{sl} = \gamma_{sv}$$

where γ_{lv}, γ_{sv}, and γ_{sl} are the free energies of the liquid and solid surfaces, and the solid-liquid interface, respectively, and θ is the contact angle. They noted that for an equilibrium contact angle, the solid surface is in equilibrium with the vapor of the liquid, which gives rise to the $_{SV}$ subscript. Figure C.1 shows schematically this force balance.

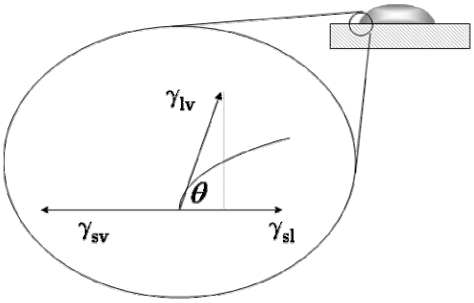

Figure C.1: Force balance diagram for Equation C.1.

Adding γ_{lv} to both sides of Equation C.1 and rearranging gives:

Equation C.2 $$\gamma_{lv}(1+\cos\theta) = \gamma_{sv} + \gamma_{lv} - \gamma_{sl}$$

The left side of the equation has been termed the reversible work of adhesion, $W = \gamma_{lv}(1+\cos\theta)$, and the right side yields the hypothetical separation of the drop, retaining its shape, from the solid surface:[2]

Equation C.3 $$W = \gamma_{sv} + \gamma_{lv} - \gamma_{sl}$$

where the liquid-solid interface is destroyed in the contact area, and new solid-vapor and liquid-vapor interfaces are created in its place. It is noted that this expression for W is defined such that after separation there remains on the solid surface an adsorbed layer in equilibrium with the vapor of the liquid. Combining Equations C.2 and C.3 yields:

Equation C.4 $$W = \gamma_{lv}\left(1+\cos\theta\right)$$

THE ZISMAN PLOT

Fox and Zisman noticed in their studies of contact angles on poly(tetrafluoroethlylene) (PTFE) that a plot of cos θ vs. probe liquid γ_{lv} produced a linear correlation for a series of homologous liquids.[3] The intercept of the line at cos θ = 1 gave "the surface tension of the liquid that would just spread on TFE," and was defined as the "critical surface tension," γ_c, of the solid. Strictly speaking, this critical surface tension is related to the interaction of the probe liquid with a given solid surface, and is not a measure of the solid surface energy. An example of this correlation is shown in Figure C.2, which is a plot of cos θ vs. γ_{lv} for a series of *n*-alkanes on PTFE.

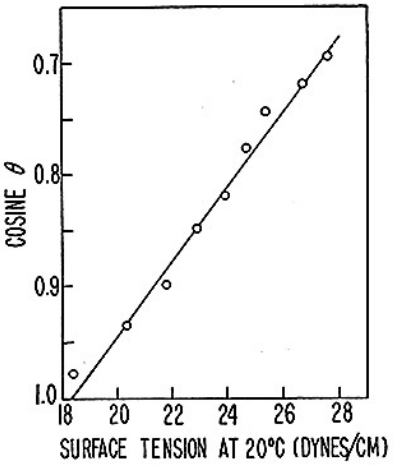

Figure C.2: Plot of cos θ vs. γ_{lv} for a series of *n*-alkanes on PTFE from Fox and Zisman.[3]

The authors probed the PTFE surface with various series of liquids, including *n*-alkanes, di(*n*-alkyl)ethers, linear polymethylsiloxanes, halocarbons, and some miscellaneous liquids. Perhaps most interesting is that the extrapolations to cos $\theta = 1$ yield different values for γ_c, depending on the type of probe liquid used. This disagreement presents some question as to whether there actually is any underlying fundamental principle in this technique.

Use of a variety of liquids, including both polar and non-polar, introduces some non-linearity.[4] Figure C.3 is a plot of cos θ vs. γ_{lv} for various liquids on fluorinated polymers.[4] It can be seen that the linear extrapolation technique holds only for $\gamma_{lv} < 40$ dynes/cm or so. This non-linearity raises some questions about extending the critical surface tension concept, and its linear extrapolation, to deduce information about the solid surface energy.

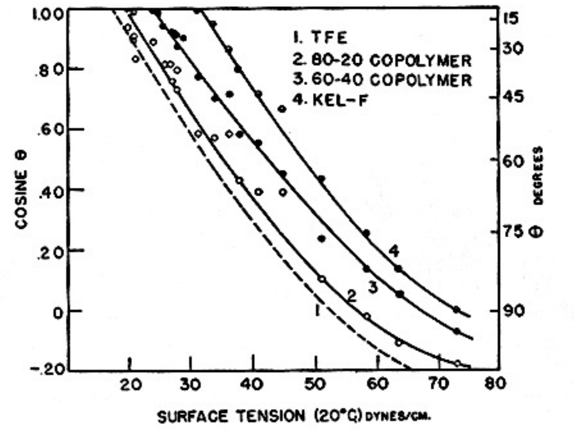

Figure C.3: Plot of cos θ vs. γ_{lv} for a series of liquids on fluorinated materials.[4] Note the non-linearity in the plots above γ_{lv} ~ 40 dynes/cm.

The present work involves creating surfaces of self-assembled monolayers that have –CF_3 groups exposed. Hare, *et al.* measured the contact angle of various liquids on acid monolayers formed on platinum foil, and in particular a perfluorinated acid with terminal –CF_3 groups.[5] Based on these data, the authors estimated the perfluorolauric acid-coated platinum foil surface to have a critical surface tension of 5.6 dynes/cm.[5] Figure C.4 shows the linear extrapolation presented in a later paper used to obtain these values;[6] note the large range of extrapolation used to obtain γ_c. Although Hare, *et al.* note some dependence of γ_c on perfluorinated chain length,[5] later publications from the group identify all –CF_3 surfaces as having critical surface tensions ~6.0 dynes/cm,[7,8] which is a bit misleading.

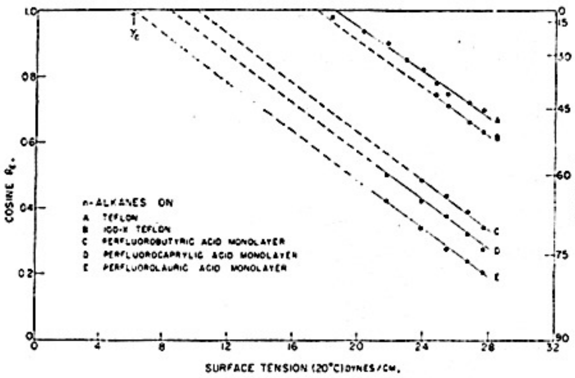

Figure C.4: Plot of cos θ vs. γ_{lv} for a series of *n*-alkanes on a perfluorolauric acid monolayer on platimum foil.[6]

There are several concerns with regard to the Zisman approach. The linear extrapolation yields information about liquid spreading on the surface, and not information about the actual surface itself. Mathematically, this spreading condition is such that $\gamma_c = \gamma_{sv} - \gamma_{sl}$, and the desired information is actually γ_{sv}, which this method cannot provide, unless one assumes information about the interfacial tension γ_{sl}. This method is also sensitive to the type of probe liquid used, as discussed above, which raises question about its validity. There are questions about the validity of the linear extrapolation, given the nonlinearity of the data in Figure C.3. Finally, for low-energy surfaces such as those found in films with –CF_3 groups exposed, as in the current work, the Zisman technique may require extrapolation well outside the range of measured contact angles. For these reasons it is concluded that this method of obtaining information about the surface energy of the solid surfaces should not be used.

SURFACE TENSION COMPONENTS:

Girifalco and Good derive a method for estimating the interfacial tension between two liquids, *a* and *b*, similar to a rearrangement of Equation C.3:[9]

Equation C.5 $$\gamma_{ab} = \gamma_a + \gamma_a - 2\Phi\sqrt{\gamma_a \gamma_b}$$

where *W* in Equation C.4 is replaced by $2\Phi(\gamma_a\gamma_b)^{1/2}$, and Φ is a constant of the particular system. The authors noted a correlation between the variation of Φ and the predicted hydrogen bonding of the system.

Fowkes first suggested existence of various components of surface energy, and the additive combining rule:[10]

Equation C.6 $$\gamma_{lv} = \gamma_{lv}^{h} + \gamma_{lv}^{w}$$

where γ_{lv} is the total liquid (in this case) surface energy, and $\gamma_{lv}{}^{d}$ and $\gamma_{lv}{}^{w}$ are the hydrogen bonding and dispersion forces, the two dominant surface forces. For a system consisting of a solid saturated hydrocarbon and water, he predicted the attractive forces would be mainly dispersive forces, so that application of Equation C.5 yields:

Equation C.7 $$\gamma_{sl} = \gamma_{sv} + \gamma_{lv} - 2\sqrt{\gamma_{sv}^{w}\gamma_{lv}^{w}}$$

where the superscripts ^{w} denote the purely dispersive character of the interaction. Combining Equations C.4 and C.7 yields:

Equation C.8
$$\gamma_{lv}\left(1+\cos\theta\right)=2\sqrt{\gamma_{lv}^{w}\gamma_{sv}^{w}}$$

which upon rearrangement yields:

Equation C.9
$$\cos\theta = 2\gamma_{sv}^{w}\frac{\sqrt{\gamma_{lv}^{w}}}{\gamma_{lv}}-1$$

This facilitates the calculation of the dispersive component of solid surface energy from the slope of the plot cos θ vs. $\sqrt{\gamma_{lv}^{w}}/\gamma_{lv}$, as long as the liquid is well characterized. An example of this is shown in Figure C.5, taken from Fowkes,[10] which is a rearrangement of some of the Shafrin[6] data into the form of Equation C.9. Given that the plot has an intercept at cos θ = -1, the estimation of γ_s^w may be made with only one data point.[10] It can be seen that this approach is useful only for systems in which one or both phases exhibits primarily dispersive character.

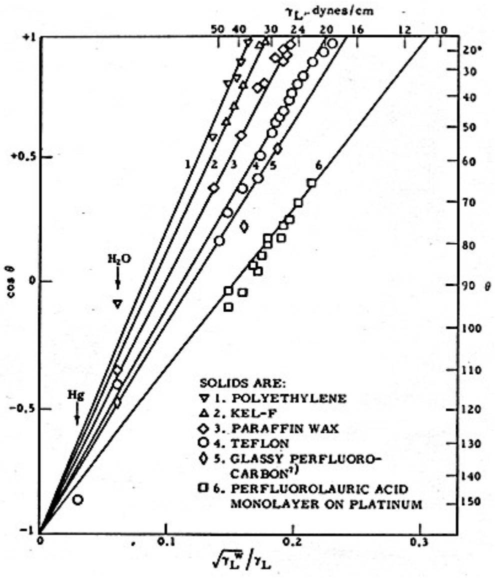

Figure C.5**:** Plot of cos θ vs. $\sqrt{\gamma_{lv}^{w}}\big/\gamma_{lv}$ for some of the data in Shafrin and Zisman.[6] This method is valid only when one or both phases are apolar.

Chaudhury pointed out that the surface energy terms due to electrodynamic interactions (London + Keesom + Debye) should be lumped together, designated γ^{LW},[11] where the superscript ^{LW} refers to combined Lifshitz-van der Waals interactions. The polar interaction is designated γ^{AB}, the superscript ^{AB} referring to acid-base interactions. Equation C.6 can be rewritten to include this new notation:[11]

Equation C.10
$$\gamma = \gamma^{LW} + \gamma^{AB}$$

where the subscripts are dropped; this equation may be applied to liquid or solid systems. The acid-base term may be written in terms of the electron-acceptor (γ^{+})

and electron-donor (γ^{-}) parameters[12] such that application of a geometric combining rule gives $\gamma^{AB} = 2\sqrt{\gamma^{+}\gamma^{-}}$. Consideration of the additional interaction in a two-material system between the various polar components, Equation C.8 is rewritten:[13]

Equation C.11
$$\gamma_{lv}\left(1+\cos\theta\right) = 2\left(\sqrt{\gamma_{lv}^{LW}\gamma_{sv}^{LW}} + \sqrt{\gamma_{lv}^{+}\gamma_{sv}^{-}} + \sqrt{\gamma_{lv}^{-}\gamma_{sv}^{+}}\right)$$

The solid surface energy has three components according to Equation C.10; for interactions involving one apolar phase Equation C.11 simplifies to Equation C.8.

The system of the current work, however, involves the transformation of a surface from very polar in nature (SiO_2) to a surface very non-polar in nature ($-CF_3$). For this investigation it is possible, as suggested by van Oss, *et al.*,[14] to probe the solid surface with three well-characterized liquids, yielding three equations, the solution of this system yielding the three components of solid surface energy, namely γ^{LW}, γ^{+}, and γ^{-}.

Several authors have raised issue with the absence of a film pressure term, π_e, in this approach.[15-18] The surface pressure can be thought of as a reduction in the surface energy of the solid (or liquid) surface due to adsorption of a lower-energy species, such that:

Equation C.12
$$\pi_e = \gamma_{s0} - \gamma_{sv}$$

where γ_{s0} is the surface energy of the material in vacuum (no adsorbed species), and γ_{sv} is the observed surface energy under experimental conditions. Good claimed that

π_e is probably negligible for non-wetting systems,[19] i.e. where the contact angle is nonzero.

Bangham and Razouk rewrote Equation (2) to include the spreading pressure:[2]

Equation C.13 $$W = \gamma_{lv} + \left(\gamma_{sv} - \gamma_{s0}\right) + \gamma_{s0} - \gamma_{sl}$$

Equation C.14 $$W = \gamma_{lv} + \gamma_{s0} - \gamma_{sl} - \pi_e$$

where W is the experimental work of adhesion. The authors introduced a new term, W_0 to define the work of adhesion in vacuum, or when the adsorbed vapor is absent from the solid surface upon separation of the liquid from the solid:

Equation C.15 $$W_0 = \gamma_{lv} + \gamma_{s0} - \gamma_{sl}$$

such that $W_0 - W = \pi_e$, which signifies that the work of adhesion is reduced by the existence of the adsorbed layer. Noting that with no adsorbed species, i.e. in vacuum, the measured contact angle may be different than in Equation C.1, the following analog of Young's equation may be written:

Equation C.16 $$\gamma_{lv} \cos\theta_0 = \gamma_{s0} - \gamma_{sl}$$

where θ_0 is the contact angle in vacuum. The vacuum analog of Equation C.11 is then:

Equation C.17
$$\gamma_{lv}\left(1+\cos\theta_0\right)=2\left(\sqrt{\gamma_{lv}^{LW}\gamma_{s0}^{LW}}+\sqrt{\gamma_{lv}^{+}\gamma_{s0}^{-}}+\sqrt{\gamma_{lv}^{-}\gamma_{s0}^{+}}\right)$$

It seems improbable that one would be able to ensure the absence of some vapor adsorption. Some authors have simply added π_e to the right side of Equation C.17,[15,17] but Schrader[20] argues that Young's verbalization,[1] and Bangham and Razouk's[2] interpretation pertain to observed contact angles in the experimental setting, and hence are correct without the surface pressure term.

In order to estimate the surface energy components, and hence the total surface energy of a solid, as discussed above, it is possible to measure the contact angle of three well characterized liquids on a solid substrate. This yields a system of three equations, and nominally three unknowns:

Equation C.18
$$\gamma_{lv1}\left(1+\cos\theta_1\right)=2\left(\sqrt{\gamma_{lv1}^{LW}\gamma_{sv1}^{LW}}+\sqrt{\gamma_{lv1}^{+}\gamma_{sv1}^{-}}+\sqrt{\gamma_{lv1}^{-}\gamma_{sv1}^{+}}\right)$$

Equation C.19
$$\gamma_{lv2}\left(1+\cos\theta_2\right)=2\left(\sqrt{\gamma_{lv2}^{LW}\gamma_{sv2}^{LW}}+\sqrt{\gamma_{lv2}^{+}\gamma_{sv2}^{-}}+\sqrt{\gamma_{lv2}^{-}\gamma_{sv2}^{+}}\right)$$

Equation C.20
$$\gamma_{lv3}\left(1+\cos\theta_3\right)=2\left(\sqrt{\gamma_{lv3}^{LW}\gamma_{sv3}^{LW}}+\sqrt{\gamma_{lv3}^{+}\gamma_{sv3}^{-}}+\sqrt{\gamma_{lv3}^{-}\gamma_{sv3}^{+}}\right)$$

where the subscripts $_{1\text{-}3}$ refer to the specific probe liquid. The subscripts have also been added to the solid surface energy components because of the presumably different effect of the vapor adsorption on the measured contact angle for the three liquids:

Equation C.21 $$\gamma_{sv1} = \gamma_{sv1}^{LW} + 2\sqrt{\gamma_{sv1}^{+}\gamma_{sv1}^{-}}$$

Equation C.22 $$\gamma_{sv2} = \gamma_{sv2}^{LW} + 2\sqrt{\gamma_{sv2}^{+}\gamma_{sv2}^{-}}$$

Equation C.23 $$\gamma_{sv3} = \gamma_{sv3}^{LW} + 2\sqrt{\gamma_{sv3}^{+}\gamma_{sv3}^{-}}$$

Strictly speaking, there is no single solution to this set, since one cannot assume that the three values of solid surface energy from Equations C.18 – C.20 will be equal. Volpe and Siboni recommend measuring contact angles from a larger set of liquids,[16] yielding an over-determined matrix, and solving the set using a least-squares method, which will converge to some value for γ_{sv} that is representative for a wide variety of probe liquids.

EQUATION OF STATE APPROACH

A newer approach taken by Neumann and coworkers involves an equation-of-state (EOS) to describe the solid-liquid-vapor interaction. Ward and Neumann [21] derive a proof of the validity of such an EOS based on thermodynamic definitions proposed by Gibbs,[22] leading to the following relation:

Equation C.24 $$\gamma_{sl} = f(\gamma_{sv}, \gamma_{lv})$$

Kwok, *et al* reinforce the relation by employing the Gibbs phase rule,[23] and conclude that there are two degrees of freedom in the sessile drop/solid substrate system. Neumann, *et al.* fit to data a second-order polynomial,[24] and labeled this equation their EOS. Further refinement of the equation yielded the following: [25]

Equation C.25
$$\cos\theta = -1 + 2\sqrt{\frac{\gamma_{sv}}{\gamma_{lv}}}e^{-\beta(\gamma_{lv}-\gamma_{sv})^2}$$

where β = 0.0001247 from empirical fit. Figure C.6 is an example of a plot using the EOS approach,[23] where it was argued based on the tight fit that $\gamma_{lv}\cos\theta = f(\gamma_{sv}, \gamma_{lv})$, and not a function of any surface tension components; in other words, the relation is in direct contradiction to earlier claims that the interaction involves a molecular approach.[9-11,14,26]

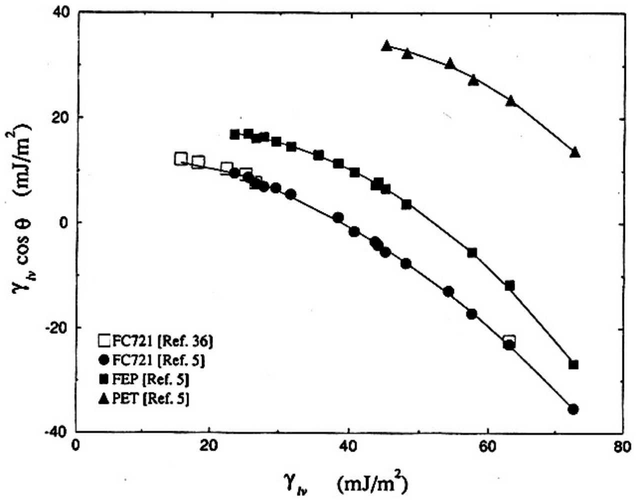

Figure C.6: A plot of $\gamma_{lv}\cos\theta$ vs. γ_{lv} for various polymer surfaces.[23] The smoothness of the curves, it is argued, justifies the assertion that $\gamma_{lv}\cos\theta$ is a function of γ_{lv} and γ_{sv} only.

While this approach seems reasonable, there has been much resistance to it. Wu, *et al* provide a review of these criticisms,[27] including the note that Neumann and coworkers calibrated Equation C.25 using only non-polar surfaces. Xu, *et al.* extended the evaluation of Equation C.25 to a mercury substrate.[15] Interestingly, the value for β as measured by the authors differed from that reported by Li and Neumann[25] by 2 orders of magnitude. Figure C.7 is a comparison of interfacial surface tensions calculated using the STC and EOS approaches to measured values. The authors concluded from this data that the STC approach provided more accurate predictions for that system.

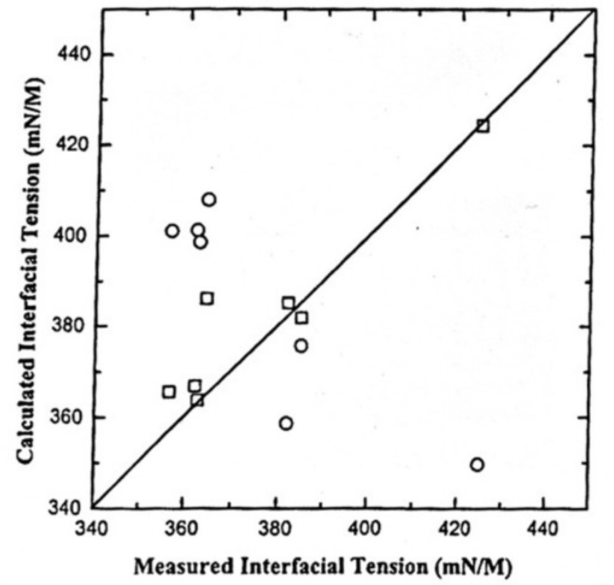

Figure C.7: Correlation between measured and calculated interfacial tensions using the fitting parameters from the STC (square) and Neumann (circle) methods.[15]

SUMMARY:

The Zisman approach[3-8,28] seems to be inadequate for obtaining information about the solid surfaces in the current work. The variation of critical surface tension with probe liquid type, along with the large extrapolations that may be necessary at full coverage, raises questions about its validity and accuracy.

The Fowkes method,[10,29,30] which is essentially a reorganization of the Zisman method to include polar and non-polar components, may be useful when probing non-polar surfaces with any liquid, or when probing any surface with a non-polar liquid. The absence of polar-polar interactions enables the linear analysis method, from which the non-polar component of the solid surface energy can me obtained. This is only moderately useful, though, since a given solid surface may only be partly described by the non-polar term.

The method of Neumann and coworkers[21,23-25,31-36] is very interesting, but it seems to be underdeveloped at this time. The EOS approach has been calibrated to polymer surfaces displaying low-surface energy, non-polar character. Extension of this concept by Xu *et al* to high-energy, polar interfaces, e.g. mercury and various liquids,[15] has resulted in inaccurate predictions of interfacial tensions.

Despite the perceived shortcomings of the STC approach pioneered by Good and coworkers,[9,11,13,14,19,37-40] as discussed above, various groups have embraced its applicability and accuracy. Xu, *et al*. found it to describe quite well the interface between mercury and other various liquids.[15] Holysz and Chibowski reported consistency between the STC predictions and recovery of barite.[41] Lee concluded, based on work on various polymers, that the STC approach is grounded in sound theory.[42] There are still some complications in using the STC approach, however, as discussed above. Unless absolutely clean samples are prepared, and probed with liquids which have ultra-low vapor pressures, or whose vapors do not adsorb to the solid in question, then a unique set of surface energy components, γ_{s0}^{LW}, γ_{s0}^{+}, and γ_{s0}^{-}, cannot be found. It is proposed, therefore, to follow the approach of Volpe and Siboni,[16] and measure contact angles with a larger set of liquids in order to obtain an "average" value of surface free energy. This data can be regressed using a least-squares algorithm to find "best-fit" values for γ_{sv}^{LW}, γ_{sv}^{+}, and γ_{sv}^{-}, where the subscripts $_{sv}$ is used to identify that there may be adsorbed vapors affecting the absolute solid surface energy.

If one requires only an estimation of the change in film coverage with changing film deposition conditions, and not a complete description of the surface energy, one probe liquid may be sufficient. Cassie,[43] and later Israelachvilli,[44] derived the correlation between the observed contact angle of a probe liquid on a heterogeneous (two species) solid surface and the relative concentrations of the two surface species.

REFERENCES

1. Young, T., Trans. R. Soc., 1805. 95: p. 65.
2. Bangham, D.H. and R.I. Razouk, Trans. Faraday Soc., 1937. 33: p. 1459, 1463.
3. Fox, H.W. and W.A. Zisman, J. Coll. Sci., 1950. 5: p. 514.
4. Fox, H.W. and W.A. Zisman, J. Coll. Sci., 1952. 7: p. 109.
5. Hare, E.F., E.G. Shafrin, and W.A. Zisman, J. Phys Chem., 1954. 58: p. 236.
6. Shafrin, E.G. and W.A. Zisman, J. Phys. Chem., 1960. 64: p. 519.
7. Zisman, W.A., Constitutional Effects on Adhesion and Abhesion, in Adhesion and Cohesion, P. Weiss, Editor. 1962, Eksevier: New York. p. 183.
8. Zisman, W.A., Relation of the Equilibrium Contact Angle to Liquid and Solid Constitution, in Contact Angle, Wettability, and Adhesion. Advances in Chemistry Series No. 43, R.F. Gould, Editor. 1964, ACS: Washington, D.C. p. 1.
9. Girifalco, L.A. and R.J. Good, J. Phys. Chem., 1957. 61: p. 904.
10. Fowkes, F.M., J. Phys. Chem., 1962. 66: p. 382.
11. Chaudhury, M.K., Short range and long range forces in colloidal and macroscopic systems, Ph.D. Thesis, Departments of Microbiology and Chemical Engineering, 1984, State Univ. of NY.

12. Kollman, P., J. Am. Chem. Soc., 1977. 99: p. 4875.

13. van Oss, C.J., M.K. Chaudhury, and R.J. Good, Adv. Coll. Int. Sci., 1987. 28: p. 35-64.

14. van Oss, C.J., R.J. Good, and M.K. Chaudhury, Langmuir, 1988. 4: p. 884-891.

15. Xu, Z., Q. Liu, and J. Ling, Langmuir, 1995. 11: p. 1044.

16. Volpe, C.D. and S. Siboni, J. Coll. Int. Sci., 1997. 195: p. 121.

17. Lee, L.-H., J. Coll. Int. Sci., 1999. 214: p. 64.

18. Greiveldinger, M. and M.E.R. Shanahan, J. Coll. Int. Sci., 1999. 215: p. 170.

19. Good, R.J., Contact angle, wetting, and adhesion: a critical review, in Contact Angle, Wettability, and Adhesion, K.L. Mittal, Editor. 1993, VPS BV: Utrecht, The Netherlands. p. 3.

20. Schrader, M.E., Langmuir, 1993. 9: p. 1959.

21. Ward, C.A. and A.W. Neumann, J. Coll. Int. Sci., 1974. 49(2): p. 286.

22. Gibbs, J.W., The Scientific Papers of J. Willard Gibbs. Vol. 1. 1961, New York: Dover.

23. Kwok, D.Y., D. Li, and A.W. Neumann, Coll. Surf. A., 1994. 89: p. 181.

24. Neumann, A.W., *et al.*, J. Coll. Int. Sci., 1974. 49(2): p. 291.

25. Li, D. and A.W. Neumann, J. Coll. Int. Sci., 1990. 137(1): p. 304.

26. Owens, D.K. and R.C. Wendt, J. Appl. Polym. Sci., 1969. 13: p. 1741.

27. Wu, W., J. R.F. Giese, and C.J. van Oss, 1995.

28. Fox, H.W. and W.A. Zisman, J. Colloid. Sci., 1952. 7: p. 428.

29. Fowkes, F.M., Indust. Eng. Chem., 1964. 56(12): p. 40.

30. Fowkes, F.M. and W.M. Sawyer, J. Phys. Chem., 1952. 20: p. 1650.

31. Kwok, D.Y., D. Li, and A.W. Neumann, Langmuir, 1994. 10: p. 1323.

32. Kwok, D.Y., *et al.*, Langmuir, 1997. 13: p. 2880.

33. Spelt, J.K., D.R. Absolom, and A.W. Neumann, Langmuir, 1986. 2: p. 620.

34. Li, D. and A.W. Neumann, J. Coll. Int. Sci., 1992. 148(1): p. 190.

35. Li, D. and A.W. Neumann, Langmuir, 1993. 9: p. 3728.

36. Chen, P., *et al.*, Axisymmetric Drop Shape Analysis (ASDA) and its Applications, in Drops and Bubbles in Interfacial Research. 1998, Elsevier: New York. p. 61.

37. Good, R.J., L.A. Girifalco, and G. Kraus, J. Phys. Chem., 1958. 62: p. 1418.

38. Good, R.J. and L.A. Girifalco, J. Phys. Chem., 1960. 64: p. 561.

39. Good, R.J., Nature, 1966. 212: p. 276.

40. van Oss, C.J., R.J. Good, and M.K. Chaudhury, J. Colloid Interface Sci., 1986. 111: p. 378.

41. Holysz, L. and E. Chibowski, Langmuir, 1992. 8: p. 303.

42. Lee, L.-H., Langmuir, 1996. 12: p. 1681.

43. Cassie, A.B.D., Faraday Disc. Chem. Soc., 1948. 3(1): p. 11.

44. Israelachvili, J.N. and M.L. Gee, Langmuir, 1989. 5: p. 288.

Appendix D: Conversion of KLA Data Files

INTRODUCTION

Inspection of wafers on KLA-Tencor inspection tools such as the 21XX series yields data files formatted specifically for KLA-Tencor tools. These files can be exported for use on various inspection and review tools, such as optical inspection microscopes and review SEMs, and can also be converted into text format for manual data manipulation in a format known as "KLARF." A KLARF file contains lot and recipe identification information, wafer identification information, as well as coordinates, sizes, and automatic classification codes for detected defects for each wafer.

EXTRACTION OF WAFER DATA FROM KLARF FILES

Reduction of KLARF Files into Individual Wafer Data Files

There are many MATLAB commands that can be used to extract information from data files, including `textread`, `dlmread`, `xlsread`, and others. After some trial and error, `xlsread` was chosen as the command easiest to use with the KLARF files. The following procedure was used in the data extraction.

A KLARF file was opened in Wordpad, and the lot header and footer information, an example of which is shown below, was removed. The remaining text in the KLARF file consisted of wafer header and footer information, as well as the die coordinates, relative X- and Y-locations within each die, size, and classification (if used) for each detected defect. The wafer information was saved to a separate delimited text file for each wafer, and these were converted to spreadsheet files in Excel format. These *.xls data files are used directly in the MatLab code that follows for further data analysis. There are undoubtedly other ways to reduce the large KLARF files for use in MatLab.

Lot Header:

```
  FileVersion 1 1;
  FileTimestamp 04-25-03 09:10:10;
  InspectionStationID "" "R2D2.exe" "NONE";
  SampleType WAFER;
  ResultTimestamp 04-24-03 18:36:28;
  LotID "SFIL_APR03_M25";
  SampleSize 1 200;
```

Lot Footer:

```
  EndOfFile;
```

Wafer Data:

```
  SampleOrientationMarkType NOTCH;
  OrientationMarkLocation DOWN;
  DiePitch 26418.7044 26406.7922;
  DieOrigin 0 0;
  WaferID "1";
  Slot 1;
  SampleCenterLocation 19729.1918 9566.0375;
  ClassLookup 0;
  DefectClusterSpec 3 THRESHOLD  MINSIZE  MERGETOL ;
  DefectClusterSetup  1000 10 3;
  RemovedDieList 15
     0 3
     ⋮
     1 -3;
  InspectionTest 1;
  SampleTestPlan 16
```

```
   2 -2
⋮
   -1 1;
AreaPerTest 1.20197e+009;
TestParametersSpec 3 PIXELSIZE …;
TestParametersList  0.6250 0 0.0000 ;
DefectRecordSpec 17 DEFECTID  …;
DefectList
1 876.1657 24790.1086 -1 1 1.8775 0.6258 1.4982 0.6258
0 1 1 0 0 0 0 0
2 2771.1696 25506.0578 -1 1 6.8841 4.3808 23.6859
4.3808 0 1 1 0 0 0 0 0
3 3000.2243 24808.8859 -1 1 3.1291 1.8775 3.0886
1.7574 0 1 1 0 0 0 0 0
⋮
SummarySpec
   5 TESTNO  NDEFECT  DEFDENSITY  NDIE  NDEFDIE ;
SummaryList
 1 2038 169.555 16 16;
```

Regression of Individual Wafer Data Files into the Desired Format

Three MatLab files were used in data regression. KLA_upper_array.m was used to extract data from the *.xls files, and called the functions KLA_array.m and KLA_defect.m, which are used to group defects in imprint order for each wafer and group defects in size bins, respectively. The `edges` variable can be modified to change the number and delineation of size bins. Output from these scripts have been used directly in the text, and have also been manipulated to yield various other, similar plots.

KLA_upper_array.m

```
%loop through KLA files - calculate defect bins
global edges
edges = [0.01 1.5 2.25 5 10 25 inf]; %designates size
bins
TOTAL = edges; %the first row in TOTAL will be defect
size
for n = 1:25 %for 25 wafers with #1 = 1st imprinted
wafer
    name = ['directory\filename' num2str(n) '.xls'];
    D = KLA_array(name);
    H = KLA_defect(D);
    TOTAL = vertcat(TOTAL,H);
end
TOT = horzcat(TOTAL,sum(TOTAL,2));
name4 = ['directory\outputfile.txt'];
dlmwrite(name4,TOT,' ')  % saves data for future use
plot(1:length(TOT)-1,TOT(2:end,1),'b+-')
hold
plot(1:length(TOT)-1,TOT(2:end,2),'r.-')
plot(1:length(TOT)-1,TOT(2:end,3),'go-')
plot(1:length(TOT)-1,TOT(2:end,4),'c*-')
plot(1:length(TOT)-1,TOT(2:end,5),'m+-')
plot(1:length(TOT)-1,TOT(2:end,6),'k.-')
hold
fontsize = 16;
set(gca,'FontSize',fontsize)
xlabel('Imprint #','FontSize',fontsize)
ylabel('Defect Count','FontSize',fontsize)
```

```
bins1 = strcat('< ',num2str(edges(2)),' 
','{\it\mu}','m');
bins2 = strcat(num2str(edges(3)));
bins3 = strcat(num2str(edges(4)));
bins4 = strcat(num2str(edges(5)));
bins5 = strcat(num2str(edges(6)));
bins6 = strcat('> ',num2str(edges(end-1)));
legend(bins1,bins2,bins3,bins4,bins5,bins6)
```

KLA_array.m

```
function [Defect] = KLA_array(name)
Array = xlsread(name);
[sizex,sizey] = size(Array);
Xindex = Array(58:sizex-5,5)-min(Array(58:sizex-
5,5))+1;
Yindex = Array(58:sizex-5,6)-min(Array(58:sizex-
5,6))+1;
die = horzcat(Xindex,Yindex);
[defectnumber,dummy2] = size(die);
% create column with imprint # for each defect
[imprint] = zeros(defectnumber,1);
Dsize = Array(58:sizex-5,10);
map = [...
        4 8 12 16;...
        3 7 11 15;... %notch
        2 6 10 14;...
        1 5 9 13];

% WAFER MAP  %
%           -1  0   1   2
```

```
%
%   1       4   8   12  16
%   0       3   7   11  15   NOTCH
%   -1      2   6   10  14
%   -2      1   5   9   13
%
% the KLA recipe setup allows notch orientation in 4
positions, so this wafer map should be manipulated to
match the specific notch orientation and wafer origin
for the recipe used
% read each defect in data file order and map it to a
particular imprint # on that wafer
for count = 1:defectnumber
    imprint(count) = map(die(count,1),die(count,2));
end
Defect = sortrows(horzcat(die,imprint,Dsize),3);
```

KLA_defect.m

```
function [defdata] = KLA_defect(D)
global edges Die1 n sizeR sizeC
n = zeros(16,1);
defdata = zeros(16,length(edges));
[sizeR sizeC] = size(D);
Die1 = zeros(16,sizeR,sizeC);
%count and index array for subsequent fracturing
for n_1 = 1:length(D)
    switch D(n_1,3)
        case 1
            n(1) = n(1) + 1;
        case 2
```

```
    n(2) = n(2) + 1;
case 3
    n(3) = n(3) + 1;
case 4
    n(4) = n(4) + 1;
case 5
    n(5) = n(5) + 1;
case 6
    n(6) = n(6) + 1;
case 7
    n(7) = n(7) + 1;
case 8
    n(8) = n(8) + 1;
case 9
    n(9) = n(9) + 1;
case 10
    n(10) = n(10) + 1;
case 11
    n(11) = n(11) + 1;
case 12
    n(12) = n(12) + 1;
case 13
    n(13) = n(13) + 1;
case 14
    n(14) = n(14) + 1;
case 15
    n(15) = n(15) + 1;
case 16
    n(16) = n(16) + 1;
```

```
    end
end
% this next subroutine counts defects of sizes
according to the "edges" variable
% a section is included to account for zero defects on
any particular die
m2 = 1;
for m1 = 1:16
    Die1(m1,m2:m2+n(m1)-1,:) = D(m2:m2+n(m1)-1,:);
    switch isempty(Die1(m1,:,:))
    case 0
        n_2 = histc(Die1(m1,:,8),edges);
    case 1
        n_2 = zeros(size(edges));
    end
    m2 = m2+n(m1);
    defdata(m1,:) = n_2;
end
```

Appendix E: Estimation of Downstream Gas Phase FOTS Concentration in a Bubbler Delivery System

INTRODUCTION

Any investigation into the kinetics of the heterogeneous reaction between tridecafluoro-1,1,2,2-tetrahydrooctyltrichlorosilane (FOTS) vapor and the silica surface requires an estimation of the FOTS gas phase concentration. In the current reaction system, the vapor is delivered into the reaction chamber by way of N_2 carrier gas flowing through a bubbler containing neat FOTS. It is assumed that the concentration of FOTS in the N_2 stream is dependent on the flowrate of N_2 through the bubbler, and hence the assumption cannot be made that the stream is saturated with FOTS.

An attempt was made to generate data of FOTS concentration as a function of N_2 flowrate through a bubbler by using infrared absorbance and vapor pressure data. The FTIR was used to acquire data consisting of absorbance as a function of flowrate through the FOTS bubbler, which was then normalized using vapor pressure data to yield concentration as a function of bubbler flowrate.

EXPERIMENTAL

FOTS (Gelest) was used as received, and was loaded into a specially designed bubbler within in a N_2-purged dry box. The bubbler had been hand blown to include three stopcocks, one for each inlet and outlet, and one for loading more liquid, a head space reservoir to reduce foaming, and a porous glass sparger to enhance bubbling activity.

FTIR spectra were collected on a Mattson RS10000 spectrometer equipped with a LN_2-cooled MCT photoconductive detector. The spectra were collected using the following conditions, which mimic as closely as possible the Coblentz Society specifications for vapor phase reference spectra[1] and the method used in Aldrich:[2] One hundred sample and background scans, 2.0 cm^{-1} resolution, 600 – 4000 cm^{-1} frequency range, 2X zero fill, double FFT symmetry, and triangle apodization. A new background was collected for each flowrate to minimize spectrometer signal drift. It was expected that the gas phase concentration of FOTS would be low due to the reported low vapor pressure near 0.3 Torr at room temperature,[3] and thus it would be difficult to collect meaningful absorbance data. In order to enhance the capabilities of the spectrometer, a Gemini VEN-0.5L/4.8M Venus Gas Cell was installed through which the FOTS/N_2 vapor would flow; this increased the path length through the gas to nearly 5 m. In the experimental FTIR apparatus, shown in Figure E.1, N_2 passed through a moisture trap (not shown), and then either through the bubbler to carry precursor or directly to the gas cell for purging. Effluent gas was either directed to a mineral oil bubbler, which was used to maintain approximately one atm pressure during data collection, or was evacuated to a mechanical pump. For each flowrate, equilibration time equivalent to at least three time constants was allowed before background or data spectra were collected, where time constant is similar to that used in CSTR analysis, and is defined as cell volume divided by inert gas flowrate.

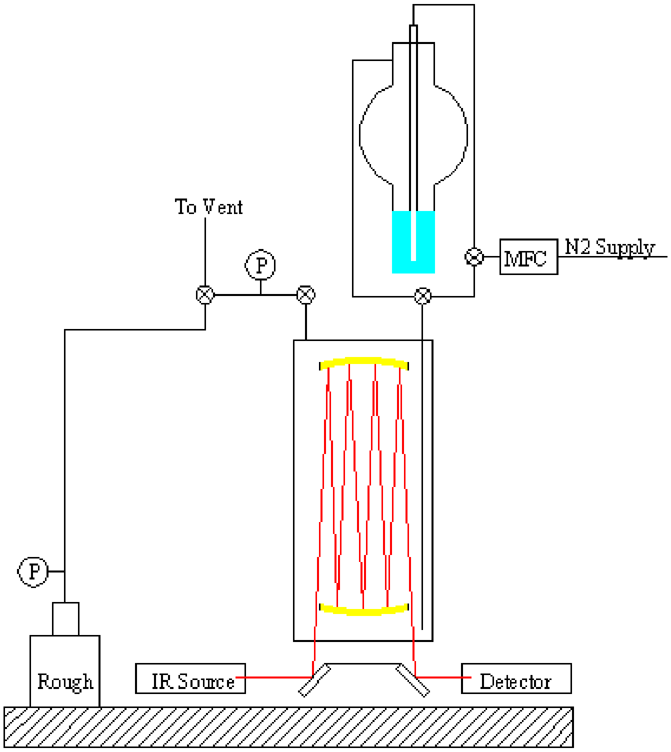

Figure E.1: Experimental FTIR apparatus for determining FOTS absorbance as a function of carrier gas flowrate.

Vapor pressure was determined using a custom built vapor pressure apparatus. A small volume of electropolished 316 SS tubing was enclosed by SS-BNVV51-C (Arthur) pneumatically-operated valves and 1 Torr and 10 Torr Baratron Type 615A bakeable capacitance manometers (MKS Instruments), which were all enclosed in a Fischer Scientific Isotemp® model 718F oven. The thermocouple reading on the oven is not accurate, and so an additional Omega type K thermocouple and readout have been added for accuracy. This thermocouple and readout combination was calibrated with boiling water (~100 ºC) and ice water (~0 ºC). Vacuum is achieved by an Edwards MK2 Diffstak diffusion pump, backed by an Alcatel 2004A roughing pump.

The valves were operated remotely by SS-2P4V fast-acting vented valves (Arthur) located in the control panel outside the oven. Each capacitance manometers was connected to a Type 270 signal conditioner (MKS Instruments). Data collection was performed by connecting the output voltage signals from the Type 270 units to Owl Dataloggers (ACR). The Type 270 units output voltages in the range of 0-10 V, which correlates to the specific pressure rating of each unit. Communication with the Owl Dataloggers was performed using Trendreader software (ACR), and the input voltage range for each Datalogger was limited to maximize voltage resolution using its 256-bit capabilities.

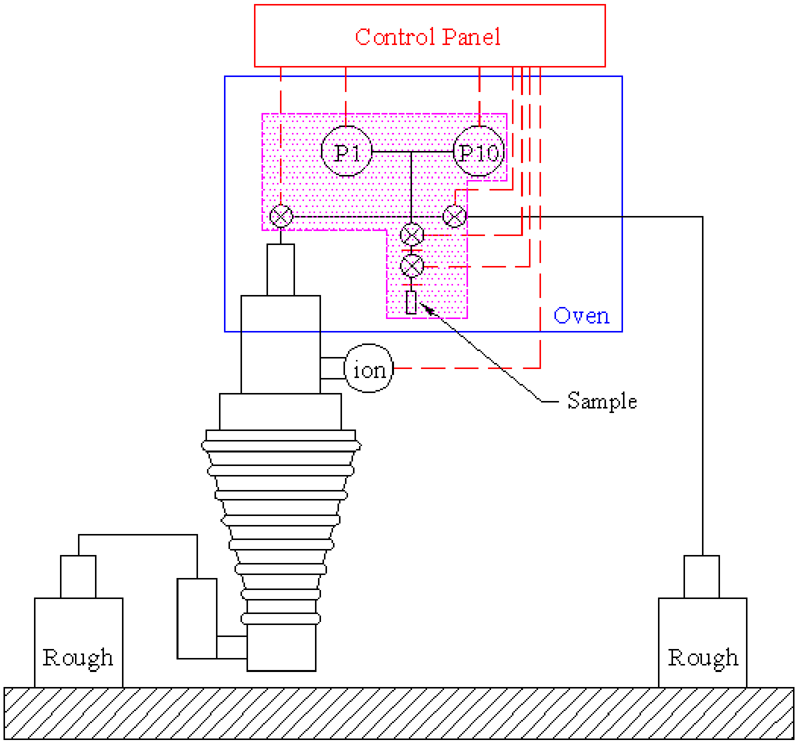

Figure E.2: Vapor pressure apparatus.

RESULTS AND DISCUSSION

Measurement of FOTS Infrared Absorbance as a Function of N_2 Flowrate

It was experimentally observed that flowing gas through the neat FOTS resulted in foam formation on the liquid surface, and without the foam-suppressing head space on the bubbler this foam occasionally escaped into the downstream SS tubing. The addition of the head space resulted in limited foam formation, and cessation of downstream FOTS leakage.

An example complete infrared spectrum of FOTS is shown in Figure E.3. There are two main regions of interest: The range of 600 to 1600 cm^{-1}, which contains C-F and Si-Cl stretch frequencies, among others, and 2700 to 3100 cm^{-1}, which contains C-H and H-Cl stretch frequencies. A close examination of the C-H region revealed clear indication of vibro-rotational splitting from a low molecular weight gas phase species that in some cases seemed to overpower the apparent FOTS C-H signal, as shown in Figure E.4. Since FOTSis not expected to exhibit such behavior, it was concluded that there was a gas phase contaminant in the gas cell. It seemed that HCl was possibly the contaminant in question, since HCl is a byproduct of FOTS hydrolysis and trace HCl likely exists in the glass FOTS bottle from the supplier and in the bubbler.

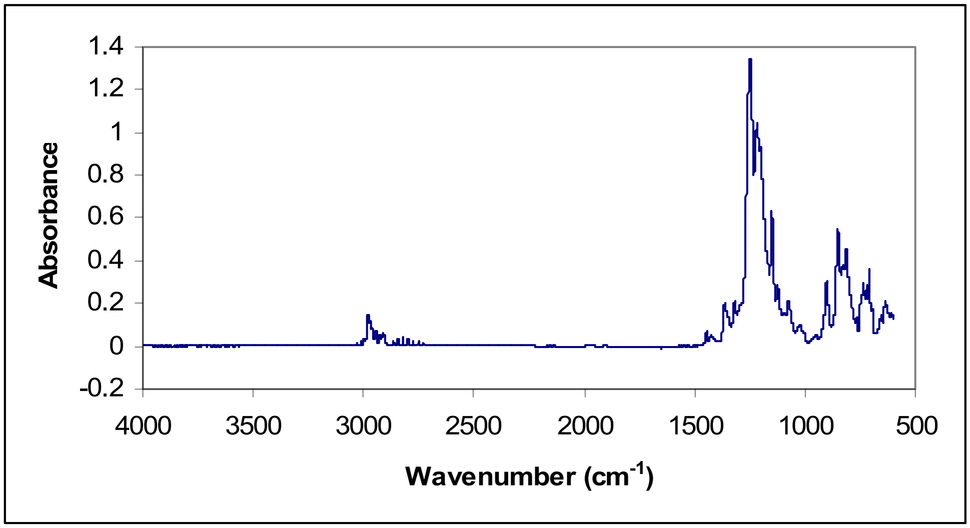

Figure E.3: Example infrared spectrum, showing the two regions of interest.

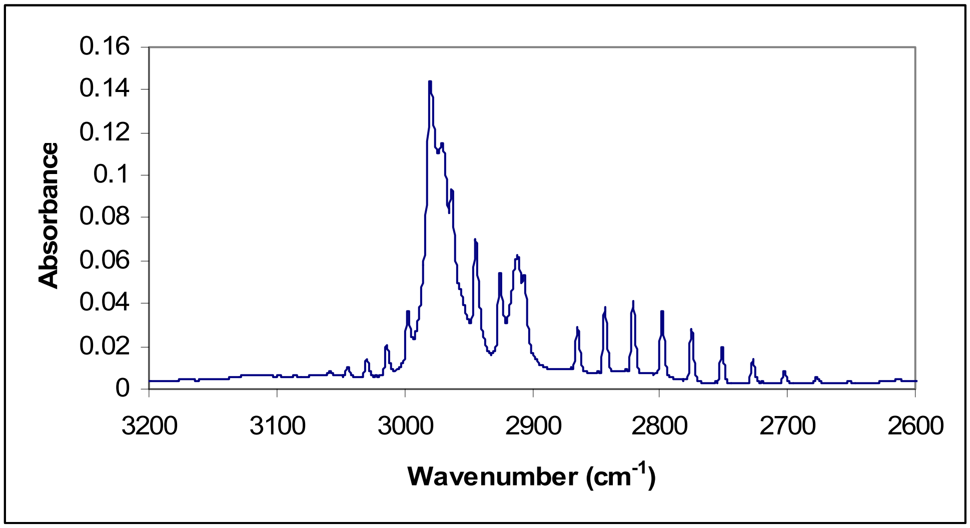

Figure E.4: Example FTIR spectrum showing the vibro-rotational features associated with low molecular weight species superimposed on two broad peaks.

To test for the existence of HCl in the gas stream, the gas cell was sealed and a small amount of HCl was injected into a reservoir in the cell. The resulting infrared spectrum reveals a high degree of similarity between the HCl spectrum and the features in the FOTS spectrum, as shown in Figure E.5. This is a strong indication that HCl is the contaminant in the FOTS spectrum. To correct for this, the HCl spectrum was multiplied by a fraction and subtracted from the FOTS spectra; the fraction used for each FOTS spectrum was that which yielded the best removal of the HCl features, as shown in Figure E.6. It was observed that subtraction of the HCl features resulted in residual baseline noise. This may be due to broadening of the HCl features in the pure HCl spectrum relative to the same features in the FOTS spectrum caused by a difference in HCl concentration. Of particular concern was the fact that the intensity of the residual noise resulting from the spectrum subtraction was different for each flowrate. The asymmetric and symmetric C-H stretch frequencies were believed to be at approximately 2979 and 2912 cm^{-1}, respectively, although no reference for this molecule was found in the literature. Also of concern was that some of these features were very close to the two C-H peaks of interest, which may result in uncertainty in peak intensity. The inset in Figure E.6 is a plot of absorbance versus bubbler flowrate for the two C-H peaks.

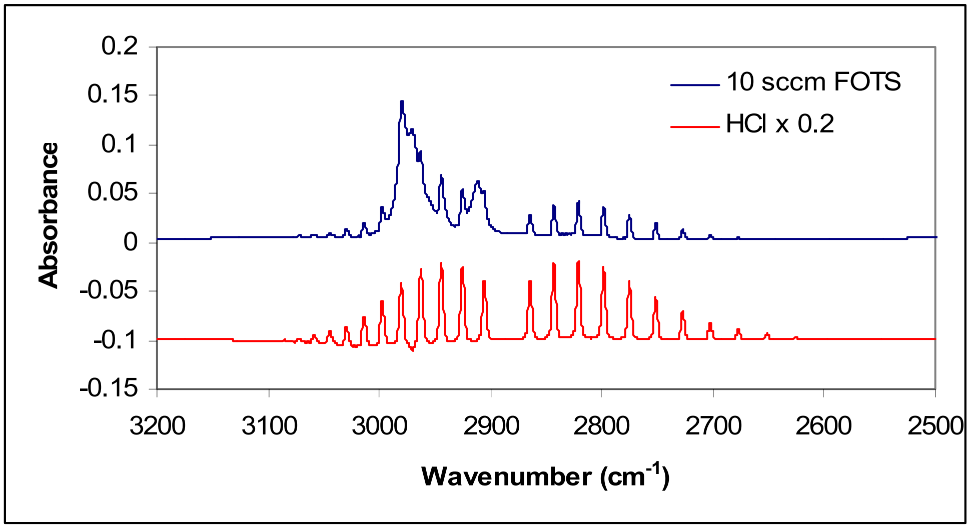

Figure E.5: Infrared spectrum of HCl vapor.

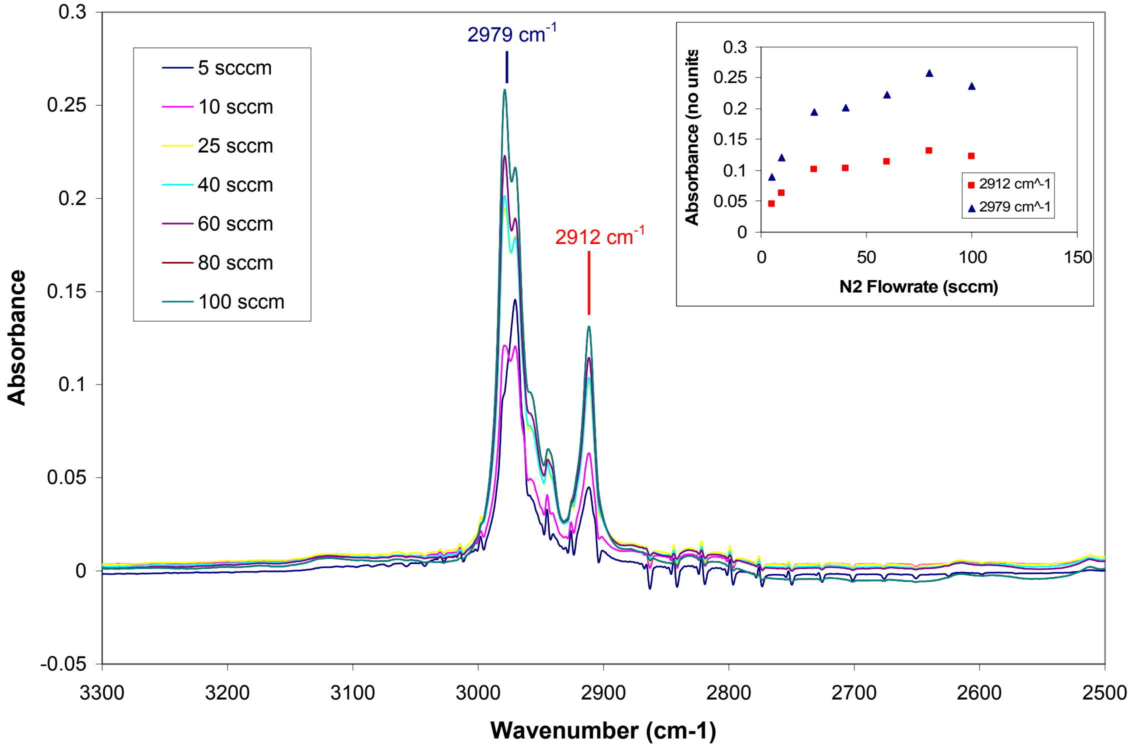

Figure E.6: Comparison of HCl-corrected infrared spectra in the C-H stretch region at various N_2 flowrates.

Due to the uncertainty in estimating the C-H absorbance caused by the HCl spectrum subtraction, it was decided to track a different absorbance peak. Blaudez identified the asymmetric and symmetric CF_2 absorbance peaks as 1205 and 1150 cm^{-1}, respectively.[4] The absorbance of the asymmetric peak at 1205 cm^{-1}, shown in Figure E.7, appears too strong to resolve differences in the spectra of higher flowrates, whereas the intensity of the symmetric peak at 1150 cm^{-1} increases with increasing flowrate through the range of flowrates. An attempt was made to acquire an absorbance spectrum of saturated FOTS vapor, which required opening the gas cell to inject neat FOTS into a liquid reservoir after which the cell was purged with N_2. The sample was allowed to equilibrate until the absorbance spectrum became stable with time, and the saturated vapor spectrum is shown in Figure E.7. A cloudy film was observed on the gold gas cell optics after this run, which was most likely comprised of hydrolyzed FOTS. It is possible that enough water vapor was introduced during sample injection to cause this level of hydrolysis. The existence of this adsorbed film introduces uncertainty into the saturated vapor spectrum, since it is believed that the equilibrium of pure, non-hydrolyzed FOTS vapor would not normally yield adsorption of such a film. Because of this, the intensity of the saturated vapor was arbitrarily taken to be midway between the strongest absorbance for the flow spectra and the absorbance for the "saturated" spectrum, as shown in Figure E.8. The trace in the plot is an exponential curve and fits the data quite well, although it is not assumed to describe the phenomenon fully.

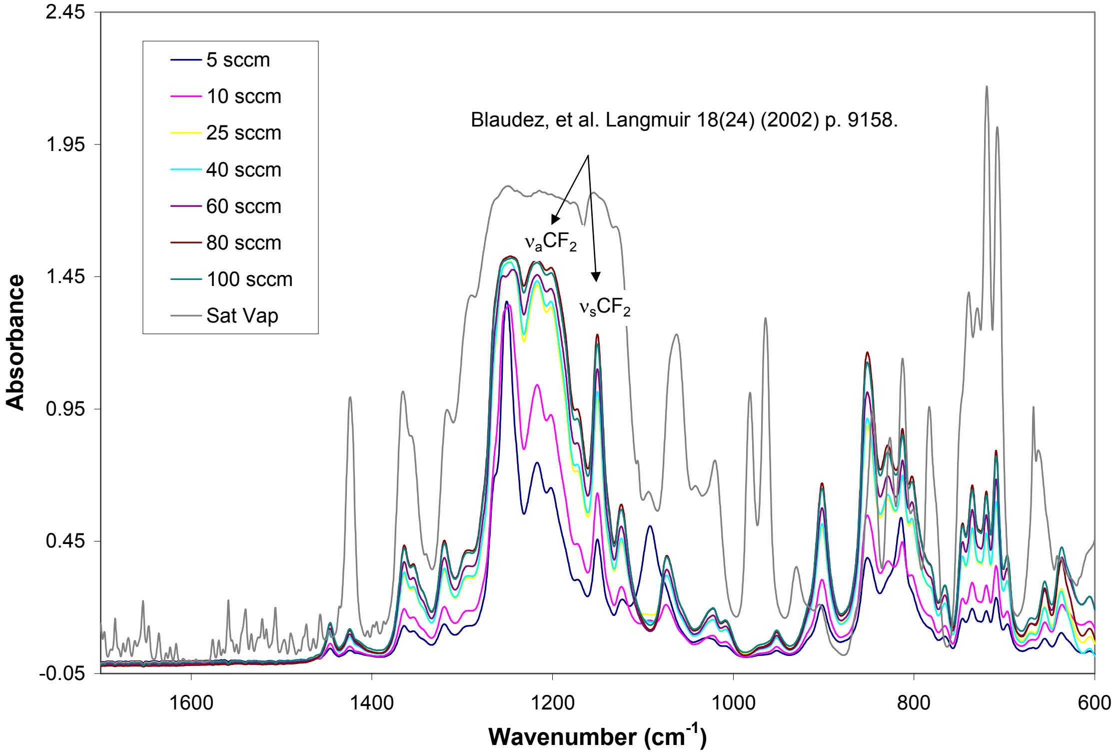

Figure E.7: Comparison of infrared spectra in the 600 – 1600 cm^{-1} region.

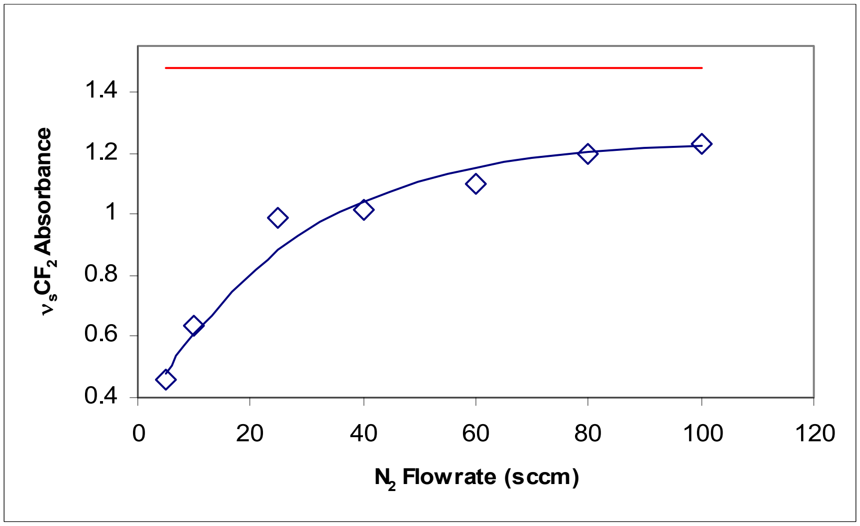

Figure E.8: Plot of absorbance versus N_2 flowrate for the symmetric CF_2 band.

Measurement of FOTS Vapor Pressure

The vapor pressure system was calibrated to a naphthalene standard by measuring pressure versus time at various temperatures, and measuring a separate background pressure rise for each temperature. The background spectrum was subtracted from the raw data, and the asymptotic approach temperature was deemed to be the vapor pressure at that particular temperature. This was performed at various temperatures, and compared to vapor pressure predicted using Antoine Equation constants from two references,[5,6] as shown in Figure E.9. The experimental data agree with the reference values, and so the vapor pressure system is assumed to be well calibrated.

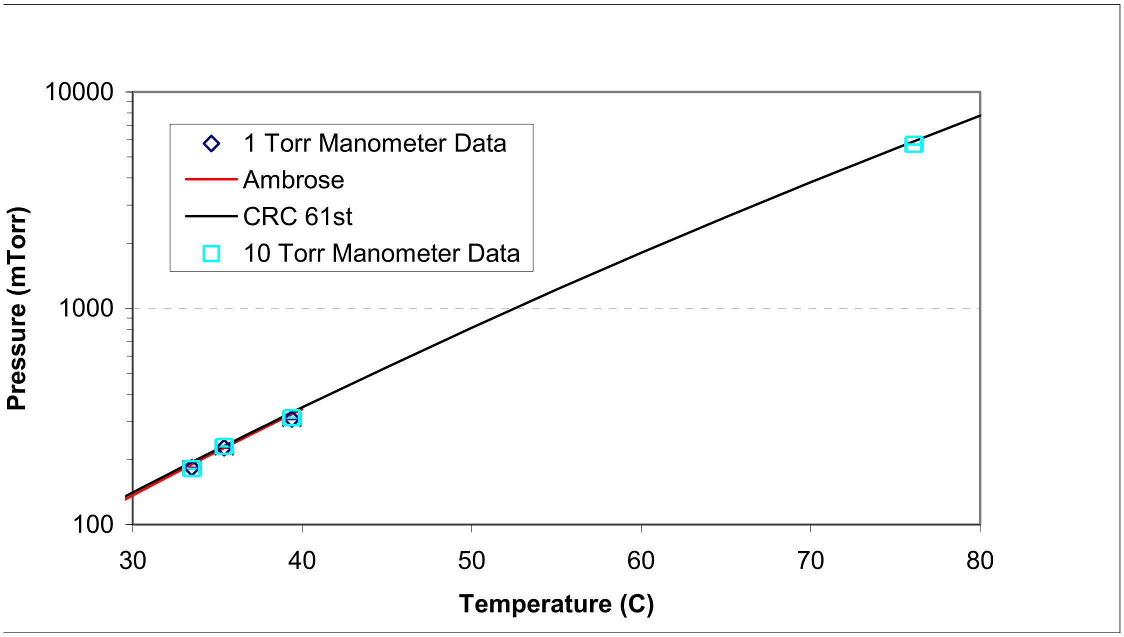

Figure E.9: Comparison of experimental vapor pressure data to two references.

Pressure versus time data were collected for FOTS at various temperatures. An example raw data curve is shown in Figure E.10, along with the baseline pressure rise and the corrected curve. This was performed a total of three times at each temperature, and the average value was used in further calculations. Regression was performed according to the Clapeyron Equation:[7]

Equation E.1 $$\ln P^{sat} = A - \frac{B}{T}$$

where P^{sat} is in Torr and T is in K. Regression results and 95% confidence limits for A and B are shown in Figure E.11. Finally, the raw data is plotted again against the Clapeyron curve calculated using A and B in Figure E.12; the data point error bars are the standard deviation of the three data points at each temperature.

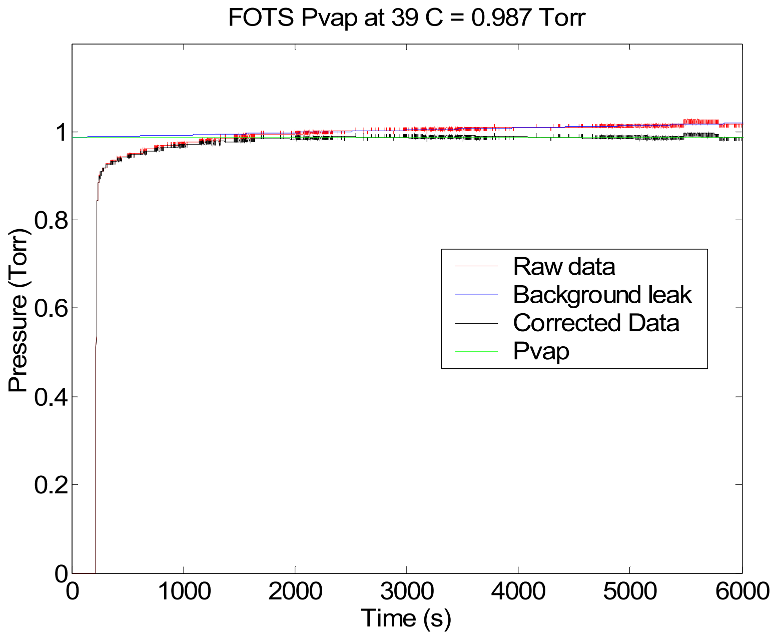

Figure E.10: Raw data, background leak rate, and corrected data for FOTS vapor pressure at 39 °C.

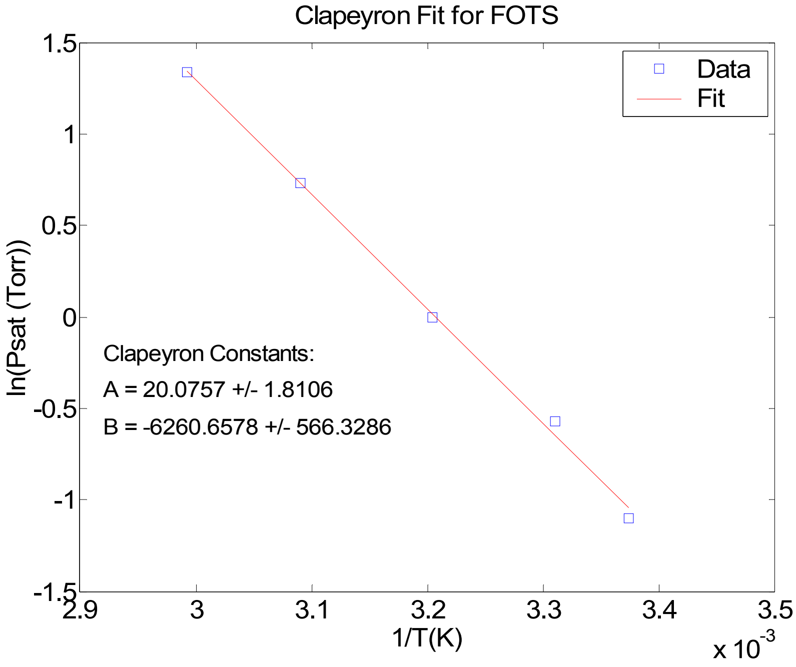

Figure E.11: Clapeyron plot and regression results for FOTS.

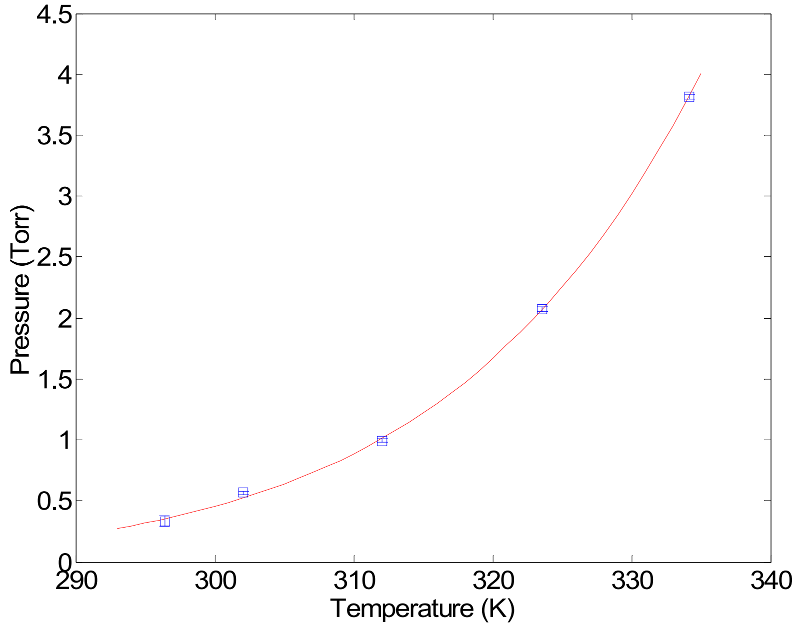

Figure E.12: Raw FOTS vapor pressure data and Clapeyron model fit.

Vapor Pressure as a Function of N_2 Flowrate through the Bubbler

The absorbance versus flowrate data shown in Figure E.8 was normalized to the predicted FOTS concentration at 72 °F, which is the temperature setpoint in the room where the FTIR data were collected; the concentration was calculated from the Ideal Gas Law. Figure E.13 shows the final results of FOTS concentration in the flow stream as a function of N_2 flowrate through the bubbler.

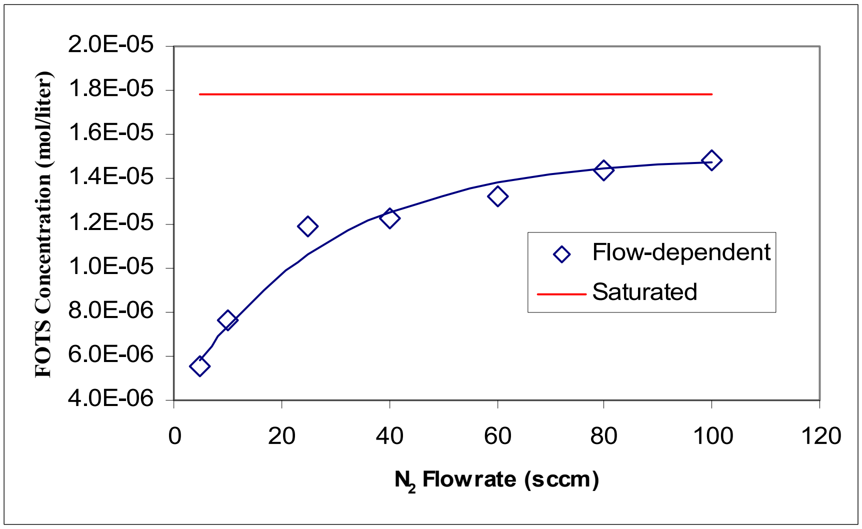

Figure E.13: Gas phase FOTS concentration as a function of N_2 carrier gas flowrate.

REFERENCES

1. Griffiths, P.R., *et al.*, Appl. Spectroscopy, 1983. 37(5): p. 458-463.

2. The Aldrich Library of FT-IR Spectra. III ed. 1997, Aldrich.

3. Mayer, T.M., *et al.*, J. Vac. Sci. Tech. B, 2000. 48(5): p. 2433-2440.

4. Blaudez, D., *et al.*, Langmuir, 2002. 18(24): p. 9158-9163.

5. CRC Handbook of Chemistry and Physics. 61st ed, ed. R.C. Weast and M.J. Astle. 1980, Boca Raton: CRC Press, Inc.

6. J.R. Elliott and C.T. Lira; http://www.egr.msu.edu/~lira/thermtxt.htm; which includes Antoine coefficients adapted from D. Ambrose, *et al.*, J Chem. Therm. 7(1975)1173.

7. Smith, J.M., H.C. Van Ness, and M.M. Abbott, eds. Introduction to Chemical Engineering Thermodynamics. 5th ed. 1996, McGraw-Hill Companies, Inc.: New York.

BIBLIOGRAPHY

3rd International SEMATECH Next Generation Lithography Workshop. 1999: Colorado.

Alam, M.J. and D.C. Cameron, Thin Solid Films, 2000. 377-378: p. 455-459.

Allara, D., A.N. Parikh, and F. Rondelez, Langmuir, 1995. 11(7): p. 2357-2360.

Ameduri, B., *et al.*, J. Polymer Sci. A, 1999. 37(1): p. 77-87.

Angst, D.L. and G.W. Simmons, Langmuir, 1991. 7(10): p. 2236-2242.

Armistead, C.G., *et al.*, J. Phys. Chem., 1969. 73(11): p. 3947-4161.

Association, S.I., International Technology Roadmap for Semiconductors. 2001: available at http://public.itrs.net/Files/2001ITRS/Home.html.

Baia, I., *et al.*, Thin Solid Films, 2001. 383: p. 244-247.

Bailey, T., *et al.*, J. Vac. Sci. Tech. B, 2000. 18(6): p. 3572.

Bailey, T., *et al.*, J. Vac. Sci. Tech. B, 2001. 19(6): p. 2806.

Bailey, T.C., *et al.*, J. Photopolymer Sci. Tech., 2002. 15(3): p. 481.

Bailey, T.C., *et al.*, Microelectron. Eng., 2001. 61-62: p. 461.

Banga, R., *et al.*, Langmuir, 1995. 11: p. 4393-4399.

Bangham, D.H. and R.I. Razouk, Trans. Faraday Soc., 1937. 33: p. 1459, 1463.

Beck, M., *et al.*, Microelectronic Eng., 2002. 61-62: p. 441-448.

Bender, M., *et al.*, Microelectronic Engineering, 2002. 61-62: p. 407.

Bendfeldt, L., *et al.*, Microelectronic Eng., 2002. 61-62: p. 455.

Bermudez, V.M., J. Phys. Chem., 1970. 74(23): p. 4160.

Bierbaum, K., *et al.*, Langmuir, 1995. 11(2): p. 512-518.

Blaudez, D., *et al.*, Langmuir, 2002. 18(24): p. 9158-9163.

Bouwhuis, G., *et al.*, Principles of Optical Disc Systems. 1985, Bristol: Adam Hilger.

Box, G.E.P., W.G. Hunter, and J.S. Hunter, Statistics for Experimenters: An Introduction to Design, Data Analysis, and Model Building. 1st ed. 1978, New York: John Wiley & Sons.

Boyd, F.R. and J.L. England, J. Geophys. Res., 1960. 65: p. 749.

Branda, M.M. and N.J. Castellani, Surface Science, 1997. 393: p. 171.

Branda, M.M., R.A. Montani, and N.J. Castellani, Surface Science, 1995. 341: p. 295.

Branda, M.M., R.A. Montani, and N.J. Castellani, Surface Science, 2000. 446: p. L89-L94.

Bronnimann, C.E., R.C. Zeigler, and G.E. Maciel, J. Am. Chem. Soc., 1988. 110(7): p. 2023.

Bruning, J.H., Proc. SPIE: Optical Microlithography, 1997. 3049: p. 14-27.

Brunner, H., *et al.*, Langmuir, 1996. 12: p. 4614.

Brunner, H., *et al.*, Langmuir, 1999. 15: p. 1899-1901.

Brzoska, J.B., I.B. Azouz, and F. Rondelez, Langmuir, 1994. 10(11): p. 4367.

Brzoska, J.B., N. Shahidzadeh, and F. Rondelez, Nature, 1992. 360: p. 719.

Bunker, B.C., *et al.*, Langmuir, 2000. 16: p. 7742.

Burneau, A., *et al.*, Langmuir, 1990. 6: p. 1364.

Calistri-Yeh, M., *et al.*, Langmuir, 1996. 12(11): p. 2747-2755.

Cao, C., A.Y. Fadeev, and T.J. McCarthy, Langmuir, 2001. 17(3): p. 757-761.

Cassie, A.B.D., Faraday Disc. Chem. Soc., 1948. 3(1): p. 11.

Chaudhury, M.K., Short range and long range forces in colloidal and macroscopic systems, Ph.D. Thesis, Departments of Microbiology and Chemical Engineering, 1984, State Univ. of NY.

Chen, P., *et al.*, Axisymmetric Drop Shape Analysis (ASDA) and its Applications, in Drops and Bubbles in Interfacial Research. 1998, Elsevier: New York. p. 61.

Chen, Y., *et al.*, J. Vac. Sci. Tech. B, 2002. 20(6): p. 2887-2890.

Choi, B.J., *et al.*, Precision Engineering, 2001. 25(3): p. 192.

Choi, B.J., *et al.*, Proc. SPIE, 2001. 4343: p. 436-439.

Chou, S.Y., *et al.*, J. Vac. Sci. Tech. B, 1997. 15(6): p. 2897.

Chou, S.Y., http://www.ee.princeton.edu/~chouweb/newproject/page3.html.

Chou, S.Y., P.R. Krauss, and L.Kong, J. Appl. Phys., 1996. 79(8): p. 6101.

Chou, S.Y., P.R. Krauss, and P.J. Renstrom, Appl. Phys. Lett., 1995. 67(21): p. 3114.

Chou, S.Y., P.R. Krauss, and P.J. Renstrom, J. Vac. Sci. Tech. B, 1996. 14(6): p. 4129.

Christou, V., *et al.*, J. Appl. Phys., 2000. 88(9): p. 5180-5187.

Chuang, I.-S. and G.E. Maciel, J. Am. Chem. Soc., 1996. 118: p. 401.

Chuang, I.-S., *et al.*, J. Phys. Chem., 1992. 96: p. 4027.

Colburn, M., *et al.*, J. Vac. Sci. Tech. B, 2001. 19(6): p. 2162.

Colburn, M., *et al.*, J. Vac. Sci. Tech. B., 2001. 19(6): p. 2685.

Colburn, M., *et al.*, Proc. SPIE, 1999. 3676(I): p. 379.

Colburn, M., *et al.*, Proc. SPIE, 2000. 3997: p. 453.

Colburn, M., *et al.*, Solid State Technology, 2001. 46(7): p. 67.

Colburn, M.E., Step and Flash Imprint Lithography: A Low-Pressure, Room-Temperature Nanoimprint Lithography, Ph.D. Thesis Thesis, Department of Chemical Engineering; Ph.D. Thesis, 2001, The University of Texas at Austin.

Coleman, M.V. and D.J.D. Thomas, Phys. Status Solidi, 1967. 22(2): p. 593-602.

Constantine, C., R. Westerman, and J. Plumhoff, Proc. SPIE, 1999. 3748: p. 153-157.

Coutts, T.J., D.L. Young, and X. Li, MRS Bulletin, 2000. 25(8): p. 58-65.

Cras, J.J., *et al.*, Biosensors and Bioelectronics, 1999. 14(8-9): p. 683-688.

CRC Handbook of Chemistry and Physics. 61st ed, ed. R.C. Weast and M.J. Astle. 1980, Boca Raton: CRC Press, Inc.

Cui, Z., P.D. Prewett, and J.G. Watson, J. Vac. Sci. Tech. B, 1996. 14(6): p. 3942-3946.

Dauksher, W.J., *et al.*, J. Vac. Sci. Tech. B, 2002. 20(6): p. 2857-2861.

Dauksher, W.J., *et al.*, J. Vac. Sci. Technol. B, 1997. 15(6): p. 2232.

Davidovits, J.V., *et al.*, Surf. Sci., 1996. 352-354: p. 369-373.

DeBoer, J.H. and J.M. Vleeskins, Proc. K. Ned. Akad. Wet., Ser. B: Palaentol., Geol., Phys., Chem., 1958. B61: p. 2-11.

Decker, C., F. Masson, and C. Bianchi, Pol. Prepr., 2001. 42(1): p. 304-305.

Donley, C., *et al.*, Langmuir, 2002. 18(2): p. 450-457.

Dressick, W.J. and J.M. Calvert, Jpn. J. Appl. Phys., 1993. 32: p. 5829.

Duval, Y., *et al.*, J. Phys. Chem. B, 2002. 106: p. 2937-2945.

Efimenko, K., W.E. Wallace, and J. Genzer, J. Coll. Int. Sci., 2002. 254: p. 306-315.

Ek, S., *et al.*, Thermochimica Acta, 2001. 379(201-212).

Evans, M., R. Jones, and R. Overstreet, Modeling Hydrochloric Acid Evaporation in ALOHATM. 1993, National Oceanic and Atmospheric Admnistration: Seattle. p. 3-6.

Fadeev, A.Y. and T.J. McCarthy, Langmuir, 1999. 15(11): p. 3759-3766.

Fadeev, A.Y. and T.J. McCarthy, Langmuir, 2000. 16(18): p. 7268-7274.

Fontaine, P., *et al.*, Appl. Phys. Lett., 1993. 62: p. 2256.

Fontaine, P., M. Goldmann, and F. Rondelez, Langmuir, 1999. 15: p. 1348.

Fowkes, F.M. and W.M. Sawyer, J. Phys. Chem., 1952. 20: p. 1650.

Fowkes, F.M., Indust. Eng. Chem., 1964. 56(12): p. 40.

Fowkes, F.M., J. Phys. Chem., 1962. 66: p. 382.

Fox, H.W. and W.A. Zisman, J. Coll. Sci., 1950. 5: p. 514.

Fox, H.W. and W.A. Zisman, J. Coll. Sci., 1952. 7: p. 109.

Fox, H.W. and W.A. Zisman, J. Colloid. Sci., 1952. 7: p. 428.

Freeman, A.J., *et al.*, MRS Bulletin, 2000. 25(8): p. 45-51.

Gao, W. and L. Reven, Langmuir, 1995. 11(6): p. 1860-1863.

Geer, R.E., *et al.*, Langmuir, 1994. 10: p. 1171-1176.

Genzer, J., K. Efimenko, and D.A. Fischer, Langmuir, 2002. 18(24): p. 9307-9311.

Gibbs, J.W., The Scientific Papers of J. Willard Gibbs. Vol. 1. 1961, New York: Dover.

Ginley, D.S. and C. Bright, MRS Bulletin, 2000. 25(8): p. 15-18.

Girifalco, L.A. and R.J. Good, J. Phys. Chem., 1957. 61: p. 904.

Goldmann, M., J.V. Davidovits, and P. Silberzan, Thin Solid Films, 1998. 327-329: p. 166-171.

Good, R.J. and L.A. Girifalco, J. Phys. Chem., 1960. 64: p. 561.

Good, R.J., Contact angle, wetting, and adhesion: a critical review, in Contact Angle, Wettability, and Adhesion, K.L. Mittal, Editor. 1993, VPS BV: Utrecht, The Netherlands. p. 3.

Good, R.J., L.A. Girifalco, and G. Kraus, J. Phys. Chem., 1958. 62: p. 1418.

Good, R.J., Nature, 1966. 212: p. 276.

Gordon, R.G., MRS Bulletin, 2000. 25(8): p. 52-57.

Greiveldinger, M. and M.E.R. Shanahan, J. Coll. Int. Sci., 1999. 215: p. 170.

Griffiths, P.R., *et al.*, Appl. Spectroscopy, 1983. 37(5): p. 458-463.

Gun'ko, V.M., *et al.*, Inter. J. Mass Spec. Ion Proc., 1998. 172: p. 161-179.

Guo, L., E. Leobandung, and S.Y. Chou, Science, 1997. 275(5300): p. 649.

Guo, L., P.R. Krauss, and S.Y. Chou, Appl. Phys. Lett., 1997. 71(13): p. 1881.

Haisma, J., *et al.*, J. Vac. Sci. Tech. B, 1996. 14(6): p. 4124.

Hare, E.F., E.G. Shafrin, and W.A. Zisman, J. Phys Chem., 1954. 58: p. 236.

Heavens, O.S., Thin Film Physics. 1970, London: Methuen & Co. Ltd.

Hertl, W., J. Phys Chem., 1968. 72(4): p. 1248-1253.

Hillebrandt, H. and M. Tanaka, J. Phys. Chem. B, 2001. 105(19): p. 4270-4276.

Hirai, Y., *et al.*, J. Photopolym. Sci. Tech., 2001. 14(3): p. 457.

Hirai, Y., *et al.*, Jpn. J. Appl. Phys., 2002. 41: p. 4186-4189.

Hiroshima, H., *et al.*, Jpn. J. Appl. Phys., 2002. 41: p. 4173-4177.

Hoffmann, P.W., M. Stelzle, and J.F. Rabolt, Langmuir, 1997. 13: p. 1887-1880.

Holländer, A., J.E. Klemberg-Sapieha, and M.R. Wertheimer, Macromolecules, 1994. 27(10): p. 2893-2895.

Holysz, L. and E. Chibowski, Langmuir, 1992. 8: p. 303.

Iler, R.K. and R.L. Dalton, 1956: p. 955-963.

Iler, R.K., The Chemistry of Silica. 1979, New York: John Wiley & Sons.

International Technology Roadmap for Semiconductors. 1999, Semiconductor Industry Association: www.semichips.org.

International Technology Roadmap for Semiconductors: 2002 Update. 2002, Semiconductor Industry Association. p. 119.

Israelachvilli, J.N. and M.L. Gee, Langmuir, 1989. 5: p. 288.

J.R. Elliott and C.T. Lira; http://www.egr.msu.edu/~lira/thermtxt.htm; which includes Antoine coefficients adapted from D. Ambrose, *et al.*, J Chem. Therm. 7(1975)1173.

Jackman, R.J., *et al.*, Langmuir, 1999. 15: p. 826-836.

Jaszewski, R.W., *et al.*, Applied Surface Science, 1999. 143: p. 301.

Jaszewski, R.W., *et al.*, Microelectronic Engineering, 1997. 35: p. 381.

Jaszewski, R.W., *et al.*, Microelectronic Engineering, 1998. 41/42: p. 575.

Jo, Y.-S., *et al.*, J. Appl. Phys., 1986. 60(7): p. 2564.

Johnson, S.C., *et al.*, Proc. SPIE: Emerging Lithographic Technologies VII, 2003. 5037: p. submitted.

Kawazoe, H., *et al.*, MRS Bulletin, 2000. 25(8): p. 28-36.

Kim, S., H.K. Christenson, and J.E. Curry, Langmuir, 2002. 18(6): p. 2125-2129.

Kinney, D.R., I.-S. Chuang, and G.E. Maciel, J. Am. Chem. Soc., 1993. 115: p. 6786.

Kloosterboer, J.G. and G.F.C.M. Lijten, Polymer, 1987. 28(7): p. 1149.

Knez, Z. and Z. Novak, J. Chem. Eng. Data, 2001. 46: p. 858-860.

Kollman, P., J. Am. Chem. Soc., 1977. 99: p. 4875.

Komuro, M., *et al.*, Jpn. J. Appl. Phys., 2000. 39(7075-7079).

Komuro, M., *et al.*, Jpn. J. Appl. Phys., 2002. 41: p. 4182-4185.

Kopylov, V.M., *et al.*, Pol. Sci. A, 1995. 37(3): p. 242-265.

Krauss, P.R. and S.Y. Chou, Appl. Phys. Lett., 1997. 71(21): p. 3174.

Kumar, A., H.A. Biebuyeck, and G.M. Whitesides, Langmuir, 1994. 10: p. 1498-1511.

Kwok, D.Y., D. Li, and A.W. Neumann, Coll. Surf. A., 1994. 89: p. 181.

Kwok, D.Y., D. Li, and A.W. Neumann, Langmuir, 1994. 10: p. 1323.

Kwok, D.Y., *et al.*, Langmuir, 1997. 13: p. 2880.

Le Grange, J.D. and J.L. Markham, Langmuir, 1993. 9: p. 1749.

Lee, L.-H., J. Coll. Int. Sci., 1999. 214: p. 64.

Lee, L.-H., Langmuir, 1996. 12: p. 1681.

Levine, S.M. and S.H. Garofalini, Surf. Sci., 1985. 163: p. 59-66.

Lewis, B.G. and D.C. Paine, MRS Bulletin, 2000. 25(8): p. 22-27.

Li, D. and A.W. Neumann, J. Coll. Int. Sci., 1990. 137(1): p. 304.

Li, D. and A.W. Neumann, J. Coll. Int. Sci., 1992. 148(1): p. 190.

Li, D. and A.W. Neumann, Langmuir, 1993. 9: p. 3728.

Li, M., *et al.* in Electron, Ion and Photon Beam Technol. and Nanofabrication. 2000. Palms Springs ,CA.

Linden, M., J.P. Slotte, and J.B. Rosenholm, Langmuir, 1996. 12(18): p. 4449-4454.

Lindén, M., J.P. Slotte, and J.B. Rosenholm, Langmuir, 1996. 12(18): p. 4449-4454.

Lisovskii, I.P., *et al.*, Thin Solid Films, 1992. 213: p. 164-169.

Litovchenko, V.G. and G.P. Romanova, Thin Solid Films, 1981. 81: p. 27-34.

Litovchenko, V.G. and V.P. Kostylev, Semiconductor Films and Layered Structures. 1977, Kiev: Naukova Dumka.

Loo, Y.-L., *et al.*, Appl. Phys. Lett., 2002. 81(3): p. 562-564.

Loo, Y.-L., *et al.*, J. Am. Chem. Soc., 2002. 124: p. 7654-7655.

Maboudian, R., W.R. Ashurst, and C. Carraro, Sensors and Actuators, 2000. 82: p. 219-223.

Macleod, H.A., Thin-Film Optical Filters. 2nd Ed. ed. 1989, New York: McGraw-Hill.

Malandrini, H., *et al.*, Langmuir, 1997. 13: p. 1337-1341.

Mancini, D.P., *et al.*, J. Vac. Sci. Tech. B, 2002. 20(6): p. 2896-2901.

Mancini, D.P., *et al.*, Proc. SPIE: 21st Annual BACUS Symposium on Photomask Technology, 2001. 4562: p. 593-599.

Martin, C.J., *et al.*, J. Vac. Sci. Tech. B, 2002. 20(6): p. 2891-2895.

Matsui, S., *et al.*, J. Vac. Sci. Tech. B, 2001. 19(6): p. 2801-2805.

Matsuzawa, T., *et al.*, J. Electrochem. Soc., 1981. 128(1): p. 184-187.

Mayer, T.M., *et al.*, J. Vac. Sci. Tech. B, 2000. 48(5): p. 2433-2440.

McGovern, M.E., K.M.R. Kallury, and M. Thompson, Langmuir, 1994. 10: p. 3607-3614.

Mergel, D., *et al.*, J. Appl. Phys., 2000. 88(5): p. 2437-2442.

Milliron, D.J., *et al.*, J. Appl. Phys., 2000. 87(1): p. 572-576.

Minami, T., MRS Bulletin, 2000. 25(8): p. 38-44.

Mitra, S.A., Phil. Mag., 1982. B45: p. 529.

Monde, T., *et al.*, J. Coll. Int. Sci., 1997. 185: p. 111-118.

Moore, G., Proc. SPIE, 1995. **2438**: p. 2-17.

Morrow, B.A. and A.J. McFarlan, Langmuir, 1991. 7: p. 1695.

Neumann, A.W., *et al.*, J. Coll. Int. Sci., 1974. 49(2): p. 291.

Ohtake, T., N. Mino, and K. Ogawa, Langmuir, 1992. 8(9): p. 2081.

Omata, T., *et al.*, Appl. Phys. A, 2000. 71: p. 609-614.

Otto, M., *et al.*, Microelectronic Eng., 2001. 57-58: p. 361-366.

Ouyang, M., *et al.*, Chem. Mater., 2000. 12(6): p. 1591-1596.

Owens, D.K. and R.C. Wendt, J. Appl. Polym. Sci., 1969. 13: p. 1741.

Pantelides, S.T. and W.A. Harrison, Phys. Rev. B, 1976. 13: p. 2667.

Paparazzo, E., Appl. Surf. Sci., 1993. 72: p. 313.

Paparazzo, E., *et al.*, J. Vac. Sci. Tech. A, 1992. 10(4): p. 2892.

Parikh, A.N., *et al.*, J. Phys. Chem., 1994. 98: p. 7577.

Pellerite, M.J., E.J. Wood, and V.W. Jones, Journal of Physical Chemistry B, 2002. 106(18): p. 4746-4754.

Peri, J.B. and A.L. Hensley, J. Phys. Chem., 1968. 72: p. 2926.

Raider, S.I., *et al.*, J. Electrochem. Soc., 1976. 123: p. 560.

Rankin, S.E. and A.V. McCormick, Chem. Eng. Sci., 2000. 55: p. 1955-1967.

Resnick, D.J., *et al.*, Proc. SPIE, 2002. 4688: p. 205.

Resnick, D.J., *et al.*, Semiconductor International, 2002(June 1).

Reymond, J.P. and F. Kolenda, Powder Tech., 1999. 103: p. 30-36.

Richter, A.G., *et al.*, Phys. Rev. E, 2000. 61(1): p. 607-615.

Rihter, A.G., *et al.*, Langmuir, 1998. 14(21): p. 5980-5983.

Ruchoeft, P., *et al.*, J. Vac. Sci. Tech. B, 1999. 17(6): p. 2965.

Ruzyllo, J., *et al.*, Proc. Electrochem Soc., 1987. 87-11: p. 281-289.

Rye, R.R., G.C. Nelson, and M.T. Dugger, Langmuir, 1997. 13: p. 2965-2972.

Scanlon, L., No P-N Intended, in Technology Review, 2003. 106(1): 88.

Scheer, H.-C., *et al.* in Electron, Ion and Photon Beam Technol. and Nanofabrication. 1998. Chicago.

Schondelmaier, D., *et al.*, Langmuir, 2002. 18: p. 6242-6245.

Schrader, M.E., Langmuir, 1993. 9: p. 1959.

Schreiber, F., Prog. Surf. Sci., 2000. 65: p. 151-256.

Schultz, H., *et al.*, J. Vac. Sci. Tech. B, 2000. 18(4): p. 1861.

Seki, S., Y. Sawada, and T. Nishide, Thin Solid Films, 2001. 388: p. 22-26.

Serway, R.A., Physics for Scientists and Engineers. 3rd ed. 1990, Philadelphia: Saunders College Publishing.

Shafrin, E.G. and W.A. Zisman, J. Phys. Chem., 1960. 64: p. 519.

Shaw, J., *et al.*, Solid State Technology, 1987. 30(6): p. 83.

Shigesato, Y., *et al.*, Vacuum, 2000. 59: p. 614-621.

Shioji, S., *et al.*, Adv. Powder Tech., 2001. 12(3): p. 331-342.

Silberzan, P., *et al.*, Langmuir, 1991. 7: p. 1647.

Sindorf, D.W. and G.E. Maciel, J. Am. Chem. Soc., 1983. 105: p. 1487.

Sindorf, D.W. and G.E. Maciel, J. Phys. Chem., 1982. 86: p. 5208.

Smith, J.M., H.C. Van Ness, and M.M. Abbott, eds. Introduction to Chemical Engineering Thermodynamics. 5th ed. 1996, McGraw-Hill Companies, Inc.: New York.

Smith, K.H., *et al.*, J. Vac. Sci. Tech. B, 2001. 19(6): p. 2906-2910.

Sneh, O. and M. George, J. Phys. Chem., 1995. 99: p. 4639.

Sneh, O., M.A.Cameron, and S.M. George, Surf. Sci., 1996. 364: p. 61-78.

Spelt, J.K., D.R. Absolom, and A.W. Neumann, Langmuir, 1986. 2: p. 620.

Srinivasan, U., *et al.* in Proc. Solid-State Sens. Act. Workshop. 1998. Hilyon Head.

Stevens, M.J., Langmuir, 1999. 15: p. 2773-2778.

Sugimura, H. and N. Makagiri, Jpn. J. Appl. Phys., 1997. 36: p. L968.

Sugimura, H., *et al.*, J. Vac. Sci. Tech. B, 2002. 20(1): p. 393-395.

Sugimura, H., *et al.*, Langmuir, 2000. 16: p. 885.

Sung, M.M., G.J. Kluth, and R. Maboudian, J. Vac. Sci. Tech. A, 1998. 17(2): p. 540-544.

Swadener, J.G., K.M. Liechti, and A.L. de Lozanne, J. Mech. Phys. Sol., 1999. 47: p. 223-258.

Taniguchi, J., *et al.*, Jpn. J. Appl. Phys., 2002. 41: p. 4194-4197.

Terzini, e., P. Thilakan, and C. Minarini, Materials Science and Engineering, 2000. B77: p. 110-114.

The Aldrich Library of FT-IR Spectra. III ed. 1997, Aldrich.

Thompson, L.F., C.G. Willson, and M.J. Bowden, Introduction to Microlithography. 2nd ed. 1994, Washington, D.C.: ACS.

Tripp, C.P. and M.L. Hair, Langmuir, 1995. 11: p. 1215.

Tripp, C.P. and M.L. Hair, Langmuir, 1995. 11: p. 149.

Tripp, C.P., R.P.N. Veregin, and M.L. Hair, Langmuir, 1993. 9: p. 3518.

Tristram, C., Supercomputing Resurrected, in Technology Review, 2003. 106(1): 52-60.

Ugliengo, P., *et al.*, Chem. Phys. Lett., 1992. 191: p. 537.

Une, A., *et al.*, Microelectronic Eng., 2002. 61-62: p. 113.

Vallant, T., *et al.*, J. Phys. Chem. B, 1998. 102: p. 7190-7197.

Vallant, T., *et al.*, Langmuir, 1999. 15: p. 5339-5346.

van Oss, C.J., M.K. Chaudhury, and R.J. Good, Adv. Coll. Int. Sci., 1987. 28: p. 35-64.

van Oss, C.J., R.J. Good, and M.K. Chaudhury, J. Colloid Interface Sci., 1986. 111: p. 378.

van Oss, C.J., R.J. Good, and M.K. Chaudhury, Langmuir, 1988. 4: p. 884-891.

Veiseh, M., M.H. Zareie, and M. Zhang, Langmuir, 2002. 18(17): p. 6671-6678.

Volpe, C.D. and S. Siboni, J. Coll. Int. Sci., 1997. 195: p. 121.

Wang, D., *et al.*, Appl. Phys. Lett., 1997. 70(12): p. 1593.

Wang, J., *et al.*, Applied Physics Letters, 1999. 75(18): p. 2767.

Wang, J., *et al.*, J. Vac. Sci. Tech. B, 1999. 17(6): p. 2957.

Wang, R. and S.L. Wunder, Langmuir, 2000. 16(11): p. 5008-5016.

Wang, R., *et al.*, Langmuir, 2000. 16(2): p. 568-576.

Ward, C.A. and A.W. Neumann, J. Coll. Int. Sci., 1974. 49(2): p. 286.

Wasson, J.R., *et al.*, J. Vac. Sci. Tech. B, 2001. 19(6): p. 2635-2640.

Watanabe, H. and Y. Todokoro, J. Vac. Sci. Tech. B, 1993. 11(6): p. 2669-2674.

Wei, Q., H. Zheng, and Y. Huang, Solar Energy Mat. & Solar Cells, 2001. 68: p. 383-390.

Werst, D.W. and E.I. Vinokur, J. Phys. Chem. B, 2001. 105(8): p. 1587-1593.

Widden, T.K., *et al.*, Nanotechnology, 1996. 7: p. 447.

Wieber, G., *et al.* in Organic-Inorganic Hybrids Conference. 2000. University of Surrey, Guilford, UK.

Wu, W., J. R.F. Giese, and C.J. van Oss, 1995.

Xia, Y. and G.M. Whitesides, Angew. Chem. Int. Ed. Engl., 1998. 37: p. 550.

Xu, Z., Q. Liu, and J. Ling, Langmuir, 1995. 11: p. 1044.

Young, T., Trans. R. Soc., 1805. 95: p. 65.

Yu, Z., S.J. Schablitsky, and S.Y. Chou, Appl. Phys. Lett., 1999. 74(16): p. 2381.

Zhang, W. and S.Y. Chou, J. Vac. Sci. Tech. B, 2001. 79(6): p. 845-847.

Zhao, X. and R. Kopelman, J. Phys. Chem., 1996. 100: p. 11014.

Zhuravlev, L.T., Coll. Surf. A, 2000. 173: p. 1-38.

Zisman, W.A., Constitutional Effects on Adhesion and Abhesion, in Adhesion and Cohesion, P. Weiss, Editor. 1962, Eksevier: New York. p. 183.

Zisman, W.A., Relation of the Equilibrium Contact Angle to Liquid and Solid Constitution, in Contact Angle, Wettability, and Adhesion. Advances in Chemistry Series No. 43, R.F. Gould, Editor. 1964, ACS: Washington, D.C. p. 1.

VITA

Todd Christopher Bailey was born in the Columbia Hospital for Women in Washington, D.C. in October 20, 1967. His mother and father are Sandra Staples Geisinger and Alfred Graham Bailey, Sr., and his stepmother and stepfather are Sheryl Blase Bailey and David Wayne Geisinger. Todd attended Shenedehowa High School in Clifton Park, NY, and was graduated with a New York State Regents Diploma in June, 1985. He received his Associate of Science in Engineering Science from Hudson Valley Community College in May, 1996, and his Science Baccalaureate in Chemical Engineering from the Massachusetts Institute of Technology in June, 1998. While at The University of Texas, Todd interned at Philips Analytical from June – October, 1999, and at Motorola Physical Sciences Research Laboratories from June – August, 2001.

Permanent address: 11160 Jollyville Road #434, Austin, TX 78759

This dissertation was typed by Todd Christopher Bailey.